frontiers | Research Topics

Organic matter accumulation in organic-rich shales

Edited by
Qian Zhang, Ruyue Wang, George Kontakiotis, Ken'ichi Matsumoto and Leibo Bian

Published in
Frontiers in Earth Science

ISSN 1664-8714
ISBN 978-2-8325-4399-3
DOI 10.3389/978-2-8325-4399-3

About Frontiers

Frontiers is more than just an open access publisher of scholarly articles: it is a pioneering approach to the world of academia, radically improving the way scholarly research is managed. The grand vision of Frontiers is a world where all people have an equal opportunity to seek, share and generate knowledge. Frontiers provides immediate and permanent online open access to all its publications, but this alone is not enough to realize our grand goals.

Frontiers journal series

The Frontiers journal series is a multi-tier and interdisciplinary set of open-access, online journals, promising a paradigm shift from the current review, selection and dissemination processes in academic publishing. All Frontiers journals are driven by researchers for researchers; therefore, they constitute a service to the scholarly community. At the same time, the *Frontiers journal series* operates on a revolutionary invention, the tiered publishing system, initially addressing specific communities of scholars, and gradually climbing up to broader public understanding, thus serving the interests of the lay society, too.

Dedication to quality

Each Frontiers article is a landmark of the highest quality, thanks to genuinely collaborative interactions between authors and review editors, who include some of the world's best academicians. Research must be certified by peers before entering a stream of knowledge that may eventually reach the public - and shape society; therefore, Frontiers only applies the most rigorous and unbiased reviews. Frontiers revolutionizes research publishing by freely delivering the most outstanding research, evaluated with no bias from both the academic and social point of view. By applying the most advanced information technologies, Frontiers is catapulting scholarly publishing into a new generation.

What are Frontiers Research Topics?

Frontiers Research Topics are very popular trademarks of the *Frontiers journals series*: they are collections of at least ten articles, all centered on a particular subject. With their unique mix of varied contributions from Original Research to Review Articles, Frontiers Research Topics unify the most influential researchers, the latest key findings and historical advances in a hot research area.

Find out more on how to host your own Frontiers Research Topic or contribute to one as an author by contacting the Frontiers editorial office: frontiersin.org/about/contact

Organic matter accumulation in organic-rich shales

Topic editors

Qian Zhang — Peking University, China

Ruyue Wang — State Key Laboratory of Shale Oil and Gas Enrichment Mechanisms and Efficient Development, China

George Kontakiotis — National and Kapodistrian University of Athens, Greece

Ken'ichi Matsumoto — Toyo University, Japan

Leibo Bian — Aarhus University, Denmark

Citation

Zhang, Q., Wang, R., Kontakiotis, G., Matsumoto, K., Bian, L., eds. (2024). *Organic matter accumulation in organic-rich shales*. Lausanne: Frontiers Media SA.

doi: 10.3389/978-2-8325-4399-3

Table of contents

05 Editorial: Organic matter accumulation in organic-rich shales
Qian Zhang

08 Three-dimensional numerical simulation study of pre-cracked shale based on CT technology
Yuhan Yang, Zhonghu Wu, Yujun Zuo, Huailei Song, Wentao Wang, Motian Tang and Hengtao Cui

20 Physical properties variation of crude oil under natural laboratory and its geological implications: Dongying Sag, eastern China
Yazhou Liu, Jianhui Zeng, Shuning Liu and Hui Long

43 Cyclostratigraphy and high-frequency sedimentary cycle framework for the Late Paleozoic Fengcheng Formation, Junggar Basin
Guoyong Liu, Rui Zhang, Xiangwu He, Ren Wei, Rukai Zhu, Yong Tang, Wenjun He, Menglin Zheng, Qiusheng Chang, Ran Wang and Xinmei Zhao

56 Sweet spot areas for shale oil and shale gas plays in the Upper Cretaceous rocks of the Middle Magdalena Valley, Colombia: insights from basin modeling
Andrés Pastor-Chacón, Roberto Aguilera, Jorge Luis Triana, Manuel Paez-Reyes, Maria Cantisano, Luis Bravo, Néstor Gamba, Miled Niño, Alexandra Delgado, Gabriel Mendoza, Juan David Rodriguez, Oscar Romero-Ballén, Maria Cecilia Ruiz, Hugo Buitrago and Humberto Fuenzalida

75 Distribution pattern of natural fractures in lacustrine shales: a case study of the Fengcheng formation in the Mahu Sag of the Junggar Basin, China
Guoyong Liu, Zhijun Jin, Sen Yang, Lianbo Zeng, Wenjun He, Xiaoyu Du, Guoqing Lu and Guoping Liu

85 Distribution characteristics of organic matter in the Fengcheng Formation in Mahu Sag, Junggar Basin: implications for hydrocarbon generation model in alkaline lacustrine deposition
Minjie Ni, Yuanyuan Zhang, Yong Tang and Wenjun He

102 Cyclostratigraphy of Lower Permian alkaline lacustrine deposits in the Mahu Sag, Junggar basin and its stratigraphic implication
Yong Tang, Wenjun He, Ran Wang, Haijiao Ren, Zhijun Jin, Zhuang Yang and Yuanyuan Zhang

112 Controlling factors of organic matter accumulation and lacustrine shale distribution in Lianggaoshan Formation, Sichuan Basin, SW China
Rui Fang, Yuqiang Jiang, Shasha Sun, Yao Luo, Lin Qi, Dazhong Dong, Qiang Lai, Yuzhuo Luo and Zengzheng Jiang

124 Source-reservoir rock assemblages and hydrocarbon accumulation models in the Middle-Lower Jurassic of eastern Sichuan Basin, China
Rong Bai, Shaomin Zhang, Haitao Hong, Chunyu Qin, Yucong Li, Changhong Cai, Xiangye Kong, Nan Li, Dong Lei, Xin Lei, Changyong Wang, Tao Jin, Jinliang Gao and Wenbin Tang

133 Early–middle Jurassic source to sink evolution and its tectonic significance in the northeastern Sichuan Basin
HaiTao Hong, ChunYu Qin, ShaoMin Zhang, ZhiJie Zhang, XiaoJuan Wang, Nan Li, DaWei Cheng and Wenbin Tang

frontiers | Frontiers in Earth Science

TYPE Editorial
PUBLISHED 19 January 2024
DOI 10.3389/feart.2024.1347462

OPEN ACCESS

EDITED AND REVIEWED BY
David R. Lentz,
University of New Brunswick
Fredericton, Canada

*CORRESPONDENCE
Qian Zhang,
amadozhang@pku.edu.cn

RECEIVED 30 November 2023
ACCEPTED 08 January 2024
PUBLISHED 19 January 2024

CITATION
Zhang Q (2024), Editorial: Organic matter accumulation in organic-rich shales.
Front. Earth Sci. 12:1347462.
doi: 10.3389/feart.2024.1347462

Editorial: Organic matter accumulation in organic-rich shales

Qian Zhang*

Institute of Energy, School of Earth and Space Science, Peking University, Beijing, China

KEYWORDS

organic-rich shale, accumulation, deposition, shale oil, shale gas

Editorial on the Research Topic
Organic matter accumulation in organic-rich shales

Shale oil and gas have been regarded as alternative resources for conventional petroleum in recent decades. The exploration and development of shale oil and gas are, however, confronted with dilemmas. One of the most striking challenges for petroleum geologists is the "sweet spot identification", for which the assessment criteria are not fully clearly. Nevertheless, it is widely accepted that the "sweet spot" of shale oil and gas is a comprehensive embodiment of multiple optimal parameters, including desirable organic matter type, appropriate thermal maturity, excellent petrophysical and rock mechanical properties, and so on (Littke et al., 1991; Bechtel et al., 2002; Sachsenhofer et al., 2003; Bechtel et al., 2012; Rippen et al., 2013; Sun et al., 2013; Ghazwani et al., 2018; Zhang et al., 2019; Zhang et al., 2020; Cai et al., 2022; Deng et al., 2022; Zheng et al., 2022; Zheng et al., 2023a; Zheng et al., 2023b). These properties are largely controlled by the processes of organic-rich shale formation. Consequently, a better understanding of the organic matter accumulation in organic-rich shales is vital for successful shale oil and gas exploration and extraction.

Yang et al. numerically simulated three-dimensional characteristics of cracked shale based on CT technology. The finite element software RFPA-3D was employed to create a three-dimensional non-uniform numerical model, which can be used to present the meso structure of rock mass. The results showed that prefabricated fractures and quartz content will significantly affect the tensile strength and weaken the destructive strength of shales. The crack initiation angle was supposed to be controlled by the angle of prefabricated crack. The modes of shale damage were divided into four categories. This study helps for revealing the mechanisms of fracture initiation and propagation in the hydraulic fracturing process.

Pastor-Chacón et al. analyzed the sweet spot areas for shale oil and shale gas plays in the Upper Cretaceous rocks of the Middle Magdalena Valley, Colombia, using basin modeling approaches. A three-dimensional basin model for three Upper Cretaceous source rocks within the Middle Magdalena Valley Basin has been established in this study. The results showed that the sweet spot areas in the studied basin primarily reply on porosity, thermal maturity, gas-oil ratios, and retained oil and gas volumes, and they may also be affected by natural fractures and pore pressure conditions. This study helps in sweet spot identification in the study area and probably offers insights in shale oil and gas exploration in other basins and areas.

Liu et al. studied the physical properties of shale oil in the Dongying Sag, Bohai Bay Basin, eastern China. The Dongying Sag has experienced decades of conventional petroleum exploration and development, and it contains several sets of high-quality source rock formations. Integrated petrographic and geochemical approached were adopted to analyze the organofacies and thermal maturity proxies of the Eocene Es3 and Es4 formations, which were linked to the physical properties of crude oil. The results showed that crude oil physical and geochemical properties can be ascribed to the differences in organofacies and thermal maturity. This study is likely helps in screening beneficial facies and thermal maturity stages for the sweet spots of shale oil formations.

Liu et al. reconstructed the sedimentary framework of the world's oldest alkaline lake during the Late Paleozoic period when the Fengcheng Formation in the Mahu Sag, Junggar Basin, China was formed using astronomical methods. The results showed that a period of 405 kyr eccentricity played a key role in dividing and correlating the high-frequency sedimentary sequences in lacustrine shales. The lake levels reached their highest value during the deposition of the second member of Fengcheng Formation. The spatial distribution of lithofacies in the Fengcheng Formation was proved within the isochronous cycle framework under the constraints of long eccentricity cycles. These findings are beneficial for characterizing alkaline lacustrine sequences and forecasting favorable areas for shale oil exploration with higher accuracy.

Liu et al. characterized the distribution pattern of natural fractures in the Fengcheng Formation in the Mahu Sag, Junggar Basin, China. The results showed that transformational shear fracture, intraformational open fracture and bed-parallel shear fracture were observed in the Fengcheng Formation, among which the intraformational open fracture is the most developed type. The abundance and extent of fracture were primarily controlled by lithology and brittle mineral content. These fractures are closely related to fault activity and are caused by regional stress fields. Gaining knowledge on the spatiotemporal distribution of natural fracture in shale could help in shale oil and gas exploration and extraction.

Bai et al. analyzed source-reservoir rock assemblages and hydrocarbon accumulation models in the Middle-Lower Jurassic of eastern Sichuan Basin, China. The results demonstrated that a range of reservoir rocks were developed in the Jurassic strata of eastern Sichuan. Among those several sets of rocks, the Da'anzhai, Dongyuemiao, and Liangshan shale formations should be the primary exploration targets, especially the parts deposited in the synclines of semi-deep lake. Then, the Liangshan and Shaximiao sandstone formations could be the secondary exploration targets, particularly in the anticline areas with better sealing conditions. Limestone formations only distributed in limited areas, and those with high and steep fractures are preferable for petroleum exploration.

Fang et al. investigated the distribution lacustrine shale and primary controls of organic matter accumulation in the Middle Jurassic Lianggaoshan Formation in the Sichuan Basin, southwestern China based on seismic interpretation, core observation, high-frequency geochemical analysis. The results showed that the migration of depocenters plays a key role in the distribution of lacustrine organic-rich shale. Organic matter accumulation in first and second Members of organic-rich shale was controlled by paleoproductivity and preservation condition caused by lake-level rise. In contrast, the primary controls of OM accumulation in the third Member are the joint effects of terrestrial OM input and the preservation condition created by rapid deposition.

Ni et al. studied the distribution characteristics of organic matter in the Fengcheng Formation in Mahu Sag, Junggar Basin, China. Mineralogical, organic geochemical and petrographic methods were adopted to characterize the abundance, type, and bio-precursors of organic matter, as well as mineral composition. The results suggested that the Fengcheng Formation can be divided into three zones based on alkaline mineral assemblages, namely, the inner zone dominated by sodium carbonate minerals, the transitional zone containing of higher borosilicate mineral content, and the marginal zone hosting abundant calcite. Lamalginite and telalginite were observed in both the inner and transitional zones, while a certain amount of terrigenous input, mainly inertinite were identified in the marginal zone. The slight variation in pre-cursors resulted in tiny difference in organic matter type in the three zones.

Hong et al. assessed the source to sink of Early-Middle Jurassic strata and revealed its tectonic significance in northeastern Sichuan Basin. Several formations mainly comprise of detrital sediments, lacustrine and fluvial-delta deposits. The orogenesis on the periphery of the basin, e.g., the uplifting of Micangshan Mountain, Dabashan Mountain and Qinling Mountain, were thought to control the sedimentary environment and source property.

Tang et al. carried out cyclostratigraphical and sedimentological analysis of the Lower Permian alkaline lacustrine deposits in the Mahu Sag, Junggar Basin, China. A detailed astronomical cycle and an astronomical time scale, as well as an isochronous sedimentary framework of the Lower Permian Fengcheng Formation in the northern Mahu Sag were constructed by using different wells based on cyclostratigraphy. The spatio-temporal variation in the lithofacies within the Fengcheng Formation was reconstructed based on lithofacies identification.

In summary, this Research Topic collected research articles primarily involving the formation conditions of organic-rich shales. A few of them offer us the physical properties of both rock and crude oil. It is obviously that, although the 10 papers have various research focuses, the Research Topic of articles in this Research Topic helps in gaining new knowledge in this research area and enriching the datasets in the different study blocks. Hopefully, this Research Topic brings some novel insights into shale oil and gas exploration and development.

Author contributions

QZ: Writing–original draft.

Funding

The author(s) declare financial support was received for the research, authorship, and/or publication of this article. This work was supported by National Natural Science Foundation of China (Grant No. 42090025) and China Postdoctoral Science Foundation (Grant No. 2021TQ0003).

Acknowledgments

The reviewers are acknowledged for their constructive and valuable comments that improved the published papers. Guest editors' supports in organizing this Research Topic are much appreciated.

Conflict of interest

The author declares that the research was conducted in the absence of any commercial or financial relationships that could be construed as a potential conflict of interest.

Publisher's note

All claims expressed in this article are solely those of the authors and do not necessarily represent those of their affiliated organizations, or those of the publisher, the editors and the reviewers. Any product that may be evaluated in this article, or claim that may be made by its manufacturer, is not guaranteed or endorsed by the publisher.

References

Bechtel, A., Jia, J., Strobl, S. A., Sachsenhofer, R. F., Liu, Z., Gratzer, R., et al. (2012). Palaeoenvironmental conditions during deposition of the Upper Cretaceous oil shale sequences in the Songliao Basin (NE China): implications from geochemical analysis. *Org. Geochem.* 46, 76–95. doi:10.1016/j.orggeochem.2012.02.003

Bechtel, A., Sachsenhofer, R. F., Kolcon, I., Gratzer, R., Otto, A., and Püttmann, W. (2002). Organic geochemistry of the Lower Miocene Oberdorf lignite (Styrian Basin, Austria): its relation to petrography, palynology and the palaeoenvironment. *Int. J. Coal Geol.* 51 (1), 31–57. doi:10.1016/s0166-5162(02)00079-4

Cai, Y., Zhu, R., Luo, Z., Wu, S., Zhang, T., Liu, C., et al. (2022). Lithofacies and source rock quality of organic-rich shales in the cretaceous qingshankou formation, songliao basin, NE China. *Minerals* 12 (4), 465. doi:10.3390/min12040465

Deng, E., Zhang, Q., Jin, Z., Zhu, R., Yan, Z., Jiang, B., et al. (2022). Non-overmature equivalents confirmed a high initial hydrocarbon generation potential of the Permian Longtan Shale in southern China. *Int. J. Coal Geol.* 259, 104043. doi:10.1016/j.coal.2022.104043

Ghazwani, A., Littke, R., Gaus, G., and Hartkopf-Fröder, C. (2018). Assessment of unconventional shale gas potential of organic-rich Mississippian and Lower Pennsylvanian sediments in western Germany. *Int. J. Coal Geol.* 198, 29–47. doi:10.1016/j.coal.2018.08.008

Littke, R., Leythaeuser, D., Rullkötter, J., and Baker, D. R. (1991). Keys to the depositional history of the posidonia shale (toarcian) in the hils syncline, northern Germany. *Geol. Soc. Lond. Spec. Publ.* 58 (1), 311–333. doi:10.1144/gsl.sp.1991.058.01.20

Rippen, D., Littke, R., Bruns, B., and Mahlstedt, N. (2013). Organic geochemistry and petrography of Lower Cretaceous Wealden black shales of the Lower Saxony Basin: the transition from lacustrine oil shales to gas shales. *Org. Geochem.* 63, 18–36. doi:10.1016/j.orggeochem.2013.07.013

Sachsenhofer, R. F., Bechtel, A., Reischenbacher, D., and Weiss, A. (2003). Evolution of lacustrine systems along the Miocene Mur-Mürz fault system (Eastern Alps, Austria) and implications on source rocks in pull-apart basins. *Mar. Petroleum Geol.* 20 (2), 83–110. doi:10.1016/s0264-8172(03)00018-7

Sun, P., Sachsenhofer, R. F., Liu, Z., Strobl, S. A., Meng, Q., Liu, R., et al. (2013). Organic matter accumulation in the oil shale-and coal-bearing Huadian Basin (Eocene; NE China). *Int. J. Coal Geol.* 105, 1–15. doi:10.1016/j.coal.2012.11.009

Zhang, Q., Grohmann, S., Xu, X., and Littke, R. (2020). Depositional environment and thermal maturity of the coal-bearing Longtan Shale in southwest Guizhou, China: implications for shale gas resource potential. *Int. J. Coal Geol.* 231, 103607. doi:10.1016/j.coal.2020.103607

Zhang, Q., Littke, R., Zieger, L., Shabani, M., Tang, X., and Zhang, J. (2019). Ediacaran, cambrian, ordovician, silurian and permian shales of the upper yangtze platform, south China: deposition, thermal maturity and shale gas potential. *Int. J. Coal Geol.* 216, 103281. doi:10.1016/j.coal.2019.103281

Zheng, T., Grohmann, S., Arysanto, A., Baniasad, A., Zhang, Q., and Littke, R. (2023a). Petrographical and geochemical investigation on maturation and primary migration in intact source rock micro-plugs: insight from hydrous pyrolysis on Woodford Shale. *Int. J. Coal Geol.* 266, 104170. doi:10.1016/j.coal.2022.104170

Zheng, T., Zhang, Q., and Deng, E. (2023b). Applications of low molecular weight polycyclic aromatic hydrocarbons (PAHs) and diamondoids ratios/indices on the maturity assessment of coal-bearing source rock: insight from mature to overmature Longtan Shale. *Int. J. Coal Geol.* 269, 104209. doi:10.1016/j.coal.2023.104209

Zheng, T., Zieger, L., Baniasad, A., Grohmann, S., Hu, T., and Littke, R. (2022). The shahejie Formation in the dongpu depression, Bohai Bay Basin, China: geochemical investigation of the origin, deposition and preservation of organic matter in a saline lacustrine environment during the Middle Eocene. *Int. J. Coal Geol.* 253, 103967. doi:10.1016/j.coal.2022.103967

frontiers | Frontiers in Earth Science

TYPE Original Research
PUBLISHED 09 January 2023
DOI 10.3389/feart.2022.1120630

OPEN ACCESS

EDITED BY
Ken'ichi Matsumoto,
Toyo University, Japan

REVIEWED BY
Cao Rihong,
Central South University, China
Chun Zhu,
Hohai University, China

*CORRESPONDENCE
Zhonghu Wu,
wuzhonghugzu@163.com

SPECIALTY SECTION
This article was submitted to Economic Geology,
a section of the journal
Frontiers in Earth Science

RECEIVED 10 December 2022
ACCEPTED 19 December 2022
PUBLISHED 09 January 2023

CITATION
Yang Y, Wu Z, Zuo Y, Song H, Wang W, Tang M and Cui H (2023), Three-dimensional numerical simulation study of pre-cracked shale based on CT technology.
Front. Earth Sci. 10:1120630.
doi: 10.3389/feart.2022.1120630

Three-dimensional numerical simulation study of pre-cracked shale based on CT technology

Yuhan Yang[1], Zhonghu Wu[1]*, Yujun Zuo[2], Huailei Song[1], Wentao Wang[1], Motian Tang[1] and Hengtao Cui[3]

[1]College of Civil Engineering, Guizhou University, Guiyang, China, [2]Mining College, Guizhou University, Guiyang, China, [3]School of Civil Engineering, Southwest Jiaotong University, Chengdu, China

Due to the heterogeneity of rock media, it is difficult to truly reflect its internal three-dimensional microstructure in physical tests or numerical simulation. In this study, CT scanning technology and numerical image processing technology are used, and the finite element software RFPA-3D is used to establish a three-dimensional non-uniform numerical model that can reflect the meso structure of rock mass. In order to study the fracture mechanism of shale with prefabricated fractures, seven groups of three-dimensional numerical models with prefabricated fractures from different angles were constructed, and Brazilian fracturing numerical simulation tests were carried out. The results show that method of reconstructing 3D numerical models by CT scanning is feasible and provides a viable method for in-depth study of the micromechanics of shale. Prefabricated fractures and quartz minerals have significant effects on the tensile strength of shale, and both will weaken the destructive strength of shale specimens. The damage modes of Brazilian disc specimens containing prefabricated fissures can be divided into four categories. The damage process is divided into budding, plateauing and surge periods by acoustic emission. The crack initiation angle of the prefabricated fissure tip increases with increasing fissure angle, and the MTS criterion can be used as a basis for judging prefabricated fissure initiation. The results of the study are important guidance for the fracture initiation mechanism and fracture expansion law of the fractured layer containing natural fractures in the hydraulic fracturing process.

KEYWORDS

shale, CT scan, 3D numerical model, prefabricated fissures, brazilian splitting test

1 Introduction

Shale gas, as a new energy resource, now accounts for 40% of the total natural gas, and its share is increasing (Zou et al., 2010; Wang et al., 2016; Wu et al., 2017). China has abundant shale gas resources with huge potential for development. Improving the efficiency of shale gas extraction is of great importance to the development of resources. There are still many problems in the shale gas extraction process that prevent efficient production of shale gas, such as the optimization problem of hydraulic fracturing and the destabilization of well walls. The pores of shale gas storage have a large proportion of nano-scale fractures, and the poor permeability is not conducive to extraction, so shale reservoirs must be fractured and modified to increase permeability (Darabi et al., 2012; Padin et al., 2014; Tahmasebi et al., 2016; Yang et al., 2021). In actual shale rock engineering, in addition to bedding, there are a large number of defects such as natural fractures and artificial fractures at different scales inside the rock mass, and these defects are one of the main internal factors controlling the mechanical properties such as deformation and strength of the rock mass. Under the action of hydraulic pressure and ground stress, the

natural fractures in the rock can easily be extended to interpenetrate with the hydraulic fractures, and hydraulic fractures can also expand in other directions under local stress perturbations caused by natural fractures, thus affecting the recovery of shale gas (Bowker 2007; Perez 2010; Liu et al., 2021). Therefore, the study of the extension mechanism as well as the physical properties of shale containing fractures has great engineering significance.

The fracture properties of shale containing fractures have been studied extensively by many scholars. For example, Zuo et al. (Zuo et al., 2019) performed a three-point bending test on shale specimens containing different angular incisions and observed them by scanning electron microscopy (SEM), the results show that the crack usually extends from the tip of the notch towards the loading point, with a more tortuous path as the tilt angle of the notch becomes larger. Shi et al. (Shi et al., 2018) cut prefabricated fissure at different angles in the cis-bedding plane and used a dynamic rock triaxial test system to simulate hydraulic fracturing tests. The results show that the greater the angle of the prefabricated fissure, the greater the maximum pore pressure at which the specimen ruptures. The damage pattern also shows various anisotropies with the fracture's angle (Yang et al., 2019). used Hopkinson compression bars for impact loading of semicircular bent shale specimens containing cracked notches, the results show that the laminar surface changes the direction of crack extension. Brazil splitting test is a method to measure the tensile properties of rocks. It is not only used to indirectly test the tensile strength of rocks, but also often used to study the fracture properties of rocks. Many scholars have already studied rocks containing Prefabricated fissure using the Brazilian splitting test. Xiong et al. (Xiong et al., 2019) measured shales with type I fracture toughness based on Brazilian cleavage, and investigated the effects on fracture toughness in terms of clay minerals, brittle minerals, temperature, and hydration in shales, respectively. Zhou et al. (Zhou and Wang 2016) investigated the mechanism of fissures expansion by compressing Brazilian disc specimens containing single and double fissures based on Non-ordinary state-based peridynamic theory (NOSB-PD). The effect of specimen size and crack inclination on the damage load of specimens with prefabricated fissures is also considered. Several scholars have used the digital image correlation (DIC) method to study the process of crack emergence and expansion in specimens with prefabricated fissures under different loading angles (Xi et al., 2020; Zhou et al., 2021).

However, the limitations of physical tests are that the crack extension process cannot be observed frame by frame and there are certain errors from one specimen to another. Nowadays, numerical simulation is also widely used in the field of oil and gas extraction and rock damage. For example, He and Liu et al. (Liu et al., 2020; He et al., 2021) simulated Brazilian splitting tests using PFC2D software, and a numerical model of rocks containing double fractures was developed to analyze the indirect tensile mechanical behavior of anisotropic disc specimens. The RFPA -dynamic program was used to build numerical models to study the impact properties and mechanisms of different numbers of prefabricated parallel cracks on the specimens (Zhang et al., 2020). The above studies are all based on the two-dimensional case to consider the crack expansion. However, the real crack expansion occurs in three-dimensional space. Therefore, some scholars have also considered various properties of rocks in three-dimensional conditions. For example, based on the RFPA3D finite element program, different 3D models have been constructed to study the rupture mechanism of the specimens by direct shear test, SHPB test, and Brazilian splitting test (Dai et al., 2015; Liao et al., 2020; Zhang et al., 2021). The higher order term coefficients of the Williams series expansion of the central cracked Brazilian disc under compressive loading were obtained using the digital image correlation (3D-DIC) method and the finite element method (Moazzami et al., 2018). Luo et al. (Luo et al., 2017) used digital image correlation technique (3D-DIC) to record the deformation of the specimens under the Brazilian splitting test, and the effects of cracks with different dip angles and lengths present in the Brazilian disc on its mechanical properties, fracture initiation and extension were investigated.

However, due to the complex mineral composition of shale, it contains many brittle minerals. The previous research understanding and practical experience show that the better the brittleness of shale is, the stronger the fracture making ability is, the easier it is to form a complex fracture network, and the better the fracture transformation effect is. Quartz is the main brittle mineral, and its content can effectively reflect the brittleness of shale. However, the general numerical model construction method cannot reflect the shape and distribution characteristics of irregular brittle minerals in real rock mass, and cannot simulate the real mineral distribution characteristics in rock. CT scanning technology is a non-destructive testing method, CT images can well reflect the pore structure inside the rock. In recent years, many scholars have applied CT scanning technology to geotechnical research, and certain research progress has been made (He et al., 2016; Zhou et al., 2016; Li et al., 2017; Dong et al., 2018). The above study lays the foundation for the reconstruction of 3D models from CT scan images.

Therefore, this paper takes shale containing prefabricated fissure as the research object, obtains the internal structure image of shale by CT scan. Combined with this image, a three-dimensional model was built in RFPA-3D, which can reflect the internal meso structure of rocks and characterize the heterogeneity of shale. This model is highly consistent with the real rock sample. Conducted Brazilian splitting tests to study the damage pattern,

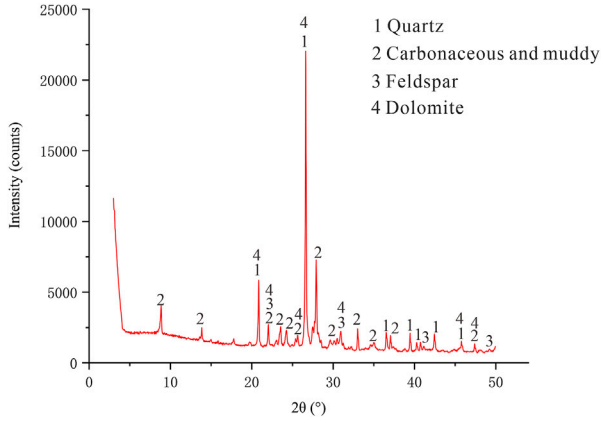

FIGURE 1
XRD whole rock diffraction analysis diagram.

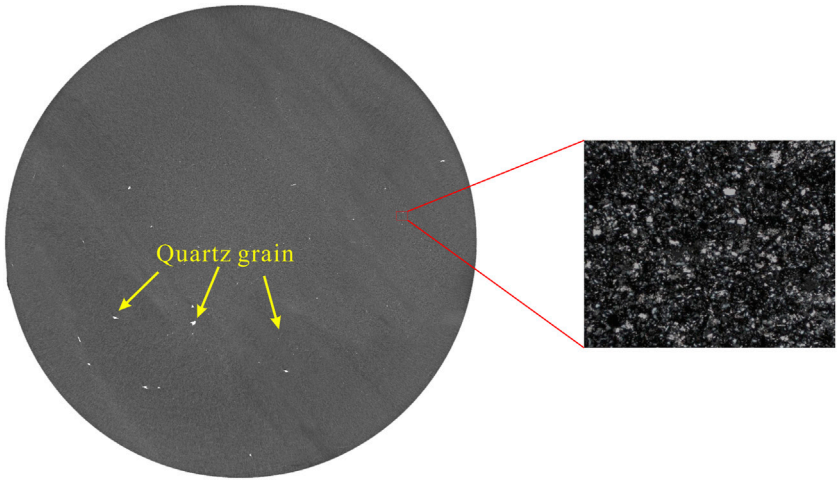

FIGURE 2
CT scanning image.

tensile strength and acoustic emission properties of shale containing prefabricated fissure.

2 XRD whole rock diffraction and CT scanning test

2.1 XRD whole rock diffraction analysis

This test piece is taken from the shale of the Lower Cambrian Niutitang Formation in northern Guizhou. The lithology of the study area is mainly black carbonaceous shale, and the mineral composition of the shale is mainly clay minerals and brittle minerals. Brittle minerals mainly include quartz, calcite and carbonate minerals. Generally, the higher the content of brittle minerals and the lower the content of clay minerals in shale, the easier it is to form natural fractures under the action of tectonic stress field or induced fractures during hydraulic fracturing. Therefore, mineral components have a very important influence on the formation of fractures in shale reservoirs. This paper conducts XRD whole rock diffraction analysis and clay mineral analysis on shale of Niutitang Formation of Lower Cambrian. Figure 1 shows the results of XRD diffraction analysis. The results show that the average content of quartz is 40%, the average content of carbon shale is 29%, and the average content of feldspar is 15%. The average content of dolomite is 10%, the average content of pyrite is 5%, and the average content of biotite is 1%.

2.2 CT scanning test

The instrument used in this CT scanning experiment is the X-ray three-dimensional ultra precision micro nano structure detector, and the model is Voxel-3502E. The instrument's X-ray source voltage is 20–190KV, and the highest spatial resolution of the instrument can reach 0.5 μm. The instrument uses a large field of view flat detector and objective coupling detector together for

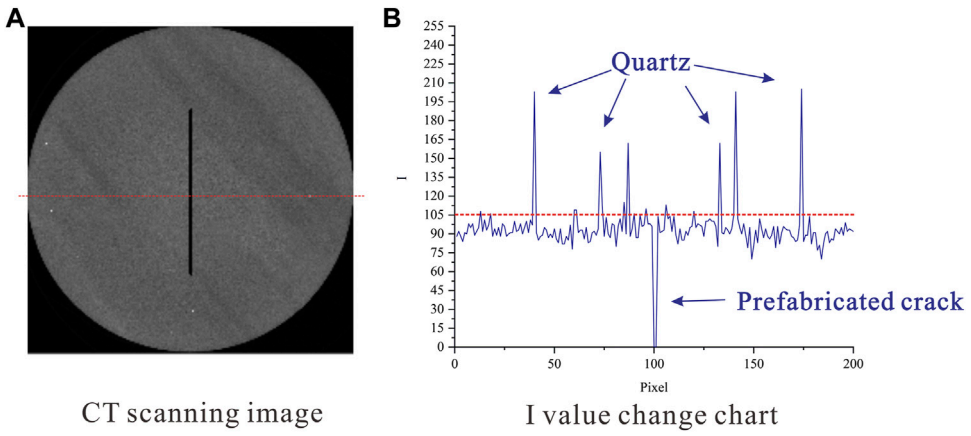

FIGURE 3
I-value change curve. **(A)** CT scanning image. **(B)** I value change chart.

test imaging, using the current advanced algorithm for three-dimensional accurate and rapid reconstruction of the image. Obtain three-dimensional body data that reflect the real spatial structure inside the sample, and improve the resolution by reducing the size of the detector unit with an optical magnification system.

The principle of CT scanning is that after X-rays penetrate a substance, the degree of attenuation of X-ray intensity is proportional to the density of the object and the thickness of the object. The grayscale value of the CT scan image directly shows the degree of X-ray attenuation: the color changes from black to white, the greater the density of the substance, the higher the degree of X-ray attenuation, and the grayscale value is large (Xue et al., 2015). In the scanning process, During scanning, the positions of the X-ray source and detector are always kept unchanged. The sample rotates at a constant speed from −180° to 180°. One picture is taken every n degrees of rotation. The CT scanning image is shown in Figure 2. The scanning image is 1246 × 1246 pixels, the gray black part of the image is shale matrix. Through thin section identification, the bright spot part is mainly quartz granular ore, the particles are in point line contact or no contact with each other, sub round sub angular, with medium sorting preference, and the particle size range is 0.01–0.1 mm.

3 CT image processing and 3D material structure reconstruction

3.1 Image preprocessing

Cut the CT image, and obtain the microstructure information of the image by histogram threshold method. A prefabricated crack with a length of 25 mm and a thickness of 0.8 mm is set on the scanning image by using the numerical image processing technology, and the sharp crack tip is obtained by reducing the pixel points at the tip. The Brazilian splitting test was performed by spacer loading, with two loading plates set up at both ends of the specimen.

Due to the limitation of computing power, the slice image pixel of CT scan was reduced to 200 × 200. Image processing selects multi threshold segmentation in HSI (Hue is chromaticity, Saturation is saturation, Intensity is brightness) color space by changing the brightness I value. To determine the image segmentation threshold I, a scanning line passing through the rock matrix and quartz mineral at the same time is randomly selected in Figure 3A. Counts the grayscale value of each pixel point on this scan line. The grayscale values of the shale matrix in the scanned image shown in Figure 3B are located below the dashed line and the grayscale values of the quartz are located above the dashed line. The finalized grayscale values were determined by multiple threshold segmentation tests to distinguish between shale matrix and cavity units (I = 40), shale matrix and quartz minerals (I = 105). The image after threshold segmentation is shown in Figure 4.

3.2 Shale 3D model reconstruction

To build a 3D digital specimen of the shale, 50 CT image slices were uniformly selected, and 50 digital images of the fine structure of the shale represented were imported into RFPA3D for superimposition. In the reconstruction process, it is assumed that the material slice image can represent the fine structure of a material with a small thickness d. If d is small, the error in the fine structure characterization can be neglected, and the slice thickness d = 0.2 mm is taken. Figure 5 shows the flow chart of 3D numerical model building, and the final 3D numerical model of shale is shown in Figure 5C. The model size is a Brazilian disk with a diameter of 50 mm and a thickness of 25 mm. The entire model is divided into two million units. The prefabricated fissure is set as a cavity unit, the elastic modulus of the loading plate is set to 10 times larger than the material, the compressive strength is set to 500 MPa, and the loading plate is fixed.

Weibull distribution function (Weibul, 1939) in RFPA3D was used to assign values to non-uniform shale specimens. The values

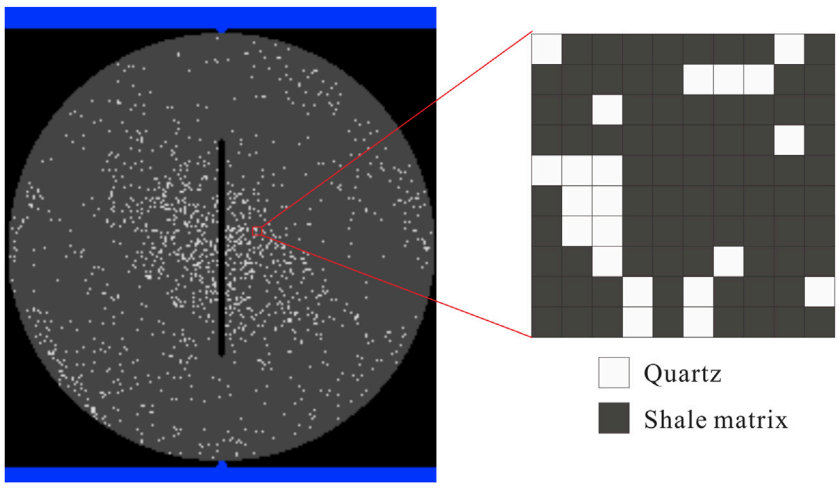

FIGURE 4
Image after threshold segmentation.

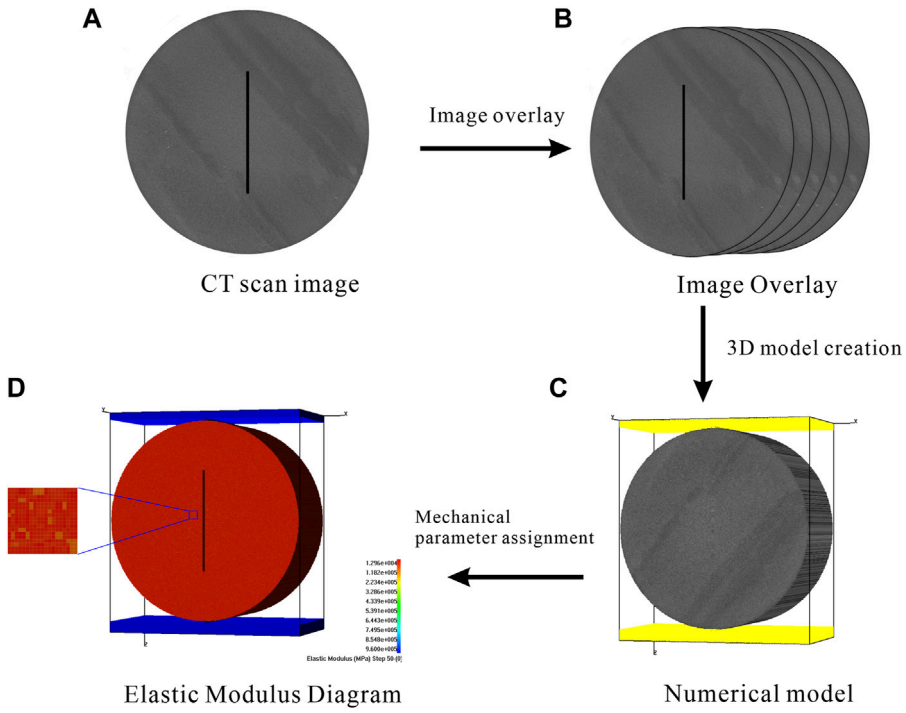

FIGURE 5
Flow chart of 3D numerical model reconstruction. **(A)** CT scan image. **(B)** Image overlay process. **(C)** Numerical model. **(D)** Diagram of elastic modulus of numerical model.

TABLE 1 Material parameters of shale specimens.

Material	Elastic modulus (GPa)	Poisson's ratio	Compressive strength (MPa)	Friction angle (°)	Pull-to-pressure ratio
Shale matrix	51.6 (5)	0.22 (100)	145.63 (5)	35	14
Quartz	96.0 (7)	0.08 (100)	210.00 (7)	60	15

of strength, Poisson's ratio, modulus of elasticity and density of the fine unit are assigned by the following equation:

$$f(x) = \frac{m}{\beta} \cdot \left(\frac{x}{\beta}\right)^{m-1} \cdot e^{-\left(\frac{x}{\beta}\right)^{m}}, x \geq 0 \quad (1)$$

Where x denotes the material medium matrix physical properties parameters (elastic modulus, strength, Poisson's ratio, density, *etc.*). β denotes the average of the parameters of the physical properties of the primitive, m indicates the nature parameter of the distribution function, whose physical meaning reflects the homogeneity of the material medium, defined as the homogeneity coefficient of the material medium, reflecting the degree of homogeneity of the material, $f(x)$ is the density of the statistical distribution of the physical properties x of the material (rock) primitive. The material parameters in this test are derived from the mechanical parameters of shale in the Lower Cambrian Niutitang Formation in north area of Guizhou (Wu et al., 2020), and are summarized in Table 1, where the values in brackets represent the uniformity coefficient of this parameter. The elastic modulus diagram after the assignment is shown in Figure 5D.

4 Test results and analysis

The prefabricated fracture angle α is the angle between the fracture and the loading direction. In this paper, the prefabricated fracture angles were selected at equal intervals of 15°, which were 0°, 15°, 30°, 45°, 60°, 75°, 90° and complete specimens for a total of eight groups of prefabricated fracture specimens. Eight groups of undivided quartz test pieces were made synchronously as the control group. The established model sets the loading direction as Z-axis and uses displacement loading method with initial displacement of 0.0001 mm/step and loading displacement of 0.0002 mm/step at each step until the specimen is damaged.

4.1 Mechanical characteristics analysis

The mechanical properties of the pressed solids were determined by the Brazil test. The maximum fracture strength σ_r is given by the following equation.

$$\sigma_r = \frac{2F}{\pi RB} \quad (2)$$

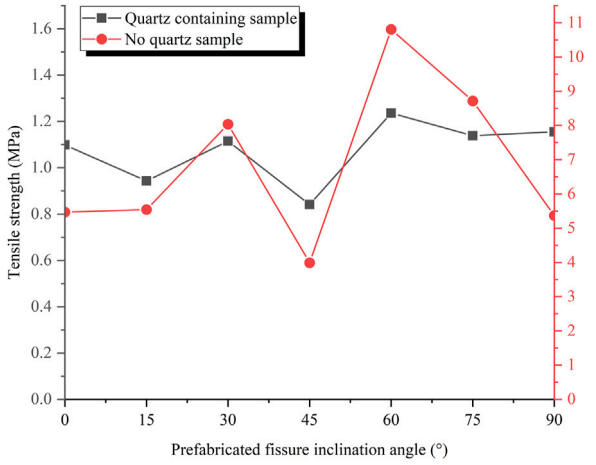

FIGURE 6
Effect of prefabricated fissure angle on the peak stress of the specimen.

where F is the damage load, and R and B are the diameter and thickness of the sample, respectively.

4.1.1 Failure strength analysis

Figure 6 shows the influence of prefabricated crack angle on the tensile strength of the test piece. It can be seen from the figure that the tensile strength of the two kinds of test pieces is greatly affected by the prefabricated crack angle, and the tensile strength curves are in "M" shape. The tensile strength is significantly affected by the 45° angle specimen. When the crack angle α = 45°, the tensile strength of both test pieces is the minimum; When the crack angle α = 60°, the tensile strength of both test pieces is the maximum. The reason for the large difference in tensile strength is that the existence of prefabricated cracks makes the rock sample produce obvious structural effect. Near the cracks, the bonding force between the rock particles that make up the rock mass is lower than that of the complete rock mass, and the tensile strength of the rock mass will have a large difference under different inclinations. Comparing the failure strength of the two specimens, it can also be found that the failure strength of the specimens containing quartz minerals is far lower than the tensile strength of the specimens without quartz minerals, and the strength of the specimens without quartz minerals changes greatly. The main reason for this difference is that quartz is a typical brittle mineral with high elastic modulus, low Poisson's ratio and low toughness. Under the effect of fracturing, the internal cohesion of the rock will be broken, and under certain stress, the rock will not undergo obvious deformation and will break directly. Therefore, quartz mineral will greatly affect the failure strength of the test piece. For shale with high quartz content, the more brittle it is, the stronger its fracture making ability is, the easier it is to form a complex fracture network, and the more ideal the volume fracturing effect is.

To sum up, prefabricated cracks and quartz minerals have a significant impact on the failure strength of the component. On the one hand, this effect is manifested in the substantial weakening of quartz on the strength, and on the other hand, it is manifested in the anisotropy of the angle of the prefabricated crack on the strength, that is, the strength of the specimen varies greatly with the angle of the prefabricated crack.

4.1.2 Stress-strain curve analysis

Figure 7 shows the stress-strain curve of the numerical simulation test. It can be seen from the figure that the strength of shale is greatly weakened by prefabricated cracks, and the tensile strength of both specimens is far lower than that of complete specimens. The failure stages of the two specimens are also quite different. For the test piece containing quartz, the failure can be divided into three stages: elastic stage, plastic stage and failure stage. At the beginning of loading, the stress changes linearly with strain, and at this time it is in the elastic stage, only a relatively small number of units rupture and no obvious cracks are produced. To reach the peak stress when the curve begins to flatten out and a microcrack begins to sprout, at which point it is the yielding stage. When the peak stress is reached, the stress falls rapidly, at which time the internal unit ruptures in large numbers and the crack sharply begins to extend and expand until it penetrates the specimen, at which point it is the damage stage.

For the test piece without quartz, the fracture dip angle α= 60° and 75°, compared with the above conditions, the residual failure stage occurs after the instability failure of the specimen, and the specimen has a certain residual strength, showing a certain plastic characteristics. The main reason is that this model does not

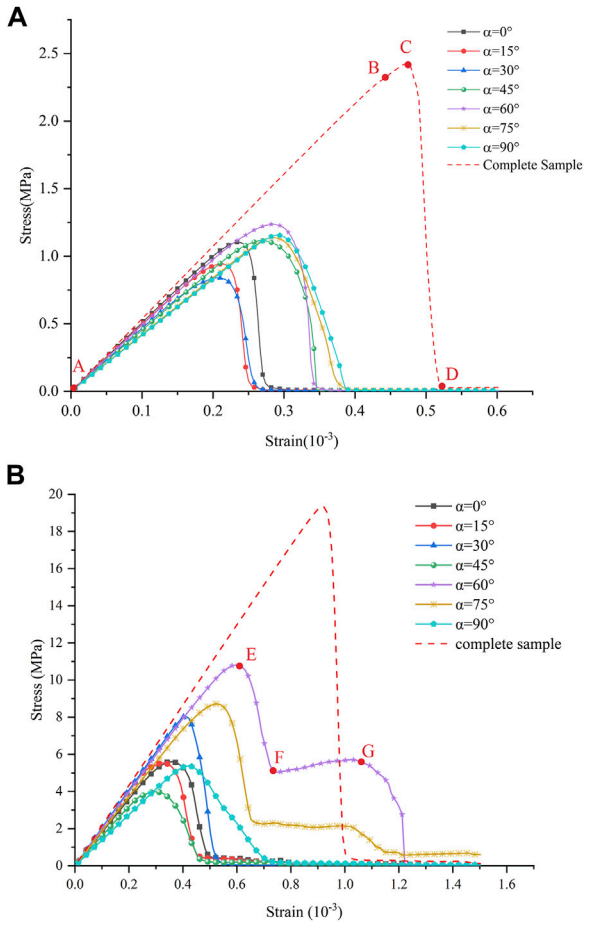

FIGURE 7
Numerical simulation test stress-strain curve. **(A)** Sample containing quartz. **(B)** Sample without quartz.

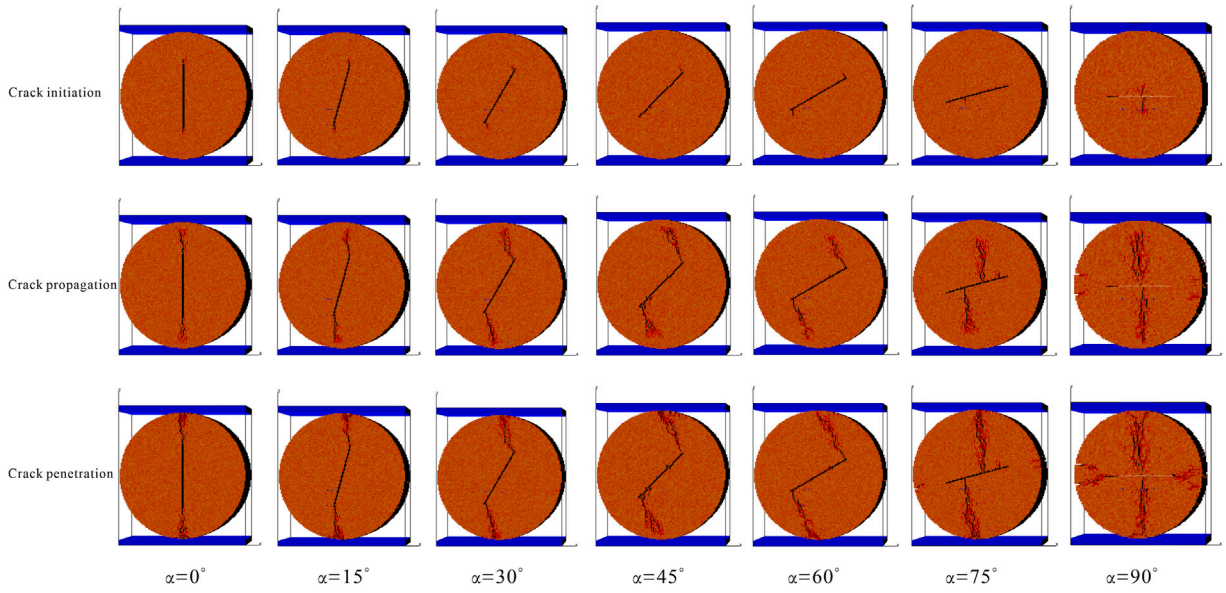

FIGURE 8
Crack extension pattern of numerical simulation specimen.

separate the main brittle mineral quartz through the threshold value. The mechanical parameters of the remaining shale matrix are mainly the mechanical parameters of clay minerals. The elastic modulus is far lower than quartz, and the Poisson's ratio is far higher than quartz, which has a certain plasticity. Therefore, when the inclination angle is α= 60° and 75°, the shear stress concentration appears at both ends of the prefabricated crack, the crack does not penetrate the test piece instantaneously, and the test pieces on both sides continue to bear a certain compressive stress.

To sum up, quartz minerals will affect the variation characteristics of the stress-strain curve, and the test pieces containing quartz show good brittleness characteristics. The mechanical action stage includes linear elastic stage (A-B), strain hardening stage (B-C) and failure stage (C-D). In the quartz free specimen, after the 60° and 75° specimens reach the peak stress again, there are post peak softening stage (E-F) and residual strength stage (F-G).

4.2 Fracture characteristics analysis

4.2.1 Crack extension analysis

Figure 8 shows the fracture process of specimens with different fissures dip angles, which clearly shows the progressive fracturing process of disc specimens with different angles of prefabricated fissure. The whole process can be divided into the stage of crack emergence, the stage of crack expansion, and the stage of crack penetration. According to the location of crack sprouting (Deng et al., 2017), classified the cracks into primary and secondary cracks. Among them, primary cracks are sprouted from prefabricated fissures and expand along the loading direction; secondary cracks are sprouted from near the loading point or the edge of the specimen and expand along the direction of the crack tip.

When the prefabricated crack dip angle α = 0°–60°, at the early stage of loading, the unit near the tip of the prefabricated fissure starts to break down, and the primary crack sprouting at the tip gradually extends to the loading end, followed by a small number of secondary cracks sprouting near the loading point to intersect with the primary crack or expand in the direction of the crack tip. When the prefabricated crack dip angle α = 75°, in the crack budding stage, a unit rupture began around the prefabricated crack, producing some cracks with a tendency to expand toward the loading point. Subsequently, the main crack sprouts at the non-tip, but near the middle part of the fissure, and the main crack extended to the loading point and stopped loading. When the prefabricated fissure dip angle α = 90°, the location of crack sprouting starts from the middle part of the prefabricated crack. After a period of loading, secondary cracks begin to sprout on the left and right edges of the specimen expanding towards the tip of the crack. Eventually the primary cracks connect to the loading point and the secondary cracks connect to the tip of the prefabricated fissure, and the loading ends when the cracks all penetrate each other. The location of crack initiation around the prefabricated crack is mainly determined by the location of its maximum tensile stress. With the increase of the prefabricated crack angle, the location of the maximum tensile stress gradually shifts from the crack tip to the middle of the crack.

4.2.2 Theoretical analysis of crack initiation

Based on the damage results of the specimens from the numerical simulation and similar simulation tests, the crack dip angle of the prefabricated fissure tip can be measured, and the measured results are shown in Table 2. The cracking angle of the prefabricated fissure tip characterizes the cracking orientation of the prefabricated fissure tip, because the cracking point of the specimens with α = 75° and 90° is not at the prefabricated fissure tip, so it is not valid measurement result.

Based on the peak load P_{max} of the test damage, refer to the calculation method of Erarslan and Atkinson (Atkinson et al., 1982; Erarslan 2013), the test data were substituted into Eqs 4, 5 to obtain the type I fracture toughness value K_I and type II fracture toughness value

TABLE 2 Prefabricated fissure tip starting angle.

Prefabricated slits Angle (°)	Starting cracking angle (°)		Average starting cracking angle (°)
0	0	0	0
15	23.5	22.5	23
30	56.1	50.1	53.1
45	70.3	59.0	64.7
60	86.4	77.5	81.9

TABLE 3 Calculation results of fracture toughness values.

Prefabricated slits Angle (°)	Peak load/(kN)	Fracture toughness value/(MPa·m$^{1/2}$)	
		Type I	Type II
0	10.996	1.919	0
15	10.885	0.645	2.781
30	15.784	−1.660	4.403
45	7.833	−1.773	1.905
60	21.218	−6.783	3.393
75	17.118	−6.099	0.977
90	10.541	−3.917	0

K_{II} for different prefabricated fissure angle specimens, and the calculated results are shown in Table 3.

$$K_I = \frac{P\sqrt{a}}{\sqrt{\pi}RB} N_I = \frac{P\sqrt{a}}{\sqrt{\pi}RB} \sum_{i=1}^{n} T_i \left(\frac{a}{R}\right)^{2i-2} A_i(\alpha) \tag{3}$$

$$K_{II} = \frac{P\sqrt{a}}{\sqrt{\pi}RB} N_{II} = \frac{2P\sqrt{a}}{\sqrt{\pi}RB} \sin 2\alpha \sum_{i=1}^{n} S_i \left(\frac{a}{R}\right)^{2i-2} B_i(\alpha) \tag{4}$$

Where p is the peak load at the time of specimen damage, a is the half-length of the prefabricated fissure, R is the radius of the Brazilian disc, B is the thickness of the Brazilian disc, T_i, S_i, A_i and B_i represent numerical factors. See the literature for specific meanings (Atkinson et al., 1982).

According to the theory of fracture mechanics, stress concentration occurs at the tip of the crack under external load, and when a limit state is reached, the crack starts to crack and expand, and then a penetration crack is formed and the specimen breaks. The maximum tangential stress criterion (MTS) is one of the most widely used criteria in rock fracture mechanics, which can effectively predict the crack extension characteristics under mixed loading mode (Aliha et al., 2008). In this paper, the MTS criterion is introduced to analyze the fracture mechanism of Brazilian disc specimens containing prefabricated fissure.

According to the Williams (Williams 1957) infinite series expansion, in the I-II mixed loading mode, the tangential stress component at the crack tip can be expressed in the following form if only the action of the singular term is considered:

$$\sigma_{\theta\theta} = \frac{1}{\sqrt{2\pi r}} \cos\frac{\theta}{2}\left[K_I \cos^2\frac{\theta}{2} - \frac{3}{2}K_{II}\sin\theta\right] \tag{5}$$

Where r and θ are the polar coordinate components of the crack tip, and K_I and K_{II} are the type I and II fracture toughness values, respectively. According to the MTS criterion, the crack initiation angle θ_0 can be determined by the following equation:

$$\left.\frac{\partial \sigma_{\theta\theta}}{\partial \theta}\right|_{\theta=\theta_0} = 0 \Rightarrow K_I \sin\theta_0 + K_{II}(3\cos\theta_0 - 1) = 0 \tag{6}$$

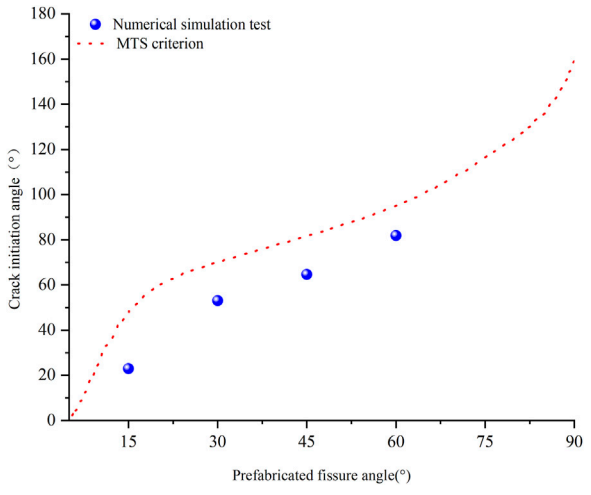

FIGURE 9
Comparison of the experimental results of starting cracking angle with the predicted results of MTS criterion.

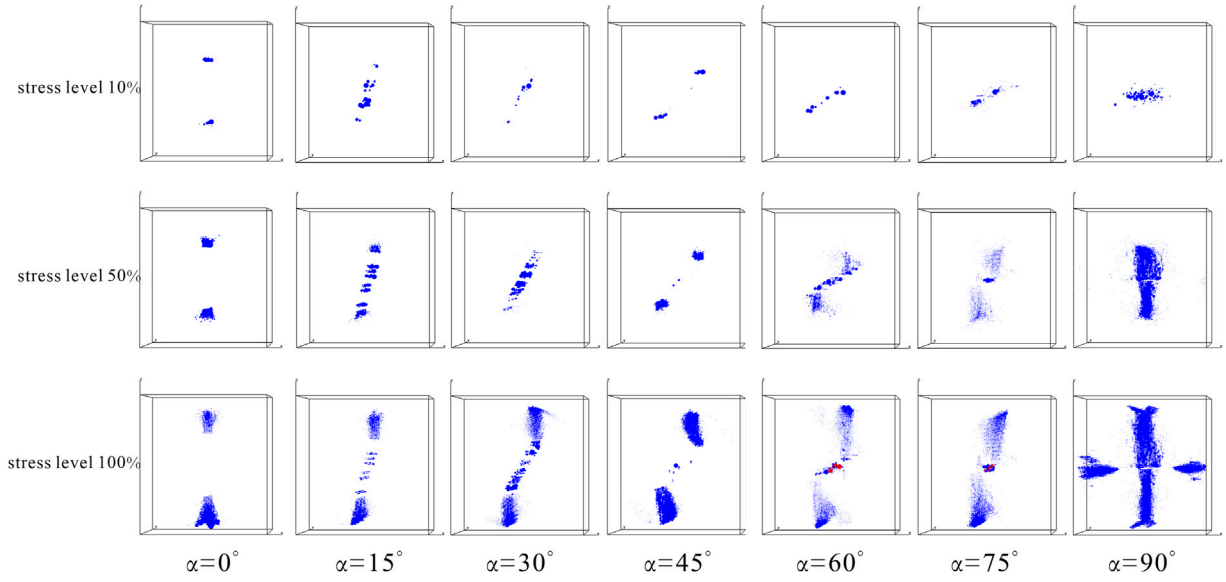

FIGURE 10
Spatial distribution of acoustic emission points at different dip angles and stress levels.

Figure 9 shows the comparison between the experimental results of starting cracking angle and the predicted results of the MTS criterion, and it can be seen from the figure that the experimental results are in good agreement with the MTS criterion. The validity of the numerical simulation is illustrated, and it can be seen that the crack initiation angle is controlled by the prefabricated fissure angle, and the starting cracking angle increases with the increase of the prefabricated fissure dip angle. When the prefabricated crack angle reaches near 75°, the crack initiation position deviates from the prefabricated crack tip.

4.3 Acoustic emission characterization

4.3.1 Distribution evolution and failure mode analysis of acoustic emission

When the internal structural units of a brittle material are damaged, acoustic energy is released, so this phenomenon of rapid energy release in a localized area can be called acoustic emission (AE). The acoustic emission characteristics of the Brazilian disc specimen are related to the whole loading process, and the acoustic emission properties can reflect the degree of damage to the structure. The spatial cumulative distribution of acoustic emission points for each specimen at three stress levels (σ/σ_{max}) is shown in Figure 10, corresponding to the ground acoustic emission can be divided into budding, plateauing and surge periods. A ball in the figure represents an acoustic emission event, blue and red circles represent tensile and shear damage, respectively.

The spatial evolution of acoustic emission can be seen from the diagram: at lower stress levels (10%), a small number of acoustic emission points appear around the fissure due to the concentration of stress around the fissure. Among them, 0° and 45° specimens only have acoustic emission points near the crack tip. As the stress level rises, the damage within the specimen continues to accumulate and acoustic emission points appear with the direction of crack extension. When the peak stress is reached, the number of acoustic emissions skyrockets, and in terms of the density of the spheres, the number of acoustic emissions is highest at 90° and less at 0° and 15°, which is consistent with the number of cracks. From the overall view, the damage modes of α = 0°–45° and 90° are dominated by tensile damage. For α = 60° and 75° specimens, shear damage occurred internally at a stress level of 100%, so the damage mode is a tensile and shear composite damage mode.

The failure modes of Brazilian disc specimens with prefabricated fissure can be divided into four categories: The tensile failure along the central part of the specimen (Type I), the tensile failure along the dip direction of the precast crack (Type II), the tensile failure at the precast crack tip (Type III), and the tensile and shear composite failure near the precast crack tip (Type IV). From the above analysis of the damage pattern map and the acoustic emission distribution map. It can be concluded that when α=0°–45°, the damage mode of the numerical model specimen is type III; when α=60° and 75°, the damage mode is type IV; when α=90°, the damage mode is a combination of type I and type II.

4.3.2 Acoustic emission counting analysis

Acoustic emission activity can be realistically simulated in RFPA3D, including acoustic emission counting and cumulative energy release. The cumulative AE damage number reflects the degree of damage, and the cumulative damage number is D. The calculation formula is as follows:

$$D = \frac{\sum_{i=1}^{s} n_i}{N} \tag{7}$$

Where s is the number of calculation steps, n_i is the number of damaged cells in step i, and N is the total number of cells in the model (Tang et al., 2000).

Figure 11 shows the trend of stress, AE, and cumulative AE with strain for seven groups of different prefabricated angles of fractures. The acoustic emission counting curves during the whole loading

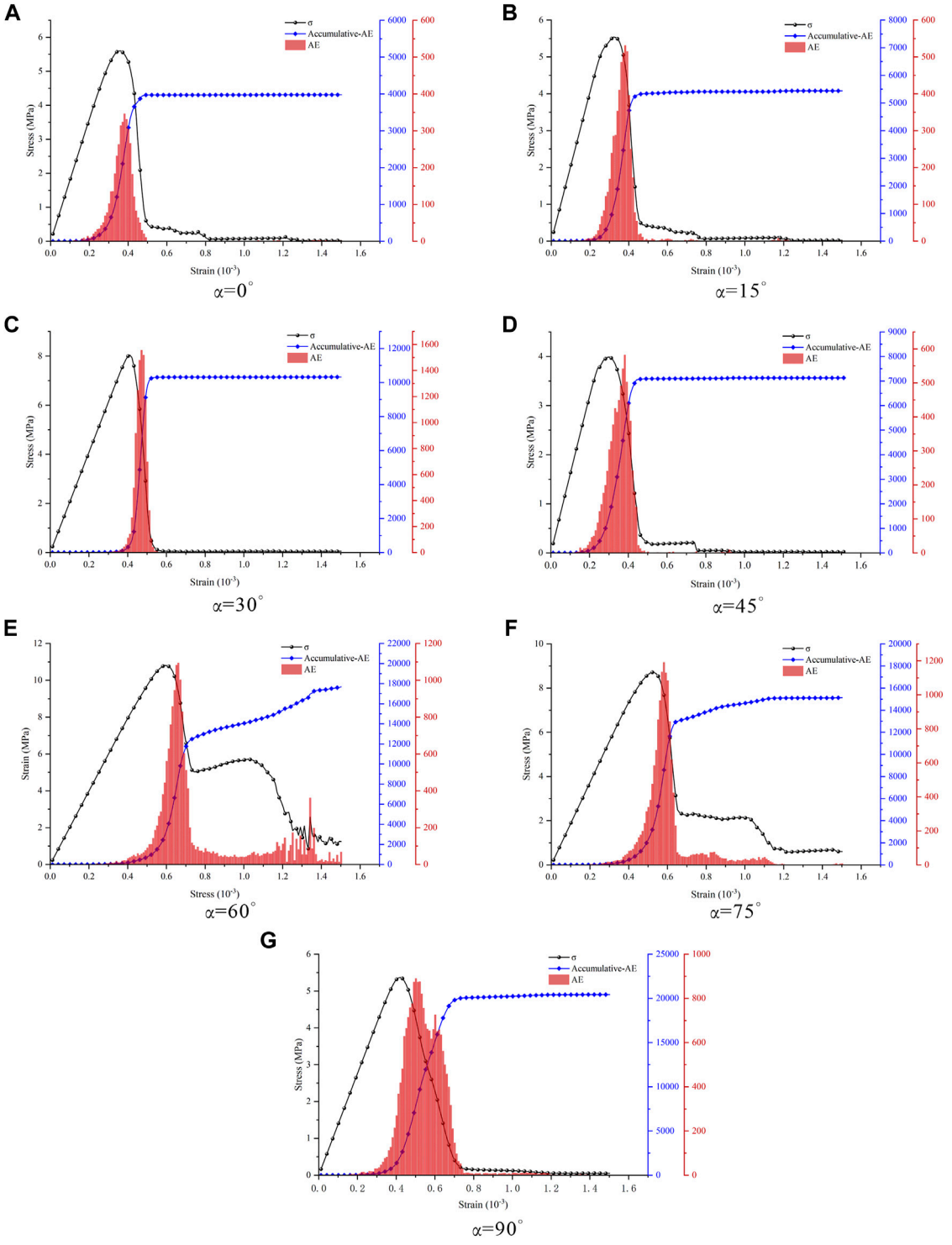

FIGURE 11
Trend of stress, AE, and cumulative AE with strain at different α. **(A)** α = 0°. **(B)** α = 15°. **(C)** α = 30°. **(D)** α = 45°. **(E)** α = 60°. **(F)** α = 75°. **(G)** α = 90°.

process can be divided into two modes: one is peak distribution type, i.e. the specimen shows one or two peaks of acoustic emission counting respectively during the whole loading process; the other is peak and uniform distribution type, i.e. there is still uniform acoustic emission generation after the peak. From Figure 11, it can be seen that the characteristic pattern of acoustic emission counting curves for α = 0°–45° and 90° specimens is peak distribution type. Where α = 0°–45° specimens acoustic emission counts reach a peak and then rapidly drop to 0, indicating that the damage of the specimens is a transient process, showing obvious characteristics of brittle damage. The characteristic pattern of the acoustic emission count curve of the α = 90° specimen is of the double-peak distribution type, as shown in Figure 11. (g) The acoustic emission count exhibits two higher peaks. Combined with the acoustic emission spatial distribution diagram

(Figure 10), it can be analyzed that this is due to the fact that while the primary crack of the specimen with α = 90° expands towards the loading point, secondary cracks also sprout from the left and right edges of the specimen towards the tip of the prefabricated fissure. The first AE peak occurs due to the extension of the primary crack and the second AE peak occurs due to the extension of the secondary crack. The characteristic pattern of acoustic emission counting curves for α=60° and 75° specimens is peak and uniform distribution type. Although the acoustic emission count of the specimen has reached the peak, the cumulative acoustic emission number is still increasing, indicating that the crack has not been fully penetrated and the specimen still has a certain residual strength. As loading proceeded, there were still acoustic emission events occurring and the cumulative AE counts were increasing in small amounts.

In summary, the acoustic emission characteristics of disc specimens containing prefabricated fissure have certain correlation characteristics with the fracture mode of the specimens, and such correlation characteristics are mainly manifested as follows: When the specimen is purely tensile damage, the acoustic emission counting curve of the specimen shows single-peak distribution characteristics (0°–45°); when the specimen shows compound tensile damage, the acoustic emission counting curve of the specimen mainly shows double-peak distribution characteristics (90°); When the specimen exhibits tensile and shear compound damage, the acoustic emission counting curve of the specimen mainly exhibits the characteristics of peak and uniform distribution. This indicates that the more single the damage mode of the specimen and the more obvious the characteristics of tensile damage, the more obvious the characteristics of the peak distribution of the acoustic emission counting curve.

5 Conclusion

In this paper, a 3D model of the real fine structure is constructed based on the slice images obtained by CT scan scanning technology combined with RFPA3D software, using shale as the research object. The splitting process of Brazilian disc specimens containing prefabricated fissure was simulated, and the effects of different prefabricated dip angles on the tensile strength, crack extension process, damage mode, and damage evolution process of shale were analyzed. The following conclusions were finally obtained.

1) Identification of shale specimen sections based on CT image scanning and CT image analysis processing techniques, and reconstructed the shale 3D digital specimen reconstruction, and established a shale 3D numerical specimen model. It provides a feasible method for an in-depth study of the fine mechanics mechanism of rocks.
2) Prefabricated fractures and quartz minerals will weaken the tensile strength of shale specimens. The presence of quartz will increase the brittleness of shale. The higher the brittleness, the easier it is to fracture, and the stronger the ability of shale to create fractures. Different fracture inclination angles are affected differently, where the damage strength is the smallest at α=45°, 0.84 MPa, and the largest at α=60°, 1.23 MPa.
3) The crack initiation angle is controlled by the prefabricated crack angle, which increases as the prefabricated crack dip angle increases. The MTS criterion can be used as a basis for judging the crack initiation of prefabricated fissure, and it also verifies the accuracy of the numerical model.
4) The damage modes can be divided into four categories: The tensile failure along the central part of the specimen (Type I), the tensile failure along the dip direction of the precast crack (Type II), the tensile failure at the precast crack tip (Type III), and the tensile and shear composite failure near the precast crack tip (Type IV).
5) According to the results of acoustic emission characteristics analysis, it can be seen that the more single the damage mode of the specimen, and the more obvious the characteristics of tensile damage, the more obvious the characteristics of the peak distribution of the acoustic emission counting curve. The cumulative AE counts can be divided into budding, plateauing and surge periods.

Data availability statement

The original contributions presented in the study are included in the article/supplementary material, further inquiries can be directed to the corresponding author.

Author contributions

Conceptualization, YY, ZW, and YZ; Data curation, YY and HS; Formal analysis, YY and WW; Funding acquisition, MT and HC; Methodology, YY and ZW; Writing—original draft, YY; Writing-review and editing, YY and ZW. All authors have read and agreed to the published version of the manuscript.

Funding

This research was funded by the National Natural Science Foundation of China, grant number 51964007, 51774101 and 52104080, Guizhou Science and Technology Fund, grant number [2020]4Y046, [2019]1075, and [2018]1107.

Conflict of interest

The authors declare that the research was conducted in the absence of any commercial or financial relationships that could be construed as a potential conflict of interest.

Publisher's note

References

Aliha, M., Ayatollahi, M., and Pakzad, R. (2008). Brittle fracture analysis using a ring-shape specimen containing two angled cracks. *Int. J. Fract.* 153 (1), 63–68. doi:10.1007/s10704-008-9280-9

Atkinson, C., Smelser, R., and Sanchez, J. (1982). Combined mode fracture via the cracked Brazilian disk test. *Int. J. Fract.* 18 (4), 279–291. doi:10.1007/BF00015688

Bowker, K. (2007). Barnett shale gas production, fort worth basin: Issues and discussion. *AAPG Bull.* 91 (4), 523–533. doi:10.1306/06190606018

Dai, F., Wei, M., Xu, N., Ma, Y., and Yang, D. (2015). Numerical assessment of the progressive rock fracture mechanism of cracked chevron notched Brazilian disc specimens. *Rock Mech. Rock Eng.* 48 (2), 463–479. doi:10.1007/s00603-014-0587-8

Darabi, H., Ettehad, A., Javadpour, F., and Sepehrnoori, K. (2012). Gas flow in ultra-tight shale strata. *J. Fluid Mech.* 710, 641–658. doi:10.1017/jfm.2012.424

Deng, Q., Gong, L., Ma, F., Xue, Y., Geng, X., and Hu, S. (2017). Analysis of crack propagation of crack straight through brazilian disc using particle flow code. *J. Eng. Geol.* 25 (2), 402–409. doi:10.13544/j.cnki.jeg.2017.02.018

Dong, H., Sun, J., Lin, Z., Fang, H., Li, Y., Cui, L., et al. (2018). 3D pore-type digital rock modeling of natural gas hydrate for permafrost and numerical simulation of electrical properties. *J. Geophys. Eng.* 15 (1), 275–285. doi:10.1088/1742-2140/aa8a8e

Erarslan, N. (2013). A study on the evaluation of the fracture process zone in CCNBD rock samples. *Exp. Mech.* 53 (8), 1475–1489. doi:10.1007/s11340-013-9750-5

He, B., Liu, J., Zhao, P., and Wang, J. (2021). PFC2D-based investigation on the mechanical behavior of anisotropic shale under Brazilian splitting containing two parallel cracks. *Front. Earth Sci.* 15 (4), 803–816. doi:10.1007/s11707-021-0895-8

He, P., Kulatilake, P., Liu, D., He, M., and Chen, X. (2016). A procedure to detect, construct, quantify, numerically simulate and validate fracture networks in coal blocks. *Geomechanics Geophys. Geo-Energy Geo-Resources* 2 (4), 257–274. doi:10.1007/s40948-016-0035-1

Jarvie, D. M., Hill, R. J., Ruble, T. E., and Pollastro, R. M. (2007). Unconventional shale-gas systems: The Mississippian Barnett Shale of north-central Texas as one model for thermogenic shale-gas assessment. *AAPG Bull.* 91 (4), 475–499. doi:10.1306/12190606068

Li, J., Jiang, H., Wang, C., Zhao, Y., Gao, Y., Pei, Y., et al. (2017). Pore-scale investigation of microscopic remaining oil variation characteristics in water-wet sandstone using CT scanning. *J. Nat. Gas Sci. Eng.* 48, 36–45. doi:10.1016/j.jngse.2017.04.003

Liao, Z., Ren, M., Tang, C., and Zhu, J. (2020). A three-dimensional damage-based contact element model for simulating the interfacial behaviors of rocks and its validation and applications. *Geomechanics Geophys. Geo-Energy Geo-Resources* 6 (3), 45–21. doi:10.1007/s40948-020-00171-z

Liu, S., Wang, H., Xu, W., Qu, X., and Xie, W. (2020). Numerical Brazilian split test of pre-cracked granite with randomly distributed micro-components. *Eng. Comput.* 37 (8), 2641–2657. doi:10.1108/EC-03-2019-0123

Liu, Z., Wang, S., Ye, H., Yang, L., Yang, D., Lian, H., et al. (2021). Experimental study on the effects of pre-cracks, fracturing fluid, and rock mechanical characteristics on directional hydraulic fracturing with axial pre-cracks. *Geomechanics Geophys. Geo-Energy Geo-Resources* 7 (2), 29. doi:10.1007/s40948-021-00225-w

Luo, L., Li, X., Qiu, J., and Zhu, Q. (2017). Study on fracture initiation and propagation in a Brazilian disc with a preexisting crack by digital image correlation method. *Adv. Mater. Sci. Eng.* 2017, 1–13. doi:10.1155/2017/2493921

Moazzami, M., Ayatollahi, M., Chamani, H., Guagliano, M., and Vergani, L. (2018). Determination of higher order stress terms in cracked Brazilian disc specimen under mode I loading using digital image correlation technique. *Opt. Laser Technol.* 107, 344–352. doi:10.1016/j.optlastec.2018.06.010

Ougier-Simonin, A., Renard, F., Boehm, C., and Vidal-Gilbert, S. (2016). Microfracturing and microporosity in shales. *Earth-Science Rev.* 162, 198–226. doi:10.1016/j.earscirev.2016.09.006

Perez, R. (2010). Application of LMR inversion and clustering analysis in the Barnett Shale. SEG Technical Program Expanded Abstracts 2010: Society of Exploration Geophysicists. p 2236–2239. doi:10.1190/1.3513294

Shi, X., Zhang, X., Wang, B., Tang, T., and Han, W. (2018). Hydraulic fracturing test with prefabricated crack on anisotropic shale: Laboratory testing and numerical simulation. *J. Petroleum Sci. Eng.* 168, 409–418. doi:10.1016/j.petrol.2018.04.059

Tahmasebi, P., Javadpour, F., Sahimi, M., and Piri, M. (2016). Multiscale study for stochastic characterization of shale samples. *Adv. Water Resour.* 89, 91–103. doi:10.1016/j.advwatres.2016.01.008

Tang, C., Liu, H., Lee, P., Tsui, Y., and Tham, L. (2000). Numerical studies of the influence of microstructure on rock failure in uniaxial compression — Part I: Effect of heterogeneity. *Int. J. Rock Mech. Min. Sci.* 37, 555–569. doi:10.1016/S1365-1609(99)00121-5

Wang, R., Ding, W., Zhang, Y., Wang, Z., Wang, X., He, J., et al. (2016). Analysis of developmental characteristics and dominant factors of fractures in lower cambrian marine shale reservoirs: A case study of Niutitang Formation in cen'gong block, southern China. *J. Petroleum Sci. Eng.* 138, 31–49. doi:10.1016/j.petrol.2015.12.004

Weibul, W. (1939). A statistical theory of the strength of materials. *Swed R. Inst. Eng. Res.* 151, 1–45. doi:10.1090/S0002-9939-1966-0198262-1

Williams, M. (1957). On the stress distribution at the base of a stationary crack. *J. Appl. Mech.* 24 (1), 109–114. doi:10.1115/1.4011454

Wu, Z., Lou, Y., Yin, S., Wang, A., Liu, H., Sun, W., et al. (2020). Acoustic and fractal analyses of the mechanical properties and fracture modes of bedding-containing shale under different seepage pressures. *Energy Sci. Eng.* 8 (10), 3638–3656. doi:10.1002/ese3.772

Wu, Z., Zuo, Y., Wang, S., Chen, J., Wang, A., Liu, L., et al. (2017). Numerical study of multi-period palaeotectonic stress fields in lower cambrian shale reservoirs and the prediction of fractures distribution: A case study of the Niutitang Formation in feng'gang No. 3 block, South China. *Mar. Petroleum Geol.* 80, 369–381. doi:10.1016/j.marpetgeo.2016.12.008

Xi, X., Wu, X., Guo, Q., and Cai, M. (2020). Experimental investigation and numerical simulation on the crack initiation and propagation of rock with pre-existing cracks. *Ieee Access* 8, 129636–129644. doi:10.1109/ACCESS.2020.3009230

Xiong, J., Liu, K., Liang, L., Liu, X., and Zhang, C. (2019). Investigation of influence factors of the fracture toughness of shale: A case study of the longmaxi formation shale in sichuan basin, China. *China. Geotechnical Geol. Eng.* 37 (4), 2927–2934. doi:10.1007/s10706-019-00809-0

Xue, H., Xu, R., Jiang, P., and Zhou, S. (2015). Characterization of rock microstructure using 3D x-ray computed tomography. *Chin. J. Theor. Appl. Mech.* 47 (6), 1073–1078. doi:10.6052/0459-1879-15-102

Yang, B., Xue, L., Duan, Y., and Wang, M. (2021). Correlation study between fracability and brittleness of shale-gas reservoir. *Geomechanics Geophys. Geo-Energy Geo-Resources* 7 (2), 31–13. doi:10.1007/s40948-021-00231-y

Yang, G., Li, X., Bi, J., and Cheng, S. (2019). Dynamic crack initiation toughness of shale under impact loading. *Energies* 12 (9), 1636. doi:10.3390/en12091636

Zhang, Y., Liu, H., Yin, G., Ou, C., Lu, J., and He, J. (2020). Impact failure of flattened Brazilian disc with cracks—process and mechanism. *Sci. Ed.* 35 (5), 1003–1010. doi:10.1007/s11595-020-2348-8

Zhang, Y., Ou, C., Liu, H., Lu, J., Cheng, C., and He, J. (2021). Experimental and numerical study on the dynamic fracture of flattened Brazilian discs with prefabricated cracks. *Eng. Fract. Mech.* 254, 107885. doi:10.1016/j.engfracmech.2021.107885

Zhou, G., Zhang, Q., Bai, R., and Ni, G. (2016). Characterization of coal micro-pore structure and simulation on the seepage rules of low-pressure water based on CT scanning data. *Minerals* 6 (3), 78. doi:10.3390/min6030078

Zhou, J., Zeng, Y., Guo, Y., Chang, X., Liu, L., Wang, L., et al. (2021). Effect of natural filling fracture on the cracking process of shale Brazilian disc containing a central straight notched flaw. *J. Petroleum Sci. Eng.* 196, 107993. doi:10.1016/j.petrol.2020.107993

Zhou, X., and Wang, Y. (2016). Numerical simulation of crack propagation and coalescence in pre-cracked rock-like Brazilian disks using the non-ordinary state-based peridynamics. *J. Rock Mech. Min. Sci.* 89, 235–249. doi:10.1016/j.ijrmms.2016.09.010

Zou, C., Dong, D., Wang, S., Li, J., Li, X., Wang, Y., et al. (2010). Geological characteristics and resource potential of shale gas in China. *Petroleum Explor. Dev.* 37 (6), 641–653. doi:10.1016/S1876-3804(11)60001-3

Zuo, J., Li, Y., Liu, C., Liu, H., Wang, J., Li, H., et al. (2019). Meso-fracture mechanism and its fracture toughness analysis of Longmaxi shale including different angles by means of M-SENB tests. *Eng. Fract. Mech.* 215, 178–192. doi:10.1016/j.engfracmech.2019.05.009

frontiers | Frontiers in Earth Science

TYPE Original Research
PUBLISHED 20 April 2023
DOI 10.3389/feart.2023.1169318

OPEN ACCESS

EDITED BY
Leibo Bian,
Aarhus University, Denmark

REVIEWED BY
Zhe Cao,
SINOPEC Petroleum Exploration and Production Research Institute, China
Guo Chen,
Yangtze University, China

*CORRESPONDENCE
Jianhui Zeng,
zengjh@cup.edu.cn

RECEIVED 19 February 2023
ACCEPTED 10 April 2023
PUBLISHED 20 April 2023

CITATION
Liu Y, Zeng J, Liu S and Long H (2023), Physical properties variation of crude oil under natural laboratory and its geological implications: Dongying Sag, eastern China.
Front. Earth Sci. 11:1169318.
doi: 10.3389/feart.2023.1169318

Physical properties variation of crude oil under natural laboratory and its geological implications: Dongying Sag, eastern China

Yazhou Liu[1,2], Jianhui Zeng[1,2]*, Shuning Liu[1,2] and Hui Long[1,2]

[1]State Key Laboratory of Petroleum Resources and Prospecting, China University of Petroleum (Beijing), Beijing, China, [2]College of Geosciences, China University of Petroleum (Beijing), Beijing, China

The Dongying Sag in eastern China is a mature exploration area and contains a wide variety of accumulations ranging from extra heavy oil to light oil. This multi-source lacustrine rift basin provides meaningful insights into the relationships between organofacies, maturity, charging, mixing, and oil properties. The Es3 source rocks are in the immature to mid-mature stage, while the Es4 source rocks are in the immature to late mature stage. Among them, Es4 source rocks were deposited in an anoxic, stratified, brackish water environment. Based on the kinetic model, it appears that the oil generation rate of Es4 source rocks is higher than that of Es3 source rocks, and the oil generation time of Es4 source rocks was earlier than that of Es3 source rocks. Whether in Es4 or Es3 members, source rocks with the kerogen type I have the greatest oil yield compared with other kerogens. The variations in oil physical and geochemical properties can be attributed to differences in organofacies and thermal maturity, which is in agreement with the results of source rock geochemistry and macerals analysis. Because the concentrations of maturity-related biomarkers or non-biomarkers show several orders of magnitude variation across maturity windows, these maturity parameters do not reliably characterize the maturity signals in mixed oil scenarios. Maturity parameters based on biomarker ratios can produce biases that overemphasize the contribution of low maturity oils and thus track the signals of low maturity end-member oils. In contrast, maturity parameters based on aromatic isomers are more sensitive to mixing processes and reflect the mixing degree of the accumulated oils. The same series of maturity parameters can track hydrocarbon migration pathways and relative maturity, while multiple series of maturity parameters can reconstruct hydrocarbon charging and mixing histories.

KEYWORDS

oil properties, organofacies, thermal maturity, oil maturity, charging and mixing, Dongying Sag

1 Introduction

Migration and accumulation models have evolved from simply predicting the presence or absence of hydrocarbons to predicting the hydrocarbon phase behavior, as well as their physical properties. Among these qualities, oil physical properties such as API gravity, dynamic viscosity and sulfur content can be used not only to evaluate the market value of oil, but also to decipher the processes of oil generation, migration, accumulation and alteration (Stainforth, 2004; Jahn et al., 2008; Dembicki, 2022).

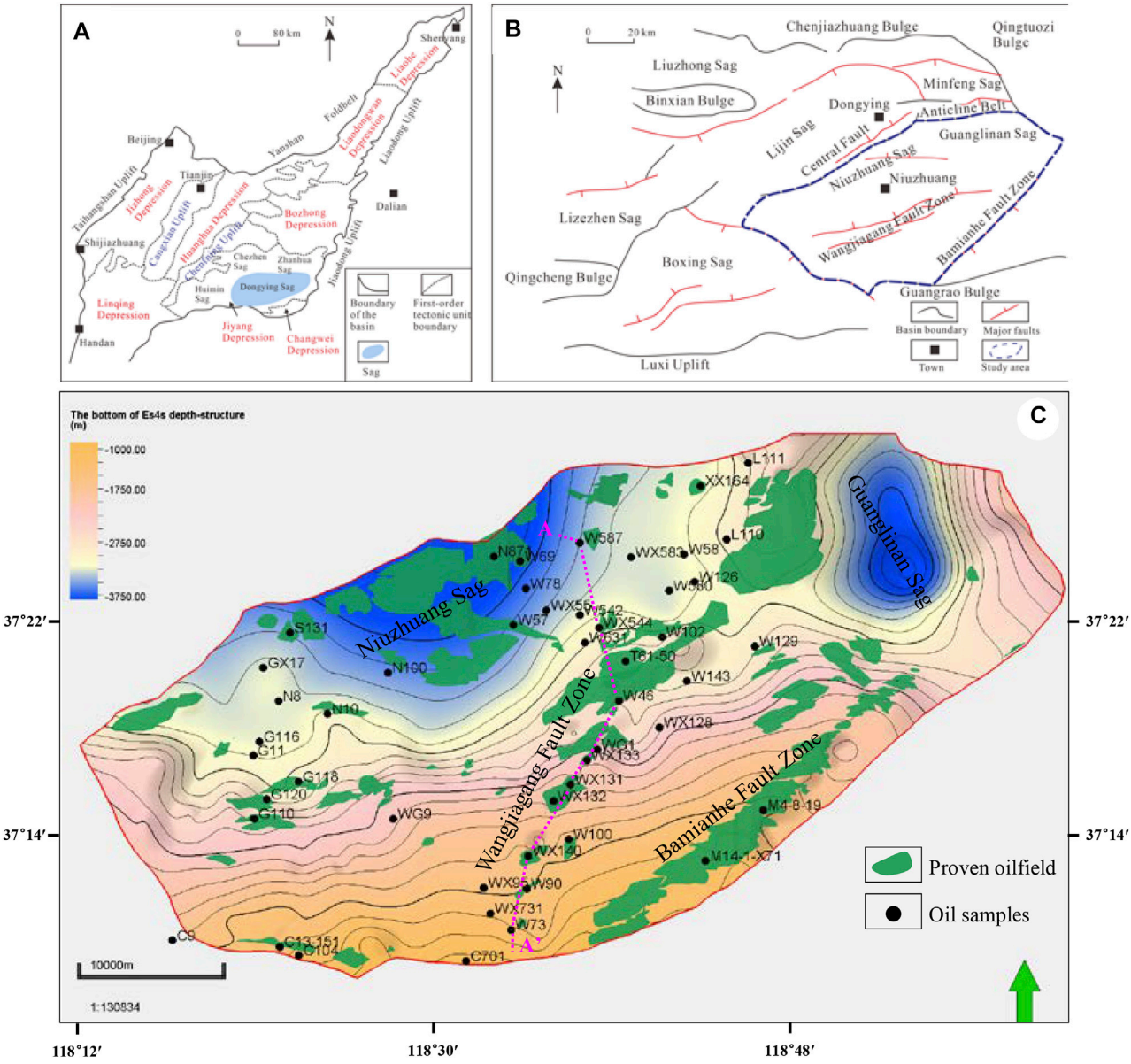

FIGURE 1
Geological map of the study area and oil samples. **(A)** Location map of the Dongying Sag (revised from Wang et al., 2019); **(B)** The major tectonic units in the Dongying Sag (revised from Shi et al., 2021); **(C)** Bottom the Es4s member depth structure map and oil sample location in the study area.

Unfortunately, no universal classification standard has been established worldwide for crude oils (Dandekar, 2006; Baur, 2019). In this work, the crude oil classification scheme of Feng et al. (2021) is followed: extra heavy oil (<10° API), heavy oil (10°–22.3° API), medium oil (22.3°–31.1° API), light oil (31°–50° API) and gas/condensate (>50° API). The expelled and captured oil shows a progressive evolution of physical properties and compositions at different maturity stages (Pepper and Corvi, 1995; di Primio and Horsfield, 2006). Generally, oil with low API gravity and high dynamic viscosity is either derived from products of low maturity source rocks, especially sulfur-rich source rocks, or the result of secondary alteration, such as biodegradation and water washing (Evans et al., 1971; Hughes, 1984; Jones, 1984; Orr, 1986). In contrast, oil with high API gravity and low dynamic viscosity often implies the products of high maturity or gas-prone source rocks (Hunt, 1991; Katz et al., 1991). Therefore, oil API gravity and dynamic viscosity depend not only on maturity or organofacies, but also on secondary alteration. Cornford et al. (1983) attributed the variations in petroleum properties in the United Kingdom. North Sea to differences in maturity of a single marine source rock (the Kimmeridge Clay Formation hot shales), followed by secondary alteration during migration or within the reservoir. Feng et al. (2021) compared the variations in API gravity of crude oils from three sags in the Erlian rift basin, attributing their differences to organofacies and thermal maturity of the same lacustrine source

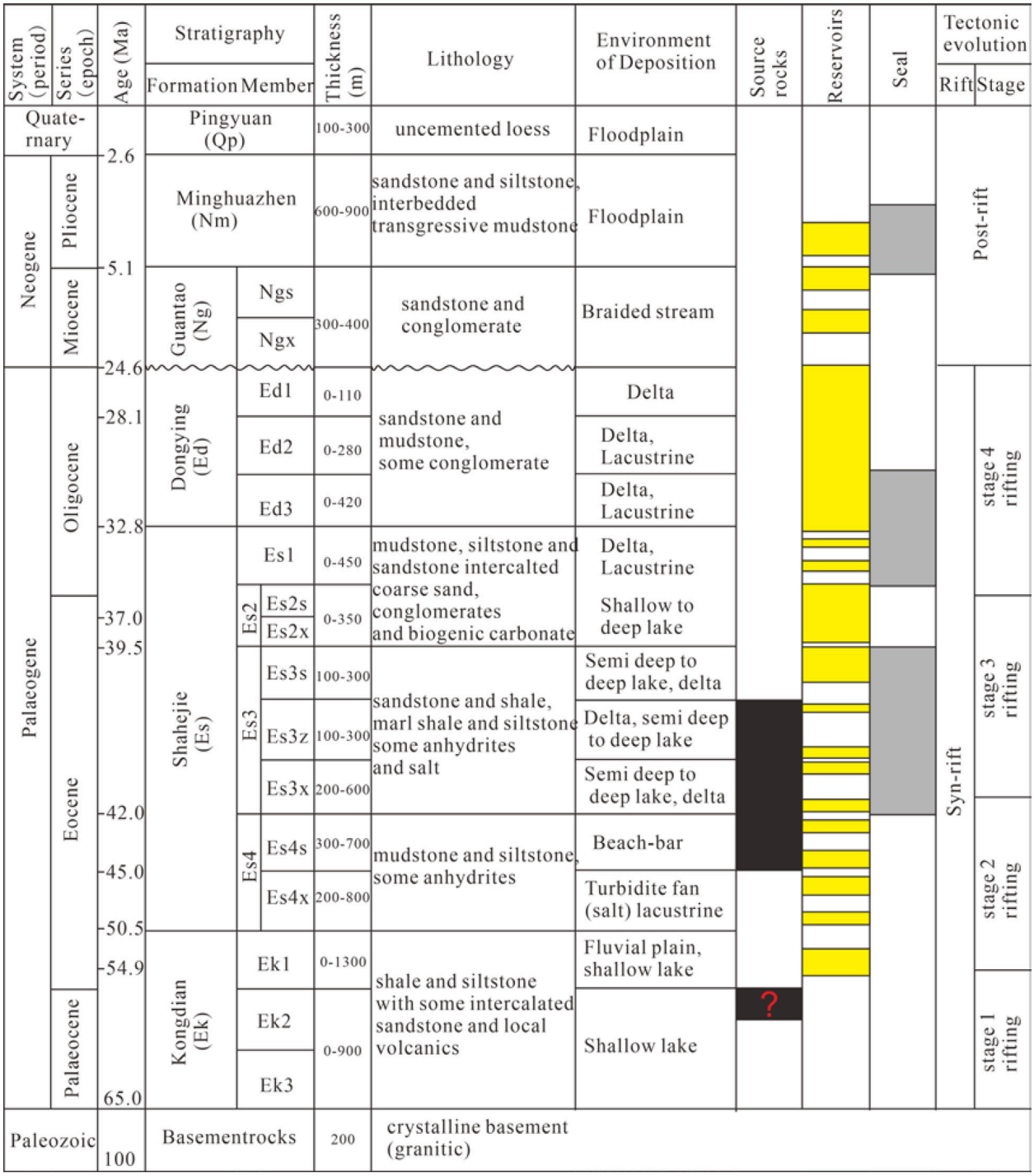

FIGURE 2
Generalized Palaeogene-Quaternary tectonic and sedimentary evolution stages and major petroleum system elements in the Dongying Sag (revised from Zahid et al., 2016).

rock. However, there is a lack of systematic investigations on fluid properties and distribution in lacustrine multiple source systems.

Hydrocarbon accumulation is a dynamic balancing process, and accumulations are always in the process of adjustment and modification. The charging and leaking of hydrocarbons are mutually constrained and define the scale of hydrocarbon accumulations. Oil mixing has always been a characteristic of petroleum systems (Wilhelms and Larter, 2004; Larter et al., 2012; Wang et al., 2021; Huang et al., 2022). Reconstructing the charging and mixing histories cannot only provide insight into the

TABLE 1 Physical properties of crude oil from different formations in the study area.

Reservoirs	Depth (m)	API (°)	Dynamic viscosity (mPa·s)	Sulfur content (%)	Pour point (°C)	Wax content (%)	Initial boiling point (°C)
Ng	762.8–1,033.4	10.20–13.40 (15.57)	410–587 (102)	1.60–1.86 (1.70)	−11–22 (0)	5.74–5.74 (5.74)	228–274 (247)
Ed	1,114.0–1,167.8	15.10–22.64 (15.57)	90.7–2,770 (2,393)	0.49–1.15 (0.92)	−16–20 (−4)	6.75–6.75 (6.75)	182–234 (225)
Es1	1,118.2–2021.0	14.38–32.29 (24.95)	13.4–3,537 (76.25)	0.26–1.90 (0.80)	−13–34 (28)	6.89–6.89 (6.89)	147–162 (154.5)
Es2	922.0–2,321.4	9.92–31.89 (16.82)	14–20948 (1,049)	0.17–3.05 (0.94)	−24–36 (9.5)	2.28–33.52 (14.30)	100–253 (170)
Es3s	998.1–3,377.3	7.80–33.42 (24.55)	12.7–66286 (156.5)	0.07–2.74 (1.48)	-8–46 (30.5)	3.25–28.06 (10.13)	66–255 (154)
Es3z	914.2–3,436.6	7.40–34.85 (28.89)	8.83–845576 (28.35)	0.04–3.93 (0.36)	−17–50 (33)	1.78–28.06 (9.79)	66–281 (121)
Es3x	928.8–3,639.0	7.80–34.85 (27.36)	8.13–66286 (40.7)	0.11–2.78 (0.55)	−11–47 (32)	5.52–28.19 (10.73)	66–254 (146)
Es4s	885.9–4,030.1	−7.98–35.88 (25.03)	4.49–72485 (96.1)	0.08–4.52 (1.19)	−14–83 (26)	0.91–33.45 (13.16)	59–280 (128)
Es4x	897.3–3,795.0	−2.79–30.27 (22.93)	14.4–58607 (340.5)	0.10–3.87 (0.90)	−15–53 (29)	0.91–54.03 (4.81)	71–275 (135)
Ek	912.1–3,308.6	5.93–45.73 (29.11)	2.94–44615 (133)	0.04–2.22 (0.25)	0–54 (41)	1.72–57.86 (23.07)	81–264 (137)

Min-Max (median).

hydrocarbon accumulation histories, but also guide the exploration of the next prospects. However, mixed oil generally includes the characteristics of each end member oil, resulting in conflicting or even opposite evaluation results of different geochemical parameters (Ross et al., 2010; Zhang et al., 2014). This also causes ambiguity in both reservoir accumulation process analysis and remaining resource potential evaluation. The obvious scenario for mixing is the charging of fresh oil into heavily biodegraded oil (Holba et al., 1996; George et al., 1998). Migration-contamination is another example of oil mixing (Curiale, 2002; Peters and Fowler, 2002). Nevertheless, not all end-member oils can be easily identified. For example, if a low-maturity oil is mixed with a high- or over-maturity oil, the biomarker maturity parameters of the mixed oil will show the characteristics of the low-maturity oil without reflecting the information of the high- or over-mature oil (Wilhelms and Larter, 2004; Wang et al., 2021; Huang et al., 2022).

The Dongying Sag is a typical lacustrine rift basin in eastern China. The multi-cyclic properties of sedimentary evolution and the diversity of source rock organic matter inevitably result in the complexity of hydrocarbon accumulation processes. Firstly, products generated at different maturity stages of source rocks have different geochemical properties and compositions; secondly, traps developed at different stages can capture hydrocarbons generated at different maturity stages; furthermore, accumulations can experience various secondary alteration processes, which make the composition and properties of hydrocarbons more complicated. Although many researchers have conducted in-depth studies on accumulation description and resource evaluation in this area (Li et al., 2003; Pang et al., 2005; Zhan et al., 2019; Niu et al., 2022), a comprehensive understanding of the oil properties is not available. In this work, there is also an attempt to decipher the deeper concepts of oil maturity using molecular maturity parameters based on biomarkers and aromatics, and to reconstruct oil charging and mixing histories.

2 Geological settings

The Bohai Bay Basin is considered to be one of the most important petroliferous basins in eastern China. The Dongying Sag is situated in the southeastern part of the Bohai Bay Basin (Figure 1A), covering an area of about 5,700 Km^2, and is characterized by a “dustpan-shaped” lacustrine basin (Zhan et al., 2019; Wang et al., 2021). It is bordered by the Qingtuozi and Guangrao bulges to the east, the Luxi Uplift to the south, the Qingcheng and Binxian bulges to the west, and the Chenjiazhuang bulge to the north (Figure 1B). From north to south, the basin can be divided into five secondary tectonic zones: the northern steep-slope zone, the northern subsidence zone, the central fault-anticline zone, the southern subsidence zone, and the southern gentle-slope zone (Zhang et al., 2009; Guo et al., 2012). Furthermore, the depression can be further divided into five sags, namely, Minfeng, Niuzhuang, Guanglinan, Lijin, and Boxing sags (Figure 1B). The study area is located in the eastern part of the Dongying Depression, with an area of about 1900 Km^2. It mainly includes Niuzhuang and Guanglinan sags, Wangjiagang and Bamianhe fault zones, and the southern gentle-slope zone.

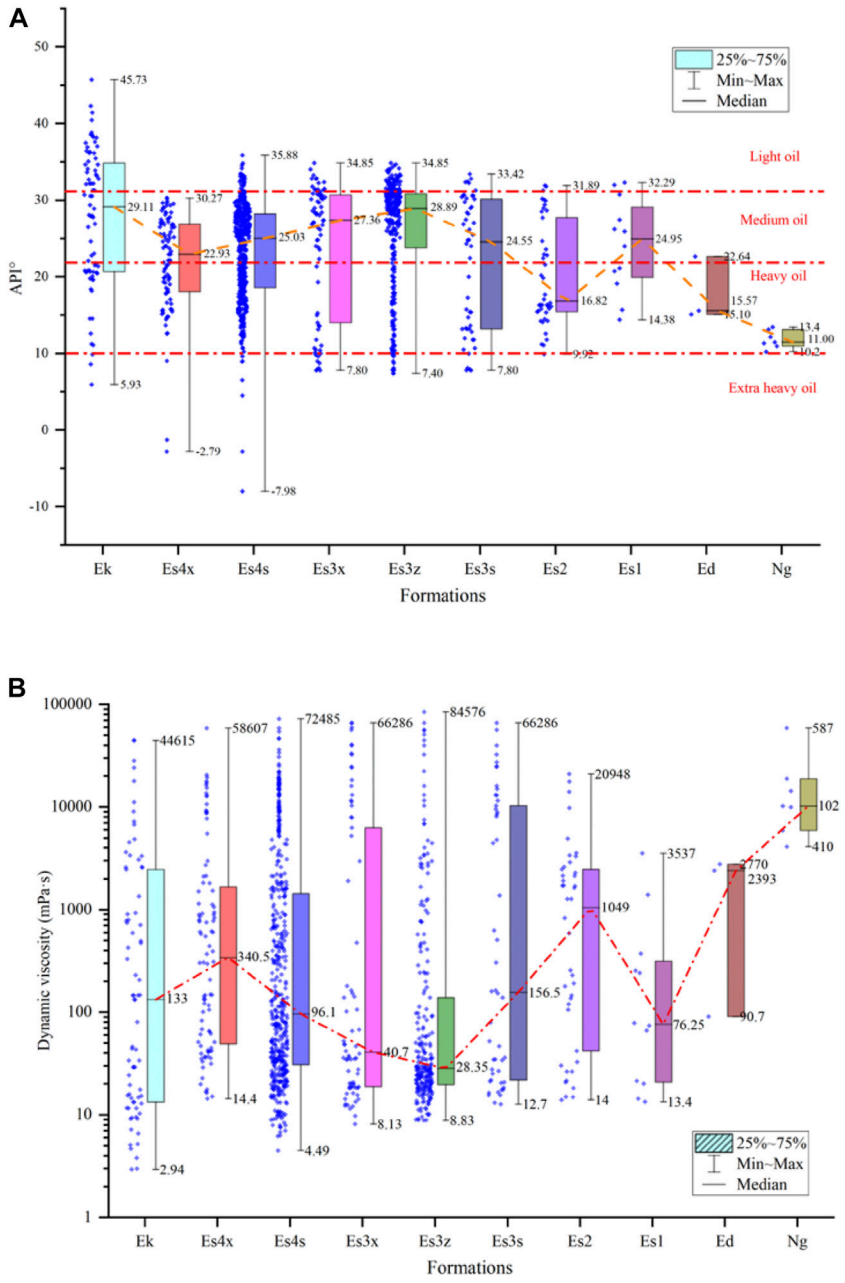

FIGURE 3
Continued.

The Paleogene formations in the Dongying Sag are unconformably overlaid on Paleozoic crystalline basement (Figure 2). Based on the tectonic evolution history and sedimentary sequence, the Dongying Sag can be divided into two stages: syn-rift (65.0–24.6 Ma) and post-rift (24.6 Ma-present) (Xie et al., 2006). During the syn-rift stage, the sediments are mainly developed in the lacustrine environment. Sediments from the Paleogene Kongdian (Ek), Shahejie (Es), and Dongying (Ed) formations, as well as the Neogene Guantao (Ng), Minghuazhen (Nm), and Quaternary Pingyuan (Qp) formations, fill the Dongying Sag. The Kongdian formation mainly consists of shallow lake shale and siltstone interbedded with some sandstone, along with the development of different levels of red beds (Zhan et al., 2019; Tao et al., 2022). The Shahejie formation is dominated by semi-deep to deep lake mudstone and siltstone sediments and coarse deltic sandstone interbedded with conglomerates. The Dongying formation comprises sandstones, mudstones and some conglomerates that developed in deltaic and shallow lacustrine environments. The Guantao and Minghuazhen formations are characterized by braided stream conglomerates, sandstones and floodplain siltstones. During the late Oligocene and early Miocene, regional tectonic uplift caused different degrees of erosion throughout the Dongying Sag (Chang et al., 2018; Liu et al., 2018).

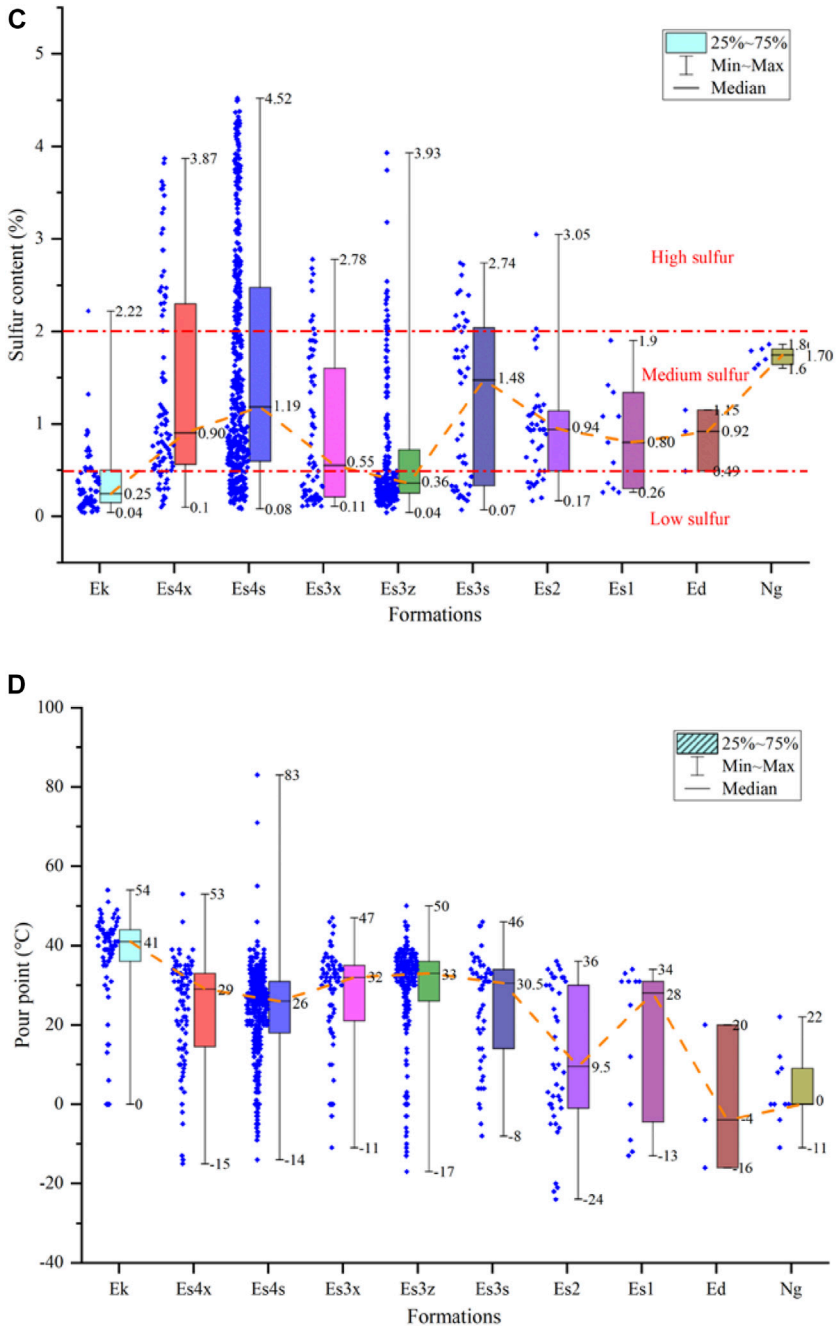

FIGURE 3
(Continued). Box plots showing the variation of crude oil physical properties in different formations. **(A)** API gravity. **(B)** Dynamic viscosity. **(C)** Sulfur content. **(D)** Pour point.

Hydrocarbon generation and accumulation in the Dongying Sag is mainly distributed in the Paleogene formations (Tao et al., 2022). Previous studies have shown that three sets of primary source rocks were developed in the Eocene Shahejie formation, namely, Es4s, Es3x, and Es3z (Zhang et al., 2019; Song et al., 2020; You et al., 2020) (Figure 2). In addition, the Ek2 member is a potential set of source rocks (Wang et al., 2018). The source rocks of the Es3 and Es4 members were deposited in different paleoclimates. Among them, the Es4 member is characterized by hypersaline lacustrine sediments deposited under arid conditions, while the Es3 member is characterized by freshwater lacustrine sediments deposited under humid conditions (Wang et al., 2008; Hao et al., 2009; Wang et al., 2021). The turbidite fans and deltaic sandstones in the Es4 and Es3 members constitute the main reservoirs in the Dongying Sag (Guo et al., 2016; Wang et al., 2016; Tao et al., 2022).

3 Materials and methods

The database comprises 1020 crude oil samples and 550+ source rock samples, from which physical properties, reservoir saturation

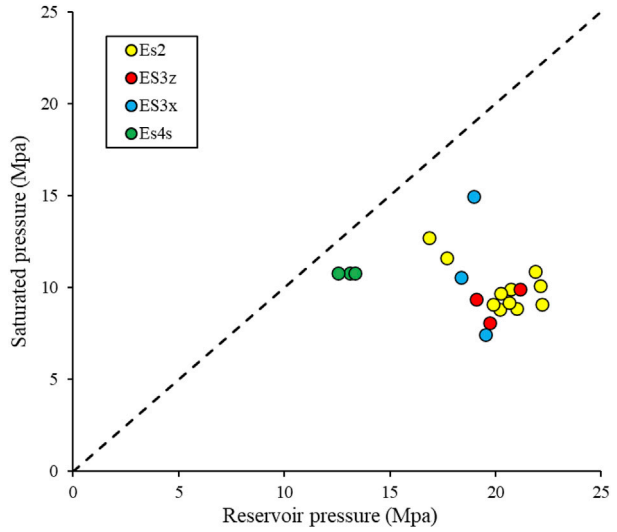

FIGURE 4
Plot of reservoir pressure *versus* saturation pressure for different formations in the study area.

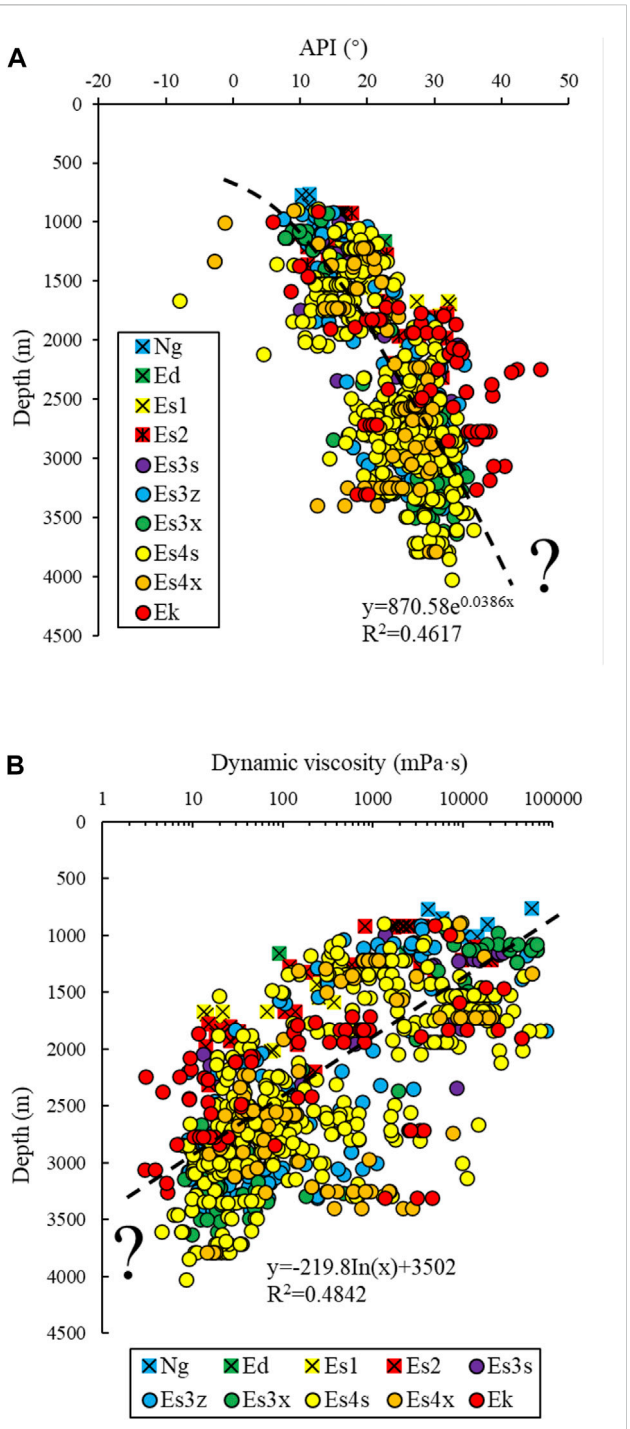

FIGURE 5
Trends of **(A)** API gravity and **(B)** dynamic viscosity of oil samples with present-day reservoir depth.

pressure, gas chromatography-mass spectrometry (GC-MS), and total organic carbon (TOC), Rock-Eval pyrolysis and vitrinite reflectance were available. The locations of the oil samples are shown in Figure 1C. There is a typical oil sample for almost every proven oilfield in the basin. Compounds in the saturated and aromatic hydrocarbon fractions were analyzed in the PRG laboratory at the University of Calgary using an Agilent 7890B gas chromatograph attached to an Agilent 5977A MSD system. The detailed procedures and experimental settings are the same as those described by Bennett et al. (2022). Two internal standards, cholestane-d4 was used to calculate the absolute concentrations of steranes, while dibenzothiophene-d8 was used to calculate the absolute concentration of methyl-dibenzothiophene. The relative response factors of the target compounds to the internal standards were considered to be one. To ensure the accuracy of the data, one blank sample and one duplicate sample were treated in the same way as the other samples. Organic petrographic observations of the source rocks were made with a Leica DMRXP microscope under reflected light and fluorescent light.

4 Results

4.1 Fluid characteristics

4.1.1 Physical properties

The physical properties of crude oil at each formation in the study area are presented in Table 1 and Figure 3, indicating good correlations between API gravity and other physical parameters and bulk chemical properties including dynamic viscosity, sulfur content, pour point and wax content. In Figure 4, the proven reservoir pressures are higher than the saturation pressures, indicating that the present reservoirs are unsaturated and secondary alteration processes have had little effect on the physical properties of the crude oil. The physical properties of crude oil from different formations in the study area show significant variations; therefore, this provides the opportunity to explore the factors influencing the physical properties in the natural laboratory.

In terms of crude oil density (Figure 3A), the crude oil in the study area is dominated by heavy-medium oil; among them, crude oil in the Es4, Es3s and above members are heavier compared with the crude oil in other members. In terms of dynamic viscosity (Figure 3B), the dynamic viscosity of crude oils in Es3x [8.13–66286 (40.7) mPas] and

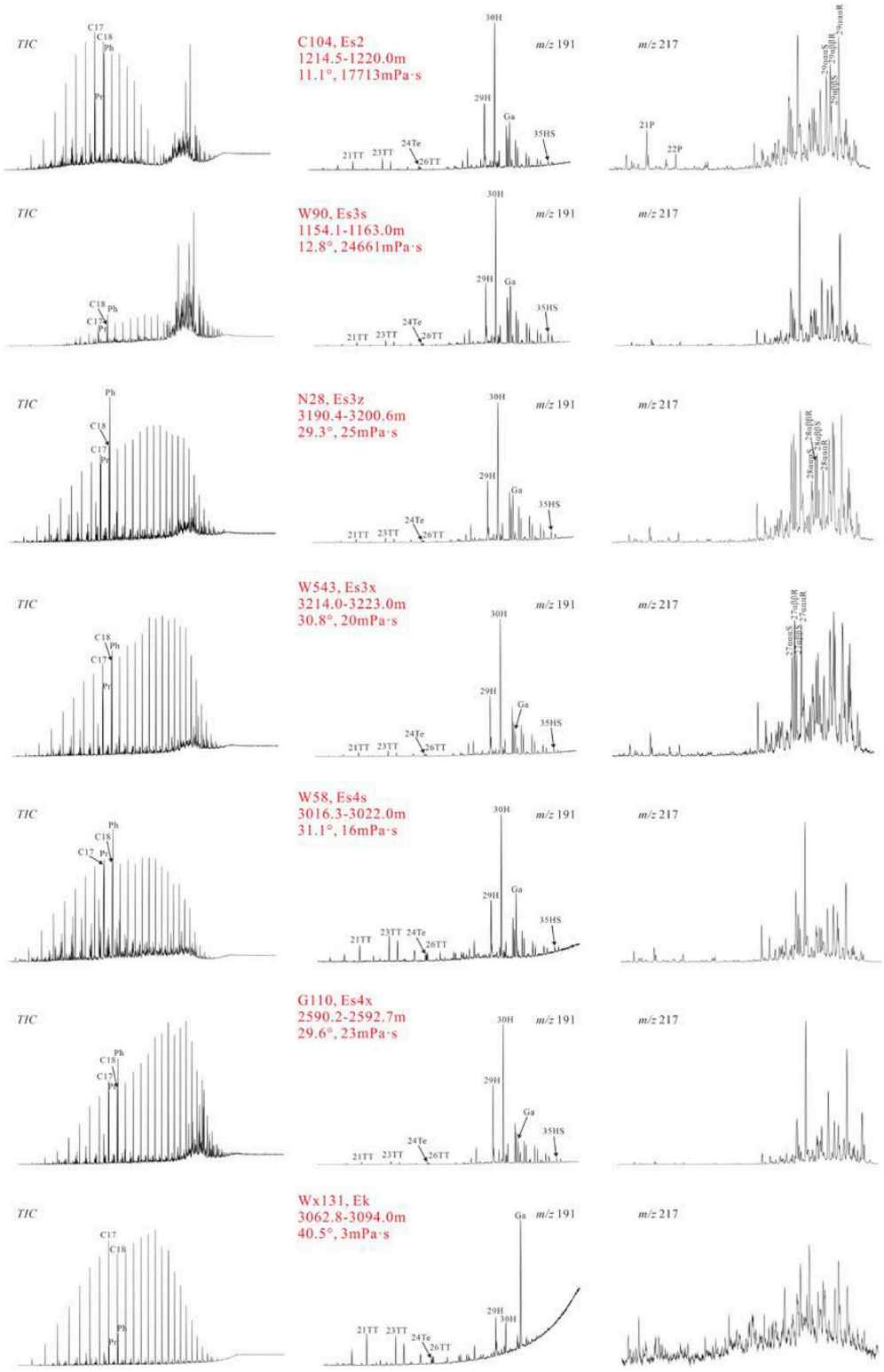

FIGURE 6
Representative gas chromatograms, *m/z* 191 and 217 mass chromatograms from oil samples showing the distribution of aliphatic fractions. Key: C17, C17 normal alkane; Pr, Pristane, Ph, Phytane; 21TT, C21 tricyclic terpane; 24Te, C24 tetracyclic terpane; 30H, C30 αβ hopane; Ga, Gammacerane; 35HS, C35 αβ 22S homohopane; 21P, C21 ααα pregnane; 22P, C22 ααα homopregnane; 27αααS, C27 ααα 20S sterane.

TABLE 2 Maturity-, lithology-, depositional environment- and source-related biomarker ratios for crude oil samples from different formations in the study area.

Strata	A	B	C	D	E	F	G	H	I	J	K	L	M	N
Es2	1.03–1.52 (1.28)	0.46–0.63 (0.55)	0.36–0.40 (0.37)	0.38–0.45 (0.42)	0.65–0.74 (0.71)	0.28–0.29 (0.28)	0.43–0.45 (0.44)	0.50–0.64 (0.56)	0.24–0.49 (0.38)	2.79–3.31 (3.03)	0.23–0.31 (0.27)	0.53–0.62 (0.58)	1.35–1.53 (1.41)	0.62–0.63 (0.62)
Es3s	1.92–3.29 (2.60)	0.65–0.83 (0.74)	0.24–0.32 (0.28)	0.32–0.34 (0.33)	0.66–0.77 (0.71)	0.25–0.34 (0.30)	0.28–0.42 (0.35)	0.64–0.81 (0.72)	0.27–0.34 (0.31)	0.76–3.90 (2.33)	0.17–0.27 (0.22)	0.56–0.65 (0.61)	1.31–1.51 (1.41)	0.99–1.23 (1.11)
Es3z	0.81–2.63 (1.67)	0.47–1.54 (0.71)	0.24–0.44 (0.37)	0.31–0.50 (0.40)	0.63–1.07 (0.75)	0.18–0.39 (0.27)	0.29–0.67 (0.44)	0.40–1.28 (0.67)	0.24–1.90 (0.44)	0.13–6.44 (1.51)	0.18–0.37 (0.27)	0.50–3.81 (0.76)	0.94–1.58 (1.35)	0.52–1.43 (0.91)
Es3x	0.72–1.24 (1.00)	0.42–0.56 (0.49)	0.37–0.45 (0.41)	0.34–0.55 (0.48)	0.72–0.76 (0.73)	0.23–0.29 (0.27)	0.37–0.46 (0.42)	0.42–0.65 (0.49)	0.46–0.61 (0.51)	0.24–2.29 (1.56)	0.28–0.47 (0.34)	0.55–0.73 (0.64)	1.31–1.40 (1.36)	0.43–0.80 (0.55)
Es4s	0.31–20.58 (2.81)	0.38–4.52 (0.89)	0.20–0.48 (0.32)	0.19–0.63 (0.37)	0.55–0.88 (0.72)	0.15–0.43 (0.30)	0.01–0.53 (0.35)	0.39–1.39 (0.85)	0.17–1.37 (0.39)	0.16–10.64 (3.52)	0.09–0.50 (0.28)	0.41–1.59 (0.62)	1.13–1.82 (1.42)	0.44–1.50 (1.00)
Es4x	1.55–2.25 (1.91)	0.70–0.80 (0.75)	0.24–0.51 (0.37)	0.28–0.49 (0.40)	0.66–0.84 (0.77)	0.24–0.36 (0.31)	0.36–0.57 (0.43)	0.57–1.01 (0.74)	0.30–0.52 (0.38)	1.47–13.31 (7.37)	0.18–0.37 (0.25)	0.52–0.75 (0.60)	1.19–1.51 (1.31)	0.58–0.99 (0.82)
Ek	0.30–7.37 (1.31)	0.14–1.32 (0.41)	0.26–0.56 (0.41)	0.30–0.54 (0.44)	0.60–0.73 (0.69)	0.20–0.26 (0.23)	0.36–0.87 (0.47)	0.39–0.65 (0.54)	0.29–0.58 (0.46)	3.21–38.73 (11.69)	0.15–0.44 (0.28)	0.22–0.64 (0.40)	1.37–1.67 (1.46)	0.21–0.78 (0.38)

Min-Max (average). Key: A, Ph/nC_{18}; B, Pr/nC_{17}; C, C29 αββ/(ααα+αββ) sterane; D, C29 ααα 20S/(20S+20R) sterane; E, C24 tetracyclic terpanes/C23 tricyclic terpanes; F, C22/C21 tricyclic terpanes; G, C29 norhopane/C30 hopane; H, C35S homohopane/C34S homohopane; I, Pr/Ph; J, Gammacerane/C30 Hopane; K, C29 norneohopane/C29 hopane; L, C24 tetracyclic terpanes/C26 tricyclic terpanes; M, C23/C24 tricyclic terpanes; N, C27ααaR sterane/C29ααaR sterane.

Es3z [8.83–84576 (28.35) mPas] members are lower than that of other members. In terms of sulfur content (Figure 3C), the crude oil in the study area is characterized by medium sulfur. Among them, the Ek [0.04–2.22 (0.25)%], Es3x [0.11–2.78 (0.55)%] and Es3z [0.04–3.93 (0.36)%] crude oils have lower sulfur contents compared with other members. In terms of pour point (Figure 3D), the Ek [0–54 (41)°C], Es3x [−11–47 (32)°C] and Es3z [−17–50 (33)°C] crude oils have higher pour points compared with other members. This series of phenomena indicates some variations in organofacies, thermal maturity and charging and mixing processes. The API gravity of crude oil shows a poor correlation with present-day reservoir depth (Figure 5A). Likewise, the dynamic viscosity of the oil correlates poorly with current depth (Figure 5B). Some oil samples at the same depth differ in dynamic viscosity by several orders of magnitude. Interestingly, the density and dynamic viscosity of some oil samples from the Ek Formation are lower than those of crude oil from other formations at the same depth.

4.1.2 Geochemistry characteristics

Figure 6 and Table 2 present representative mass chromatograms of the aliphatic fractions for representative crude oil samples and the related biomarker ratios. Most of the crude oil samples show no biodegradation and have complete normal alkane distributions. However, crude oils in shallow reservoirs (<1,300 m) show slight biodegradation and mixing (Figure 6). For example, crude oil from well C104 experienced multiple episodic charges of varying maturities and origins, where highly mature crude oil was mixed into immature fractions (Wang et al., 2021). The crude oil samples from different formations do not show odd-to-even carbon number predominance, revealing that these oils are considered to be expelled from source rocks with a maturity equivalent to a vitrinite reflectance (% Ro) higher than 0.5%. Moreover, the relative abundances of acyclic isoprenoids, tricyclic terpenes, gammacerane, and C_{30} 4α-methylsteranes in crude oil from different formations show different degrees of variation. A small number of crude oil samples from the Ek formation show high relative abundances of gammacerane due to the cracking of hopanes (Zhang et al., 2020).

The maturity parameters [Pr/*n*-C_{17} and Ph/*n*-C_{18}, C_{29} ααα 20S/(20S + 20R) and C_{29} αββ/(ααα + αββ)] also indicate variations in the maturity of crude oils from different formations (Figures 7A, B). The C_{29} sterane isomerization parameters, Pr/*n*-C_{17} and Ph/*n*-C_{18}, of the crude oil from the Ek formation reveal the highest maturity among all the formations. These crude oils are considered to have been expelled from source rocks with vitrinite reflectance (% Ro) above 1.0. The number of crude oil samples from the Es4s member is relatively high and is a mixture of maturity products (a full maturity spectrum oil) ranging from immature to late-mature. Furthermore, oil samples from the Es3x and above formations are dominated by early-mature to peak-mature. Various tricyclic terpanes and hopanes ratios, such as C_{22}/C_{21}TT, C_{24}/C_{23}TT (Figure 7C) and C_{29}/C_{30} hopane, $C_{35}S/C_{34}S$ homohopane (Figure 7D) are employed to differentiate the lithologies of source rocks (Zumberge, 1984; Connan et al., 1986; Mello et al., 1988). Based on these, it can be inferred that all oil samples in the study area are derived from lacustrine shale depositional environments. Obvious differences in biomarker ratios reflecting variations in water column stratification can be observed between oil samples from different formations. The Pr/Ph and Ga/C_{30}H ratios are widely used as indicators of redox

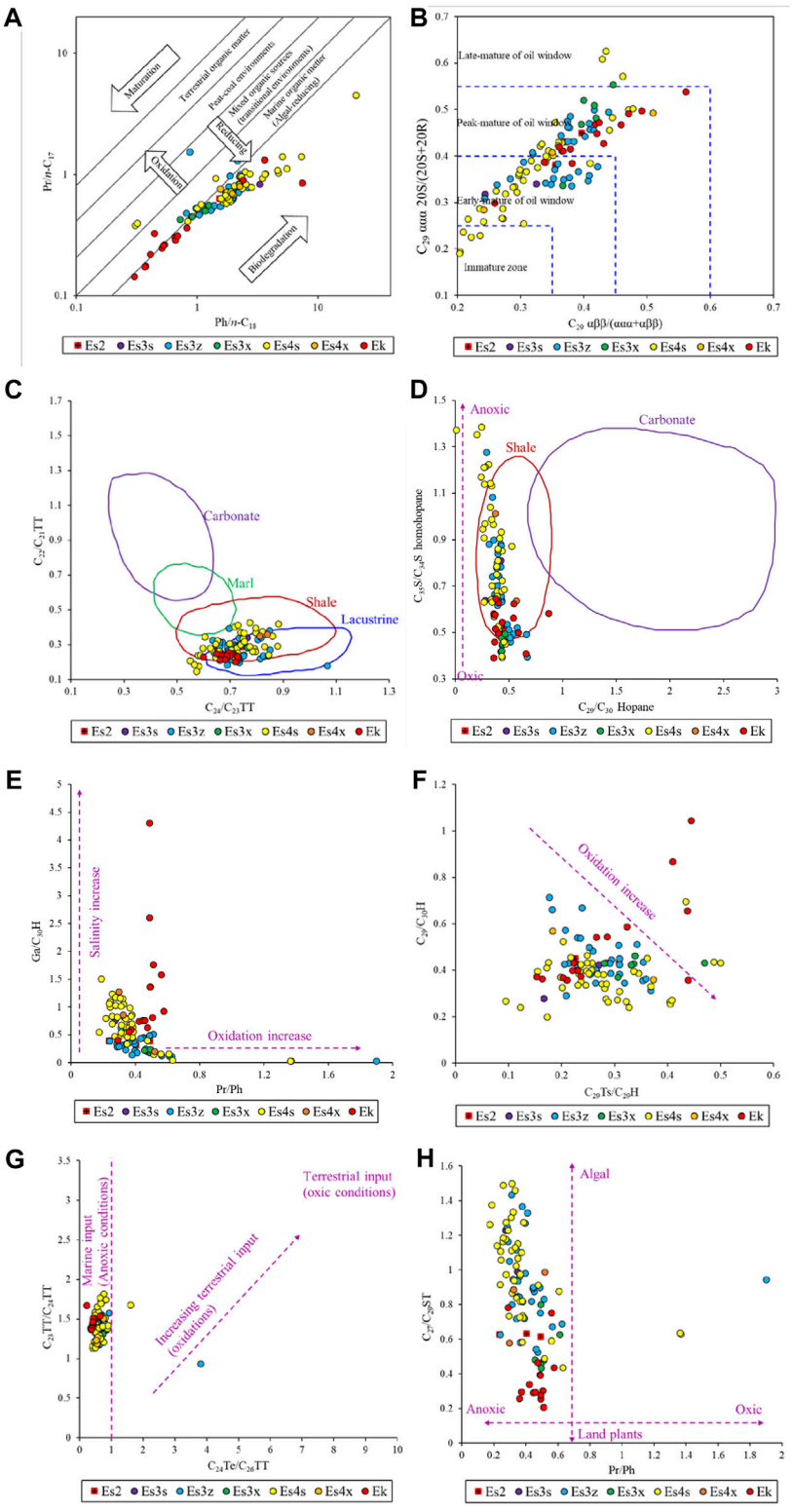

FIGURE 7
Scatter plots of maturity, lithology depositional environment and source indicators showing the variations of oil samples from different formations. **(A)** Pr/*n*-C_{17} and Ph/*n*-C_{18}. **(B)** C_{29} αββ/(ααα+αββ) and C_{29} ααα 20S/(20S+20R). **(C)** C_{24}/C_{23} TT and C_{22}/C_{21} TT. **(D)** C_{29}/C_{30} Hopane and $C_{35}S/C_{34}S$ homohopane. **(E)** Pr/Ph and Ga/C_{30}H. **(F)** C_{29}Ts/C_{29}H and C_{29}/C_{30}H. **(G)** C_{24}Te/C_{26}TT and C_{23}TT/C_{24}TT. **(H)** Pr/Ph and C_{27}/C_{29}ST. [**(A)** revised from Shanmugam, 1985; **(B)** revised from Hakimi et al., 2022; **(C,D)** revised from Al-Khafaji et al., 2022].

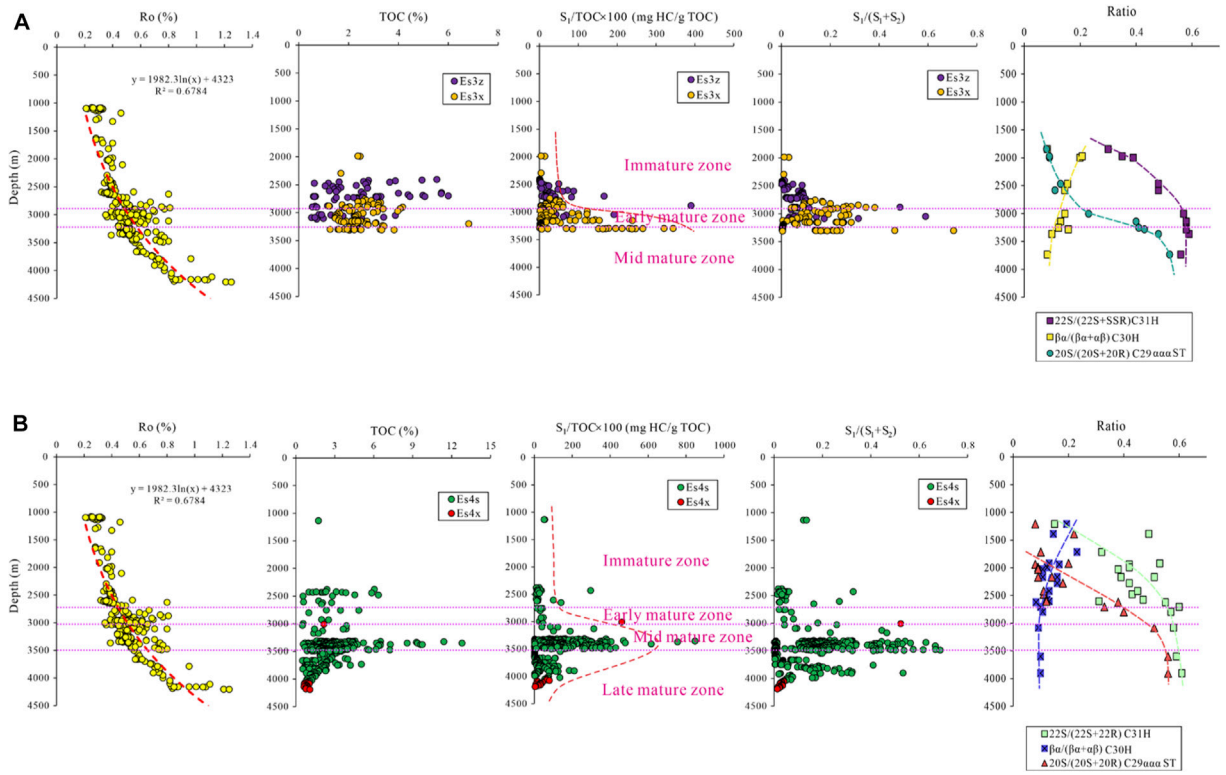

FIGURE 8
Oil generation expressed by %Ro, TOC, S_1/TOC, $S_1/(S_1+S_2)$, and biomarker maturity ratios of source rocks with burial depth. The maturity zones are determined by the shape of the curves, and the sterane and hopane ratios of the source rock extracts (Wilhelms et al., 1998). **(A)** Es3 member. **(B)** Es4 member.

TABLE 3 Results of Rock-Eval pyrolysis of source rocks with different organic matter types in the Es3 and Es4 members. The determination of organic matter types is based on Tmax and HI (Espitalié et al., 1985). Note that the data for these samples were obtained from the published literature (Li et al., 2018; Sun et al., 2019).

Well	Strata	S_1 (mg/g)	S_2 (mg/g)	Tmax (°C)	TOC (%)	HI(mg/g)	Organic matter types
W57	Es3	10.38	397.95	451	59.83	665	I
FY1-1	Es3	4.3	17.84	444	3.72	480	II_1
FY1-2	Es3	2.61	11.86	445	2.87	413	II_1
FY1-3	Es3	2.53	2.69	440	1.09	247	II_2
FY1-4	Es3	2.6	5.44	439	1.69	322	II_2
W161	Es4	12.08	351.43	436	49.22	714	I
FY1-5	Es4	1.99	3.99	450	1.75	228	II_1
FY1-6	Es4	2.26	23.68	450	6.08	389	II_1
FY1-7	Es4	4.41	6.02	441	2.63	229	II_2
FY1-8	Es4	5.84	10.28	438	3.86	266	II_2

conditions and water column stratification during source rock formation (Moldowan et al., 1985; Ten Haven et al., 1987). The Pr/Ph ratios of crude oil in different formations are almost all lower than 0.8, representing anoxic conditions (Figure 7E). Gammacerane is more abundant in most of the crude oils from the Ek and Es4 formations compared to those from other formations, suggesting that the source rocks are formed in water column stratification or hypersaline environments. Other depositional environmental indicators, such as $C_{29}Ts/C_{29}H$ and $C_{29}/C_{30}H$, also indicate that these crude oils originate from source rocks in anoxic environments (Figure 7F). These depositional environmental indicators illustrate an anoxic environment when the source rocks were formed. Among them, the source rocks for the crude oil in the Es4 and Ek formations were deposited in an anoxic, stratified,

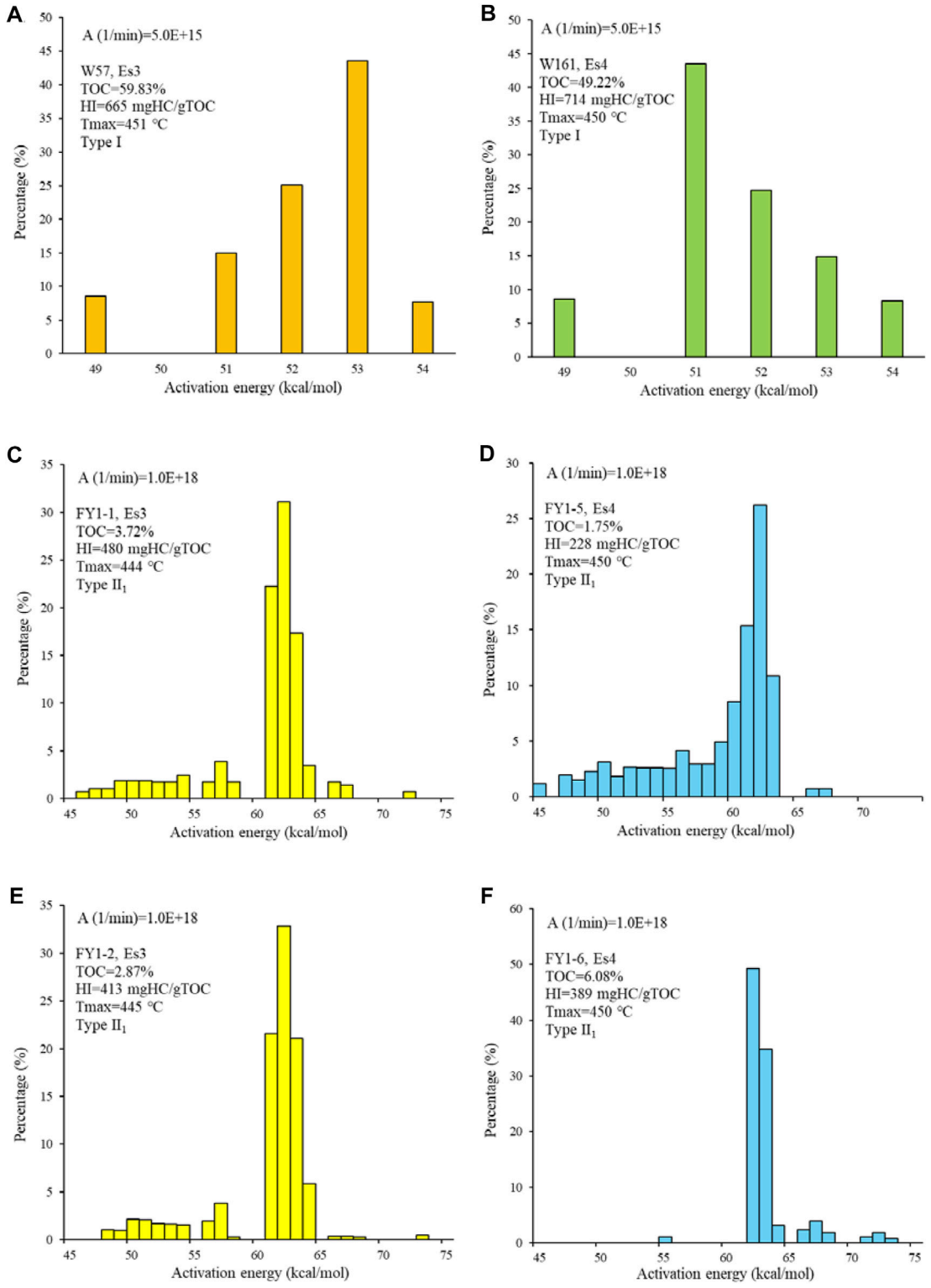

FIGURE 9
Continued.

brackish water environment. The Pr/*n*-C_{17} and Ph/*n*-C_{18} ratios in Figure 7A demonstrate that the crude oil samples from the different formations are distributed in the area interpreted as the algal source. The higher $C_{23}TT/C_{24}TT$ ratio is compatible with the lower C_{24}Te/

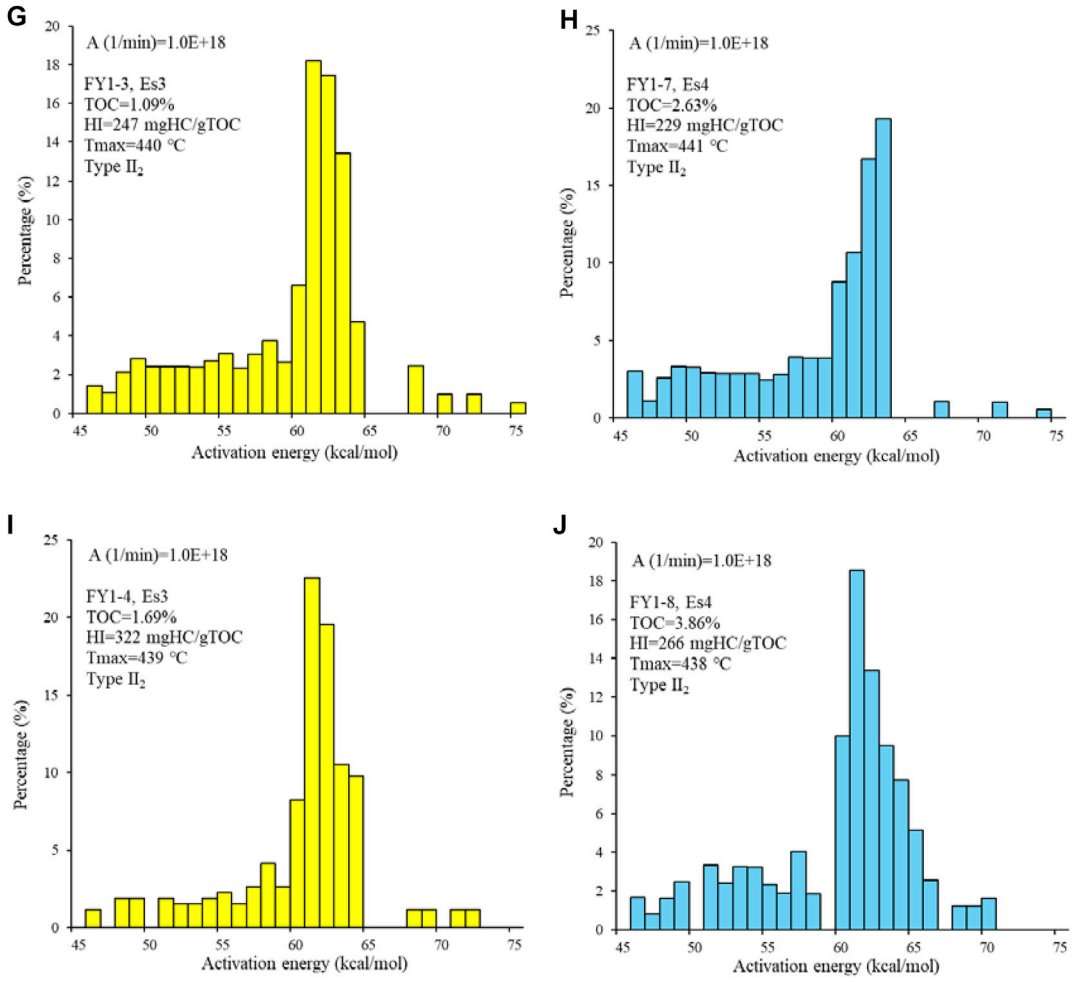

FIGURE 9
(Continued). Activation energy distribution and frequency factor of source rocks with different organic matter types in the Es3 and Es4 members. **(A)** W57. **(B)** W161. **(C)** FY1-1. **(D)** FY1-5. **(E)** FY1-2. **(F)** FY1-6. **(G)** FY1-3. **(H)** FY1-7. **(I)** FY1-4. **(J)** FY1-8. The determination of organic matter types is based on Tmax and HI (Espitalié et al., 1985). Note that the data for these samples were obtained from the published literature (Li et al., 2018; Sun et al., 2019).

C_{26}TT ratio (<1), further suggesting that these crude oils are derived from source rocks containing algal organic matter and were deposited under anoxic environmental conditions (Figure 7G). The relative abundances of C_{27} ααaR sterane and C_{29} ααaR sterane in the analyzed crude oil samples demonstrate the contribution of algae and terrestrial land plants to the source rocks. Among them, oil samples from the Ek formation have more terrigenous organic matter input, while oil samples from the Es4s and Es3z members have more algal organic matter input, and other oil samples are intermediate between them (Figure 7H).

4.2 Source rock characteristics

4.2.1 Natural maturity shale sequences

Plots of source rock geochemical parameters such as %Ro, S_1/TOC and HI as a function of burial depth or formation temperature are commonly employed to characterize petroleum formation within source rocks under natural maturity sequences (Wilhelms et al., 1998). These curves can quantitatively show the process of petroleum (C_{15+} hydrocarbons) generation and delineate maturity zones (Cornford et al., 1983). Figures 8A, B show the geochemical parameters of the source rocks in the Es3 and Es4 members under natural conditions as a function of burial depth. Based on the shape of the bell curve, some differences in the maturity zones of the source rocks in the Es3 and Es4 members can be found. The maturity zones of source rocks in the Es4 member can be divided into four zones, namely, immature zone—no significant increase in hydrocarbon generation (<2800 m); early mature zone-increase in hydrocarbon generation (2800–3000 m); mid mature zone—peak hydrocarbon generation (3000–3500 m); late mature zone—heavy hydrocarbon cracking to lighter products (>3500 m). The maturity zones of source rocks in the Es3 member can be classified into three zones, i.e., immature zone (<3000 m); early mature zone (3000–3300 m); mid mature zone (>3300 m). From this, it can also be found that the source rocks from the Es4 member enter the thresholds of their respective maturity zones earlier than

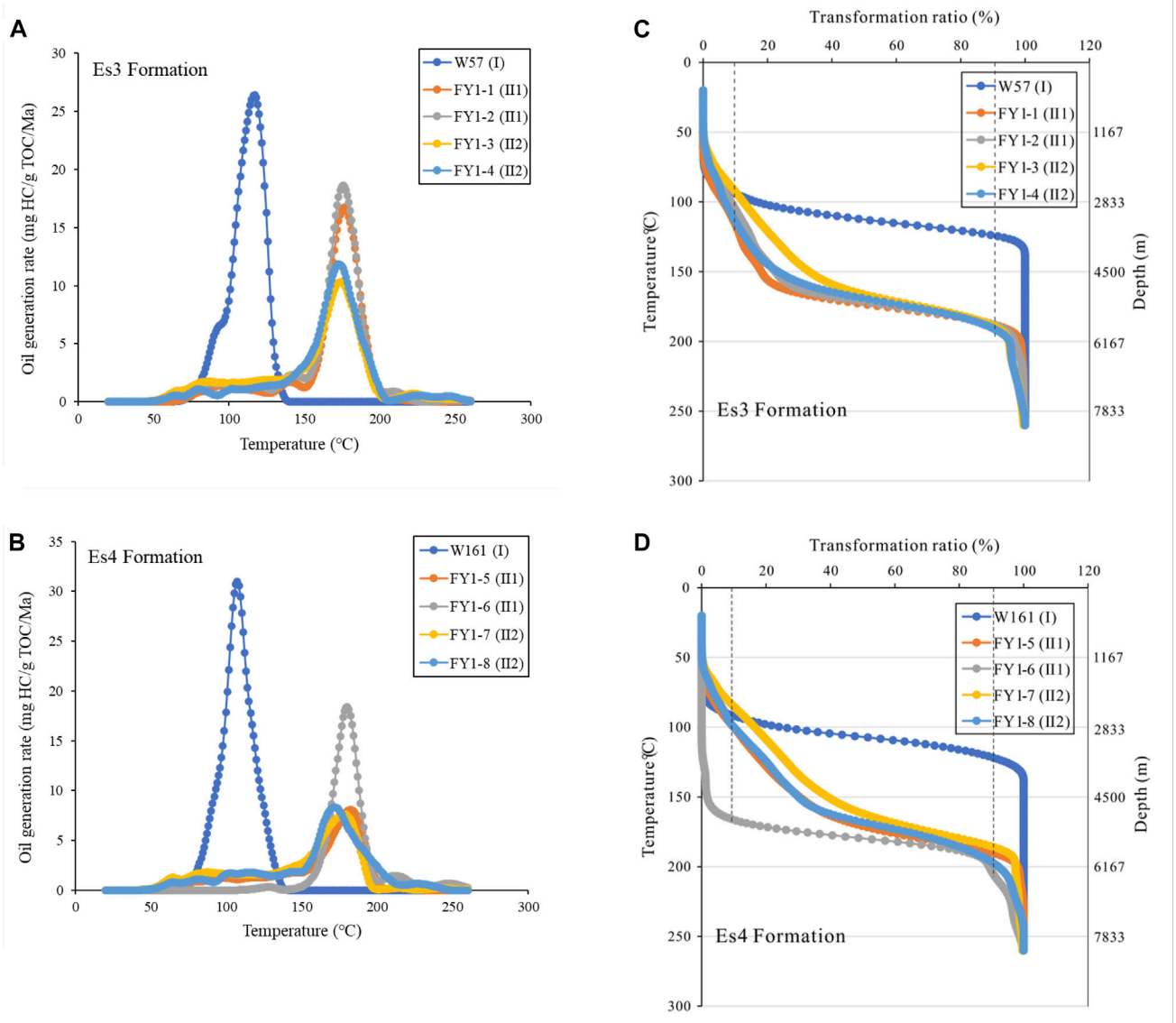

FIGURE 10
Geological extrapolation to obtain oil generation rates and transformation ratios from kinetic experimental results of the Es3 and Es4 samples assuming a geological heating rate of 3°C/Ma. **(A)** Oil generation rate *versus* temperature in the Es3 formation; **(B)** Oil generation rate *versus* temperature in the Es4 formation; **(C)** Transformation ratio *versus* temperature and depth in the Es3 formation; **(D)** Transformation ratio *versus* temperature and depth in the Es4 formation.

those from the Es3 member. Assuming that the hydrocarbons generated from source rocks are retained *in situ* and there is no disturbance of migrating hydrocarbons, the $S_1/(S_1+S_2)$ ratio can approximately characterize the transformation ratio of source rocks. Although this assumption is difficult to validate, it can also be observed from Figure 8 that the transformation ratio of source rocks in the Es4 member is higher than that of the Es3 member source rocks. Interestingly, the vitrinite reflectance and molecular thermal maturity indicators are not consistently distributed in the study area, especially for source rocks entering the hydrocarbon generation threshold. Previous studies have shown that the high hydrogen-rich alginite content has a suppressive effect on the vitrinite reflectance in the studied lacustrine shales (Guo et al., 2010; Chen et al., 2019). As discussed above, this phenomenon is consistent with the results of the interpretation of molecular source parameters from crude oil samples (Figure 7A, G, H).

4.2.2 Kinetic modeling

Table 3 and Figure 9 illustrate the Rock-Eval pyrolysis results and associated activation energy distributions for source rock samples of different organic matter types in the Es3 and Es4 members. Hydrocarbon generation kinetic data differ for samples from different organic matter types and members. When fixing the frequency factor A at 5.0E+15/min, the activation energy of the whole rock ranges from 49 to 54 kcal/mol (Figures 9A, B); And, when the frequency factor A is at 1.0E+18/min, the activation energy of the whole rock is

TABLE 4 Summary of some published kinetic experiments on lacustrine source rocks containing type I kerogen.

Sample	Rock type	Depositional environment	Kerogen type	Activation energy (kcal/mol)	Frequency factor (/s)	Pyrolysis methods	References
W57 (Es3)	Whole rock	Lacustrine	I	49–54 (53)	8.33E+13	Open system	This study
W161 (Es4)	Whole rock	Lacustrine	I	49–54 (51)	8.33E+13	Open system	This study
Qingshankou Mudstone	Kerogen	Lacustrine	I	45–59 (55)	1.63E+14	Open system	Zhou and Littke. (1999)
Green River Shale	Whole rock	Lacustrine	I	51–58 (56)	1.11E+15	Open system	Dieckmann (2005)
Bryne Mudstone	Whole rock	Lacustrine	I	55–65 (55)	1.23E+14	Open system	Petersen et al. (2011)
Wenchang Mudstone	Whole rock	Lacustrine	I	51–60 (53)	3.18E+11	Open system	Li et al. (2016)
Yacoraite Shale	Whole rock	Lacustrine	I	48–56 (52)	3.16E+13	Open system	Romero-Sarmiento et al. (2019)
Sleipner Mudstone	Kerogen	Lacustrine	I	54–58 (54)	1.34E+14	Open system	Killops et al. (2022)

Min-Max (peak).

between 45 and 75 kcal/mol (Figures 9C–J). Under the conditions of similar frequency factors, the main peaks of activation energy distributions of the Es4 source rocks are lower than those of the Es3 source rocks, revealing that the Es4 source rocks generate oil earlier than the Es3 source rocks. The distribution of activation energy becomes broader and more scattered in order from kerogen type I to II_2. The whole rock of FY1-6 has narrower activation energy distributions (63–74 kcal/mol) than the other samples, indicating that the organic matter in the FY1-6 whole rock samples has higher thermal stability than the other samples (Figure 9F). These kinetic experimental results are extrapolated to geological conditions at a constant geological heating rate (3°C/Ma) using the KMOD program. Figure 10 shows the oil generation rate and transformation ratio from different source rocks under geological conditions. It can be observed that the kerogen type I in Es4 source rocks reaches the peak oil generation earlier than in Es3 source rocks (Figures 10A, B). The oil generation rate decreases sequentially from kerogen type I to II_2, regardless of whether it is in the Es3 or Es4 member. Given a surface temperature of 15°C and a geothermal gradient of 30°C/km, the products of kerogen type I from the Es3 and Es4 source rocks are both dominated by oil, and more than 90% of the kerogen has been transformed into oil at 120°C, corresponding to a depth of ca. 3,600 m (Figures 10C, D). However, the conversion of kerogen type II_1 and II_2 to oil needs to occur at greater depths. The transformation ratio curves of both Es3 and Es4 source rocks suggest that kerogen type I makes a major contribution to the distribution of hydrocarbon resources in the study area.

The hydrocarbon generation characteristics of lacustrine source rocks containing type I kerogen have been extensively studied in different basins around the world. Degradation of kerogen in the study area is characterized by extremely narrow activation energy distributions with peaks at 53 and 51 kcal/mol, respectively, indicating that type I kerogen is more stable (Figures 9A, B). Similar, very narrow activation energy distributions have been observed for the Qingshankou Mudstone in the Songliao Basin (Zhou and Littke., 1999), the Green River Shale in the Uinta Basin (Dieckmann, 2005), the Bryne Mudstone in the SØGNE Basin (Petersen et al., 2011), the Wenchang Mudstone in the Pearl River Mouth Basin (Li et al., 2016), the Yacoraite Shale in the Salta Basin (Romero-Sarmiento et al., 2019) and the Sleipner Mudstone of Utsira High (Killops et al., 2022) (Table 4). The narrow activation energy distribution is usually associated with the predominance of aliphatic chains in type I kerogen (Behar and Vandenbroucke, 1987). Compared with other lacustrine source rocks containing type I kerogen, there are some differences in the petroleum generation kinetic parameters of the study area. The lower values of single activation energy of the source rocks in the study area indicate slightly lower thermal stability, which is beneficial to the formation of abundant hydrocarbon resources (Table 4).

5 Discussion

5.1 Thermal maturity and physical properties

The compositional variations in molecular structure, attributed to maturation, were previously identified by plotting source rock extraction data *versus* sample depth (Mackenzie et al., 1981; Chandra et al., 1994). Based on these, a large number of maturity indicators are built (Tissot et al., 1987). However, care must also be taken in the interpretation of such indicators, as reservoir oils are often mixtures, derived from products of different evolutionary stages of the same source rock or multiple source rocks (Wilhelms and Larter, 2004). Thus, reservoirs at different locations in the basin may

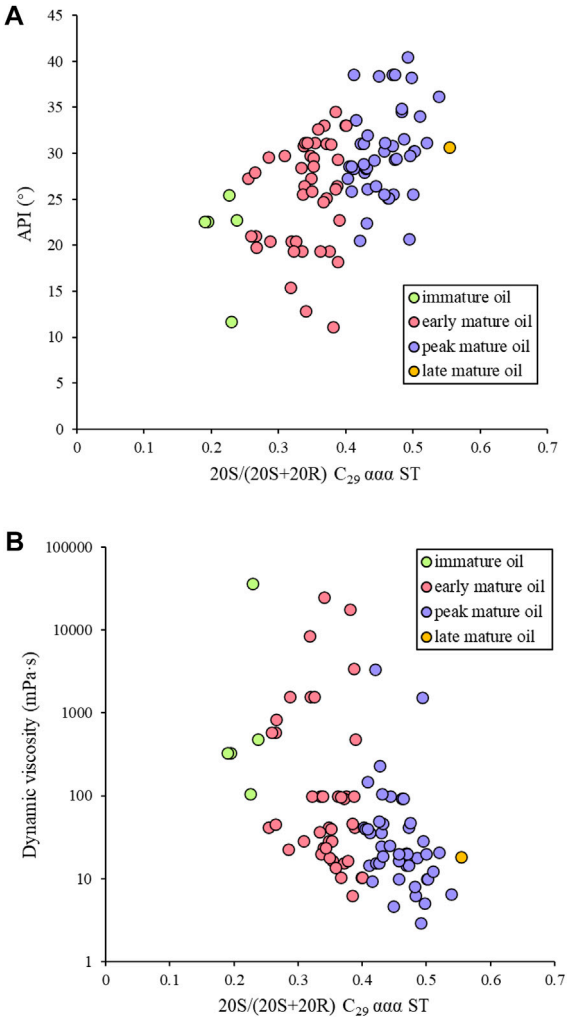

FIGURE 11
Scatter plots of the 20S/(20S+20R) C_{29} ααα ST against API gravity **(A)**, dynamic viscosity **(B)**.

successively capture the products of early, early + medium, and early + medium + late mature source rocks (Figures 8A, B). The type of hydrocarbons ultimately captured in the reservoir depends on the hydrocarbon generation, hydrocarbon expulsion, migration pathways and the effectiveness of the traps. In the absence of effective hydrocarbon expulsion, the hydrocarbons may be retained *in situ* until the products saturate the source rocks, with the eventual expulsion of mid to late mature products. In addition, the retained hydrocarbon amount depends largely on the hydrocarbon generation and carrier systems in many lacustrine depositional systems. The potentially greater hydrocarbon generation and lack of well-developed carrier systems can result in a more limited ability to expel and mobilize oils, thereby increasing the viability of these potential unconventional plays (Katz and Lin, 2014). It is to be noted when using maturity molecular parameters that the early mature oils are relatively small in volume but usually contain high concentrations of biomarkers. The medium- and late-mature oils are relatively large in volume, but the concentrations of biomarkers are decreased by multiple orders of magnitude (Wilhelms and Larter, 2004; Huang et al., 2022). Thus, the maturity molecular indicators obtained from the reservoir oils are only a qualitative indicator of the range of the source rock maturities indicating their contribution to the oils captured in the reservoirs (Cornford et al., 1983). The two C_{29} sterane isomerization parameters [20S/(20S+20R) and αββ/(αββ+ααα)] are effective in assessing maturity from immature to late maturity windows (Mackenzie et al., 1983; Beaumont et al., 1985; Peters et al., 1996). However, Seifert and Moldowan (1981) suggested αββ/(αββ+ααα) C_{29} steranes as a migration indicator based on laboratory simulations. Therefore, the 20S/(20S+20R) C_{29} ααα steranes are adopted in this paper to characterize the oil maturity. Based on the relationships between the 20S/(20S+20R) C_{29} ααα and API gravity and dynamic viscosity of crude oils, It can be seen that the density and dynamic viscosity of the crude oils decrease with increasing crude oil maturity (Figures 11A, B). It further indicates that capturing crude oils with medium to late maturity is beneficial to improve reservoir oil physical properties. It is worth noting that crude oils in the early mature or peak oil windows have significantly different API gravities and dynamic viscosities, suggesting that their physical properties are also influenced by other factors.

5.2 Organofacies variation and physical properties

Organicfacies refer to a class of kerogen assemblages that originate from the same organic precursors and have experienced similar depositional environments and early diagenesis (Pepper and Corvi, 1995). Source rocks with different organicfacies generate distinctly different products during thermal evolution, including physical and geochemical properties (di Primio and Horsfield, 2006; Baur, 2019; Feng et al., 2021). In this paper, the classification scheme of lacustrine source rocks proposed by Pepper and Corvi (1995) is adopted, namely, organicfacies C, D/E, and F. Organicfacies C are oil-prone source rocks. The organic matter in these source rocks is mainly derived from algae and bacteria, and large quantities of lamalginites and telalginites can be observed under the microscope. In the immature stage, the hydrogen index (HI) of organicfacies C source rocks generally exceeds 400 mg HC/g TOC. Organicfacies D/E and F are gas-prone source rocks that are mainly developed in environments with high terrestrial organic matter input. The HI of organicfacies D/E source rocks generally ranges from 200 to 400 mg HC/g TOC in the immature stage, while the HI of organicfacies F source rocks is generally less than 200 mg HC/g TOC. The maceral composition of these two organofacies is dominated by vitrinite and inertinite. The relative frequency distribution histograms of HI for source rocks in different members are shown in Figure 12. The source rocks in Es4s and Es4x mainly consist of organicfacies C (Figures 12C, D), while those in Es3z and Es3x are characterized by organicfacies D/E and F (Figures 12A, B), suggesting that the input of terrigenous organic matter increases from Es4 to Es3 members. The organic macerals of the source rocks in the study area are mostly composed of algal-derived liptinite macerals, including lamalginite, bituminite, and vitrinite (Figure 13). These characteristics are consistent with the geochemical characteristics of the crude oils (Figures 7A, G, H). The analysis of organicfacies and organic petrology of source rocks

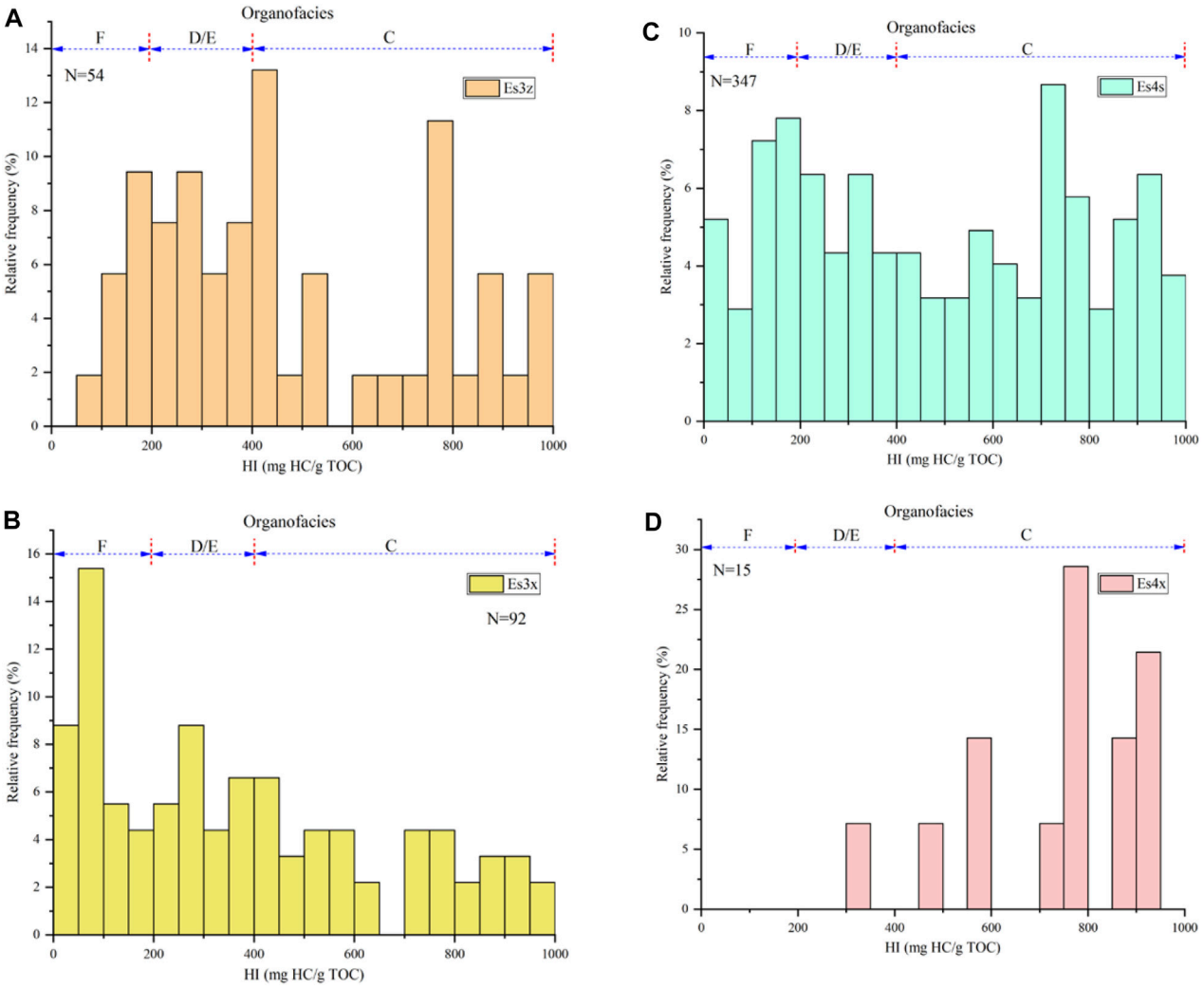

FIGURE 12
Relative frequency distribution histogram of HI for source rocks in different members. **(A)** Es3z member; **(B)** Es3x member; **(C)** Es4s member; **(D)** Es4x member.

suggests that the quality of source rocks in different members is mainly due to the different relative proportions of algae and terrigenous organic matter in kerogens. Source rocks with different organicfacies present different oil expulsion thresholds and physical properties of crude oils (Pepper, 1991; Petersen, 2017). The source rocks with greater HI values expel oil earlier and more efficiently (Pepper, 1991; Feng et al., 2021), which is consistent with the actual conditions in the study area. Compared with Es3 crude oils, Es4 crude oils have higher density, dynamic viscosity and sulfur content, covering a wide thermal maturity range from immature to late mature.

5.3 Charging and mixing process

Thermal maturation of organic matter is a temperature/time-driven disproportionation reaction that converts sedimentary organic matter into oil and gas (Peters and Cassa, 1994). Although maturity is one of the most widely used terms in petroleum geology, its actual meaning is rarely defined, resulting in many confusing and conflicting evaluation results. However, determining the oil maturity is important for understanding the oil generation and expulsion process, accumulation history and exploration potential evaluation. Because crude oils are fluid, oils captured in the reservoirs may originate from products formed in different evolutionary stages of a single uniform source rock or from multiple source systems. Thus, nearly all reservoir oils are complex mixtures that have experienced charging at different times or with different source rock types. Those different molecular maturity parameters (biomarkers and non-biomarkers) represent different maturity levels, but none of them reflect the maturity of crude oil. The molecular maturity parameters currently utilized to assess crude oil maturity are based on the relative abundance of two stereoisomers (Seifert and Moldowan, 1978; Radke et al., 1982; Grantham, 1986; Radke et al., 1986). During thermal evolution, the absolute concentration of the less stable isomers decreases

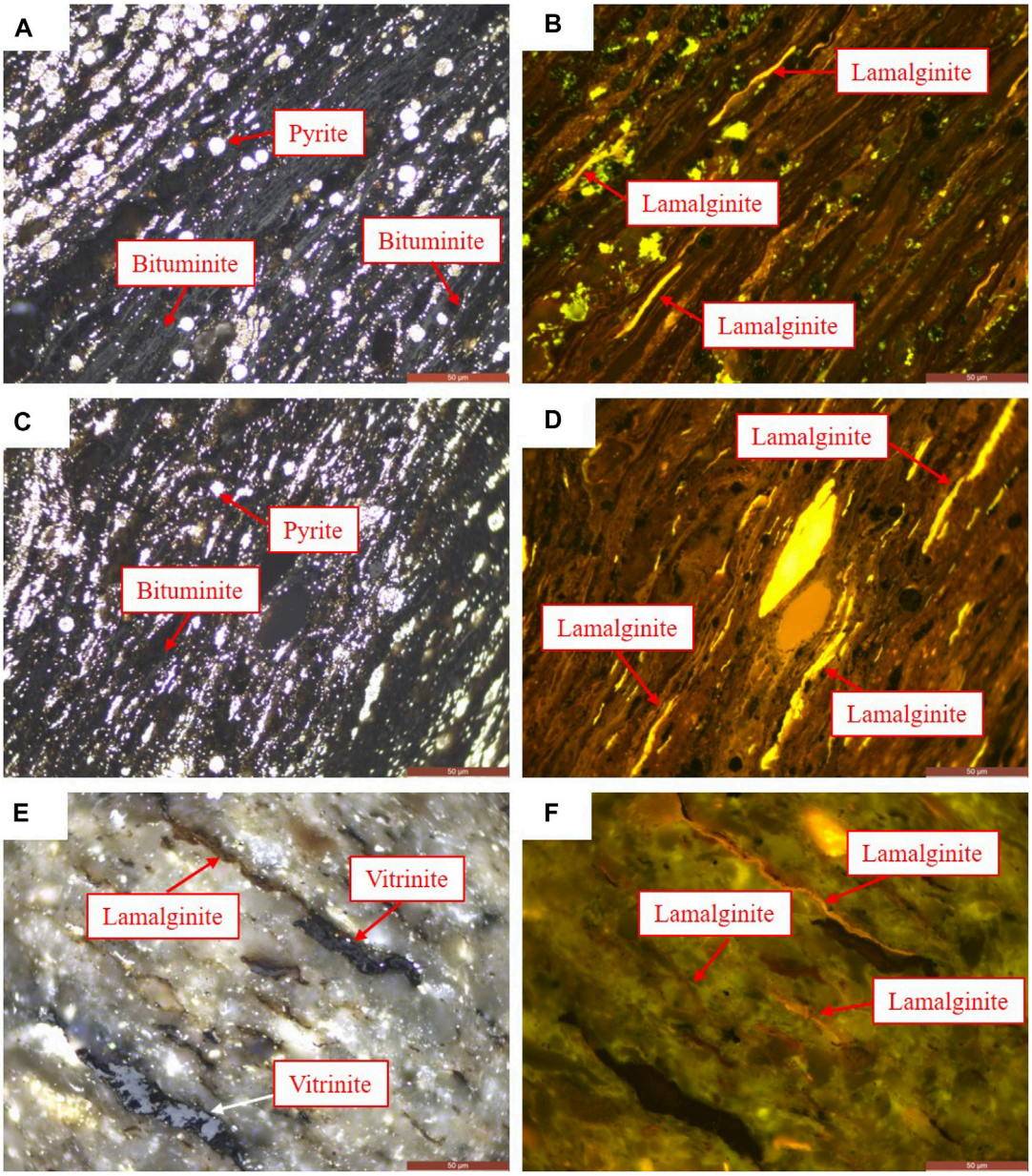

FIGURE 13
Organic macerals in source rocks from the study area, including lamalginite, bituminite and vitrinite; **(A,C,E)** under reflected light; **(B,D,F)** under fluorescent light.

relatively, while the absolute concentration of the more stable isomers increases relatively. The absolute concentrations of different compounds in crude oil vary greatly from the dead oil to the condensate stage (Wilhelms and Larter, 2004). While the concentrations of *n*-alkanes and isoprenoid hydrocarbons (pristane and phytane) in crude oils vary essentially by 1-2 orders of magnitude, the absolute concentrations of aromatics (methylphenanthrenes) and light hydrocarbons in most oils vary by more than two orders of magnitude. Among these compounds, biomarkers (hopanes and steranes) and diamondoid hydrocarbons (dimethyl diamantanes) showed the largest range of absolute concentration variation. The absolute concentrations of biomarkers change by nearly five orders of magnitude, while the diamondoid hydrocarbons change by three orders of magnitude.

Oil mixing is a common phenomenon in oil and gas fields (Wilhelms and Larter, 2004; Larter et al., 2012; Wang et al., 2021; Huang et al., 2022). Because the concentrations of maturity-related biomarkers or non-biomarkers vary greatly across maturity levels, deeper concepts of petroleum maturity need to be elucidated. Different oil maturity parameters often record information about different stages of charging and mixing. The maturity parameters related to saturated and aromatic hydrocarbons are the most

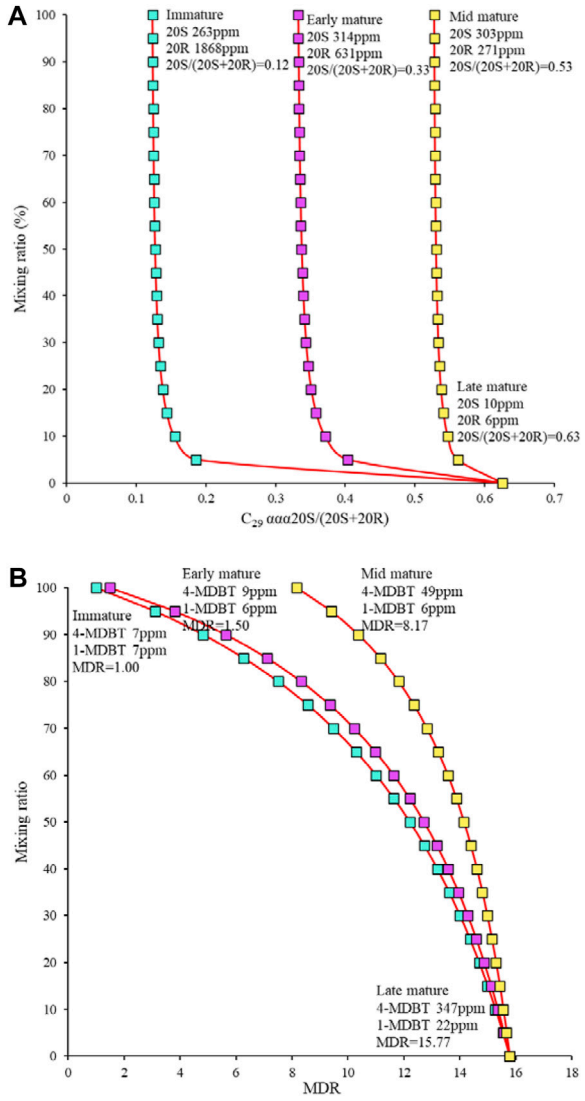

FIGURE 14
Variations of C_{29} aaaα 20S/(20S+20R) **(A)** and MDR **(B)** ratios after mixing with different maturity crude oils.

common evaluation parameters in the field of petroleum geology. Here, we use two cases to illustrate how biomarkers and aromatics concentration-related maturity parameters are recorded for oil charging and mixing histories. The concentration data for these specific components are derived from a mature source rock sequence. During the process of source rock maturation, the concentrations of biomarker compounds drop sharply or even disappear. If the reservoir receives charge from multiple oils, maturity parameters based on biomarker ratios will produce a bias to overemphasize the contribution of low maturity oils, indicating the oil captured in earlier reservoirs. Here, C_{29} aaa 20S/(20S+20R) is taken as an example, which is highly specific for the immature to the late mature range (Mackenzie et al., 1983; Beaumont et al., 1985; Peters et al., 1996). Figure 14A shows cross-plots of C_{29} aaa 20S/(20S+20R) and mixing ratios for end-member oils of different maturities, and the concentrations of each component in the mixed oil. When immature, early mature or mid-mature oil is mixed with late mature oil, respectively, the biomarker parameters show signatures of lower maturity end member oil even when this mixture contains 95% late mature oil (Figure 14A). In contrast, maturity parameters based on aromatic isomers are more sensitive to the mixing process and even biased towards the signatures of higher maturity end-member oils. As the thermal maturity increases, the kerogen becomes increasingly enriched in aromatic structures and the concentrations of the generated free alkylated aromatics usually also increase before oil-to-gas cracking (Huang et al., 2022). The MDR (MDR=4-MDBT/1-MDBT) ratio is well suited for assessing maturity from immature to the end of the condensate/wet gas maturity window (Radke, 1988; Chakhmakhchev and Suzuki, 1995; Chakhmakhchev et al., 1997). When immature, early mature or mid-mature oils are mixed with late-mature oils, respectively, the MDR ratio easily resolves the effect of the mixing process (Figure 14B). Thus, maturity parameters based on aromatic isomers tend to reflect the degree of mixing of captured crude oils in mid-to late-stage reservoirs.

As discussed previously, the charging and mixing histories of the study area are reconstructed based on molecular maturity parameters. Firstly, the biomarkers and aromatic maturity parameters need to be converted to generally accepted vitrinite reflectances (%R_o). The %R_o cutoff values for maturity windows vary in the literature (Dow, 1977; Lewan, 1987; Dembicki, 2009; Srinivasan et al., 2022). The following %Ro cutoff values are used in this study: 0.25–0.5 for immature, 0.5–0.7 for early oil window, 0.7–1.0 for peak oil window, 1.0–1.35 for late oil window, 1.35–2.0 for condensate/wet gas window, and 2.0 and above for dry gas window (Lewan, 1983). Based on the C_{29} aaa 20S/(20S+20R) values, the maturity window of lower maturity end member oils captured by the reservoir is determined (Mackenzie et al., 1983; Beaumont et al., 1985; Peters et al., 1996). Generally, there is a direct relationship between aromatic molecular maturity parameters and equivalent %R_o values. Six equations (for Eqs 1–6) for calculating the equivalent %R_o are adopted based on the relationship between multiple %R_o values and MDR (Jarvie et al., 2001; Wust et al., 2013; Evenick, 2021; Lohr and Hackley, 2021; Srinivasan et al., 2022). In order to more accurately assess the oil maturity, the six equivalent %R_o values are averaged to obtain the final equivalent % R_o. Comparing the maturity windows obtained from biomarkers [R_o % (Bio)] and the equivalent %R_o gained from MDR [R_o% (MDR)], three geological scenarios can be identified. Scenario 1: If the R_o% (MDR) value is higher than the maturity window defined by the R_o% (Bio) value, it indicates that crude oil with the maturity of R_o% (Bio) is captured in the early reservoir, and oil with the maturity higher than R_o% (MDR) is continuously charged and mixed in the mid-to late-stage reservoir and accounts for a significant contribution; Scenario 2: If the R_o% (MDR) value falls within the maturity window defined by the R_o% (Bio) value, it means that the reservoir has only captured oil from that maturity window, where the larger the R_o% (MDR) value the higher the maturity of the oil; Scenario 3: If the R_o% (MDR) value is lower than the maturity window defined by the R_o% (Bio) value, it means that the R_o% (MDR) is an invalid value and the reservoir may be charged and mixed with high maturity oil. Figure 15 illustrates the oil charging and mixing model from sag to slope in the study area. Peak oil is captured early in the reservoir near well W587, accompanied by late oil charging in the mid to late stages. The reservoirs near wells

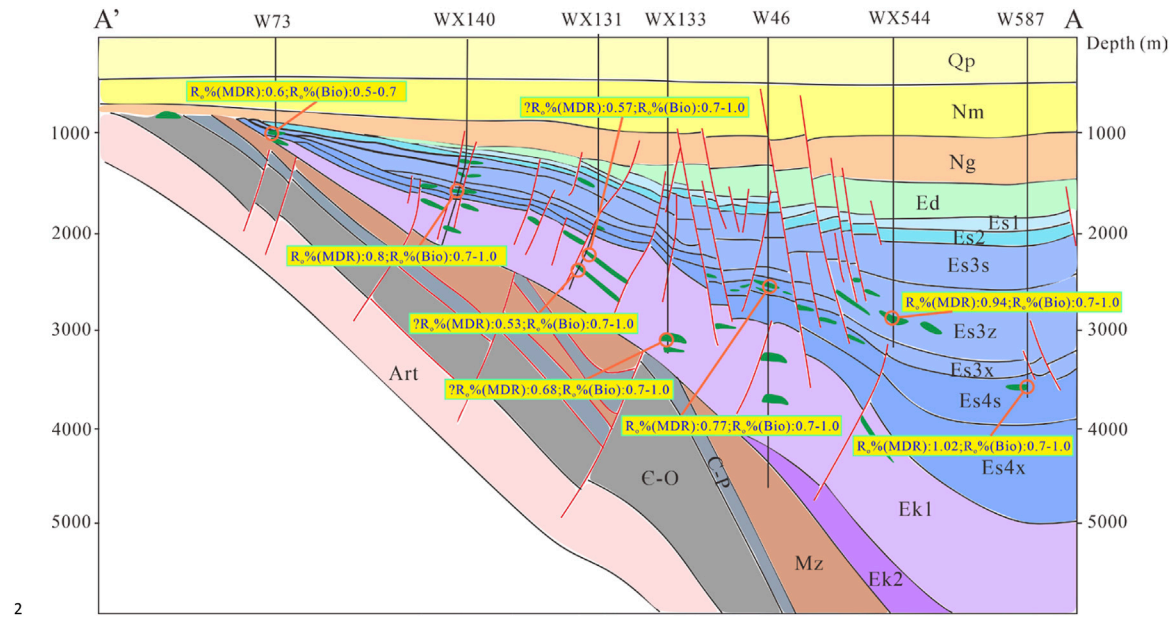

FIGURE 15
Oil charging and mixing model from sag to slope in the study area (Profile location in Figure 1C). The maturity window defined by R_o% (Bio) values is derived from C_{29} ααα 20S/(20S+20R) values, while R_o% (MDR) values are derived from MDR values.

WX544, W46 and WX140 only capture peak oil, and the oil maturity decreases from sag to slope. In contrast, the reservoir near well W73 only captures early oil. The relatively anomalous R_o% (MDR) values from the Ek reservoir are smaller than the maturity window defined by the R_o% (Bio) values, suggesting high maturity oil charging and mixing.

$$R_o = 0.4505 \times \ln(MDR) + 0.4517 \quad (1)$$
$$R_o = 0.1847 \times \ln(MDR) + 0.6083 \quad (2)$$
$$R_o = 0.2558 \times \ln(MDR) + 0.6054 \quad (3)$$
$$R_o = 0.2117 \times \ln(MDR) + 0.5780 \quad (4)$$
$$R_o = 0.2582 \times \ln(MDR) + 0.6495 \quad (5)$$
$$R_o = 0.2465 \times \ln(MDR) + 0.6651 \quad (6)$$

5.4 Recommendations for the future

In terms of oil charging and mixing models, the oils captured in the reservoirs are a mixture and maturity parameters in light hydrocarbons, biomarkers and aromatics can be considered to comprehensively characterize the oil maturity. Integrating methods such as oil maturity and tectonic evolution to reconstruct hydrocarbon migration and accumulation processes, constrain basin models and reduce exploration risk. At present, only the charging and mixing of two end-member oils are considered, and the number and amount of multiple episodes or continuous charging need to be further explored. Moreover, the contribution of different oil maturities to the reservoir requires quantification. The same series of maturity parameters trace hydrocarbon migration pathways and relative maturity, while multiple series of maturity parameters provide a good characterization of the hydrocarbon charging and mixing histories.

6 Conclusion

The Es3 lacustrine source rocks in the study area are in the immature to mid-mature stage, while the Es4 source rocks are in the immature to late mature stage. Among them, the source rocks in the Es4 and Ek formations were deposited in an anoxic, stratified, brackish water environment. Based on the activation energy distribution of different organic matter types, it can be observed that the main peaks of the activation energy distribution of Es4 source rocks are lower than those of Es3 source rocks, revealing that Es4 source rocks generate oil earlier than Es3 source rocks. Whether in Es4 or Es3 members, source rocks with the kerogen type I have the greatest oil yield compared with other kerogens. The orderly spatial distribution of crude oil physical properties can reflect the results of hydrocarbon generation and expulsion of organofacies C, D/E and F at different maturity stages. Generally, the density and dynamic viscosity of oil decrease with increasing oil maturity.

Basically, all oil is a mixture of different compositions charged from a single uniform source rock or multiple source systems at different maturity stages. Because the concentrations of maturity-related biomarkers or non-biomarkers display several orders of magnitude variations across maturity stages, deeper concepts of oil maturity need to be elucidated. Maturity parameters based on biomarker ratios can produce a bias to overemphasize the contribution of low-maturity oils, revealing information about the oils captured early in the reservoir. In contrast, maturity parameters based on aromatic isomers are more sensitive to the mixing process reflecting the degree of mixing of oil captured in mid-to late-stage reservoirs. The oil charging and mixing histories of the study area from sag to slope are reconstructed based on

molecular maturity parameters. Peak oil is captured early in the reservoir in the sag, accompanied by late oil charging in the mid to late stages. Reservoirs in the slope area capture only peak to early oil in sequence and the oil maturity decreases from sag to slope. The same series of maturity parameters can trace the direction of hydrocarbon migration and relative maturity, while multiple series of maturity parameters can reconstruct the hydrocarbon charging and mixing histories.

Data availability statement

The original contributions presented in the study are included in the article/Supplementary Material, further inquiries can be directed to the corresponding author.

Author contributions

YL: conceptualization, methodology, writing—original draft, writing—review and editing. JZ: conceptualization, methodology, supervision, funding acquisition, resources. SL: guidance, editing. HL: supervision, editing.

Funding

This work was financially supported by the National Natural Science Foundation of China (Grant No. 41972147), the 2020 AAPG Foundation Grants-in-Aid Program (The Institut Français du Pétrole Grant) and the 2021 AAPG Foundation Grants-in-Aid Program (The Roger W. Stoneburner Memorial Grant).

Acknowledgments

We sincerely thank Prof. Steve Larter, Prof. Haiping Huang and Qianru Wang from the University of Calgary for their help in promoting the process of this study. Meanwhile, I would like to express my gratitude and miss to my grandmother who passed away during the COVID-19 epidemic.

Conflict of interest

The authors declare that the research was conducted in the absence of any commercial or financial relationships that could be construed as a potential conflict of interest.

Publisher's note

References

Al-Khafaji, A. J., Al-Najm, F. M., Al-Refaia, R. A., Sadooni, F. N., Al-Owaidi, M. R., and Al-Sultan, H. A. (2022). Source rock evaluation and petroleum generation of the Lower Cretaceous Yamama Formation: Its ability to contribute to generating and expelling petroleum to cretaceous reservoirs of the Mesopotamian Basin, Iraq. *J. Petroleum Sci. Eng.* 217, 110919. doi:10.1016/j.petrol.2022.110919

Baur, F. (2019). Predicting petroleum gravity with basin modeling: New kinetic models. *AAPG Bull.* 103, 1811–1837. doi:10.1306/12191818064

Beaumont, C., Boutilier, R., Mackenzie, A. S., and Rullkoetter, J. (1985). Isomerization and aromatization of hydrocarbons and the paleothermometry and burial history of Alberta Foreland Basin. *AAPG Bull.* 69, 546–566.

Behar, F., and Vandenbroucke, M. (1987). *Chemical modeling of kerogen*. United Kingdom: Org. Geochem.

Bennett, B., Larter, S. R., and Taylor, P. N. (2022). Geochemical rationalisation for the variable oil quality in the Orcutt reservoir, California, USA. *OG* 163, 104348. doi:10.1016/j.orggeochem.2021.104348

Chakhmakhchev, A., Suzuki, M., and Takayama, K. (1997). Distribution of alkylated dibenzothiophenes in petroleum as a tool for maturity assessments. *OG* 26, 483–489. doi:10.1016/s0146-6380(97)00022-3

Chakhmakhchev, A., and Suzuki, N. (1995). Saturate biomarkers and aromatic sulfur compounds in oils and condensates from different source rock lithologies of Kazakhstan, Japan and Russia. *OG* 23, 289–299. doi:10.1016/0146-6380(95)00018-a

Chandra, K., Mishra, C., Samanta, U., Gupta, A., and Mehrotra, K. (1994). Correlation of different maturity parameters in the Ahmedabad-Mehsana block of the Cambay basin. *OG* 21, 313–321. doi:10.1016/0146-6380(94)90193-7

Chang, J., Qiu, N., Zhao, X., Shen, F., Liu, N., and Xu, W. (2018). Mesozoic and Cenozoic tectono-thermal reconstruction of the Western Bohai Bay Basin (East China) with implications for hydrocarbon generation and migration. *J. Asian Earth Sci.* 160, 380–395. doi:10.1016/j.jseaes.2017.09.008

Chen, Z., Chai, Z., Cao, Y., Liu, Q., Zhang, S., and Yuan, G. (2019). Suppression of thermal maturity indicators in lacustrine source rocks: A case study of dongying depression, eastern China. *Mar. Petroleum Geol.* 109, 108–127. doi:10.1016/j.marpetgeo.2019.05.041

Connan, J., Bouroullec, J., Dessort, D., and Albrecht, P. (1986). The microbial input in carbonate-anhydrite facies of a sabkha palaeoenvironment from Guatemala: A molecular approach. *OG* 10, 29–50. doi:10.1016/0146-6380(86)90007-0

Cornford, C., Morrow, J., Turrington, A., Miles, J., and Brooks, J. (1983). Some geological controls on oil composition in the UK North Sea. *Geol. Soc. Lond. Spec. Publ.* 12, 175–194. doi:10.1144/gsl.sp.1983.012.01.16

Curiale, J. (2002). A review of the occurrences and causes of migration-contamination in crude oil. *OG* 33, 1389–1400. doi:10.1016/s0146-6380(02)00109-2

Dandekar, A. Y. (2006). *Petroleum reservoir rock and fluid properties*. Florida, United States: CRC Press.

Dembicki, H., Jr (2009). Three common source rock evaluation errors made by geologists during prospect or play appraisals. *AAPG Bull.* 93, 341–356. doi:10.1306/10230808076

Dembicki, H. (2022). *Practical petroleum geochemistry for exploration and production*. Amsterdam, Netherlands: Elsevier.

di Primio, R., and Horsfield, B. (2006). From petroleum-type organofacies to hydrocarbon phase prediction. *AAPG Bull.* 90, 1031–1058.

Dieckmann, V. (2005). Modelling petroleum formation from heterogeneous source rocks: The influence of frequency factors on activation energy distribution and geological prediction. *Mar. Petroleum Geol.* 22, 375–390. doi:10.1016/j.marpetgeo.2004.11.002

Dow, W. G. (1977). Kerogen studies and geological interpretations. *J. Geochem. Explor.* 7, 79–99. doi:10.1016/0375-6742(77)90078-4

Espitalié, J., Deroo, G., and Marquis, F. (1985). La pyrolyse Rock-Eval et ses applications. Deuxième partie. *Rev. l'Institut français Pétrole* 40, 755–784. doi:10.2516/ogst:1985045

Evans, C., Rogers, M., and Bailey, N. (1971). Evolution and alteration of petroleum in Western Canada. *Chem. Geol.* 8, 147–170. doi:10.1016/0009-2541(71)90002-7

Evenick, J. C. (2021). Examining the relationship between Tmax and vitrinite reflectance: An empirical comparison between thermal maturity indicators. *J. Nat. Gas Sci. Eng.* 91, 103946. doi:10.1016/j.jngse.2021.103946

Feng, W., Wang, F., Shi, Y., Jiang, T., Wang, Y., Zhou, H., et al. (2021). Oil properties variation among the China Erlian Rift Basin petroleum systems: Correlation with organofacies and maturity. *Mar. Petroleum Geol.* 127, 104960. doi:10.1016/j.marpetgeo.2021.104960

George, S. C., Lisk, M., Summons, R. E., and Quezada, R. A. (1998). Constraining the oil charge history of the South Pepper oilfield from the analysis of oil-bearing fluid inclusions. *OG* 29, 631–648. doi:10.1016/s0146-6380(98)00085-0

Grantham, P. (1986). Sterane isomerisation and moretane/hopane ratios in crude oils derived from Tertiary source rocks. *OG* 9, 293–304. doi:10.1016/0146-6380(86)90110-5

Guo, X., He, S., Liu, K., Song, G., Wang, X., and Shi, Z. (2010). Oil generation as the dominant overpressure mechanism in the cenozoic dongying depression, Bohai Bay Basin, China. *AAPG Bull.* 94, 1859–1881. doi:10.1306/05191009179

Guo, X., Liu, K., He, S., Song, G., Wang, Y., Hao, X., et al. (2012). Petroleum generation and charge history of the northern dongying depression, Bohai Bay Basin, China: Insight from integrated fluid inclusion analysis and basin modelling. *Mar. Petroleum Geol.* 32, 21–35. doi:10.1016/j.marpetgeo.2011.12.007

Guo, X., Liu, K., Jia, C., Song, Y., Zhao, M., and Lu, X. (2016). Effects of early petroleum charge and overpressure on reservoir porosity preservation in the giant Kela-2 gas field, Kuqa depression, Tarim Basin, northwest China. *AAPG Bull.* 100, 191–212. doi:10.1306/11181514223

Hakimi, M. H., Gharib, A. F., Abidin, N. S. Z., Ahmed, A., Nady, M. M. E., Yahya, M., et al. (2022). Biomarker and carbon isotope composition of the oil stains from the north hadramaut high area of eastern Yemen: Implications on the nature of organic matter input and their characteristics. *Arabian J. Sci. Eng.* 47, 709–723. doi:10.1007/s13369-021-05772-8

Hao, F., Zhou, X., Zhu, Y., Zou, H., Bao, X., and Kong, Q. (2009). Mechanisms of petroleum accumulation in the Bozhong sub-basin, Bohai Bay Basin, China. Part 1: Origin and occurrence of crude oils. *Mar. Petroleum Geol.* 26, 1528–1542. doi:10.1016/j.marpetgeo.2008.09.005

Holba, A., Dzou, L., Hickey, J., Franks, S., May, S., and Lenney, T. (1996). Reservoir geochemistry of south pass 61 field, gulf of Mexico: Compositional heterogeneities reflecting filling history and biodegradation. *OG* 24, 1179–1198. doi:10.1016/s0146-6380(96)00101-5

Huang, H., di Primio, R., Pedersen, J. H., Silva, R., Algeer, R., Ma, J., et al. (2022). On the determination of oil charge history and the practical application of molecular maturity markers. *Mar. Petroleum Geol.* 139, 105586. doi:10.1016/j.marpetgeo.2022.105586

Hughes, W. B. (1984). "Use of thiophenic organosulfur compounds in characterizing crude oils derived from carbonate versus siliciclastic sources," in *Petroleum Geochemistry and Source Rock Potential of Carbonate Rocks*. Editor J. G. Palacas (American Association of Petroleum Geologists), 181–196.

Hunt, J. M. (1991). Generation of gas and oil from coal and other terrestrial organic matter. *OG* 17, 673–680. doi:10.1016/0146-6380(91)90011-8

Jahn, F., Cook, M., and Graham, M. (2008). *Hydrocarbon exploration and production*. Amsterdam, Netherlands: Elsevier.

Jarvie, D., Claxton, B., Henk, F., and Breyer, J. (2001). "Oil and shale gas from the barnett shale, ft, worth basin, Texas (abs.)," in *AAPG annual meeting Program, 3 june 2001* (Denver, Colorado, USA.

Jones, R. (1984). *Comparison of carbonate and shale source rocks*.

Katz, B., Kelley, P., Royle, R., and Jorjorian, T. (1991). Hydrocarbon products of coals as revealed by pyrolysis-gas chromatography. *OG* 17, 711–722. doi:10.1016/0146-6380(91)90015-c

Katz, B., and Lin, F. (2014). Lacustrine basin unconventional resource plays: Key differences. *Mar. Petroleum Geol.* 56, 255–265. doi:10.1016/j.marpetgeo.2014.02.013

Killops, S., Stefanowicz, S., Frey, B., Øygard, K., and Beattie, T. (2022). Occurrence of mid jurassic, organic-rich, lacustrine deposits on the southern Utsira high. *Mar. Petroleum Geol.* 143, 105784. doi:10.1016/j.marpetgeo.2022.105784

Larter, S., Huang, H., Adams, J., Bennett, B., and Snowdon, L. R. (2012). A practical biodegradation scale for use in reservoir geochemical studies of biodegraded oils. *OG* 45, 66–76. doi:10.1016/j.orggeochem.2012.01.007

Lewan, M. (1983). Effects of thermal maturation on stable organic carbon isotopes as determined by hydrous pyrolysis of Woodford Shale. *Geochimica Cosmochimica Acta* 47, 1471–1479. doi:10.1016/0016-7037(83)90306-x

Lewan, M. (1987). *Petrographic study of primary petroleum migration in the Woodford Shale and related rock units*. Francis: Collection colloques et séminaires-Institut français du pétrole, 113–130.

Li, M., Chen, Z., Ma, X., Cao, T., Li, Z., and Jiang, Q. (2018). A numerical method for calculating total oil yield using a single routine rock-eval program: A case study of the eocene Shahejie formation in dongying depression, Bohai Bay Basin, China. *Int. J. Coal Geol.* 191, 49–65. doi:10.1016/j.coal.2018.03.004

Li, S., Pang, X., Li, M., and Jin, Z. (2003). Geochemistry of petroleum systems in the Niuzhuang south slope of Bohai Bay Basin—part 1: Source rock characterization. *OG* 34, 389–412. doi:10.1016/s0146-6380(02)00210-3

Li, Y., Jiang, Z., Liang, S., Zhu, J., Huang, Y., and Luan, T. (2016). Hydrocarbon generation in the lacustrine mudstones of the Wenchang formation in the baiyun sag of the Pearl River Mouth basin, northern south China Sea. *Energy & Fuels* 30, 626–637. doi:10.1021/acs.energyfuels.5b02034

Liu, Q., He, L., and Chen, L. (2018). Tectono-thermal modeling of Cenozoic multiple rift episodes in the Bohai Bay Basin, eastern China and its geodynamic implications. *Int. J. Earth Sci.* 107, 53–69. doi:10.1007/s00531-017-1550-1

Lohr, C. D., and Hackley, P. C. (2021). Relating Tmax and hydrogen index to vitrinite and solid bitumen reflectance in hydrous pyrolysis residues: Comparisons to natural thermal indices. *Int. J. Coal Geol.* 242, 103768. doi:10.1016/j.coal.2021.103768

Mackenzie, A., Hoffmann, C., and Maxwell, J. (1981). Molecular parameters of maturation in the toarcian shales, Paris Basin, France—iii. Changes in aromatic steroid hydrocarbons. *Geochimica Cosmochimica Acta* 45, 1345–1355. doi:10.1016/0016-7037(81)90227-1

Mackenzie, A. S., Disko, U., and Rullkötter, J. (1983). Determination of hydrocarbon distributions in oils and sediment extracts by gas chromatography—High resolution mass spectrometry. *OG* 5, 57–63. doi:10.1016/0146-6380(83)90003-7

Mello, M., Gaglianone, P., Brassell, S., and Maxwell, J. (1988). Geochemical and biological marker assessment of depositional environments using Brazilian offshore oils. *Mar. petroleum Geol.* 5, 205–223. doi:10.1016/0264-8172(88)90002-5

Moldowan, J. M., Seifert, W. K., and Gallegos, E. J. (1985). Relationship between petroleum composition and depositional environment of petroleum source rocks. *AAPG Bull.* 69, 1255–1268.

Niu, Z., Meng, W., Wang, Y., Wang, X., Li, Z., Wang, J., et al. (2022). Characteristics of trace elements in crude oil in the east section of the south slope of Dongying Sag and their application in crude oil classification. *J. Petroleum Sci. Eng.* 209, 109833. doi:10.1016/j.petrol.2021.109833

Orr, W. L. (1986). Kerogen/asphaltene/sulfur relationships in sulfur-rich Monterey oils. *OG* 10, 499–516. doi:10.1016/0146-6380(86)90049-5

Pang, X., Li, M., Li, S., and Jin, Z. (2005). Geochemistry of petroleum systems in the Niuzhuang south slope of Bohai Bay Basin: Part 3. Estimating hydrocarbon expulsion from the Shahejie formation. *OG* 36, 497–510. doi:10.1016/j.orggeochem.2004.12.001

Pepper, A. S., and Corvi, P. J. (1995). Simple kinetic models of petroleum formation. Part I: Oil and gas generation from kerogen. *Mar. petroleum Geol.* 12, 291–319. doi:10.1016/0264-8172(95)98381-e

Pepper, A. S. (1991). Estimating the petroleum expulsion behaviour of source rocks: A novel quantitative approach. *Geol. Soc. Lond. Spec. Publ.* 59, 9–31. doi:10.1144/gsl.sp.1991.059.01.02

Peters, K. E., and Cassa, M. R. (1994). "Applied source rock geochemistry," in *The Petroleum System: From Source to Trap*. Editors L. B. Magoon and W. G. Dow (Tulsa: American Association of Petroleum Geologists), 93–120.

Peters, K. E., and Fowler, M. G. (2002). Applications of petroleum geochemistry to exploration and reservoir management. *OG* 33, 5–36. doi:10.1016/s0146-6380(01)00125-5

Peters, K. E., Moldowan, J. M., McCaffrey, M. A., and Fago, F. J. (1996). Selective biodegradation of extended hopanes to 25-norhopanes in petroleum reservoirs. Insights from molecular mechanics. *OG* 24, 765–783. doi:10.1016/s0146-6380(96)00086-1

Petersen, H., Holme, A., Thomsen, E., Whitaker, M., Brekke, T., Bojesen-Koefoed, J., et al. (2011). Hydrocarbon potential of middle jurassic coaly and lacustrine and upper jurassic–lowermost cretaceous marine source rocks in the søgne basin, north Sea. *J. Petroleum Geol.* 34, 277–304. doi:10.1111/j.1747-5457.2011.00506.x

Petersen, H. I., Hertle, M., and Sulsbrück, H. (2017). Upper Jurassic–lowermost Cretaceous marine shale source rocks (Farsund Formation), North Sea: Kerogen composition and quality and the adverse effect of oil-based mud contamination on organic geochemical analyses. *Int. J. Coal Geol.* 173, 26–39. doi:10.1016/j.coal.2017.02.006

Radke, M. (1988). Application of aromatic compounds as maturity indicators in source rocks and crude oils. *Mar. petroleum Geol.* 5, 224–236. doi:10.1016/0264-8172(88)90003-7

Radke, M., Welte, D. H., and Willsch, H. (1982). Geochemical study on a well in the western Canada basin: Relation of the aromatic distribution pattern to maturity of organic matter. *Geochimica Cosmochimica Acta* 46, 1–10. doi:10.1016/0016-7037(82)90285-x

Radke, M., Welte, D., and Willsch, H. (1986). Maturity parameters based on aromatic hydrocarbons: Influence of the organic matter type. *OG* 10, 51–63. doi:10.1016/0146-6380(86)90008-2

Romero-Sarmiento, M.-F., Rohais, S., and Littke, R. (2019). Lacustrine type I kerogen characterization at different thermal maturity levels: Application to the late cretaceous yacoraite formation in the Salta Basin–Argentina. *Int. J. Coal Geol.* 203, 15–27. doi:10.1016/j.coal.2019.01.004

Ross, A. S., Farrimond, P., Erdmann, M., and Larter, S. R. (2010). Geochemical compositional gradients in a mixed oil reservoir indicative of ongoing biodegradation. *OG* 41, 307–320. doi:10.1016/j.orggeochem.2009.09.005

Seifert, W. K., and Moldowan, J. M. (1978). Applications of steranes, terpanes and monoaromatics to the maturation, migration and source of crude oils. *Geochimica cosmochimica acta* 42, 77–95. doi:10.1016/0016-7037(78)90219-3

Seifert, W. K., and Moldowan, J. M. (1981). Paleoreconstruction by biological markers. *Geochimica cosmochimica acta* 45, 783–794. doi:10.1016/0016-7037(81)90108-3

Shanmugam, G. (1985). Significance of coniferous rain forests and related organic matter in generating commercial quantities of oil, Gippsland Basin, Australia1. *AAPG Bull.* 69, 1241–1254.

Shi, C., Dong, C., Lin, C., Ren, L., Luan, G., and Li, Y. (2021). A semi-confined turbidite system in the eocene lacustrine: An example from Niuzhuang Sag, Bohai Bay Basin, Eastern China. *J. Petroleum Sci. Eng.* 206, 108924. doi:10.1016/j.petrol.2021.108924

Song, M., Liu, H., Wang, Y., and Liu, Y. (2020). Enrichment rules and exploration practices of Paleogene shale oil in jiyang depression, Bohai Bay Basin, China. *Petroleum Explor. Dev.* 47, 242–253. doi:10.1016/s1876-3804(20)60043-x

Srinivasan, P., Jacobi, D., Atwah, I., Karg, H., and Azzouni, A. (2022). Integration of methyldibenzothiophene and pyrolysis techniques to determine thermal maturity in sulfur-rich Type II-S source rocks and oils. *OG* 163, 104333. doi:10.1016/j.orggeochem.2021.104333

Stainforth, J. G. (2004). New insights into reservoir filling and mixing processes. *Geol. Soc. Lond. Spec. Publ.* 237, 115–132. doi:10.1144/gsl.sp.2004.237.01.08

Sun, J., Liang, T., Lin, X., Wang, Y., Zhang, Z., and Zou, Y. (2019). Oil generation and retention kinetics from the upper Es4 source rock in the Dongying Depression. *Geochimica* 48, 370–377.

Tao, Z., He, Z., Alves, T. M., Guo, X., Gao, J., He, S., et al. (2022). Structural inheritance and its control on overpressure preservation in mature sedimentary basins (Dongying depression, Bohai Bay Basin, China). *Mar. Petroleum Geol.* 137, 105504. doi:10.1016/j.marpetgeo.2021.105504

Ten Haven, H., De Leeuw, J., Rullkötter, J., and Damsté, J. S. (1987). Restricted utility of the pristane/phytane ratio as a palaeoenvironmental indicator. *Nature* 330, 641–643. doi:10.1038/330641a0

Tissot, B., Pelet, R., and Ungerer, P. (1987). Thermal history of sedimentary basins, maturation indices, and kinetics of oil and gas generation. *AAPG Bull.* 71, 1445–1466.

Wang, G., Wang, T.-G., Simoneit, B. R., Chen, Z., Zhang, L., and Xu, J. (2008). The distribution of molecular fossils derived from dinoflagellates in Paleogene lacustrine sediments (Bohai Bay Basin, China). *OG* 39, 1512–1521. doi:10.1016/j.orggeochem.2008.07.013

Wang, H., Wu, W., Chen, T., Yu, J., and Pan, J. (2019). Pore structure and fractal analysis of shale oil reservoirs: A case study of the Paleogene Shahejie formation in the dongying depression, Bohai Bay, China. *J. Petroleum Sci. Eng.* 177, 711–723. doi:10.1016/j.petrol.2019.02.081

Wang, Q., Huang, H., and Li, Z. (2021). Mixing scenario of a vagarious oil in the dongying depression, Bohai Bay Basin. *Fuel* 294, 120589. doi:10.1016/j.fuel.2021.120589

Wang, X., He, S., Wei, A., Liu, Q., and Liu, C. (2016). Typical disequilibrium compaction caused overpressure of Paleocene Dongying formation in northwest Liaodongwan depression, Bohai Bay Basin, China. *J. Petroleum Sci. Eng.* 147, 726–734. doi:10.1016/j.petrol.2016.09.014

Wang, Y., Hao, X., and Hu, Y. (2018). Orderly distribution and differential enrichment of hydrocarbon in oil-rich sags: A case study of dongying sag, jiyang depression, Bohai Bay Basin, east China. *Petroleum Explor. Dev.* 45, 840–850. doi:10.1016/s1876-3804(18)30087-9

Wilhelms, A., and Larter, S. (2004). Shaken but not always stirred. Impact of petroleum charge mixing on reservoir geochemistry. *Geol. Soc. Lond. Spec. Publ.* 237, 27–35. doi:10.1144/gsl.sp.2004.237.01.03

Wilhelms, A., Teln, N., Steen, A., and Augustson, J. (1998). A quantitative study of aromatic hydrocarbons in a natural maturity shale sequence—The 3-methylphenanthrene/retene ratio, a pragmatic maturity parameter. *OG* 29, 97–105. doi:10.1016/s0146-6380(98)00112-0

Wust, R. A., Nassichuk, B. R., Brezovski, R., Hackley, P. C., and Willment, N. (2013). *Vitrinite Reflectance Versus Pyrolysis Tmax Data: Assessing Thermal Maturity in Shale Plays with Special Reference to the Duvernay Shale Play of the Western Canadian Sedimentary Basin, Alberta, Canada, SPE Unconventional Resources Conference and Exhibition-Asia Pacific*. Brisbane, Australia: Society of Petroleum Engineers.

Xie, X., Fan, Z., Liu, X., and Lu, Y. (2006). Geochemistry of formation water and its implication on overpressured fluid flow in the Dongying Depression of the Bohaiwan Basin, China. *J. Geochem. Explor.* 89, 432–435. doi:10.1016/j.gexplo.2005.11.026

You, B., Ni, Z., Zeng, J., Luo, Q., Xiao, H., Song, G., et al. (2020). Oil-charging history constrained by biomarkers of petroleum inclusions in the Dongying Depression, China. *Mar. Petroleum Geol.* 122, 104657. doi:10.1016/j.marpetgeo.2020.104657

Zahid, M. A., Chunmei, D., Lin, C., Gluyas, J., Jones, S., Zhang, X., et al. (2016). Sequence stratigraphy, sedimentary facies and reservoir quality of Es4s, southern slope of Dongying Depression, Bohai Bay Basin, East China. *Mar. Petroleum Geol.* 77, 448–470. doi:10.1016/j.marpetgeo.2016.06.026

Zhan, Z.-W., Lin, X.-H., Zou, Y.-R., Li, Z., Wang, D., Liu, C., et al. (2019). Chemometric differentiation of crude oil families in the southern dongying depression, Bohai Bay Basin, China. *OG* 127, 37–49. doi:10.1016/j.orggeochem.2018.11.004

Zhang, H., Huang, H., Li, Z., and Liu, M. (2020). Impact of maturation on the validity of paleoenvironmental indicators: Implication for discrimination of oil genetic types in lacustrine shale systems. *Energy & Fuels* 34, 6962–6973. doi:10.1021/acs.energyfuels.0c00868

Zhang, L., Liu, Q., Zhu, R., Li, Z., and Lu, X. (2009). Source rocks in mesozoic–cenozoic continental rift basins, east China: A case from dongying depression, Bohai Bay Basin. *OG* 40, 229–242. doi:10.1016/j.orggeochem.2008.10.013

Zhang, P., Lu, S., and Li, J. (2019). Characterization of pore size distributions of shale oil reservoirs: A case study from dongying sag, Bohai Bay Basin, China. *Mar. Petroleum Geol.* 100, 297–308. doi:10.1016/j.marpetgeo.2018.11.024

Zhang, S., Huang, H., Su, J., Zhu, G., Wang, X., and Larter, S. (2014). Geochemistry of paleozoic marine oils from the tarim basin, NW China. Part 4: Paleobiodegradation and oil charge mixing. *OG* 67, 41–57. doi:10.1016/j.orggeochem.2013.12.008

Zhou, Y., and Littke, R. (1999). Numerical simulation of the thermal maturation, oil generation and migration in the Songliao Basin, Northeastern China. *Mar. Petroleum Geol.* 16, 771–792. doi:10.1016/s0264-8172(99)00043-4

Zumberge, J. E. (1984). "Source rocks of the La luna formation (upper cretaceous) in the middle magdalena valley, Colombia," in *Petroleum geochemistry and source rock potential of carbonate rocks*. Editor J. G. Palacas (Tulsa, OK: AAPG), 127–133.

frontiers | Frontiers in Earth Science

TYPE Original Research
PUBLISHED 10 May 2023
DOI 10.3389/feart.2023.1206835

OPEN ACCESS

EDITED BY
George Kontakiotis,
National and Kapodistrian University of Athens, Greece

REVIEWED BY
Ruoyuan Qiu,
institute of geology and geophysics, China
Yang Li,
Shandong University of Science and Technology, China

*CORRESPONDENCE
Rui Zhang,
ruizhangxu@pku.edu.cn

RECEIVED 16 April 2023
ACCEPTED 02 May 2023
PUBLISHED 10 May 2023

CITATION
Liu G, Zhang R, He X, Wei R, Zhu R, Tang Y, He W, Zheng M, Chang Q, Wang R and Zhao X (2023), Cyclostratigraphy and high-frequency sedimentary cycle framework for the Late Paleozoic Fengcheng Formation, Junggar Basin. *Front. Earth Sci.* 11:1206835. doi: 10.3389/feart.2023.1206835

Cyclostratigraphy and high-frequency sedimentary cycle framework for the Late Paleozoic Fengcheng Formation, Junggar Basin

Guoyong Liu[1], Rui Zhang[2,3]*, Xiangwu He[2,3], Ren Wei[2,3], Rukai Zhu[2,4], Yong Tang[1], Wenjun He[1], Menglin Zheng[1], Qiusheng Chang[1], Ran Wang[1] and Xinmei Zhao[1]

[1]PetroChina Xinjiang Oilfield Company, Karamay, China, [2]Institute of Energy, Peking University, Beijing, China, [3]State Key Laboratory of Shale Oil and Gas Enrichment Mechanisms and Effective Development, Sinopec, Beijing, China, [4]PetroChina Research Institute of Petroleum Exploration and Development, Beijing, China

The Late Paleozoic Fengcheng Formation within the Mahu Sag of the Junggar Basin (China) harbors the world's oldest alkaline lake hydrocarbon source rocks. Spectral analysis of the natural gamma-ray (GR) series obtained from four boreholes traversing the Fengcheng Formation, with wavelength ranges of 28.4 m–50 m, 5.9 m–12.6 m, 2.3 m–3.9 m, and 1.2 m–2.7 m. These were controlled by Early Permian astronomical cycles, including 405 kyr long eccentricity, 100 kyr short eccentricity, 34.2 kyr obliquity, and 20.7–17.4 kyr precession. The most significant cycle was notably that of the 405 kyr long eccentricity, which was instrumental for dividing and correlating the high-frequency sedimentary sequences in lacustrine shales. Nine intermediate-term and 36 short-term base-level cycles were identified in the P_1f_1 and P_1f_2 members of the Fengcheng Formation. These cycle types are equal to the 405 kyr long eccentricity cycle and ~100 kyr short eccentricity cycle, respectively. The paleolake-level variations in the Fengcheng Formation were reconstructed using sedimentary noise modeling, revealing that lake levels reached their highest value during the deposition of the P_1f_2 Member. The spatial distribution patterns of lithofacies in the Fengcheng Formation can be clearly demonstrated within the isochronous cycle framework under the constraints of long eccentricity cycles. The use of astronomical cycles in isochronous stratigraphic correlation offers great potential for characterizing alkaline lacustrine sequences and predicting favorable areas for shale oil exploration with higher accuracy.

KEYWORDS

Milankovitch cycles, Mahu Sag, alkaline lacustrine, lake-level variations, isochronous stratigraphic correlation, cyclostratigraphy

1 Introduction

The sedimentary geological record preserves patterns of repetitive sedimentary cycles (Weedon, 2003; Kodama and Hinnov, 2014). According to cyclostratigraphy theory, rhythmic features in the sedimentary record worldwide are indicative of past climate signatures related to variations in the total solar insolation encountered on the surface

of the Earth owing to quasiperiodic parameter variabilities in the planet's orbit (Boulila et al., 2011; Hinnov and Hilgen, 2012; Eldrett et al., 2015). Previous studies have derived a link between cyclostratigraphy and an astronomical time scale (ATS) by modeling the stratigraphic records of such cycles with astronomical solutions (Laskar et al., 2004; Waltham, 2015). For example, successful orbital tuning in eastern North America's Newark rift basin has revealed a wide range of lake-level changes related to precession periods (Olsen and Kent, 1996; Kent et al., 2017). Liu et al. (2022) established a floating timeline that was calibrated to the long eccentricity cycles (405 kyr) and redefined the high-resolution marine sequence framework of the organic-rich Qiongzhusi shale of Early Cambrian age in the Sichuan Basin.

The development of terrestrial basin sedimentary sequences is controlled by climate cycling driven by the Earth's orbital cycles (Du et al., 2020; Huang et al., 2021; Wu et al., 2022). The continuity and stability of fine-grained lacustrine deposits around the world have been clearly demonstrated to be linked to the Milankovitch cycle (Olsen and Kent, 1996; Meyers, 2019; Fang et al., 2023). The division of high-frequency shale-series cycles helps to clarify the spatiotemporal characteristics of organic-rich shale distributions, thereby providing a foundation for the development of shale oil and gas exploration. However, deep shale deposits show a uniform structure, which makes it difficult to identify key sequence interfaces. Identifying the Milankovitch cycle within the strata has allowed sedimentary cycles to be divided with time connotations and isochronous correlations with regional and even global stratigraphic sequences (Zhang et al., 2019; Wei et al., 2023). The sedimentary rhythm of calcium sulfate in the Permian Castile and Bell Canyon Formations of the Delaware Basin records an average period of ~20 kyr precession (Anderson, 1982). The evaporite-rich stratigraphic sequence of the Qianjiang Formation in the Jianghan Basin also records lake cycles alternating between saline water and fresh water in pace with orbital eccentricity cycles on an ~100-kyr timescale (Huang and Hinnov, 2019).

The Fengcheng Formation is a Lower Permian stratigraphic sequence within the Mahu Sag in the Junggar Basin that contains the oldest alkaline lake hydrocarbon source rocks on Earth (Zhang et al., 2018; Huang et al., 2021; Tang et al., 2022). Although previous studies have reported climatically forced evaporite-containing sediments (Cao et al., 2020), the detailed relationships between alkaline lacustrine development and orbital forcing remain to be determined. This can mainly be explained by the low resolution of the age framework and absence of a higher-resolution and reliable paleoclimate model for the Fengcheng Formation, thereby making it challenging to constrain the essential mechanisms that power the hydrological processes responsible for evaporite formation in this region. To address this question, we conducted cyclostratigraphic analyses of lacustrine deposits in the Early Permian Fengcheng Formation using logs of gamma-ray (GR) spectra from four boreholes. The primary purposes of this work are as follows: 1) to determine the prominent depositional cycles and to construct a floating ATS for the Fengcheng Formation; 2) to reconstruct the Early Permian lake-level changes during the Fengcheng Formation's deposition; and 3) to categorize a high-frequency sedimentary cycle framework for the Fengcheng Formation using the periodic filtering curves of orbital parameters. This study therefore provides a typical case study for delineating high-frequency sequences in terrestrial black shales and serves as a valuable reference for predicting the distribution of shale oil deposits in alkaline–lacustrine basins.

2 Geological setting

Located in northwestern China (~45°N, 85°E), the Junggar Basin is a huge inland lake basin that is tectonically constricted by the Hala'alate and Zhayier Mountains to the northwest, the Kelamaili Mountains to the northeast, and the Bogda Mountains to the south (Figures 1A, B). Within the Junggar Basin, an approximately 1.5-km-thick stratigraphic sequence adequately documents important long-term features of the tectonic evolution of Central Asia, in addition to the evolution of paleoclimate and paleoenvironmental conditions of the continental region at middle to high latitudes in the Northern Hemisphere from the Paleozoic to the Cenozoic (Huang et al., 2021; Tang et al., 2022). With its location in the northwestern part of the Junggar Basin, the Mahu Sag is a major oil-bearing depression of approximately 5,000 km^2 in area (Yu et al., 2018b). The Zhongguai uplift and Wu-Xia and Ke-Bai fault zones (from south to north) occur in the Mahu Sag's western region, while the Dabasong, Xiayan, and Sangequan uplifts, Yingxi Sag, and Shiyingtan uplift (from south to north) occur in the eastern part (Figure 1C). However, the depositional processes and stratigraphic correlations within the depression remain difficult to understand due to complex tectonic deformation (Yu et al., 2018a).

The Fengcheng Formation mostly contains a mixture of fine-grained deposits from multiple sources in a moderately deep to deep alkaline lake setting and includes endogenous chemical deposits derived from a hot arid climate, rapid accumulation of fan deltaic clastic debris from the proximal end, and volcanic material sourced from peripheral volcanism during the evolution of the foreland basin, which was distributed throughout the generally margin area of the sag (Kuang et al., 2012; Zhi et al., 2021). In terms of classification, the Fengcheng Formation has been divided from bottom to top into P_1f_1, P_1f_2, and P_1f_3 members (Cao et al., 2020; Huang et al., 2021; Song et al., 2022). Recent exploration has shown that the depositional mixture of endogenous carbonates, volcanic material, and terrigenous clasts in the Fengcheng Formation produced a variety of lithotypes, such as salt rock, dolomite, mudstone, conglomerate, sandstone, tuff, and various transitional lithologies (Zhang et al., 2018). The lower member (P_1f_1) mainly consists of ignimbrite, coarse clastic rocks, mafic-intermediate volcanic rocks, and tuffs. The second member (P_1f_2) contains rhythmic evaporites, bedded dolomite, and lower volcanic with thicknesses ranging from 217 to 650 m. Moreover, alkaline minerals (e.g., searlesite, reedmergnerite, eitelite, wegscheiderite) are commonly distributed in this stratigraphic unit. The third member (P_1f_3) is dominantly characterized by mudstones containing terrigenous clastics in the upper section and dolomitic mudstones in the lower section (Cao et al., 2020; Wang et al., 2021).

Wells MY-1, XY-1, X-203, and M-49 are situated in the Wu-Xia fault zone in the Junggar Basin's western uplift. These are standard wells for exploring alkaline lacustrine shale oil in the Mahu Sag. Among them, the MY-1 borehole obtained complete geological archives regarding the Fengcheng Formation's sedimentary evolution by continuously coring more than 300 m. The P_1f_1

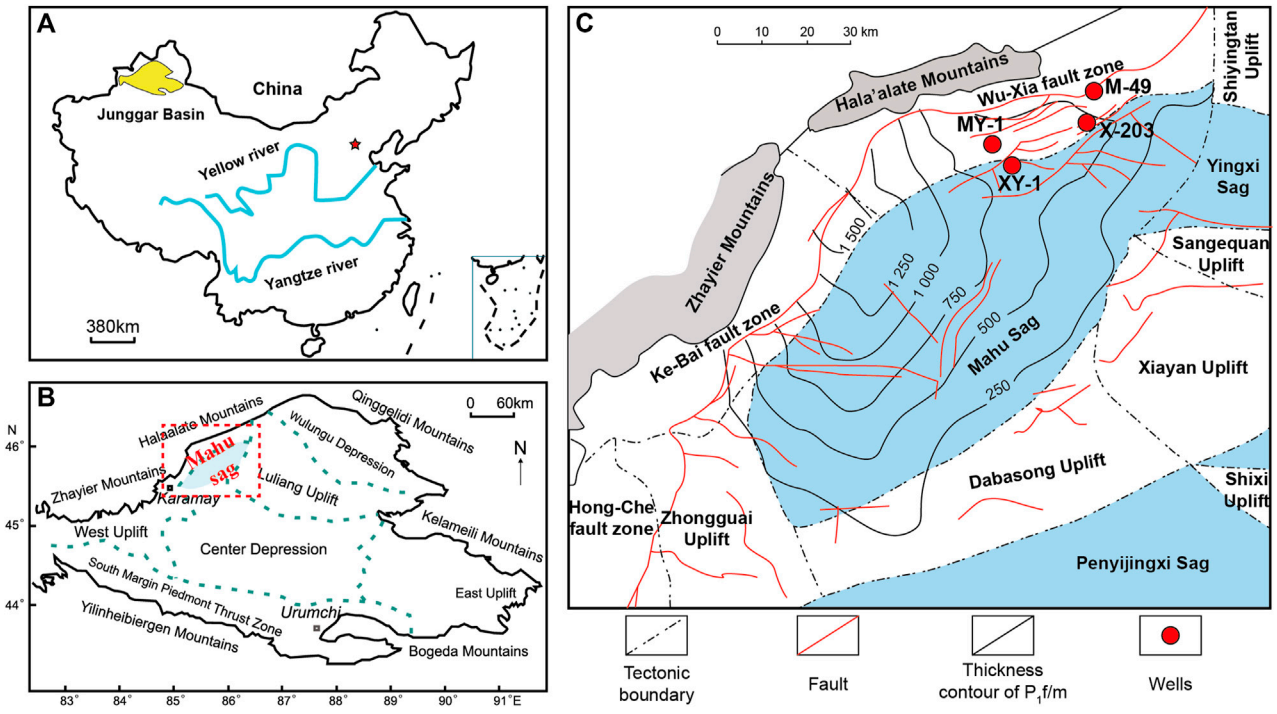

FIGURE 1
Geological setting of the Mahu Sag in the Junggar Basin (Huang et al., 2021; Wang et al., 2022). **(A)** Location of the Junggar Basin in China. **(B)** Mahu Sag and other tectonic units of the Junggar Basin. **(C)** Tectonic characteristics of the Mahu Sag and drill holes selected in this study.

Member in the MY-1 borehole comprises fine tuffaceous sandstone and gray dolomitic mudstone. The lower portion of the P_1f_1 Member is made up of pyroclastic sediment containing volcanic lithology, while the upper portion contains dolomitic rocks and organic-rich mudstone. The P_1f_2 Member contains dark gray mudstone intercalated with dolomitic mudstone, which was deposited in an evaporitic environment that contained a limited amount of clastic grains. The P_1f_3 Member comprises silty mudstone, dolomitic mudstone, and grayish-black lime mudstone. The lithological features of the other three boreholes are comparable to those of the MY-1 borehole, except for the large sets of alkaline mineral-enriched sections and dolomitic rocks in the P_1f_1 Member of the XY-1 and X-203 wells (Figure 2). Gypsum salt rocks pose a significant challenge to cyclostratigraphic analysis; volcanic rocks and tuff layers were excluded from the time series studies because they represent instantaneous events (e.g., Eldrett et al., 2015). The P_1f_1 and P_1f_2 members of the Fengcheng Formation are therefore the primary targets of our isochronous cycle framework.

3 Materials and methods

3.1 GR series

GR series are extensively used for time-series analysis owing to their high data acquisition efficiency and relatively clear lithologic variability characteristics (Li et al., 2019b; Zhang et al., 2019). Spectra from the four wells were used in this study for cyclostratigraphic analysis. The GR series reflects concentrations of uranium, thorium, and potassium (K). Lower GR values are generally associated with sandstone or carbonate-rich sediments, while higher values are typically linked with clay-rich sediments (Wang et al., 2020; Huang et al., 2021; Wei et al., 2023). Organic and clay mineral-rich sediments deposited in lake basins are known to be highly sensitive to paleoclimate and paleoenvironmental variations; GR series proxy can therefore be used as a raw signal associated with paleoclimate changes. Another feature of the GR series proxy is its higher signal-to-noise ratios than other similar proxies, which makes it a widely used tool in cyclostratigraphic studies (Wu et al., 2013; Li et al., 2019b; Huang et al., 2020; Wang et al., 2020). Overall, wet and warm depositional intervals are generally related to increased input of muddy components, which produces higher GR values, while dry and warm depositional intervals are generally linked with reduced inputs, thereby producing lower GR values. The periodic oscillations in the GR dataset are therefore a favorable proxy for the astronomical causes of climate variations in lacustrine basins (van Vugt et al., 2001; Huang and Hinnov, 2019).

3.2 Time series analysis methods

A quantitative approach to cyclostratigraphy is required to distinguish astronomical signals from spectra. This work applied a multitaper method (MTM) (Thomson, 1982; Mann and Lees, 1996) using *Acycle* v2.0 software (Li et al., 2019a). Before the analysis, the GR series were rescaled at 12.5-cm intervals to acquire unified data using linear interpolation. The removal of long-term trends from the

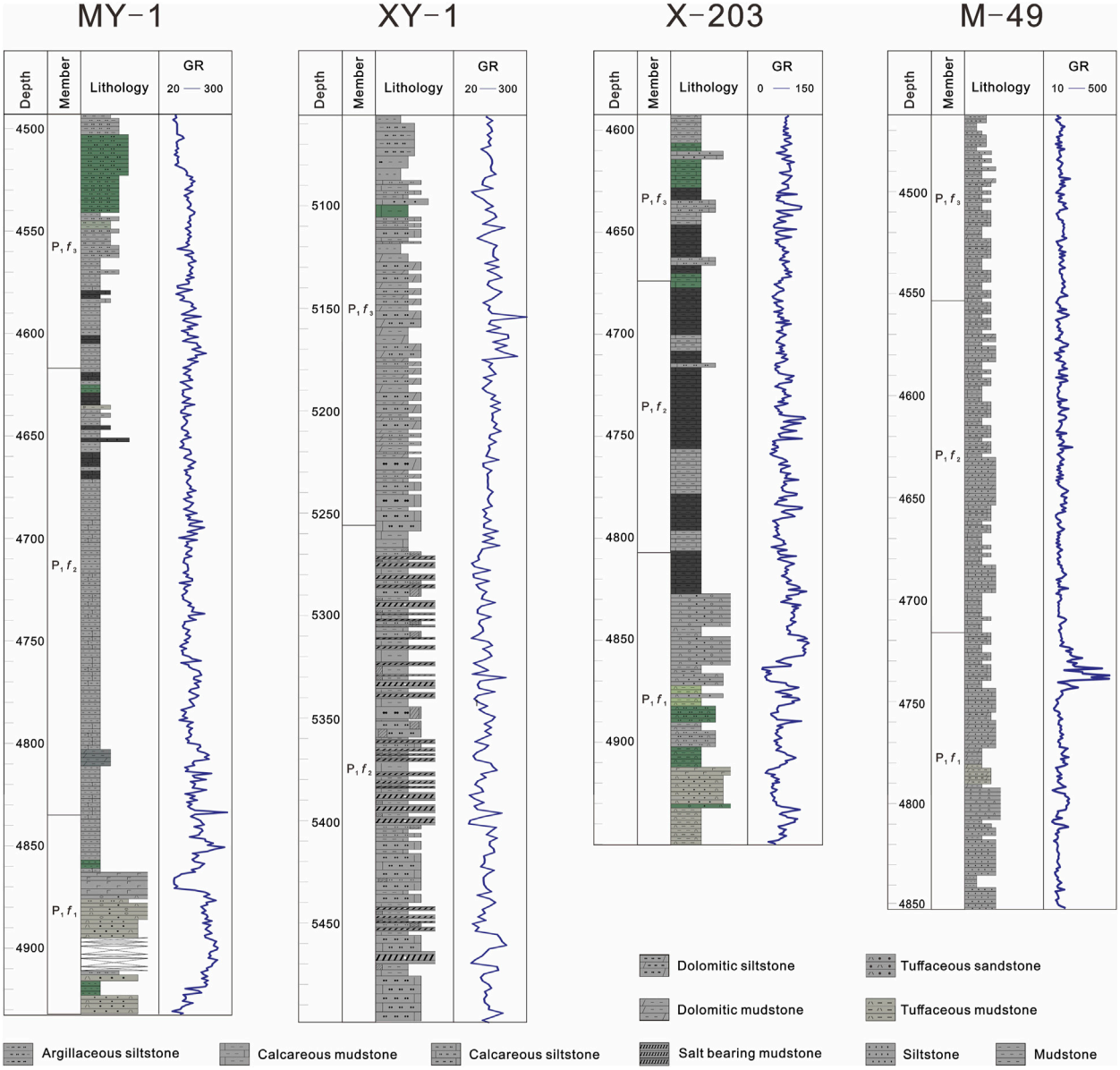

FIGURE 2
Lithological log and GR profile of well sections along the provenance direction, including wells MY-1, XY-1, X-203, and M-49.

original GR series was required to minimize distortion of the spectra's low-frequency section using the "rLOWESS" method (smoother = 20%–35%) (Cleveland, 1979). Logarithmic transformation is a common data preprocessing technique to reduce the range of data and reduce the effect of outliers when the range of values of the GR series is too large. The MTM assesses spectra obtained from detrended GR series using three 2π tapers. Gaussian bandpass filters are used to obtain interpreted signals from the GR series involving Milankovitch components (Li et al., 2019a). The significance of the rejected null AR1 models in all of the spectral analyses was calculated at confidence levels of 90%, 95%, and 99%. An evolving fast Fourier transform (FFT) spectrogram was used to investigate the frequency variations (Kodama and Hinnov, 2014).

The correlation coefficient (COCO) method can be applied to estimate the correlation coefficient between an astronomical solution and a GR series' power spectrum in the depth domain, thereby transforming the raw GR spectra from the depth measurements into a serial test of sedimentation rate in the time domain. The most plausible sedimentation rate is assumed to correspond to the maximum correlation coefficient. The evolutionary correlation coefficient method (eCOCO) has been adapted to trace variable sedimentation rates using both the COCO and running window methods (Li et al., 2018b; Wang et al., 2020; Wei et al., 2023). All of the analysis steps were performed using *Acycle* v2.0 software (Li et al., 2019a).

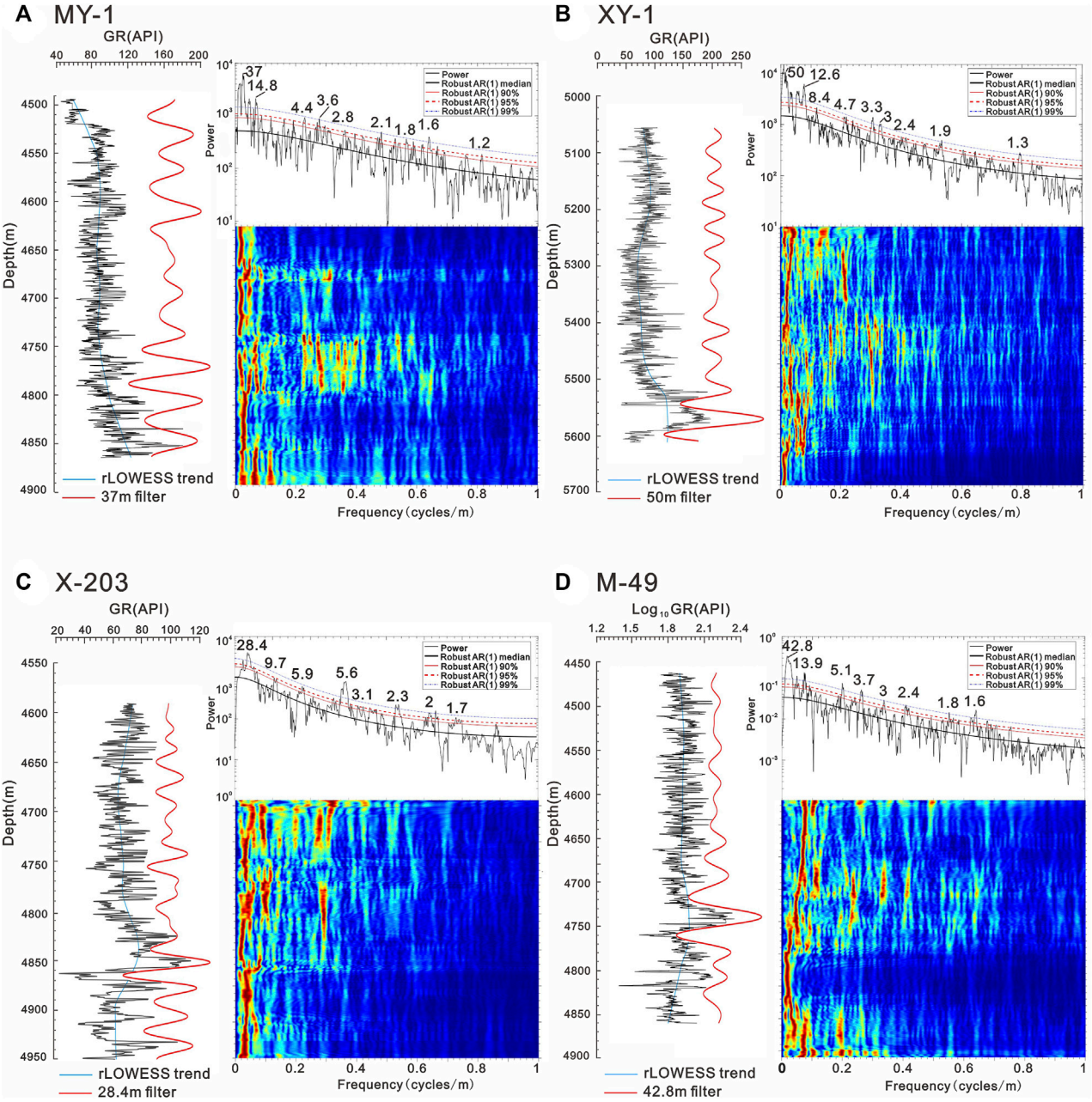

FIGURE 3
Cyclostratigraphic interpretation from wells MY-1, XY-1, X-203, and M-49 in the depth (m) domain of the Fengcheng Formation. Black curves are original GR series with 20%–35% weighted average rLOWESS trend (blue curve). The sedimentary cycles that are interpreted to be forced by the 405-kyr orbital eccentricity cycles are shown in red. **(A)** The evolutionary FFT spectrograms and 2π MTM power spectra of the untuned GR series show filter outputs at 37 m (0.027 ± 0.01 cycles/m) for well MY-1. **(B)** The evolutionary FFT spectrograms and 2π MTM power spectra of the untuned GR series show filter outputs at 50 m (0.020 ± 0.01 cycles/m) for well XY-1. **(C)** The evolutionary FFT spectrograms and 2π MTM power spectra of the untuned GR series show filter outputs at 28.4 m (0.035 ± 0.01 cycles/m) for well X-203. **(D)** The evolutionary FFT spectrograms and 2π MTM power spectra of the untuned GR series show filter outputs at 42.8 m (0.023 ± 0.01 cycles/m) for well M-49.

3.3 Lag-1 autocorrelation coefficient (ρ_1) model

Li et al. (2018a) proposed a sedimentary noise modeling method that provides a new approach to studying the variations in ancient sea-levels. Paleoclimate changes tend to incorporate prior values over a certain time frame, which is referred to as persistence or autocorrelation. The most commonly used persistence model is developed based on the lag-1 autocorrelation coefficient (ρ_1) (Mudelsee, 2002; Meyers and Hinnov, 2010; Li et al., 2018a), which is given as (Mudelsee, 2002):

$$\rho_1 = \frac{\sum_{i=2}^{n} x_{(i)}{}^{*} x_{(i-1)}}{\sum_{i=2}^{n} x_{(i-1)}^2} \quad (1)$$

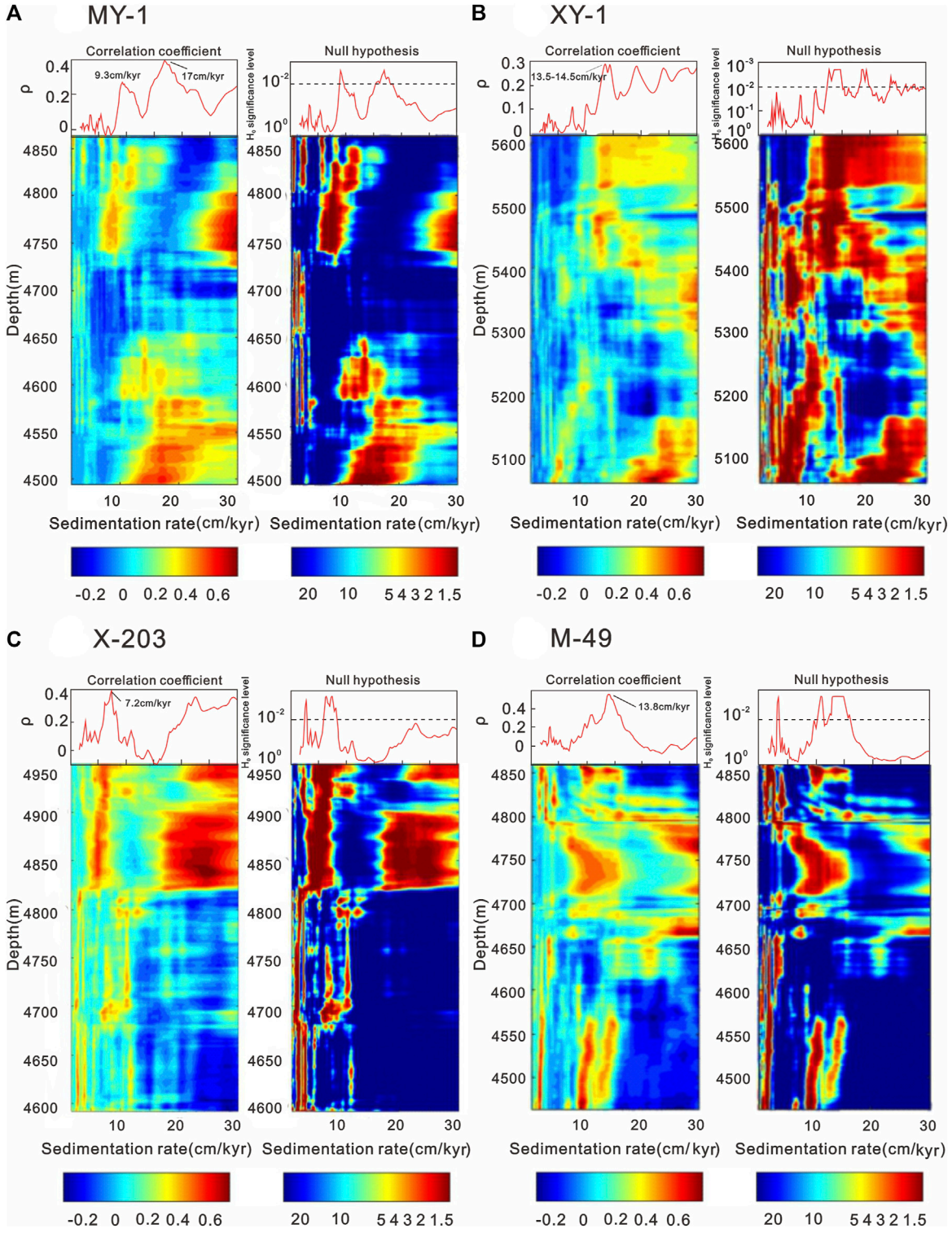

FIGURE 4
The COCO and eCOCO sedimentation rate map of the GR series of the Fengcheng Formation from wells MY-1 **(A)**, XY-1 **(B)**, X-203 **(C)**, and M-49 **(D)**. For the eCOCO analysis, the number of Monte Carlo simulations is 2,000; the sliding window is 70 m with a sliding window step of 1 m. Sedimentation rates tested ranged from 1 to 30 cm/kyr with a step of 0.2 cm/kyr.

where x refers to the orbitally tuned stratigraphic proxy series. The ρ_1 model is advantageous because it is not affected by band selection and can be used to directly evaluate the time series. The ρ_1 approach has been applied as a noise-independent indicator of changes in relative sea or lake level. Lower noise is associated with higher ρ_1 values, while higher

noise leads to a reduction in ρ_1 (Li et al., 2018a; Wang et al., 2020).

4 Results

4.1 Cycles in the stratigraphic domain

The MTM analyses of untuned GR series in well MY-1 reveal remarkably robust peaks at 37, 16.5, 8.5, 4.4, 3.6, 2.8, 2.1, and 1.2–1.32 m with confidence levels of astronomical forcing exceeding 95%. The 50, 12.6, 8.4, 4.7, 3.3–3, 2.4, and 1.9 m wavelengths were all above 95% confidence in the XY-1 borehole; the 28.4, 9.7, 5.9–5.6, 2.3–1.9, and 1.4 m wavelengths were above 95% confidence in the X-203 borehole; and the 42.8, 13.9, 11, 5.1, 3.7, 3, 2.4, and 1.8–1.6 m wavelengths also indicate high confidence levels in the M-49 borehole (Figure 3).

The COCO algorithm, which is designed for verifying optimal sedimentation rates, was conducted for 2,000 Monte Carlo simulations to ensure the accuracy of the results. Synthesis of the eCOCO analysis technique, which calculates the estimations of sedimentations with ranges consistent with those derived from the COCO method, allows the favorable geological constraint for local sedimentation rates to be determined. Using null hypothesis significance levels < 0.01, the most prominent peaks occurring at 9.3 and 17 cm/kyr represent the most likely sedimentation rates in MY-1 well (Figure 4A). Previous cyclostratigraphic analyses using density logging data indicated that the average deposition rate of the P_1f_1 and P_1f_2 members of the Fengcheng Formation was approximately 9 cm/kyr (e.g., Tang et al., 2022). We therefore preferred the 9.3 cm/kyr peak as the optimal rate of sedimentation. In this case, the 37-m wavelength in well MY-1 tended toward the long eccentricity cycle. Similarly, the COCO and eCOCO results indicate optimal rates of sedimentation in wells XY-1, X-203, and M-49 of 13.5–14.5, 7.2, and 13.8 cm/kyr, respectively (Figures 4B–D). The peaks at 50 m in well XY-1, 28.4 m in well X-203, and 42.8 m in well M-49 therefore all indicate long eccentricity cycles (405 kyr). The sedimentation rate variations in the depth domain are illustrated by the evolutionary FFT spectrograms, which show stabilized ~40–50-m-long eccentricity cycles throughout the entire succession (Figure 3). Long eccentricity cycles within the GR series were separated using Gaussian bandpass filtering (Kodama and Hinnov, 2014).

Stratigraphic correlation of the Mahu Sag reveals that the deposition of the Fengcheng Formation occurred at approximately 300 Ma, developing mainly in the Asselian stage of the Early Permian (Cao et al., 2020; Huang et al., 2021; Tang et al., 2022). In addition to stable long eccentricity, the precession and obliquity cycles also exhibited shorter periods (Berger et al., 1992; Laskar et al., 2004; Waltham, 2015). Following Berger et al. (1992), the obliquity period during the Fengcheng Formation's sedimentary stage is 34.2 kyr, and the precession periods are 20.7 and 17.4 kyr, all of which contain values obtained from the "Milankovitch calculator" of Waltham (2015) and associated errors (35.5 ± 2.9 kyr for obliquity and 21.7 ± 1.1 kyr to 17.66 ± 0.76 kyr for the precession components). This study selected orbital parameter periods of 405, 100, and 34.2 kyr for long (E) and short eccentricities (e) and obliquity (O), respectively, and 20.7 and 17.4 kyr for precession (P). These interpreted orbital cycle wavelengths of 28.4–50, 5.9–12.6, 2.3–3.9, and 1.2–2.7 m are listed in Table 1. The ratio relationship between these wavelengths is very consistent with the theoretical astronomical period ratio in the Early Permian (Berger et al., 1992; Waltham, 2015).

4.2 Cycles in the time domain

We tuned the assumed stratigraphic cycles to astronomical frequencies in the time domain to eliminate the effect of sedimentation rate variations. The preferred method for tuning (depth to time) individual stratigraphic spectral peaks to a defined target astronomical frequency is minimal tuning, thereby aligning certain stratigraphic spectral peaks to other astronomical frequencies. The long eccentricity cycle is theoretically influenced by the orbital perihelia of Jupiter and Venus. Jupiter's large mass ensures that this cycle is robustly modeled over several hundreds of Myr (Berger et al., 1992; Laskar et al., 2004; Hinnov, 2013). The long eccentricity cycle therefore serves essentially as a "metronome" in astrochronology and has accordingly been applied for calibrating the geological time scale (e.g., Hinnov and Hilgen, 2012; Wang et al., 2020; Liu et al., 2022; Wei et al., 2023). Tuning the approximately 40–50 m cycles of the time series to the long eccentricity cycle enables the number of eccentricity cycles to be recognized. Following the theoretically optimal rates of sedimentation mapped in the COCO/eCOCO spectrograms (Figure 4), we applied a Gaussian bandpass filter to extract the ~37-m cycle band from the MY-1 series, the ~50-m cycle band from the XY-1 series, the ~28.4-m from the X-203 series, and the ~42.8-m from the M-49 series, each with a bandwidth of 40%.

Figure 5 shows significant peaks (> 90%–99% confidence) in the MTM power spectra of the 405-kyr-tuned GR series from the four boreholes, which agrees well with the theoretically predicted periodicities of E, e, O, and P during the Early Permian (Berger et al., 1992; Waltham, 2015). The floating ATS for wells MY-1, XY-1, X-203, and M-49 were accordingly established as ~3.8, ~4.48, ~5.18, and ~4.7 Myr, respectively. The high-resolution ATS is an important guideline for dividing the high-frequency sedimentary framework and correlating the four wells. As mentioned, the Fengcheng Formation's P_1f_1 and P_1f_2 members are the primary focus of our cyclostratigraphic analyses. Stratigraphic correlations based on the long eccentricity cycle show that the P_1f_2 and P_1f_3 member durations are ~2.4 and ~1.2 Myr (Figure 6). We have therefore established a convincing framework of the four single wells, as well as a contemporaneous stratigraphic correlation scheme for the section along the provenance direction in the context of astronomical chronology. However, the possibility of establishing an absolute time scale for the P_1f_1 and P_1f_2 members is limited, partly owing to the deficiency of an absolute age anchor for the floating ATS.

TABLE 1 Power peaks of the GR series from the Fengcheng Formation.

Borehole	Thickness (m)	Interpreted orbital cycle (m)					Ratio
		E	e	O	P1	P2	E: e: O: P1: P2
MY-1	439.9	37	8.5	2.8	1.32	1.2	30.8:7.08:2.3:1.1:1
XY-1	555	50	12.6	3.9	2.72	2.4	20.8:5.3:1.6:1.13:1
X-203	358	28.4	5.9	2.3	1.7	1.4	20.3:4.2:1.6:1.2:1
M-49	397.76	42.8	11	3.7	1.8	1.6	26:6.9:2.3:1.1:1

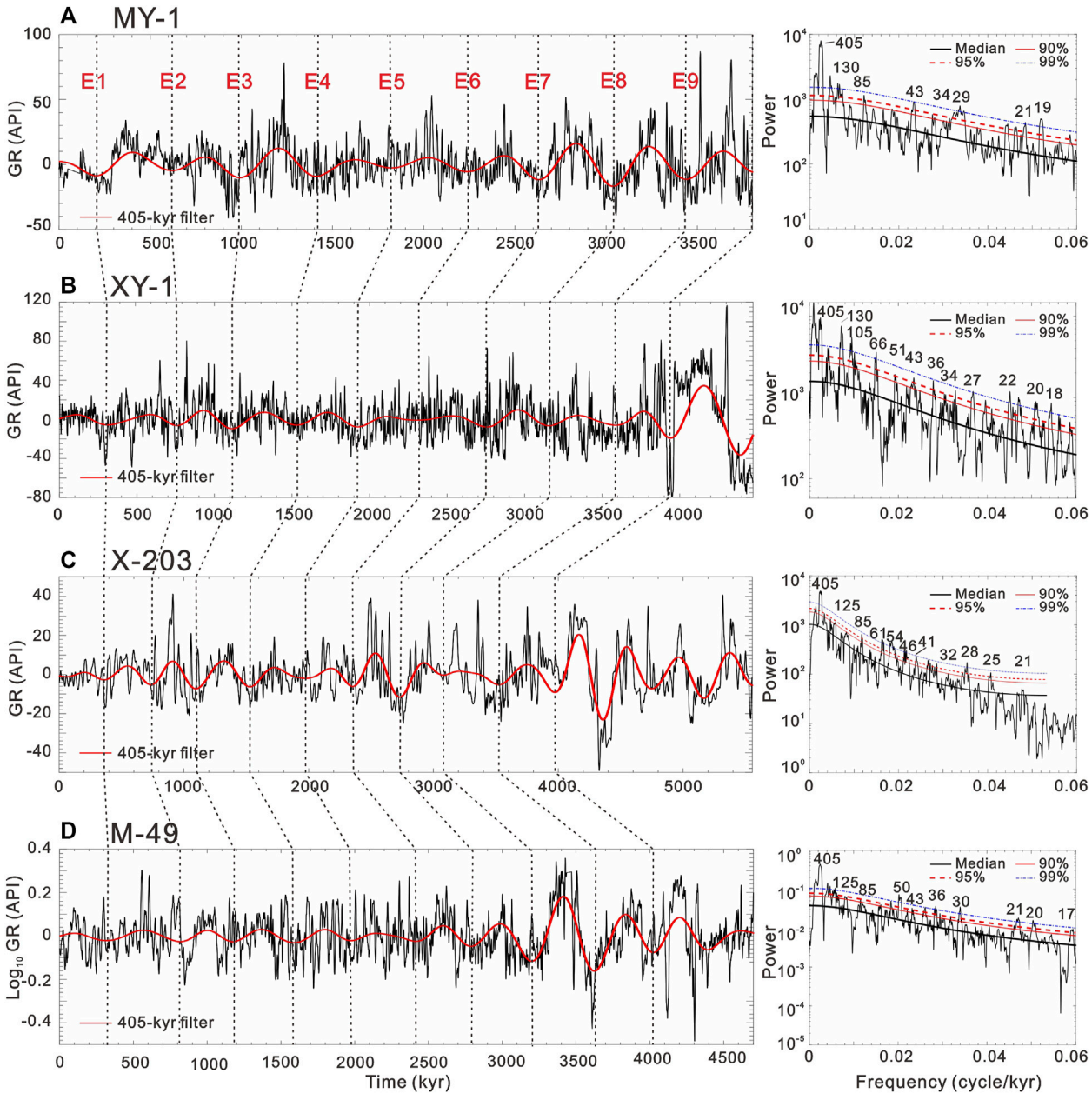

FIGURE 5
Spectral analyses of GR series from wells MY-1 **(A)**, XY-1 **(B)**, X-203 **(C)**, and M-49 **(D)** after tuning to the time domain. Also shown are the detrended GR series (black curve) and filtered long eccentricity cycles (red curve, 405 kyr) with passbands of 0.00246 ± 0.0005 cycle/kyr, and the 2π MTM analysis results of the tuned GR time series, with significant peaks labeled in units of kyr.

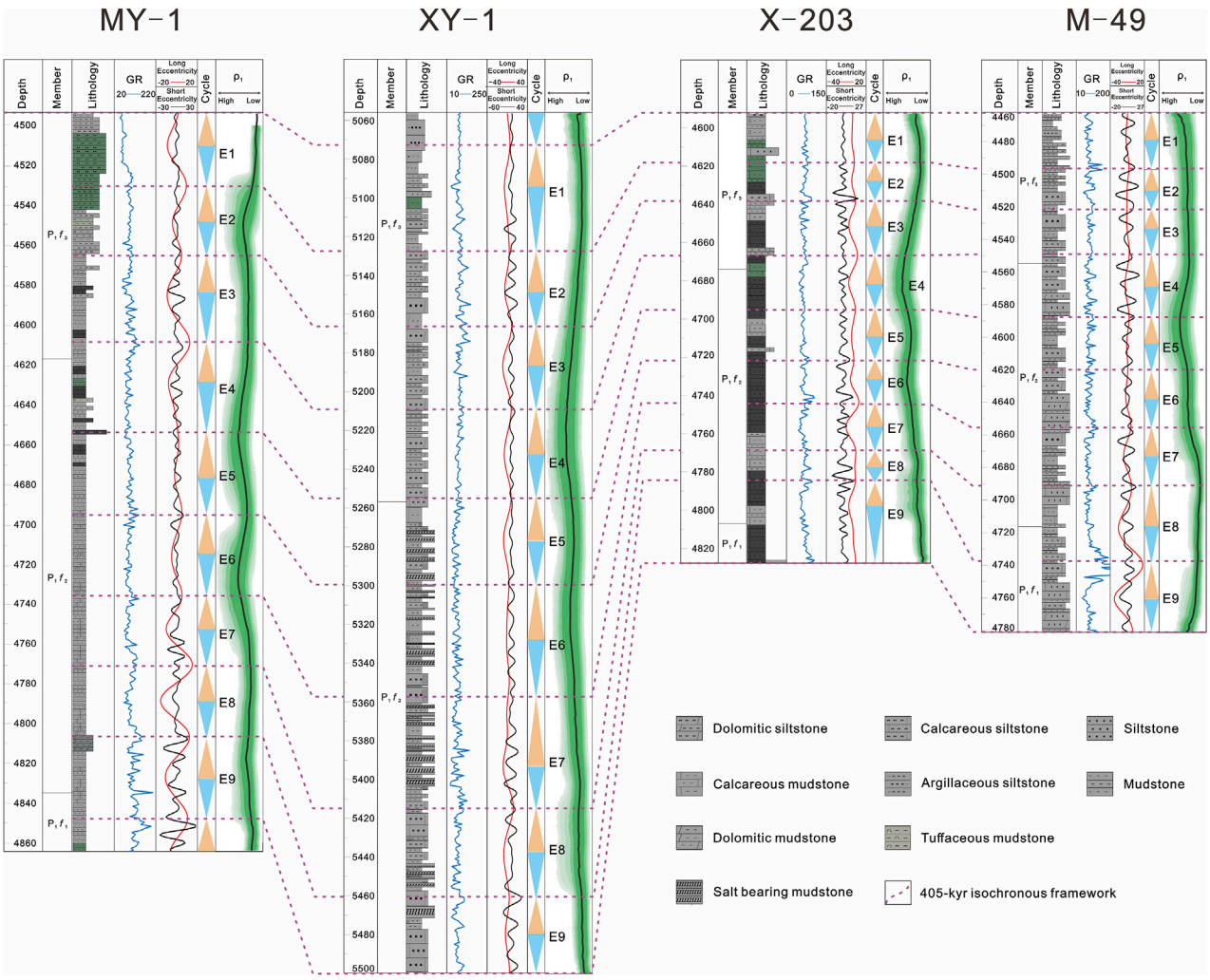

FIGURE 6
High-frequency isochronous sedimentary framework division and correlation and lake-level changes of the Fengcheng Formation in the Mahu Sag. The dashed purple line represents the boundary of 405 kyr long eccentricity cycles. The ρ_1 models of the tuned GR series were estimated using a running window of 405 kyr. A Monte Carlo analysis with 2,000 iterations was performed to estimate the confidence level.

5 Discussion

5.1 High-frequency sedimentary framework division and correlation

The sedimentary sequence hierarchy is based mostly on the timing and amplitude of sea level oscillations (e.g., Vail et al., 1977; Boulila et al., 2011). Recent reports have argued that climate change associated with orbital forcing is the major factor that controls the development of third-order and higher frequency sequences (Boulila et al., 2011; Liu et al., 2022; Wu et al., 2022). The third-order sequences may be connected to ~2.4 Myr long-period eccentricity and ~1.2 Myr long-period obliquity (e.g., Boulila et al., 2011; Cong et al., 2019; Du et al., 2020). Notably, this hierarchy can account for orbital frequency evolution throughout geological time. For example, the ~1.2- and ~2.4-Myr cycles may have undergone variations owing to the inner planets' chaotic motion (Laskar, 1989; Laskar et al., 2004). Previous theoretical work (DeConto and Pollard, 2003) suggested that glacioeustatic falls owing to orbital forcing are connected with the 405-kyr and ~2.4-Myr eccentricity minima. Fourth-order and well-documented stratigraphic sequences (Boulila et al., 2010; Boulila et al., 2011) may be reflective of the 405-kyr eccentricity cycle (Laskar et al., 2004), which is astronomically stable, and potentially the ~160–200-kyr short obliquity modulations. The fifth-order sequences may be related to the short eccentricity cycle, while sixth-order sequences could be connected to fundamental cycles of precession (~20 kyr) and/or obliquity (~40 kyr) (Boulila et al., 2010; Boulila et al., 2011). The obliquity precession components were also shorter within deep time owing to tidal dissipation (Berger et al., 1992; Laskar et al., 2004; Waltham, 2015). The simple connection between eustatic and astronomical hierarchies does not eliminate numerous stochastic feedbacks and processes that interfere with changes in sea level and climate, such as greenhouse gas effects, tectonics, and intrinsic ice dynamics.

For lacustrine shales, the climate change caused by the orbital cycle controls the development of third-to sixth-order high-frequency sequences. The third-order sequence is a lake transgression-regression sequence with large-scale lake-level changes comparable to long-term base-level cycles, and is controlled by the ~2.4 Myr long-period eccentricity and ~1.2 Myr long-period obliquity cycle (Boulila et al., 2011; Wang et al., 2020; Wei et al., 2023). The fourth-order sequence is a secondary lake transgression-regression sequence with high-amplitude water depth changes corresponding to the medium-term base-level cycle and controlled by the 405 kyr long eccentricity cycle (Boulila et al., 2011; Liu et al., 2022). The fifth-order sequence is a rhythmic transgression-regression sequence with low amplitude lake-level change corresponding to the short-term base-level cycle and controlled by the ~100 kyr short eccentricity cycle (Boulila et al., 2010; Boulila et al., 2011; Tang et al., 2022). Many scholars therefore use different orders of eccentricity cycles as a reference to divide the high-frequency cycle framework of lacustrine shale sequences (e.g., Cong et al., 2019; Du et al., 2020; Fang et al., 2023).

Cyclostratigraphic analyses of four standard wells were conducted in this study to establish an isochronous cycle framework for the Fengcheng Formation (Figure 6). Using the 405-kyr eccentricity cycle as a reference, nine medium-term base-level cycles (E1–E9) were identified within the P_1f_1 and P_1f_2 members that roughly correspond to fourth-order sequences. Each long eccentricity cycle consists of approximately four ~100-kyr short eccentricity cycles, which allows approximately 36 short-term base-level cycles to be identified, roughly corresponding to fifth-order sequences.

Under the constraints of isochronous stratigraphic framework, the Fengcheng Formation's sedimentation rate is positively correlated with the depositional thickness. During the Fengcheng Formation's depositional period, the Zaire and Haraalat Mountains, which are found on the western margin of the Junggar Basin, provided the major terrigenous supply (Song et al., 2022). The Fengcheng Formation on the northwestern margin of the Mahu Sag inherited and then developed a multisource fan delta sedimentary system. The sedimentation rate of well M-49 (13.8 cm/kyr) is higher than that of both wells MY-1 (9.3 cm/kyr) and X-203 (7.2 cm/kyr), likely because its location received more terrigenous clastic material supply. The sedimentation rate of well XY-1 (13.5 cm/kyr) is also relatively high owing to the large and rapid accumulation of alkaline minerals.

The application of astronomical cycles to stratigraphic sequences enables high-resolution isochronous stratigraphic correlation at the eccentricity cycle scale, thus overcoming the long-standing bottleneck of low precision when using traditional methods for the subdivision and correlation of deep-water shale sequences. This novel approach shows great potential for fine-scale characterization of alkaline lacustrine sequences and provides innovative insights for predicting favorable areas for shale oil exploration.

5.2 Astronomical forcing of paleolake-level variations

Sedimentary noise model involves two complementary approaches: the dynamic noise after orbital tuning (DYNOT) model and Lag-1 autocorrelation coefficient (ρ_1) model (Li et al., 2018a). While the former is typically used to examine temporal shifts in lake level, the latter is commonly used to analyze changes in lake level with respect to stratigraphic depth. The primary goal of our research is to use astronomical cycles to constrain the stratigraphic framework, focusing primarily on the ρ_1 model to reconstruct lake-level variations in the depth domain. Continental basins are sensitive to climate changes and have high sedimentation rates and high sedimentary record temporal resolutions, which can record long-term paleoclimate signals. This model has been applied in studies of lake-level changes during multiple geological epochs. Increasing evidence suggests the applicability of the sedimentary noise model (e.g., Wang et al., 2020; Huang et al., 2021; Tang et al., 2022; Wei et al., 2023). Compared with traditional methods, this approach is characterized by the direct quantitative evaluation of sedimentary noise using paleoclimate proxies in the depth domain. Compared with traditional reconstruction methods, such as sequence stratigraphy, the results are objective and independent of researcher experience.

The ρ_1 model using a tuned GR series with a 400-kyr sliding window allows the autocorrelation curve of the Fengcheng Formation to be reconstructed. Following our hypothesis in Section 3.3, we propose that the curve is representative of the relative water level variation in the paleolake. In this study, lake-level variations in the Mahu Sag exhibit significant periodicity. In particular, ρ_1 of the middle part of the Fengcheng Formation (P_1f_2 Member) is larger and shows a relatively higher lake level (Figure 6). This study identified nine mid-term base-level cycles (E1–E9) within the P_1f_1 and P_1f_2 members, each lasting approximately 405 kyr. The lake-level rise was particularly significant during cycles E9, E6, E5, and E4. The E9 cycle corresponds to the late depositional stage of the P_1f_1 Member, with a relatively low input of terrestrial debris and thin deposits of organic-rich mudstones in the Mahu Sag, indicating a reducing environment. During the early depositional stage of the P_1f_2 Member, the basin decreased in size and the regional climate became arid. The input of terrigenous debris remains relatively low, resulting in an increase in lake salinity and water stratification. Cycles E6 to E4 correspond to the middle to late stages of P_1f_2 Member deposition, during which time the basin expanded again. The climate at this time was extremely hot and dry, and the lake water salinity reached its highest level. Alkaline minerals were widely developed, and even deposits of reedmergnerite occurred (Zhang et al., 2018; Song et al., 2022). During the deposition of the P_1f_3 Member, the basin further contracted, and the salinity gradually decreased as the lake level proceeded to drop. The climate then became more humid and warmer, and the terrestrial debris input increased, but the organic matter abundance decreased. The basin developed toward freshening, characterized by an increase in the input of terrigenous clastic sediments.

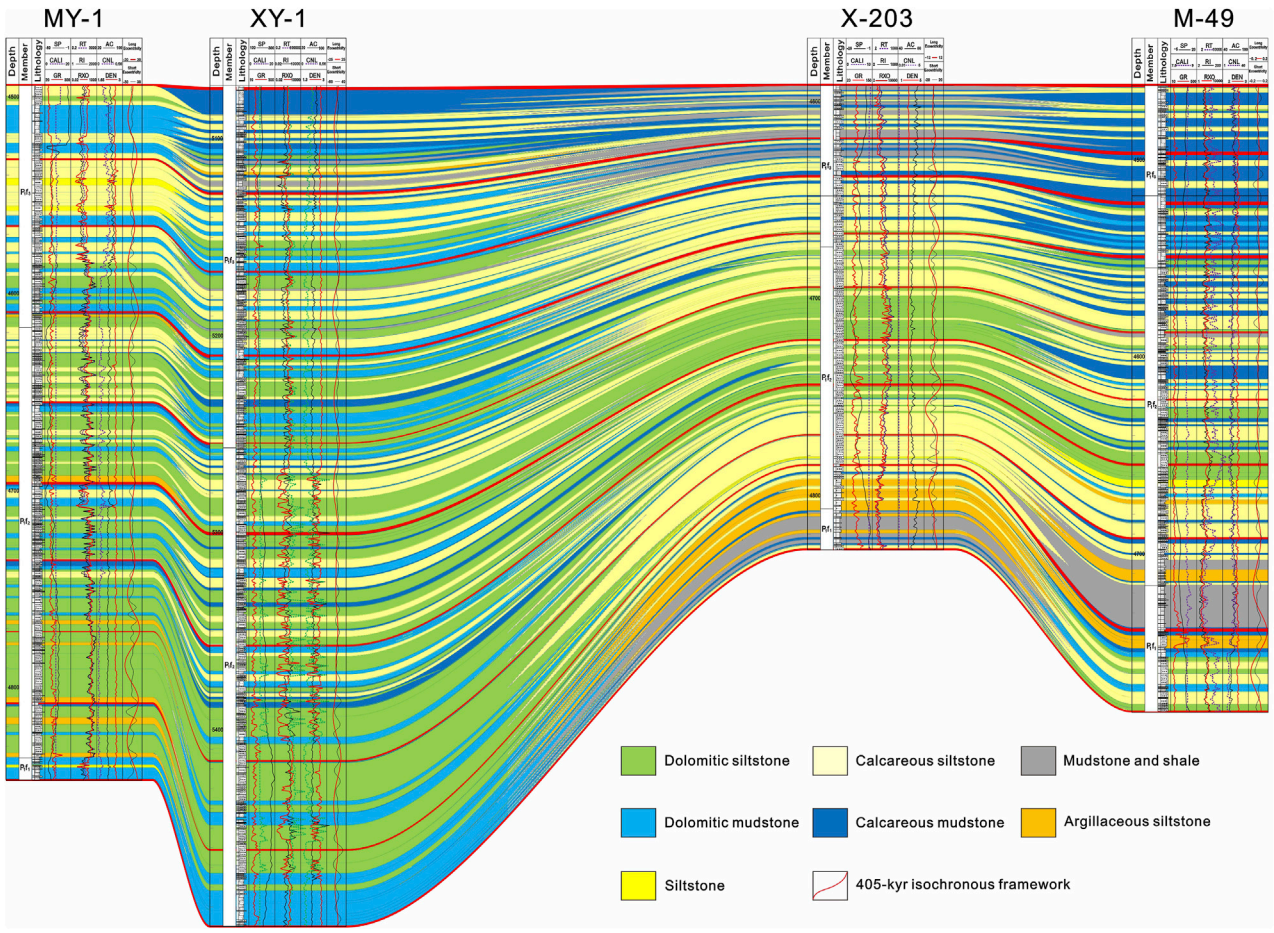

FIGURE 7
Lithofacies distribution of the Fengcheng Formation based on the high-frequency sedimentary framework in the Mahu Sag. Combined with the indicative significance of various conventional logging curves for lithofacies, the lithofacies types of the Fengcheng Formation were classified into dolomitic siltstone, dolomitic mudstone, calcareous siltstone, calcareous mudstone, mudstone and shale, argillaceous siltstone, siltstone, and other types. The red line represents the boundary of 405 kyr long eccentricity cycles. Correlation of lithofacies distribution was performed under the constraints of long eccentricity cycles.

5.3 Lithofacies distribution in the high-frequency sedimentary framework

Earth's orbital cycles can modulate the sedimentary processes and depositional environments of lacustrine shales, leading to the formation of distinct lithofacies patterns. The resulting lithofacies can reveal information about the paleoenvironmental conditions, such as climate and lake-level fluctuations, that prevailed during the deposition of the shale sequence. Regulated by changes in lake level and high-frequency cycles, the Fengcheng Formation in the Mahu Sag comprises a diverse array of sedimentary rocks, including terrestrial fan-delta clastic rocks, endogenic carbonate rocks, volcaniclastic rocks, evaporites, and mixed sedimentary rocks (Yu et al., 2018a; Zhang et al., 2018; Song et al., 2022). Further combining the significance of a variety of conventional logging curves to indicate the lithology, we classify the lithofacies types of the Fengcheng Formation into dolomitic siltstone, dolomitic mudstone, calcareous siltstone, calcareous mudstone, mudstone and shale, argillaceous siltstone, siltstone and others (Figure 7).

Isochronous stratigraphic correlation was conducted along the provenance direction in the northern area of the Mahu Sag, which reveals the presence of at least 36 short-term base-level cycles within the P_1f_1 and P_1f_2 members, with a lithofacies identification resolution reaching the level of short eccentricity (~100 kyr) (Figure 7). The spatial distribution patterns of lithofacies in the Fengcheng Formation can be clearly demonstrated within the isochronous cycle framework under the 405-kyr long eccentricity cycle constraints. Alkaline mineral lithofacies dominate in the P_1f_2 Member, while organic-rich shale lithofacies are prevalent in the upper section of the P_1f_1 Member and the lower part of the P_1f_3 Member, which are often interbedded with limestone lithofacies.

Wells MY-1 and XY-1 are located closer to the lake sedimentary center, where the thickness of evaporite deposition is greater. The duration of the P_1f_1 Member represents the early stage of alkaline lake evolution, characterized by dolomitic mudstone and calcareous mudstone lithofacies. The duration of the P_1f_2 Member is marked by the intensive deposition of alkaline minerals and the development of dolomitic mudstone and dolomite lithofacies. The duration of the P_1f_3 Member represents the extinction stage of the alkaline lake, with

dolomitic siltstone and calcareous mudstone lithofacies developed in this area. In contrast, the depositional thickness of evaporites near the slope edge of the lake (Wells X-203 and M-49) is small, and the lithofacies is characterized by calcareous siltstone and coarse clastic sediments.

Future work will involve the identification of high-frequency cycles that are enriched in shale oil, followed by the detailed characterization of the lithofacies within these cycles, to reveal the sedimentary response of organic-rich shale deposition to astronomical orbital forcing.

6 Conclusion

Cyclostratigraphic analyses in wells MY-1, XY-1, X-203, and M-49 allowed the identification that the Fengcheng Formation exhibits significant astronomical cycles, including the 405-kyr long eccentricity cycle, the ~100-kyr short eccentricity cycle, and the obliquity and precession cycle. These results show that the sedimentation process in the alkaline lacustrine areas of the Fengcheng Formation was astronomically controlled. Stratigraphic correlations based on the long eccentricity cycle show that the duration of the P_1f_2 Member is ~2.4 Myr and that of the P_1f_3 Member is ~1.2 Myr.

There is a strong correlation between Earth's orbital cycles and sedimentary sequences in the Fengcheng Formation. Nine medium-term base-level cycles (E1–E9) were identified within the P_1f_1 and P_1f_2 members, which roughly correspond to fourth-order sequences. These cycles are approximately 405 kyr and consist of approximately four ~100 kyr short eccentricity cycles, resulting in the identification of approximately 36 short-term base-level cycles, generally corresponding to fifth-order sequences. The sedimentary noise modeling method was applied to reconstruct paleolake-level variations in the Fengcheng Formation. The results revealed that the lake level significantly increased during the E9, E6, E5, and E4 cycles. The Fengcheng Formation exhibits clear spatial distribution patterns of lithofacies within the isochronous cycle framework. Future work will involve the identification of shale oil-enriched cycles and investigation of astronomical cycle control over organic matter enrichment.

Data availability statement

The original contributions presented in the study are included in the article/Supplementary Material, further inquiries can be directed to the corresponding author.

Author contributions

Conceptualization and investigation: GL, RZ, and RkZ; methodology: XH and RWe; formal analysis: WH, MZ, QC, RWa, and XZ; writing–original draft: GL, RZ, XH, and RWe; review and editing: RZ, RkZ, and YT. All authors contributed to the article and approved the submitted version.

Funding

This work was financially supported by the National Natural Science Foundation of China (Grant Nos 42090025, 42102166).

Acknowledgments

We would like to thank the editors and reviewers whose input greatly improved the quality of this manuscript.

Conflict of interest

Authors GL, RkZ, YT, WH, MZ, QC, RWa, and XZ were employed by the company PetroChina.

The remaining authors declare that the research was conducted in the absence of any commercial or financial relationships that could be construed as a potential conflict of interest.

Publisher's note

Supplementary material

The Supplementary Material for this article can be found online at: https://www.frontiersin.org/articles/10.3389/feart.2023.1206835/full#supplementary-material

References

Anderson, R. (1982). A long geo-climatic record from the Permian. *J. Geophys. Res.* 87, 7285–7294. doi:10.1029/JC087iC09p07285

Berger, A., Loutre, M., and Laskar, J. (1992). Stability of the astronomical frequencies over the Earth's history for paleoclimate studies. *Science* 255, 560–566. doi:10.1126/science.255.5044.560

Boulila, S., Galbrun, B., Hinnov, L. A., Collin, P.-Y., Ogg, J. G., Fortwengler, D., et al. (2010). Milankovitch and sub-milankovitch forcing of the oxfordian (late jurassic) terres noires formation (SE France) and global implications. *Basin Res.* 22, 717–732. doi:10.1111/j.1365-2117.2009.00429.x

Boulila, S., Galbrun, B., Miller, K. G., Pekar, S. F., Browning, J. V., Laskar, J., et al. (2011). On the origin of Cenozoic and Mesozoic "third-order" eustatic sequences. *Earth-Sci. Rev.* 109, 94–112. doi:10.1016/j.earscirev.2011.09.003

Cao, J., Xia, L., Wang, T., Zhi, D., Tang, Y., and Li, W. (2020). An alkaline lake in the late paleozoic ice age (lpia): A review and new insights into paleoenvironment and petroleum geology. *Earth-Sci. Rev.* 202, 103091. doi:10.1016/j.earscirev.2020.103091

Cleveland, W. S. (1979). Robust locally weighted regression and smoothing scatterplots. *Publ. Am. Stat. Assoc.* 74, 829–836. doi:10.1080/01621459.1979.10481038

Cong, F., Zhu, F., Cai, Z., Chen, H., Li, J., Wang, Y., et al. (2019). Orbitally forced glacio-eustatic origin of third-order sequences and parasequences in the Middle Permian Maokou Formation, South China. *Mar. Pet. Geol.* 99, 237–251. doi:10.1016/j.marpetgeo.2018.10.014

DeConto, R., and Pollard, D. (2003). Rapid Cenozoic glaciation of Antarctica induced by declining atmospheric CO_2. *Nature* 421, 245–249. doi:10.1038/nature01290

Du, W., Ji, Y., Chen, G., Wu, H., Gao, C., Li, S., et al. (2020). Cyclostratigraphy and astronomical tuning during the oligocene in the jizhong depression, bohai bay basin,

northeastern China. *Palaeogeogr. Palaeoclimatol. Palaeoecol.* 554, 109803. doi:10.1016/j.palaeo.2020.109803

Eldrett, J. S., Ma, C., Bergman, S. C., Ozkan, A., Minisini, D., Lutz, B., et al. (2015). Origin of limestone–marlstone cycles: Astronomic forcing of organic-rich sedimentary rocks from the Cenomanian to early Coniacian of the Cretaceous Western Interior Seaway, USA. *Earth Planet. Sci. Lett.* 423, 98–113. doi:10.1016/j.epsl.2015.04.026

Fang, Z., Zhang, L., and Ma, C. (2023). Development and controlling factors of shale lithofacies cycles in a continental rift basin: A case study of Es_4^u in the boxing subsag of dongying sag, bohai bay basin, China. *Front. Earth Sci.* 11, 1136012. doi:10.3389/feart.2023.1136012

Hinnov, L. A. (2013). Cyclostratigraphy and its revolutionizing applications in the Earth and planetary sciences. *Geol. Soc. Am. Bull.* 125, 1703–1734. doi:10.1130/B30934.1

Hinnov, L. A., and Hilgen, F. J. (2012). "Chapter 4 - cyclostratigraphy and astrochronology," in *The geologic time scale*. Editors F. M. Gradstein, J. G. Ogg, M. D. Schmitz, and G. M. Ogg (Boston: Elsevier), 63–83. doi:10.1016/B978-0-444-59425-9.00004-4

Huang, C., and Hinnov, L. (2019). Astronomically forced climate evolution in a saline lake record of the middle Eocene to Oligocene, Jianghan Basin, China. *Earth Planet. Sci. Lett.* 528, 115846. doi:10.1016/j.epsl.2019.115846

Huang, H., Gao, Y., Jones, M. M., Tao, H., Carroll, A. R., Ibarra, D. E., et al. (2020). Astronomical forcing of Middle Permian terrestrial climate recorded in a large paleolake in northwestern China. *Palaeogeogr. Palaeoclimatol. Palaeoecol.* 550, 109735. doi:10.1016/j.palaeo.2020.109735

Huang, H., Gao, Y., Ma, C., Niu, L., Dong, T., Tian, X., et al. (2021). Astronomical constraints on the development of alkaline lake during the carboniferous-permian period in north pangea. *Glob. Planet. Change* 207, 103681. doi:10.1016/j.gloplacha.2021.103681

Kent, D. V., Olsen, P. E., and Muttoni, G. (2017). Astrochronostratigraphic polarity time scale (APTS) for the Late Triassic and Early Jurassic from continental sediments and correlation with standard marine stages. *Earth-Sci. Rev.* 166, 153–180. doi:10.1016/j.earscirev.2016.12.014

Kodama, K. P., and Hinnov, L. A. (2014). *Rock magnetic cyclostratigraphy*. United States: Wiley. doi:10.1002/9781118561294

Kuang, L., Tang, Y., Lei, D., Chang, Q., Ouyang, M., Hou, L., et al. (2012). Formation conditions and exploration potential of tight oil in the Permian saline lacustrine dolomitic rock, Junggar Basin, NW China. *Pet. Explor. Dev.* 39, 700–711. doi:10.1016/S1876-3804(12)60095-0

Laskar, J. (1989). A numerical experiment on the chaotic behaviour of the Solar System. *Nature* 338, 237–238. doi:10.1038/338237a0

Laskar, J., Robutel, P., Joutel, F., Gastineau, M., Correia, A. C. M., and Levrard, B. (2004). A long-term numerical solution for the insolation quantities of the Earth. *Astron. Astrophys.* 428, 261–285. doi:10.1051/0004-6361:20041335

Li, M., Hinnov, L. A., Huang, C., and Ogg, J. G. (2018a). Sedimentary noise and sea levels linked to land–ocean water exchange and obliquity forcing. *Nat. Commun.* 9, 1004. doi:10.1038/s41467-018-03454-y

Li, M., Hinnov, L., and Kump, L. (2019a). Acycle: Time-series analysis software for paleoclimate research and education. *Comput. Geosci.* 127, 12–22. doi:10.1016/j.cageo.2019.02.011

Li, M., Huang, C., Ogg, J., Zhang, Y., Hinnov, L., Wu, H., et al. (2019b). Paleoclimate proxies for cyclostratigraphy: Comparative analysis using a Lower Triassic marine section in South China. *Earth-Sci. Rev.* 189, 125–146. doi:10.1016/j.earscirev.2019.01.011

Li, M., Kump, L. R., Hinnov, L. A., and Mann, M. E. (2018b). Tracking variable sedimentation rates and astronomical forcing in Phanerozoic paleoclimate proxy series with evolutionary correlation coefficients and hypothesis testing. *Earth Planet. Sci. Lett.* 501, 165–179. doi:10.1016/j.epsl.2018.08.041

Liu, S., Jin, S., Liu, Y., and Chen, A. (2022). Astronomical forced sequence infill of early cambrian Qiongzhusi organic-rich shale of Sichuan Basin, south China. *Sediment. Geol.* 440, 106261. doi:10.1016/j.sedgeo.2022.106261

Mann, M. E., and Lees, J. M. (1996). Robust estimation of background noise and signal detection in climatic time series. *Clim. Change* 33, 409–445. doi:10.1007/BF00142586

Meyers, S. R. (2019). Cyclostratigraphy and the problem of astrochronologic testing. *Earth-Sci. Rev.* 190, 190–223. doi:10.1016/j.earscirev.2018.11.015

Meyers, S. R., and Hinnov, L. A. (2010). Northern Hemisphere glaciation and the evolution of Plio-Pleistocene climate noise. *Paleoceanography* 25. doi:10.1029/2009PA001834

Mudelsee, M. (2002). Tauest: A computer program for estimating persistence in unevenly spaced weather/climate time series. *Comput. Geosci.* 28, 69–72. doi:10.1016/S0098-3004(01)00041-3

Olsen, P., and Kent, D. (1996). Milankovitch climate forcing in the tropics of pangaea during the late triassic. *Palaeogeogr. Palaeoclimatol. Palaeoecol.* 122, 1–26. doi:10.1016/0031-0182(95)00171-9

Song, Y., Yang, Z., He, W., Gan, R., Zhang, R., Huang, L., et al. (2022). Exploration progress of alkaline lake type shale oil of the permian Fengcheng Formation in Mahu sag, Junggar Basin. *China Pet. explor.* 27, 60–72.

Tang, Y., Zheng, M., Wang, X., Wang, T., Cheng, H., and Hei, C. (2022). The floating astronomical time scale for the terrestrial Early Permian Fengcheng Formation from the Junggar Basin and its stratigraphic and palaeoclimate implications. *Geol. J.* 57, 4842–4856. doi:10.1002/gj.4575

Thomson, D. J. (1982). Spectrum estimation and harmonic analysis. *Proc. IEEE* 70, 1055–1096. doi:10.1109/PROC.1982.12433

Vail, P. R., Mitchum, R. M., Todd, J. R. G., Widmier, J. M., Thompson, S., Sangree, J. B., et al. (1977). Seismic stratigraphy and global changes of sea level: Seismic stratigraphy – applications to hydrocarbon exploration. *Mem. Am. Ass. Pertol. Geol.* 26, 49–212.

van Vugt, N., Langereis, C. G., and Hilgen, F. J. (2001). Orbital forcing in pliocene–pleistocene mediterranean lacustrine deposits: Dominant expression of eccentricity versus precession. *Palaeogeogr. Palaeoclimatol. Palaeoecol.* 172, 193–205. doi:10.1016/S0031-0182(01)00270-X

Waltham, D. (2015). Milankovitch period uncertainties and their impact on cyclostratigraphy. *J. Sediment. Res.* 85, 990–998. doi:10.2110/jsr.2015.66

Wang, M., Chen, H., Huang, C., Kemp, D. B., Xu, T., Zhang, H., et al. (2020). Astronomical forcing and sedimentary noise modeling of lake-level changes in the Paleogene Dongpu Depression of North China. *Earth Planet. Sci. Lett.* 535, 116116. doi:10.1016/j.epsl.2020.116116

Wang, T., Cao, J., Carroll, A. R., Zhi, D., Tang, Y., Wang, X., et al. (2021). Oldest preserved sodium carbonate evaporite: Late paleozoic Fengcheng Formation, Junggar Basin, NW China. *GSA Bull.* 133, 1465–1482. doi:10.1130/B35727.1

Wang, X., Jin, Z., Chen, G., Peng, M., Huang, L., Wang, Z., et al. (2022). Multi-scale natural fracture prediction in continental shale oil reservoirs: A case study of the Fengcheng Formation in the Mahu sag, Junggar Basin, China. *Front. Earth Sci.* 10, 929467. doi:10.3389/feart.2022.929467

Weedon, G. P. (2003). *Time series analysis and cyclostratigraphy: Examining stratigraphic records of environmental cycles*. Cambridge, United Kingdom: Cambridge University Press.

Wei, R., Zhang, R., Li, M., Wang, X., and Jin, Z. (2023). Obliquity forcing of lake-level changes and organic carbon burial during the Late Paleozoic Ice Age. *Glob. Planet. Change* 223, 104092. doi:10.1016/j.gloplacha.2023.104092

Wu, H., Hinnov, L. A., Zhang, S., Jiang, G., Yang, T., Li, H., et al. (2022). Continental geological evidence for solar system chaotic behavior in the late cretaceous. *GSA Bull.* 135, 712–724. doi:10.1130/B36340.1

Wu, H., Zhang, S., Jiang, G., Hinnov, L., Yang, T., Li, H., et al. (2013). Astrochronology of the early turonian–early campanian terrestrial succession in the songliao basin, northeastern China and its implication for long-period behavior of the solar system. *Palaeogeogr. Palaeoclimatol. Palaeoecol.* 385, 55–70. doi:10.1016/j.palaeo.2012.09.004

Yu, K., Cao, Y., Qiu, L., Sun, P., Jia, X., and Wan, M. (2018b). Geochemical characteristics and origin of sodium carbonates in a closed alkaline basin: The lower permian Fengcheng Formation in the Mahu sag, northwestern Junggar Basin, China. *Palaeogeogr. Palaeoclimatol. Palaeoecol.* 511, 506–531. doi:10.1016/j.palaeo.2018.09.015

Yu, K., Cao, Y., Qiu, L., and Sun, P. (2018a). The hydrocarbon generation potential and migration in an alkaline evaporite basin: The Early Permian Fengcheng Formation in the Junggar Basin, northwestern China. *Mar. Pet. Geol.* 98, 12–32. doi:10.1016/j.marpetgeo.2018.08.010

Zhang, R., Jin, Z., Liu, Q., Li, P., Huang, Z., Shi, J., et al. (2019). Astronomical constraints on deposition of the middle triassic chang 7 lacustrine shales in the ordos basin, central China. *Palaeogeogr. Palaeoclimatol. Palaeoecol.* 528, 87–98. doi:10.1016/j.palaeo.2019.04.030

Zhang, Z., Yuan, X., Wang, M., Zhou, C., Tang, Y., Chen, X., et al. (2018). Alkaline-lacustrine deposition and paleoenvironmental evolution in permian Fengcheng Formation at the Mahu sag, Junggar Basin, NW China. *Pet. Explor. Dev.* 45, 1036–1049. doi:10.1016/S1876-3804(18)30107-1

Zhi, D., Tang, Y., He, W., Guo, X., Zheng, M., and Huang, L. (2021). Orderly coexistence and accumulation models of conventional and unconventional hydrocarbons in lower permian Fengcheng Formation, Mahu sag, Junggar Basin. *Pet. Explor. Dev.* 48, 43–59. doi:10.1016/S1876-3804(21)60004-6

frontiers | Frontiers in Earth Science

TYPE Original Research
PUBLISHED 17 May 2023
DOI 10.3389/feart.2023.1146126

OPEN ACCESS

EDITED BY
Salam Al-Rbeawi,
Middle East Technical University, Türkiye

REVIEWED BY
Hamid Al-Sari,
University of Misan, Iraq
Fadhil Kadhim,
University of Technology, Iraq, Iraq

*CORRESPONDENCE
Andrés Pastor-Chacón,
afpastor@sgc.gov.co

RECEIVED 17 January 2023
ACCEPTED 21 April 2023
PUBLISHED 17 May 2023

CITATION
Pastor-Chacón A, Aguilera R, Triana JL, Paez-Reyes M, Cantisano M, Bravo L, Gamba N, Niño M, Delgado A, Mendoza G, Rodriguez JD, Romero-Ballén O, Ruiz MC, Buitrago H and Fuenzalida H (2023), Sweet spot areas for shale oil and shale gas plays in the Upper Cretaceous rocks of the Middle Magdalena Valley, Colombia: insights from basin modeling.
Front. Earth Sci. 11:1146126.
doi: 10.3389/feart.2023.1146126

Sweet spot areas for shale oil and shale gas plays in the Upper Cretaceous rocks of the Middle Magdalena Valley, Colombia: insights from basin modeling

Andrés Pastor-Chacón[1]*, Roberto Aguilera[1], Jorge Luis Triana[1], Manuel Paez-Reyes[1], Maria Cantisano[1], Luis Bravo[1], Néstor Gamba[1], Miled Niño[1], Alexandra Delgado[1], Gabriel Mendoza[1], Juan David Rodriguez[1], Oscar Romero-Ballén[1], Maria Cecilia Ruiz[2], Hugo Buitrago[2] and Humberto Fuenzalida[1]

[1]Dirección de Hidrocarburos, Servicio Geológico Colombiano, Bogotá, Colombia, [2]Agencia Nacional de Hidrocarburos, Bogotá, Colombia

The Middle Magdalena Valley Basin (MMVB) in Colombia has a long history of conventional hydrocarbon exploration and production, with a cumulative production of 2.75 billion barrels of oil as of December 2021. Recent interest has been directed towards unconventional hydrocarbon plays within the basin due to the fine-grained nature of its Cretaceous source rocks and their mineralogy and mechanical properties. This study presents a three-dimensional basin model for three Upper Cretaceous source rocks, known as the "La Luna Formation," within the MMVB. The model was developed using new data from five outcrops, 7,640 km of 2D seismic lines, and forty-one boreholes, as well as additional data sets such as X-ray diffraction analyses, pyrolysis analyses, well-log correlations, facies analysis, fracture pattern prediction, pore pressure analysis, heat flow estimations, and petrophysical data. The model estimates total retained oil and gas volumes to be 7.95 billion barrels and 4.21 trillion cubic feet in most probable scenarios, after a 15% recovery factor. Seismic interpretation reveals pre-Eocene structures beneath Paleogene and Neogene sediments, and the thickness variation of the source rocks from south to north of the basin. Petrophysical modeling shows effective porosities ranging from 2%–12% and organic porosities lower than 0.1%, with parts of the succession that might correspond to a carrier bed play. From a geomechanical perspective, we identified several brittle strata based on the higher concentrations of carbonates and quartz, and the areas with a higher probability of occurrence of natural fractures. Pore pressure analysis of multiple wells shows that wells in which the Middle Eocene unconformity has beveled the source rocks have no sealing capacity, becoming a risk for the play. The results suggest potential for unconventional hydrocarbon plays in the MMVB, with sweet spot areas being primarily controlled by porosity, thermal maturity, gas-oil ratios, and retained oil and gas volumes, as well as to a lesser degree, the probability of natural fractures and pore pressure conditions. However, further exploration is needed to constrain uncertainties regarding facies and source rock quality, particularly within the depocenters of the basin, in order to prove the economic feasibility of these unconventional plays.

KEYWORDS

Middle Magdalena Valley Basin, unconventional reservoir, basin modeling, sweet spot area, Cretaceous

1 Introduction

The Middle Magdalena Valley Basin (MMVB) is located in Central Colombia and is the second most prolific hydrocarbons province of the country. Fine-grained Cretaceous rocks in northwestern South America and in the MMVB have been studied because of their importance as source rocks that feed conventional petroleum plays (e.g., Erlich et al., 2003; Rangel et al., 2017; Thompson-Butler et al., 2019). The chemistry, mineralogy, and mechanical properties of these rocks, however, have made them in more recent years the focus of attention as an unconventional play prospect (EIA, 2015). Yet-to find estimations of in-place and recoverable resources for the Cretaceous rocks within the MMVB as of December 2021 were 24.830 Tcf of gas and 7.787 Bbbl of oil (Mora et al., 2018; ANH-UPTC, 2021).

Despite the MMVB being an established hydrocarbon-producing basin, a thorough understanding of its full potential and the location of remaining undiscovered hydrocarbon resources requires a comprehensive evaluation of the petroleum system. Such an evaluation includes the determination of the total volume of hydrocarbons generated from each source rock, as well as the volumes of migrated and remaining hydrocarbons in or near the source beds for potential production. In the same way, previous interpretations of source-related biomarkers suggest the presence of an extensive petroleum system, although several questions to address around generation, migration, seal, and trap processes remain (e.g., Ramón et al., 1997; Rangel et al., 2017; Thompson-Butler et al., 2019).

The aim of this study is to analyze geological information from multiple sources, including outcrops, wells, wire-line logs, and source-rock geochemical data in order to: 1) determine rock properties; 2) develop a three-dimensional model depicting the regional basin architecture; and 3) use petroleum system analysis to evaluate the spatial distribution and petroleum potential of Upper Cretaceous source rocks across the MMVB, as unconventional reservoirs.

2 Basin geology and petroleum systems

The MMVB is an intermontane basin located in the central-northern part of the Andes in Colombia. It separates the Central and Eastern cordilleras of the country (Figure 1). The basin has a long history dating back to the Mesozoic, which was shaped by the tectonic interactions between the South American, Farallon, and Caribbean plates. During this period, the Central Cordillera was a magmatic arc, and rifted sub-basins filled with marine sediments formed to the east, each with their own subsidence history (Bayona, 2018; Sarmiento-Rojas, 2019). Compressional deformation of the Central Cordillera and the MMVB began in the Late Cretaceous, resulting in several time gaps, including the Late Campanian hiatus (Cooney & Lorente, 1997; Bayona, 2018; Etayo-Serna, 2019a). In the Cenozoic, the basin began to fill with continental sedimentary rocks, which also partially covered the Central Cordillera with valley-fill deposits along an onlapping surface (Gomez et al., 2005; Caballero et al., 2013).

Figure 2 shows the sedimentary units which comprise the MMVB. The basal units of the Cretaceous include the continental-transitional strata of the Tambor and Cumbre formations (Berriasian-Valanginian), which are related to the rifting and opening stages of the basin. The so-called "Grupo Calcareo Basal" consists of the Rosa Blanca, La Paja, and Tablazo formations (Valanginian-Aptian) and shows the evolution of transitional to shallow marine calcareous environments. The Simiti Formation (Aptian-Albian) comprises shales and might correspond to a maximum base-level rise (Etayo-Serna, 2019b). The so-called "La Luna Formation" (Late Cenomanian-Campanian) consists of the Salada, Pujamana, Galembo, and La Renta formations related to thermal post-rift conditions. The Umir and Lisama formations (Maastrichtian-Early Paleocene) contain transitional and continental rocks corresponding to the Central Cordillera uplifting and basin closure. Finally, most of the Cenozoic fill consists of the La Paz, Esmeraldas, Mugrosa, Colorado formations, and the Real Group, related to the Eastern and Central Cordilleras uplifting.

At least two intrabasinal highs divide the MMVB (Figure 1), corresponding to the La Cira-Infantas and Cachira highs (Gomez et al., 2003; 2005; Cortes et al., 2022; Reyes et al., 2022). The related depocenters to the La Cira-Infantas high are generally deeper (e.g., Nuevo Mundo-La Salina Depocenter) and contain a thicker and more complete Cretaceous-Cenozoic succession than those near the Cachira high (e.g., Santa Lucia Depocenter), which appears positive during the Oligocene (Horton et al., 2015).

The MMVB is host to a petroleum system that is composed by several elements, including source rocks, reservoirs and seals. The source rocks are found primarily in the Cretaceous formations, with the La Luna Formation being the most significant. The oils found in most Cenozoic reservoirs of the MMVB are genetically linked to the Salada, Pujamana, Galembo, and the La Renta formations (Turonian-Campanian) (Mora et al., 1996; Ramón et al., 1997; García et al., 2001; Rangel et al., 2017). Two intervals that correspond to the Cenomanian-Turonian sequence or the Salada Formation and the Coniacian-Campanian sequence that lithologically corresponds to the Galembo and La Renta formations, were deposited under anoxic conditions allowing large amounts of organic carbon to be deposited during this time (Villamil et al., 1999; Erlich et al., 2003). These intervals contain total organic carbon (TOC) greater than 4% and contain the best-quality source rocks, likely type B organofacies of Pepper & Corvi (1995). The Pujamana Formation of middle-late Turonian age on the other hand corresponds to organic-lean rocks deposited under oxic to disoxyc conditions and likely type C/D organofacies of Pepper & Corvi (1995), suggesting that these rocks have a lower hydrocarbons generation potential. Additionally, the La Paja-Tablazo interval (Barremian-Lower Albian) serves as source rock as it is proved by rock-oil correlations of lower Cretaceous rock extracts and oils

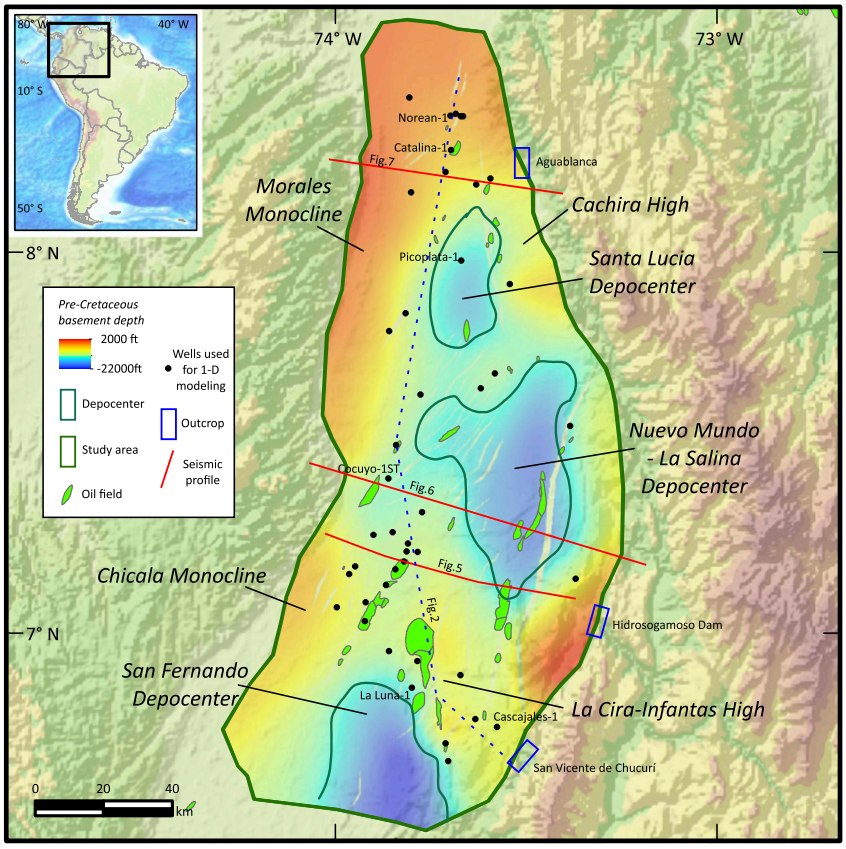

FIGURE 1
Location of the study area. Selected wells, composite seismic data, depocenters, and structural highs are also shown.

found in Cretaceous and Cenozoic rock reservoirs of the MMVB (Rangel et al., 2017; Thompson-Butler et al., 2019). This interval was also deposited under anoxic conditions enhancing organic carbon accumulation and preservation (Gaona-Narvaez et al., 2013; Jimenez et al., 2015).

Finally, the main reservoirs in the MMVB are the La Paz and Mugrosa formation and, to a lesser extent, the Lisama and Umir formations. Also, commercial reservoirs exist in the Galembo-La Renta, Salada, and Rosa Blanca formations. In the same way, the Simiti, Umir, and Colorado formations are considered regional seals, although internal local seals are also present within the reservoirs.

3 Materials and methods

This study presents an integration of a large-scale 2D seismic reflection dataset with borehole data, comprising of 7,640 km of 2D seismic data and forty-one wells, including lithological descriptions, biostratigraphic data, and velocity surveys, as well as electric logs and datasets of 1,500 X-Ray Diffraction samples (XRD), and 5,000 source rock geochemical data including vitrinite reflectance (%Ro), total organic matter (TOC), and pyrolysis. The subsurface data were primarily sourced from the Banco de Información Petrolera. The research follows a petroleum systems analysis workflow, comprising of seismic interpretation, petrophysical modeling, basin modeling, source-rock characterization, pore pressure analysis, and fracture systems characterization. The study aims to model hydrocarbon generation and predict the volumes of retained hydrocarbons, the Gas-Oil Ratio (GOR), porosity, thermal maturities in order to define sweetspots for unconventional exploration in the basin. The software used in this research include the Zetaware software suite, Techlog v2022, Petrel v2022, and Petromod v2022.

3.1 Seismic interpretation and curvature analysis

This study used three hundred 2D seismic-reflection lines in TWT to construct the regional structural framework, including the basement and key stratigraphic units. The data from thirty-five wells were tied using check-shot surveys, and data from neighboring wells were used to supplement any missing information.

The study also used lithological descriptions and stratigraphic ages from the boreholes to assign approximate ages to the marker horizons. Faults were also identified from seismic and well data. The time-to-depth conversion was done using interval velocities from check-shot surveys and synthetic seismograms. Quality control was

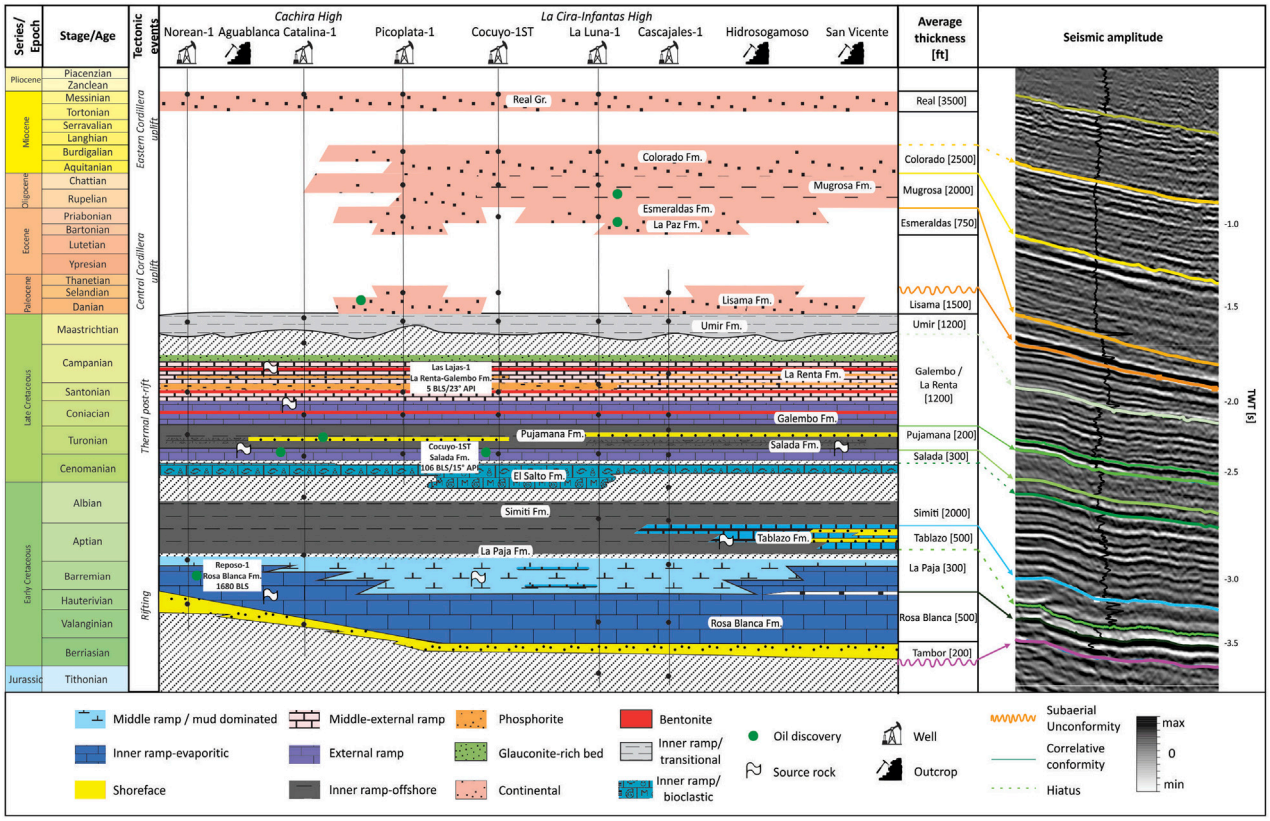

FIGURE 2
Representative stratigraphic chart of the Middle Magdalena Valley Basin. Based on geologic descriptions, tectonic events, and petroleum system elements by Morales (1958), Ramón et al. (1997), Gomez et al. (2005), Thompson-Butler et al. (2019), and Etayo-Serna (2019a). Correlation with seismic reflection data of the study area and the interpreted seismic units are shown.

performed by checking the seismic marker horizons against well tops from logs not initially involved in the interpretation, and isopach maps were created to provide a regional overview on the location of the depocenters and main structural features.

The depth structural maps obtained from the seismic interpretation were integrated into the basin modeling, and also for the analysis of strain and fractures on structural surfaces. This analysis employed the methodology proposed by Suo et al. (2012), which posits that the density and orientation of fractures are related to the curvature of a structural surface. Specifically, it states that as the curvature of a structure increases, the number of fractures also increases.

3.2 Petrophysics

Forty-one wells with triple-combo logs were evaluated to obtain petrophysical properties, including lithology, porosity, and permeability. Total organic carbon (TOC) content was estimated using mathematical models based on well-log measurements. For instance, TOC content was estimated from uranium concentrations as measured from spectral gamma ray, which involves a model based on the relationship between the uranium concentration and TOC (Fertl and Rieke, 1980). Correlations to bulk density measurements were also used, using a model that relates the bulk density of the formation to TOC (Schmoker & Hester, 1983). In addition, the mathematical model which describes the correspondence of the compressional transit time with deep resistivity (Delta log R method), was also used as a related parameter to TOC (Passey et al., 1990). Finally, the validity of the values derived from petrophysical calculations was assessed by comparison to TOC contents determined via Rock-Eval pyrolysis or LECO carbon analyzer.

A probabilistic multimineral model was applied (i.e., Quanti-Elan ®) to determine rock mineralogy and clay volumes. The Quanti-Elan model uses well logs (e.g., density, photoelectric factor, sonic, neutron, gamma ray), XRD and TOC datasets to quantify the different minerals such as quartz, carbonates, phosphates, pyrite, and clays, applying multivariate statistical methods and providing a range of probabilities for each estimated mineral type rather than a deterministic answer (Ali et al., 2022). The multimineral model and the TOC estimation are necessary to calculate effective porosity, and organic porosity. We applied Galford et al. (2013) and Alfred & Vernik (2013) methods for organic porosity estimation, constrained with pyrolysis datasets, which measure the pore spaces created by thermal maturation and conversion of the organic matter into hydrocarbons within source-rock reservoirs.

The brittleness, or ability of a rock to fracture, is a valuable criterion in predicting enhanced productive intervals or areas. The Upper Cretaceous rocks were characterized based on a mineral-based brittleness index, proposed by Wang & Gale (2009), including borehole and outcrop data. Finally, evaluation of the geopressures on most of the wells were carried out establish the presence and distribution of overpressures in the basin, integrating drilling mud-weight data and well logs following Grauls' (1999) method, in order to evaluate the sealing risks for unconventionals prospectivity in the basin.

3.3 Basin modeling

We used one-dimensional (1D) and three-dimensional (3D) models to understand how rock properties in the basin changed over time and to identify the best areas for potential production from source-rock reservoirs (sweet spots). Forty-one 1D models in the MMVB were made to evaluate changes in source-rock properties, geohistory, and thermal maturity trends during the basin evolution. These results were combined and used to calibrate a 3D geological model of the Cretaceous-Cenozoic succession to create a 3D petroleum systems model.

Subsidence analysis helps to account for how the rocks in a basin have been buried or heated over time and how deformation has affected the basin structure (e.g., Hantschel and Kauerauf, 2009). We used subsidence analysis (backstripping) to reconstruct the basin's evolution from the Cretaceous to the present day, considering sediment compaction and variations in paleobathymetry or paleotopography (Allen & Allen, 2013). From seismic interpretation and subsidence curves, erosion maps were estimated to include the eroded thicknesses of the stratigraphic units in the basin modeling Stratigraphic names, ages, unconformities, and time gaps correspond to Morales (1958), Gomez et al. (2005), Caballero et al. (2013), Sarmiento-Rojas (2019), Bayona (2018) and Etayo et al. (2019a) proposals.

We applied inverse modeling to the regional burial history model, allowing for the reconstruction of the basin time-temperature history. Inverse modeling involves using observed data to infer the underlying parameters of a geological model. For example, the use of present-day surface temperatures, paleolatitude and paleoglobal mean surface datasets, and crustal models. Based on average yearly temperature observations from the IDEAM (2022), the calculations of present-day surface temperatures are around 26 °C. To estimate paleo-temperatures, as described by Beardsmore & Cull (2001), we included paleolatitude and paleoglobal mean surface temperature datasets (e.g., Scotese et al., 1988). Also, we used crustal models to estimate the lower thermal boundary conditions of the sedimentary basin at the present day and through time. The Pre-Cretaceous basement structure is based on the Barrera-Lopez et al. (2022) model, which proposed a crustal thickness map based on geophysical and geomorphological data for northern South America, allowing us to use an average total lithospheric thickness of 120 km (to the 1,330°C isotherm). In the same way, a transient heat flow was considered to estimate the heat flow in the study area, because heat flow affects thermal maturation of the source rocks and thus the generation of hydrocarbons (e.g., Beardsmore & Cull, 2001). We also considered the role of lithospheric extension in the basin's thermal history, which only had a minor influence, since modeled crustal extension factors from wells were consistent with Early Cretaceous β values close 1.2 (Sarmiento-Rojas et al., 2001).

Forward modeling is a valuable method to address the physical properties of a basin involving the simulation of various scenarios to generate geological parameters (e.g., density, porosity, velocity) and iteratively adjusting the input parameters of the simulation until the simulated results match the observed data as closely as possible, also evaluating the reliability of the model. Lithologies for each formation were estimated based on individual wire-line log data analysis, cuttings, core descriptions, and well completion reports applying inverse modeling. Also, the lithologies and burial history were calibrated with density and/or sonic logs, and the effective porosity calculation from petrophysics. (Figure 3). The thermal histories of all 1-D models were calibrated using present-day corrected temperature data (e.g., Holgate and Gerner, 2010) and maturity indicators, including vitrinite reflectance (Ro) and Tmax. The %Ro suppression within MMVB sediments was not apparent in the available data as other authors previously mentioned (e.g., García-Gonzalez & Carvajal, 2006), and it is possible to have measurements in solid bitumen which require proper conversions to equivalent Ro (Juliao-Lemus et al., 2015), to calculate accurate paleotemperatures.

3.4 Source-rock properties

The 3D petroleum systems model for the Salada, Pujamana, Galembo and La Renta Formations also includes the estimation of the source-rock properties such as quantity and quality of the organic matter. These formations are formed up of a combination of lithologies, nomenclature broadly explained in Terraza-Melo (2019), including: phosphorites (TOC 2-3 wt%), mudstones (TOC 0.5–3 wt%), shales (TOC 0.5-1 wt%), and wackestones (TOC 0.5–3 wt%), which together create a continuum of possible source rocks with TOC values ranging from less than 1 to greater than 7 wt% (Figure 4). The hydrogen index (IH) of these rocks' ranges from 150 mg HC/g TOC to 700 mg HC/g TOC and its organofacies are described below (Section 3.4) (Figure 4).

As additional inputs to the petroleum systems model, we used an updated dataset for the MMVB, including open file TOC, rock-eval pyrolysis, and Ro data (e.g., Aguilera et al., 2010), the TOC and hydrogen index (HI) to determine properties for each source rock (Figure 4). Using measured maturity data and the suitable kinetics based on the kerogen type, as mentioned in the following section, the HIo values—which indicate the original HI of the source rock before the start of kerogen transformation—were approximated from current values.

3.5 Source rock kinetics

Modeling the kinetics of kerogen pyrolysis approximates the thermal decomposition of organic matter in source rocks, which is a key process in the generation of hydrocarbons (Pepper & Corvi, 1995). Using pyrolysis measurements, Aguilera (2022) created source-rock kinetics specific to the Cretaceous source rocks of the MMVB, using the non-linear regressions for different kerogens in Canadian basins proposed by Cheng & Jiang (2015). Most of the organic matter in the Galembo-La

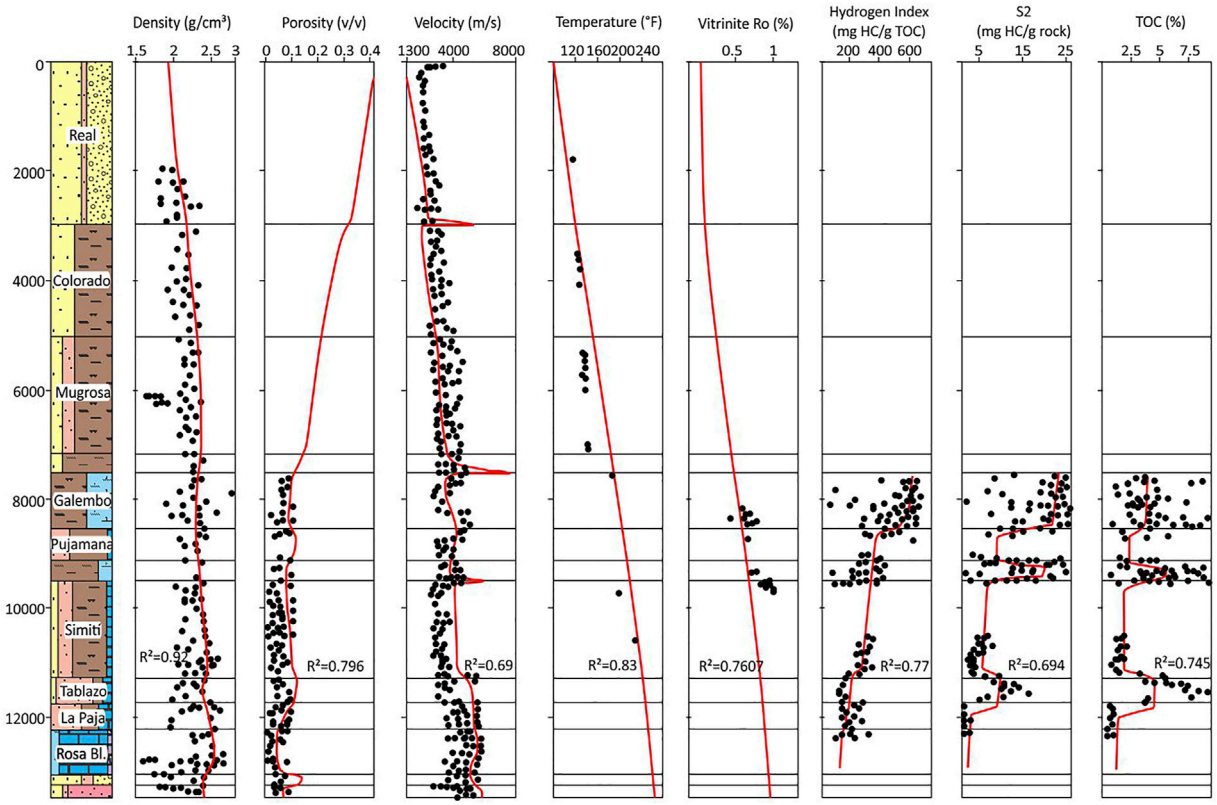

FIGURE 3
Example of forward modeling with well log data calibration for compaction, thermal and geochemical parameters for 1D models in the study area.

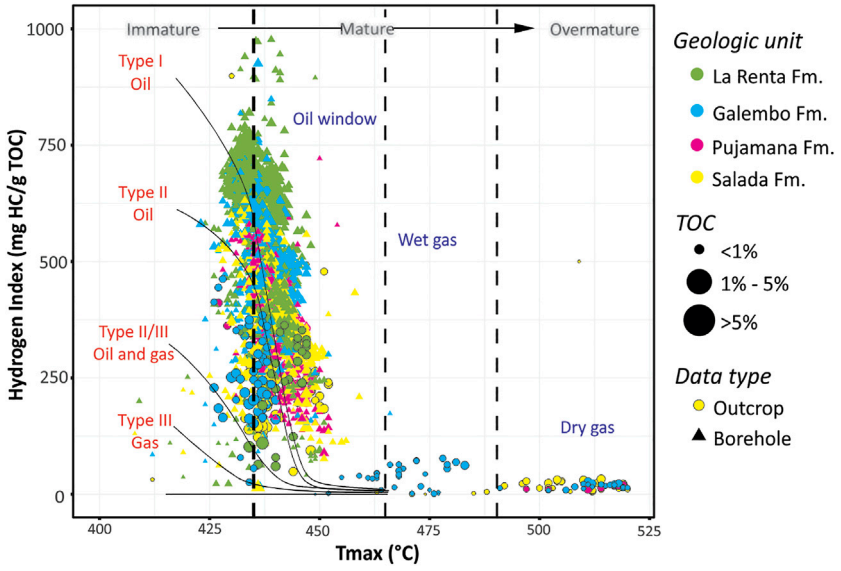

FIGURE 4
Plot of pyrolysis temperature (Tmax) versus hydrogen index (HI) and total organic content (TOC) for the Salada, Pujamana, Galembo and La Renta formations in the study area, that shows present-day kerogen quality and thermal maturity stages.

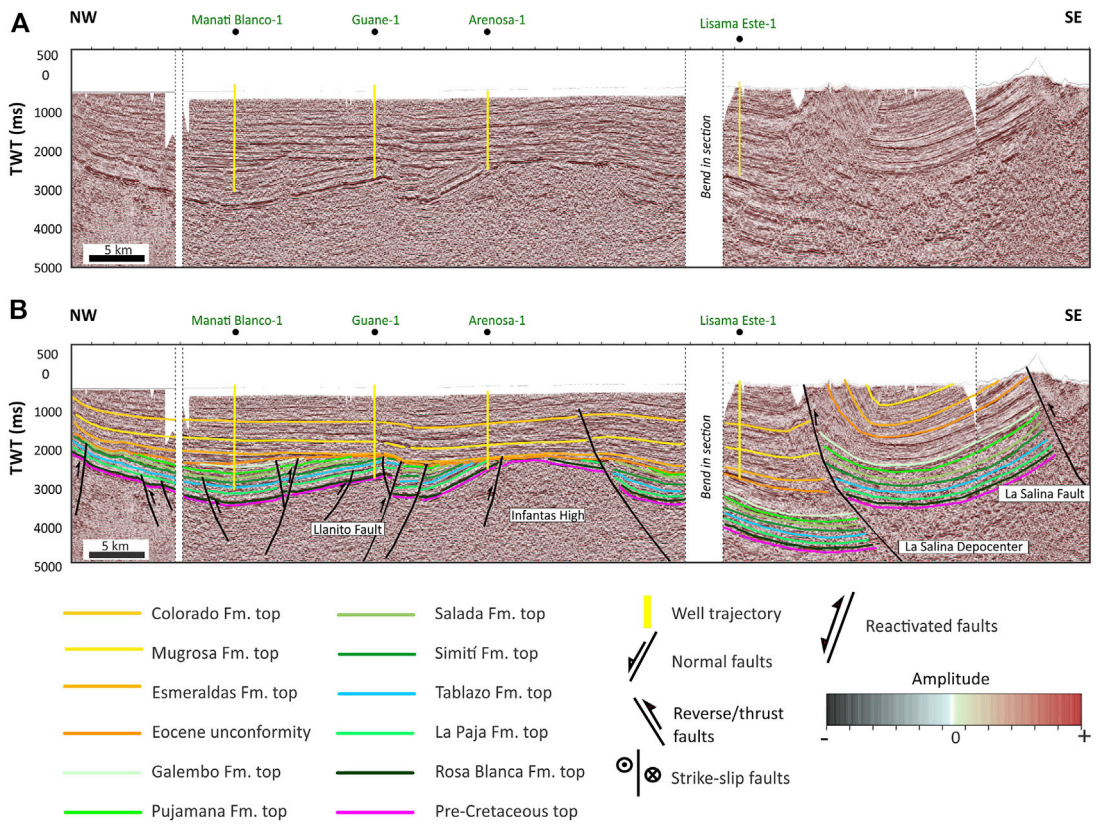

FIGURE 5
Composite seismic line traversing the Middle Magdalena Valley Basin (location in Figure 1). **(A)** Uninterpreted seismic line tied with wells. **(B)** Interpreted composite seismic line highlighting the Infantas High and the La Salina-Nuevo Mundo Depocenter.

Renta, Pujamana, and Salada is marine, following Pepper and Corvi's (1995) organofacies type B, and only a minor fraction is terrigenous non-marine, under Pepper & Corvi's (1995) organofacies types D and E.

3.6 Expulsion and retention

In order to model the volume of hydrocarbons expelled per unit area, additional data on rock density and sorption capacity were needed. The density of the inorganic rock matrix, the amount of organic matter, and the fluid contained in the pore spaces all influence bulk density, which in turn, depends on both organic and inorganic porosity. In this study, average values calculated from petrophysical estimations were applied for all three source rocks modeled. Also, adsorption models were used to describe the mass of hydrocarbons released into the free pore space of the source rock.

4 Results

4.1 Seismic interpretation and curvature analysis

The seismic succession was subdivided into eleven (11) seismic units, from the pre-Cretaceous basement to the Colorado Formation (Figure 2). The succession above the pre-Cretaceous basement is thickening southward and eastward, reaching its maximum thickness of 5.0 s TWT (ca. 7,200 m) within the Nuevo Mundo–La Salina Depocenter (NM-LSD) and 4.5 s TWT (ca. 4,800 m) within the Santa Lucia Depocenter (SLD). Northward and westward, the succession thins to a minimum thickness of 0.5 s TWT (ca. 300 m), where the basement forms the so-called Chimichagua Platform (Reyes et al., 2004), which separates the Lower Magdalena Valley Basin. The seismic units are interpreted to be deposited between the Cretaceous and Neogene based on biostratigraphic data from outcrops and boreholes (Figure 2).

The 2D seismic profiles (e.g., Figures 5–7) show pre-Eocene structures beneath the Paleogene and Neogene sediments. Most of these structures appear to be beveled and eroded before the deposition of Eocene sediments (e.g., La Cira-Infantas High, Figure 5). Also, it preserves high-angle reverse faults and east-verging fault-propagation folds cored by the basement (e.g., Figure 6). The Salina Fault System forms the western boundary of the NM-LSD (e.g., Figure 5) and suggests pre-Andean deformation related to early phases of uplifting of the Eastern Cordillera (Sarmiento-Rojas et al., 2001). Also, the seismic profiles show a progressive onlap of Cenozoic units onto the Central Cordillera basement. The timing of the Central Cordillera's uplift is evidenced in the Morales Monocline (MM) and the Cachira High (CH), which appears to occur before the

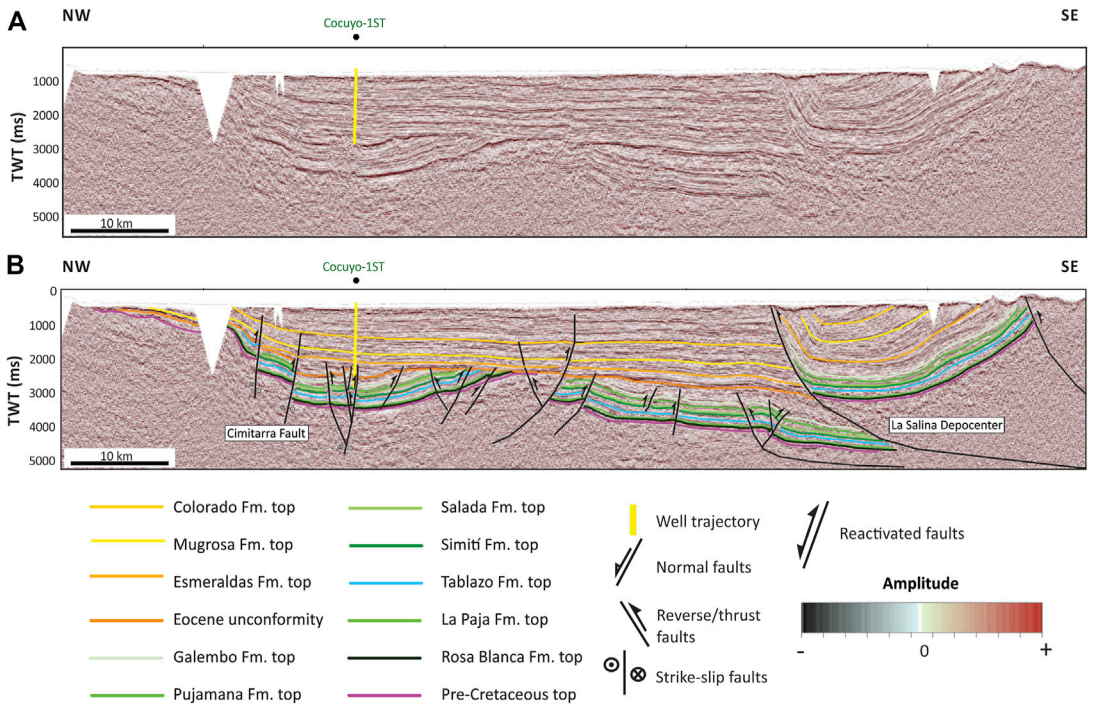

FIGURE 6
Composite seismic line traversing the Middle Magdalena Valley Basin (location in Figure 1). **(A)** Uninterpreted seismic line tied with wells. **(B)** Interpreted composite seismic line highlighting the Cimitarra Fault and and the northern part of the La Salina-Nuevo Mundo Depocenter.

Paleocene, our observations are consistent with several proposals for the study area (e.g., Suarez et al., 2000; Gomez et al., 2003; Parra et al., 2012; Cortes et al., 2022).

Figure 8 shows selected structural and isopach maps of the Galembo, Pujamana, and Salada formations. This allows us to propose three structural domains in the MMVB. To the south, the structural domain is evidenced by the presence of reactivated north-south oriented inversion faults associated with the uplift of the Eastern Cordillera, which includes oil fields such as La Cira-Infantas, Lisama, and Provincia. In the central domain, there is evidence of northeast-southwest transpressive faults associated with structural inversion, including oil fields such as Casabe, Llanito, Cantagallo, Garzas, and Cristalina. Finally, in the northern domain, there is evidence of strike-slip faults associated with the uplift of the Central Cordillera, including oil fields such as Doña Maria, Totumal, Ayombero, and Crisol. The isopach maps reveal that the Pujamana and Salada Formations are thicker in the southern and central domains than in the northern domain. However, the thickness of the Galembo Formation increases in the northern domain and could be related to increasing accommodation space due to the uplifting of the Central Cordillera.

García-Delgado & Velandia (2020) studied the tectonic geomorphology of the northern part of the Central Cordillera, the San Lucas Range, proposing two regional domains related to the Palestina Fault. Our results agree with their model since interpreted seismic reveals that most of the faults in the Central Cordillera could be mapped on the subsurface of the MMVB and have right-lateral kinematics (e.g., Cimitarra and Las Brisas faults). Also, our model is an alternative to the proposal of Guerrero et al. (2021), who considers the Cimitarra and Casabe faults as structures related to the Eastern Cordillera.

The best production values in several worldwide basins (e.g., Western Gulf Basin) are in areas with high natural fractures (Ramirez & Aguilera, 2014). Figure 9 presents the results of the curvature analysis for the Galembo, Pujamana, and Salada Formations. The maps reveal areas with higher and lower probability of the existence of natural fracture systems. The NM-LSD and the Cachira High have areas with a higher probability of natural fractures. For example, the Chuira field near the Cachira High has 16% porosity related to natural fracture systems (Acevedo et al., 2012a). On the other hand, the Morales Monocline, the San Fernando Depocenter, and the La Cira-Infantas High are areas with a lower probability of naturally induced fractures.

4.2 Petrophysics and pore pressure analysis

The petrophysical modeling allows us to suggest the Galembo, Pujamana, and Salada Formations' lithology based on quartz-feldspar-mica, carbonate, and clay content (Figure 10). We mapped these distributions to assess the lateral variations of the source rocks. Notably, the Salada Formation has carbonate contents in areas neighboring the SLD and the La Cira-Infantas High between 0.5 v/v and 1.0 v/v. This contrasts with the carbonate content of the Pujamana Formation, which in all study area is below 0.3 v/v, with small areas of the Chimichagua Platform containing values of 0.5 v/v. The Galembo Formation has carbonate contents ranging between 0.3 v/v and 0.5 v/v. For all three units, neighboring areas around the

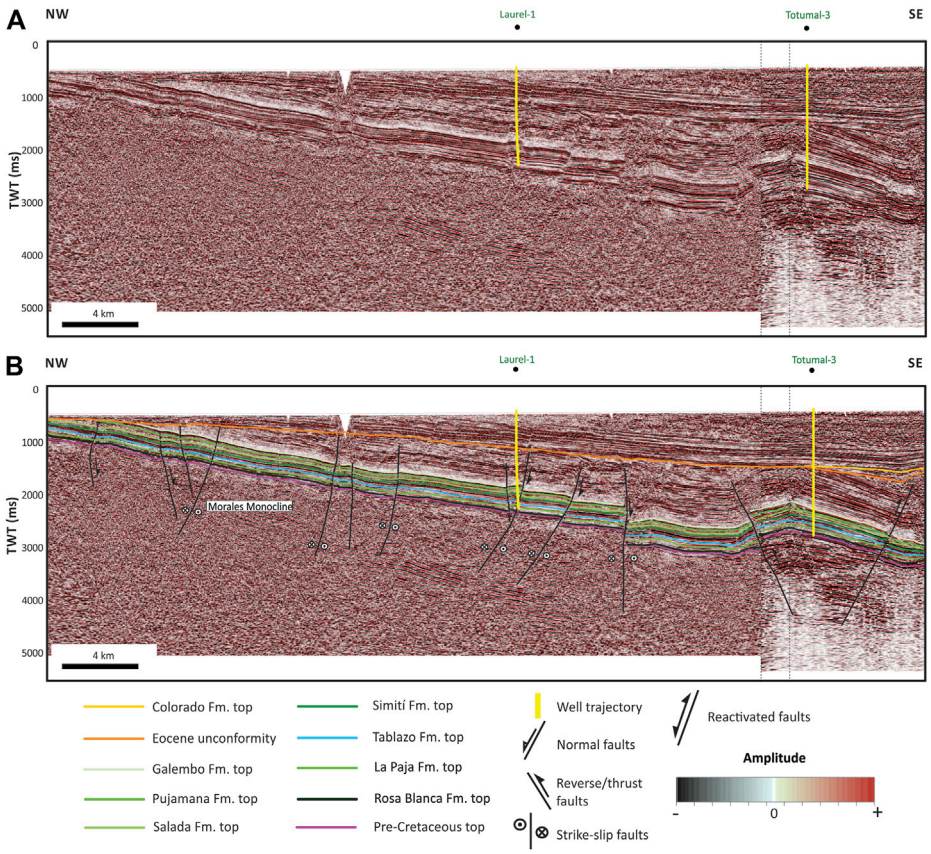

FIGURE 7
Composite seismic line traversing the Middle Magdalena Valley Basin (location in Figure 1). **(A)** Uninterpreted seismic line tied with wells. **(B)** Interpreted composite seismic line highlighting the Morales Monocline and the Totumal Field.

San Fernando Depocenter contain quartz-feldspar-mica contents between 0.4 v/v and 0.7 v/v. Also, the Galembo and Pujamana Formations have quartz-feldspar-mica contents between 0.4 v/v and 0.6 v/v in the SLD. Finally, the Pujamana Formation has the highest contents of clays, between 0.4 v/v and 0.7 v/v in most of the study area. As an alternate petrophysical mineral model, Rojas et al. (2013) applied conventional models, which include the apparent grain density (DGA), and the apparent volumetric photoelectric factor (UMA), obtaining results consistent with our proposal, despite having a limited well log and XRD dataset.

In the same way, Figure 11 presents XRD datasets plotted in a ternary diagram (Gamero-Diaz et al., 2013) of quartz-feldspar-mica, clay, and carbonates content, comparing the MMVB source rocks with worldwide shale plays from Bromhead et al. (2017) and Mews et al. (2019). Petrographic data suggest that most of the quartz in this source rocks is related to diagenetic processes rather than its depositional environment (e.g., Acevedo et al., 2012a; Galvis-Portilla et al., 2014). In all cases, clays content is lower than 40%, suggesting, that most of the units have an excellent brittleness quality which might help in future completion designs, also agreeing previously published petrophysical models which proposes at least two landing zones within the Salada and Galembo formations (e.g., Piedrahita and Aguilera, 2017a; Veiga et al., 2023). Perez et al. (2014) presented an XRD dataset of the La Luna-1 well, showing the composition of clay minerals. Their results show that illite and interstratified species compose the bulk of the clay minerals and have lesser proportions of kaolinite. However, future research in other boreholes of the basin is required to understand the composition of clay minerals and unveil their depositional and diagenetic history.

The effective porosity in the studied source rocks ranges between 2% to 12%. The La Renta Formation has the higher porosities which range between 5% to 12%. Considering this, the La Renta Formation is a probable carrier bed, despite not being modeled as an independent source rock from the Galembo Formation. We estimated TOC and organic porosity from well logs, revealing that organic porosity values range from 0.0006 v/v to 0.002 v/v for all three formations, implying low levels of organic matter conversion (Jarvie, 2014). When compared to worldwide shale plays (e.g., Barnett Shale), the estimations for the MMVB are quite low, because organic porosity values range from 0.01 v/v to 0.04 v/v (Romero-Sarmiento et al., 2013). However, our results are comparable with those obtained by Piedrahita & Aguilera (2017a, 2017b) in the study area, who used different well log estimations to obtain kerogen density and organic porosity. Also, our results match those obtained by Aguilera (2022), who applied Chen & Jiang's (2016) methodology for organic porosity estimations from pyrolysis

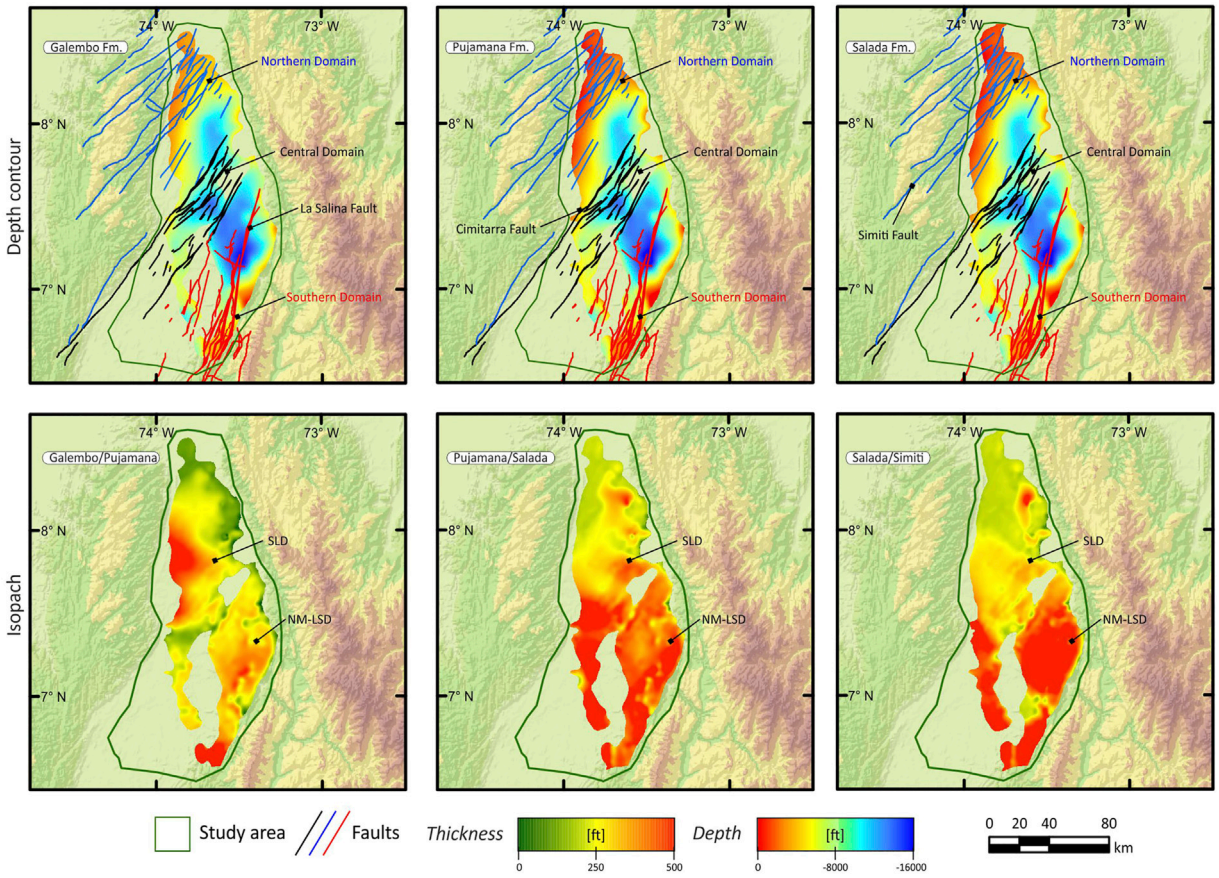

FIGURE 8
Depth contour and isopach maps (in feet) of the Salada, Pujamana and Galembo formations in the Middle Magdalena Valley Basin. The maps show the thickness trends of the source rocks from the seismic interpretation as well as the main depocenters in the study area.

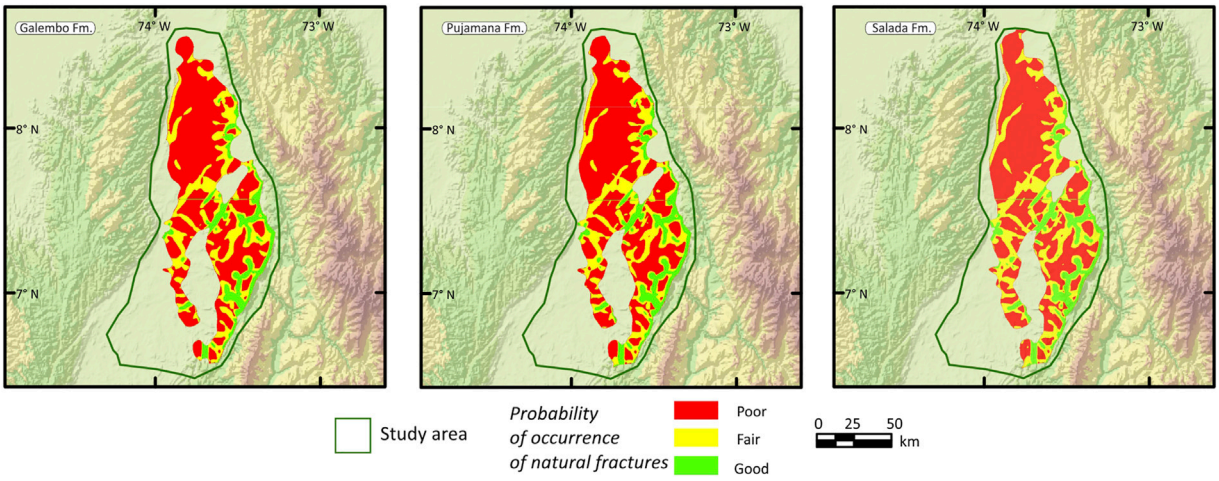

FIGURE 9
Probability of occurrence of natural fractures maps of the Salada, Pujamana, and Galembo formations in the Middle Magdalena Valley Basin.

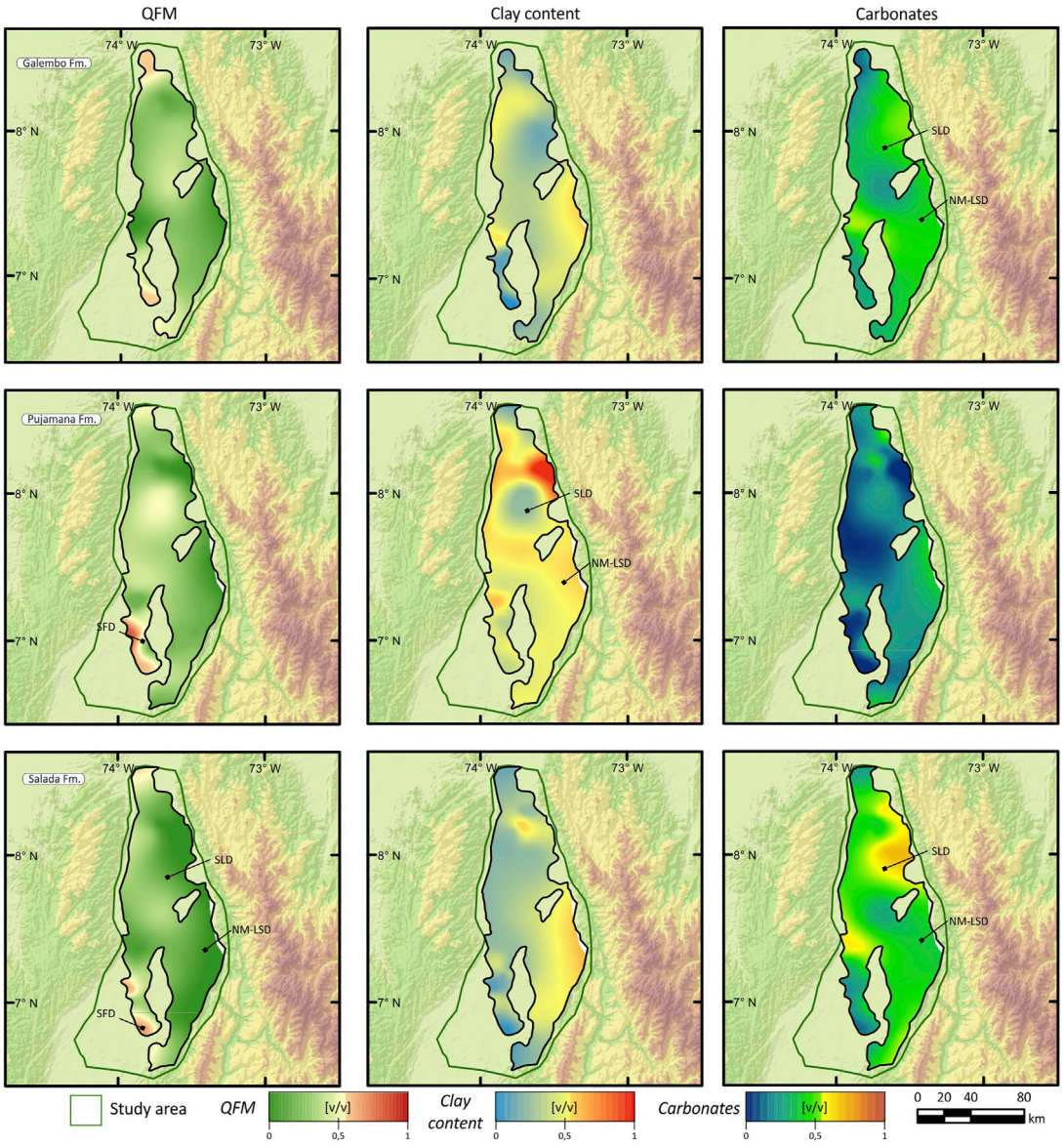

FIGURE 10
Quartz-Feldspar-Micas (QFM), clays and carbonates content maps from petrophysical modeling of the Salada, Pujamana, and Galembo formations in the Middle Magdalena Valley Basin.

datasets, and to Ceron et al. (2013) estimations using digital rock physics. Finally, should be expected higher organic porosity values in deeper parts of the study area.

The overpressure increases the production drive of liquid hydrocarbons and favors higher production rates (Gong & Rodriguez, 2017) but also is a sign of sealing integrity and capacity. As a first approach, the pore pressure analysis helps screen overpressure intervals and allows us to map the distribution of areas with low pore pressure, which might become a risk for the source-rock play (see Section 5.1). We observed two areas with low pore pressure conditions: First, areas with structures beveled by unconformities (e.g., La Cira-Infantas High), and second, areas with low overburden (e.g., Morales Monocline). Our results are consistent with those obtained by Vargas-Silva et al. (2019), revealing that factors such as water expansion have a negligible effect on the pore pressure in the basin. Although thermal stress and oil and gas generation have limited influence on the pore pressure estimation at the wells, with most of the effect related to compaction pressure, its effects could increase overpressure in deeper areas and be observed in the predicted GOR (see Section 4.5).

4.3 Heat flow and burial modeling

Progressive burial of the strata during the basin infill process promotes physical changes in rock properties, reducing their porosity and permeabilities in contrast to increasing density,

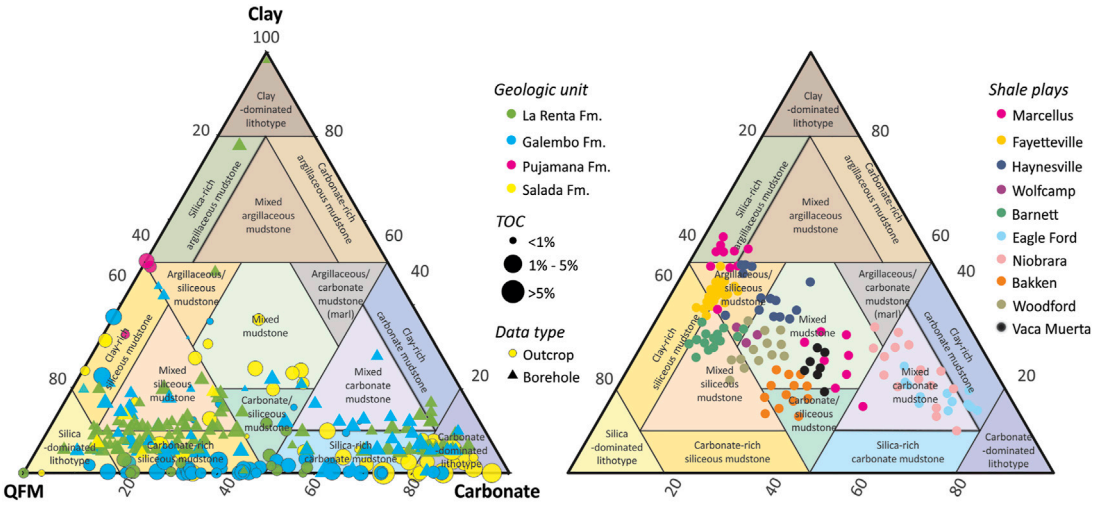

FIGURE 11
Ternary diagram of QFM, carbonates and clays content from XRD datasets of the Salada, Pujamana, Galembo and La Renta formations in the Middle Magdalena Valley Basin, and its comparison with worldwide shale plays.

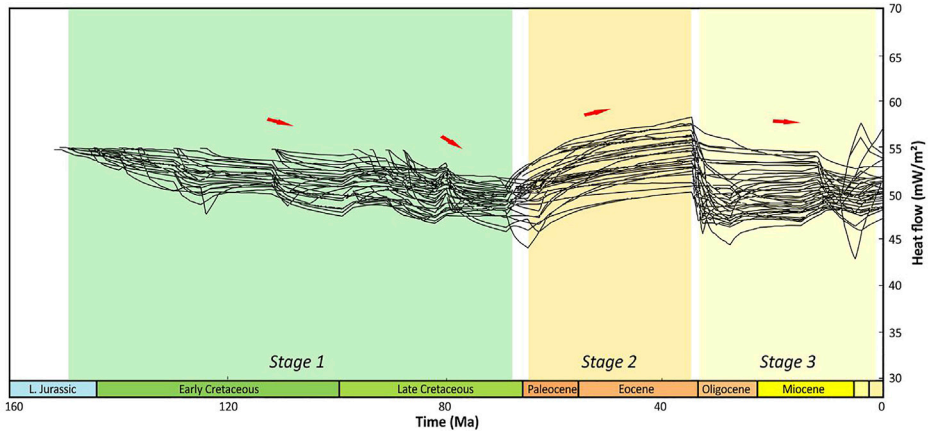

FIGURE 12
Basal heat flow variation along time from forty-one 1D models in the Middle Magdalena Valley Basin. Three main tectonic events in the basin are shown.

velocity, and heat capacity as the rock is buried and compacted by sediments. Athy's Law (Allen & Allen, 2013) explains these processes and allows empirical calculation based on porosity reduction as burial increases. In this way, the burial models of the wells were calibrated by comparing the porosity, velocity, and density profiles measured from well-logs and laboratory data to predicted data by modeling (Figure 3). As a result, burial modeling suggests at least two significant episodes of generation of accommodation space, which extend throughout the Cretaceous and from the Oligocene to the present day. In contrast, a major episode of erosion is recorded from the final part of the Late Cretaceous until the Eocene, widely observed using seismic lines and outcrop data (e.g., Section 4.1). From the Berriasian through the Hauterivian, the basin records an increased rate of tectonic subsidence (Tambor and Rosa Blanca formations). The La Paja and Tablazo formations, which span the Barremian to Aptian, undergo a low tectonic subsidence rate. The Simiti, Salada, Pujamana, Galembo-La Renta, and Umir formations, which range from the Albian to the Maastrichtian, show an increase in the basin's tectonic subsidence rate. Although the highest subsidence rates are recorded in the southern province (e.g., La Salina-Nuevo Mundo Depocenter), the central and northern provinces have areas with high subsidence rates (e.g., Santa Lucia Depocenter).

The heat flow modeling allows us to identify three stages of the basal heat flow history consistent with the major tectonic episodes described above, reflecting burial history (Figure 12). As an alternative to the heat flow model published by Gonzalez et al. (2020), during the Early Cretaceous, the basin setting could be

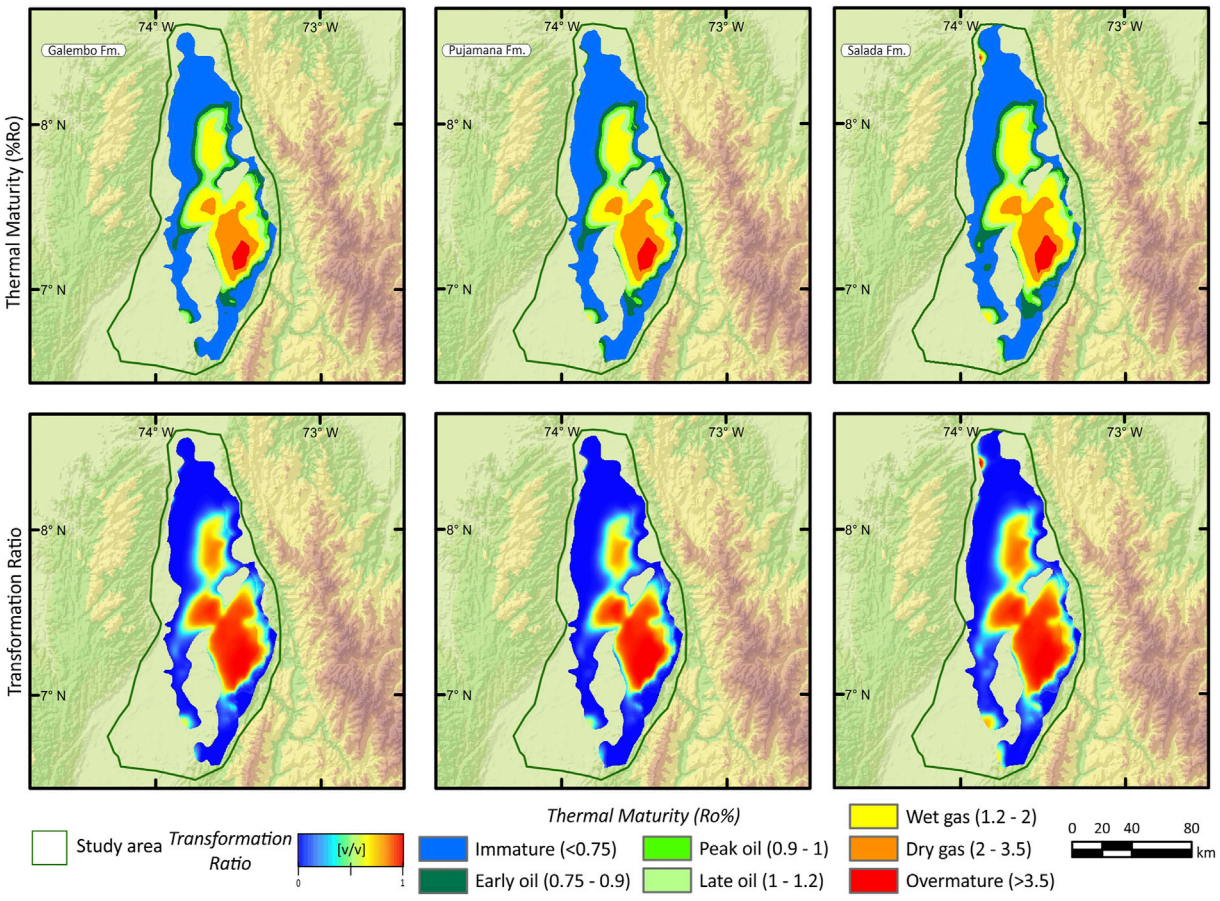

FIGURE 13
Thermal maturity (%Ro) and transformation ratio maps of the Salada, Pujamana and Galembo formations in the Middle Magdalena Valley Basin.

explained with basal heat flow values below 60 mW/m^2. Likewise, the history of basal heat flow is consistent with the subsidence history of the basin proposed by authors such as Sarmiento-Rojas et al. (2001), who suggest that the stretching factors (β) for the basin are very low (≈1.2).

4.4 Hydrocarbon generation

4.4.1 Transformation ratio

Figure 13 compares the transformation ratio and the modeled thermal maturity. The source-rock transformation ratios are quite different in the SLD and NM-LSD. The highest transformation ratios were reached in the NM-LSD, ranging between 70% to 100% (wet-gas window to overmature) for the Galembo, Pujamana, and Salada Formations. In the SLD, the highest transformation ratios range between 50% to 80% (peak-oil to the wet-gas window). The variation in the transformation ratio between depocenters is controlled by the maximum burial depth. However, the number of boreholes drilled in the depocenters is low to compare the transformation ratios' variations properly. In the same way, there is a need for more data to evaluate the effects of crustal radiogenic heat production and the conductivity of coals within the Cenozoic succession, and we hope future research assesses it.

4.4.2 Total hydrocarbons generation

The estimation of generated and retained hydrocarbons from the different source rocks is based on a volumetric material balance controlled by the kinetics of the source rock model used, in this case Pepper and Corvi's (1995) organofacies models, according to its kerogen type and thermal maturity levels reached during the maturation process. From these models an estimation of the hydrocarbons, generated and expelled, is made and a retained volume of hydrocarbons is obtained (liquid and gas phases), volume that is controlled by the organic porosity wettability, adsorption and absorption of the rock matrix, and the progressive transformation of kerogen into hydrocarbons with increasing temperature.

The total generation potential of all modeled Upper Cretaceous rocks in the MMVB is approximately 163.63 billion BOE (Table 1). Critical factors affecting total generation potential include source-rock quality and thermal maturity. The extent of the Upper Cretaceous generation pod is consistent with the location of major conventional fields (Figure 14).

TABLE 1 Total retained and generated hydrocarbons of the Upper Cretaceous rocks in the MMVB.

Source rock	Gas retained (Tcf)	Liquid retained (Bbbl)	Gas retained (Tcf)[a]	Liquid retained (Bbbl)[a]	Total HC generated (billion BOE)	Average GOR (scf/bbl)
Galembo Fm	8.30	23.53	1.24	3.52	48,77	1,508
Pujamana Fm	8.0	10.96	1.2	1.64	44,69	1,371
Salada Fm	11.82	18.6	1.77	2.79	70,16	1,577
Total	28.12	53.09	4.21	7.95	163,63	4,456

[a]After a 15% recovery factor.

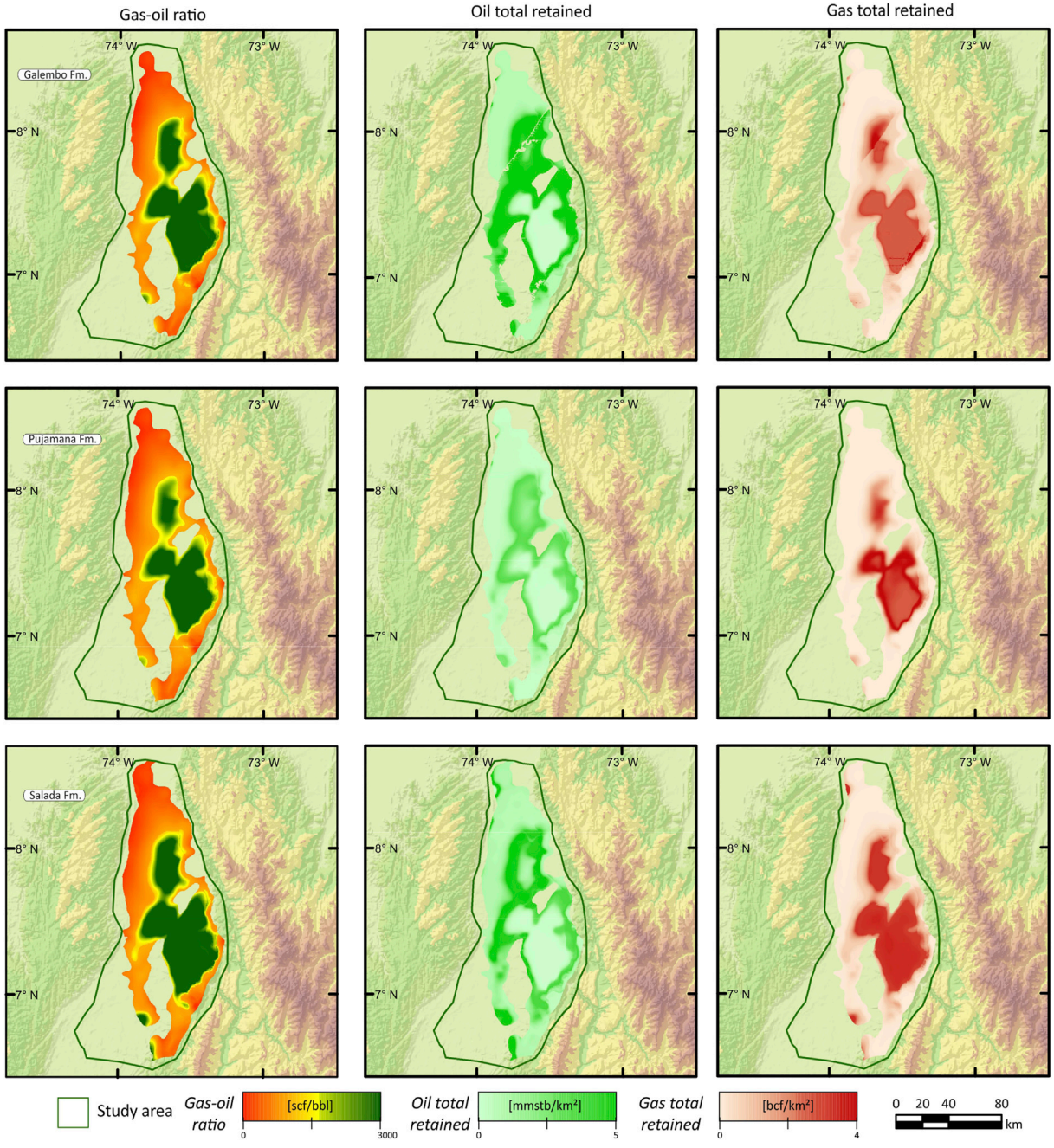

FIGURE 14
Gas-oil ratio (GOR), oil total retained, gas total retained maps of the Salada, Pujamana and Galembo formations in the Middle Magdalena Valley Basin.

TABLE 2 Cut-off values to rank sweet spot areas in the MMVB.

Criteria	No *sweet spot*	Fair	Good
Effective porosity (%)	≤2%	2%–5%	≥5%
Transformation ratio (fraction)	≤0,2	0,2–0,5	≥0,5
GOR (scf/bbl)	≤1,000	≥1,000	
Liquid retained (Bbbl/km^2)	≤1,0	1,0–5,0	≥5,0
Gas retained (Bcf/km^2)	≤0,5	≥0,5	

Determining the relative hydrocarbon quantities expelled by each source rock depends on several other critical variables, including organofacies. For example, Aguilera (2022) observed similar HIo values between Lower and Upper Cretaceous rocks (HIo 600–750 mg HC/g TOC). However, Lower Cretaceous seem to have affinity with lower quality Pepper and Corvi' (1995) B/D/E organofacies. The Upper Cretaceous rocks have a lower maturity trend and organofacies with a lesser proportion of terrigenous organic matter, which increases the volume of hydrocarbons expelled compared with the Lower Cretaceous source rocks.

The thermal maturity influences the total hydrocarbons generated because the Galembo, Pujamana, and Salada formations reached higher transformation ratios in the depocenters than in less mature margins of the basin. Although hydrocarbon generation began in the Late Cretaceous, most of the generation occurred in the Neogene, coincident with the maximum burial depth as earlier studies suggest (e.g., Gonzalez et al., 2020).

4.5 Retained hydrocarbons

The basin modeling total liquid and gas retained from the Upper Cretaceous source rocks of the MMVB are estimated at 7.95 Bbbl and 4.21 Tcf, after a 15% recovery factor respectively. Most liquids and gas retained are in the Galembo and Salada Formations rather than the Pujamana Formation (Figure 14). Although the results from this study are comparable with those from Mora et al. (2018), with modeled volumes of a similar order of magnitude, their proposal considers the Pujamana Formation with the higher total gas retained.

The predicted GOR values range between 10–3,780 scf/bbl, suggesting that the expelled products will be primarily light oil in areas below 75% transformation ratios and gas condensates in areas with higher transformation ratios (Figure 14). Despite no unconventional well test data, conventional production data help to check the consistency of the predicted GOR. For example, oil fields neighboring the Cachira High (e.g., Totumal field) produced 130 barrels from the Galembo Formation in initial tests, but its production quickly declined. Consistent with the GOR values of approximately 600 sfc/bbl predicted by the basin modeling for such interval in that part of the basin.

The volumes of hydrocarbons retained within the source rocks suggests good potential for shale oil and gas plays. Therefore, the predicted hydrocarbon type is light oil, with some gas condensate in areas of high thermal maturity. This result is consistent with the oil and gas shows reported during drilling in most wells.

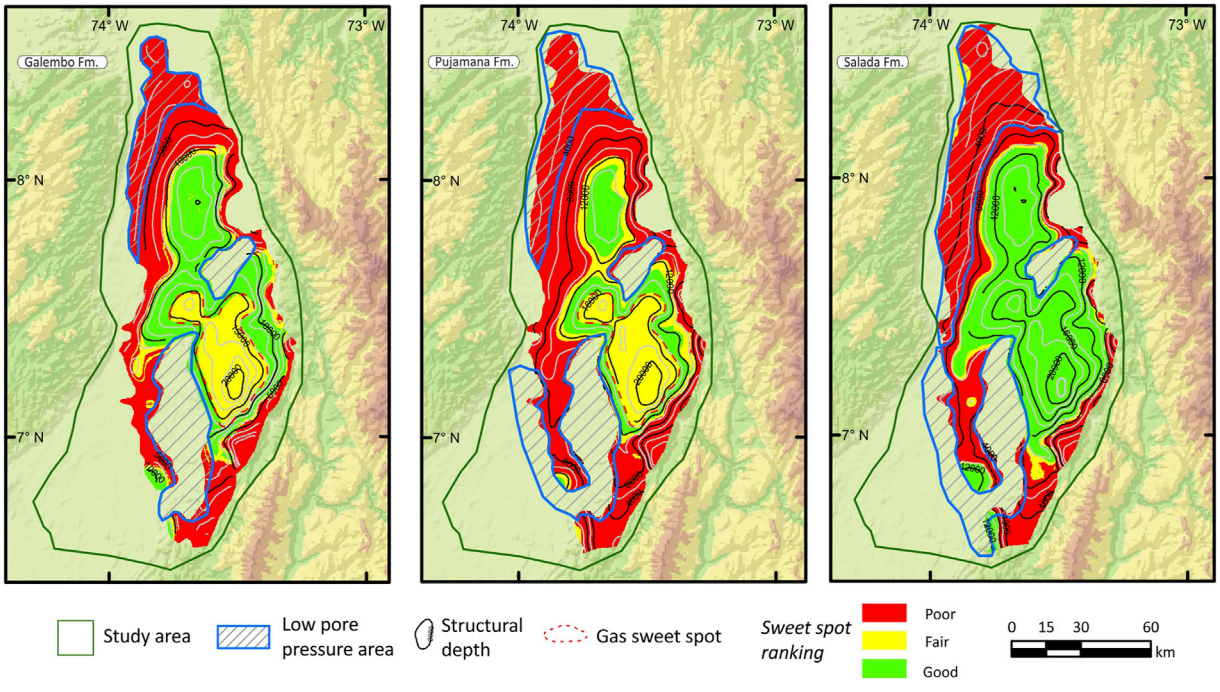

FIGURE 15
Sweet spot areas maps of the Salada, Pujamana, and Galembo formations in the Middle Magdalena Valley Basin. Low pore pressure areas and structural depth contours (in feet) are also shown.

Several authors mentioned solid bitumen remnants and extensive asphaltites within the Upper Cretaceous rocks' outcrops of the study area and boreholes drilled near the Cachira High (e.g., Acevedo et al., 2012b). A plausible explanation invokes the generation of solid bitumen in the early stages of hydrocarbon generation (Juliao-Lemus et al., 2015). However, future source-rock correlations should answer this question, although the possibility of asphaltite accumulations from hydrocarbons generated in the Lower Cretaceous source rocks cannot be ruled out.

5 Discussion

5.1 Geologic factors that control the sweet-spots areas

Each basin's geology is different, and its conditions should be evaluated to propose a *sweet spot*. In this context, we define a *sweet spot* as a geographic area with expected high production values surrounded by areas with lower production values, following Shurr & Ridgley (2002) definition. This proposal differs from the *sweet spot* considered from the net-pay at a reservoir scale (e.g., Slatt et al., 2015) or economically viable areas.

After data integration and interpretation, we suggest that the *sweet spot* areas in the MMVB for the Galembo, Pujamana and Salada Formations are driven by: 1. The effective porosity. 2. The transformation ratio. 3. The total retained gas and liquid hydrocarbons. 4. The gas-oil ratio. We propose the following cut-off values to rank and reclassify each map into good, fair, or low (Table 2).

As presented before (see Section 4.1, 4.2), the mineralogical brittleness is constrained by the facies distribution, considering that all source rocks were deposited under mixed-ramp conditions, with low deposition of clay minerals. On the other hand, the thickness variation of the source rocks along the basin remains quite constant, despite areas with higher thicknesses (see Section 4.1). The probability of natural fractures (see Section 4.1), considered a criterion that would account in combination with the *sweet spot* maps, helping to screen areas that could be produced under conventional conditions. These criteria are not deemed as factors for a definition of an unconventional *sweet spot* in the MMVB at a regional scale, because they are related to more local effects related to sedimentological heterogeneity and structural deformation within the basin. Organic porosity is another geologic criterion that does not drive the sweet spot definition and is included in the effective porosity. The basin modeling and petrophysical data show that thermal maturity in the areas outside the depocenters, where most of the wells have been drilled so far in the basin, is too low to develop significant organic porosity systems (see Section 4.2).

However, published results of mercury intrusion porosimetry reveal discrete intervals within the Salada and Galembo Formations, with pore volume constituted by 0.2–5.5 nm pore sizes (Juliao-Lemus et al., 2015; Casadiego-Quintero & Rios-Reyes, 2020), that could be produced under more conventional completions (Baek & Akkutlu, 2019).

5.2 Distribution of shale oil and shale gas sweet spots

Considering geologic constraints, we present three *sweet-spot* maps for the Galembo, Pujamana, and Salada formations (Figure 15). Contours in maps represent depth contours from each stratigraphic surface, and hatched polygons are areas with an additional risk due to low pore pressure conditions (see Section 4.2). Also, when combined with curvature analysis maps, the *sweet-spot* maps highlight areas that could be produced under unconventional completions and improve conventional completions. The green areas represent a good sweet-spot area, the yellow and red areas represent fair and no sweet-spot areas, respectively.

These maps help delineate areas representing shale oil and shale gas plays. Until now, only the Picoplata-1 well was drilled in the SLD reached the Salada Formation with promising results, but its tests were conventional. Although the La Renta Formation was not included in the sweet-spot maps, future research is required to confirm if it could be considered as a carrier bed play. Future drilling in the depocenters is required to confirm the modeling results and to address its uncertainties.

6 Conclusion

This study used petroleum systems analysis to provide a regional framework for understanding unconventional hydrocarbon prospectivity of the Upper Cretaceous source rocks in the MMVB. Results have allowed to assess the spatial distribution and petroleum generation potential of Upper Cretaceous source rocks across the basin, and the likely volumes of both expelled and retained hydrocarbons. The deterministic petroleum systems model estimated the volumes of retained hydrocarbons at 7.95 Bbls of oil and 4.21 Tcf of gas after a 15% recovery factor. The combined volumes of hydrocarbons generated from the Upper Cretaceous are mapped, highlighting the broad extent of the generation pods and their consistency with the location of major conventional fields across the basin. Source rocks within the Salada and Galembo formations are the biggest contributors to both expelled and retained hydrocarbons because these are the richest, thickest, and most extensive source facies, with good to excellent potential across the entire basin. In contrast, the hydrocarbon volumes generated by the Pujamana Formation are low because its shale facies have source rocks of lower quality.

The three sweet-spot maps for the Upper Cretaceous source rocks show areas with good potential for shale oil and shale gas to be tested. In addition, the development of these resources in such areas could contribute to the energy transition of the region. However, the distribution of the sweet-spot areas reveals that the depocenters are still to be drilled to better constrain uncertainties regarding the facies and source rock quality, and to prove the economic feasibility of the unconventional play in the MMVB.

Data availability statement

The raw data supporting the conclusion of this article will be made available by the authors, without undue reservation.

Author contributions

Project design, definition of the study area and objectives: RA, OR-B, MP-R, and AP-C. Data collection: AP-C and JT. Data curation: AP-C, RA, and JT. Data interpretation and analysis of the results: All authors. Draft manuscript preparation: AP-C. All authors reviewed the results and approved the final version of the manuscript. Funding: OR-B, HF, HB and MR.

Funding

This research was funded by the National Hydrocarbon Agency (ANH) and the Colombian Geological Survey (SGC) through an inter-administrative agreement "Convenio 048 del 2021, ANH-SGC".

Acknowledgments

We are grateful to the Hydrocarbons Division and the Editorial Board of the Colombian Geological Survey for their continuous support during the preparation of this manuscript. As part of an integral project that has involved several disciplines, we thank Cristian Benavides, Hellman Pinilla, Camilo Davila, Edgar Arciniegas, Hernando Mahecha, Laura Roman, Dayra Saenz, Sebastian Hernandez, Ruth Robayo, Johan Sierra and John Ortiz for their valuable contributions. Special thanks to Luis Quiroz, Juan Carlos Ruiz, Lucila Morales, German Pardo, Juan Sebastian Eslava, Karen Rodriguez, Xiomara Prince, Daniel Rojas, Andrea Pablos, Sergio Amaya, Alberto García, Juan Manuel Herrera and Daniela Carrera, who contributed to this research during its early stages. We would like to express our sincere gratitude to the anonymous reviewers for their valuable comments and feedback.

Conflict of interest

The authors declare that the research was conducted in the absence of any commercial or financial relationships that could be construed as a potential conflict of interest.

Publisher's note

References

Acevedo, R., Daza, D., Prince, M., Rojas, D., and Sanchez, C. (2012a). An integrated approach to the exploration of fractured reservoirs: A challenge in the cretaceous rocks of the middle Magdalena Valley Basin, Colombia. *XI Simp. Boliv. Exploración Pet. las Cuencas Subandinas*. doi:10.3997/2214-4609-pdb.330.43

Acevedo, R., Daza, D., Prince, M., Rojas, D., and Sanchez, C. (2012b). Presencia de Gilsonita y bitumen en la cuenca Valle Medio del Magdalena: Un reto para la perforación exploratoria. *XI Simp. Boliv. Exploración Pet. las Cuencas Subandinas*. doi:10.3997/2214-4609-pdb.330.164

Agencia Nacional de Hidrocarburos (Anh) & Universidad Pedagógica y Tecnológica de Colombia (Uptc) (2021). *Geologic integration, petroleum system evaluation and prospectivity of Colombian frontier basins: Northern middle Magdalena and cesar-ranchería*. Technical presentation https://www.anh.gov.co/documents/3688/UPTC_ANH_VMMN_CR_GEOLOGICAL_INTEGRATION_FEB_11_2022.pdf.Retrieved from:

Aguilera, R. C., Sotelo, V. A., Burgos, C. A., Arce, C., Gómez, C., Mojica, J., et al. (2010). Organic geochemistry atlas of Colombia. *Earth Sci. Res. J.* 14, 61–77.

Aguilera, R. (2022). "Data-driven kerogen kinetics from rock-eval data of the middle Magdalena Valley Basin, Colombia," in Implications on the prospectivity of unconventionals AAPG International Conference and Exhibition, Cartagena, Colombia, March, 2022.

Alfred, D., and Vernik, L. (2013). A new petrophysical model for organic shales. *Petrophysics* 54, 240–247. SPWLA-2013-v54n3-A4.

Ali, J., Ashraf, U., Anees, A., Peng, S., Umar, M., Thanh, H., et al. (2022). Hydrocarbon potential assessment of carbonate-bearing sediments in a meyal oil field, Pakistan: Insights from logging data using machine learning and Quanti elan modeling. *ACS Omega* 7 (43), 39375–39395. doi:10.1021/acsomega.2c05759

Allen, A. A., and Allen, R. A. (2013). *Basin analysis: Principles and applications*. 3. New Jersey, United States: Wiley-Blackwell Publishing, 632. 978-0-470-67377-5.

Baek, S., and Akkutlu, Y. (2019). Produced-fluid composition redistribution in source rocks for hydrocarbon-in-place and thermodynamic recovery calculations. *SPE J.* 24, 1395–1414. doi:10.2118/195578-PA

Barrera-Lopez, C., Mooney, W., and Kaban, M. (2022). Regional geophysics of the caribbean and northern South America: Implications for tectonics. *Geochem. Geophys. Geosystems* 23, e2021GC010112. doi:10.1029/2021GC010112

Bayona, G. (2018). El inicio de la emergencia en los Andes del norte: Una perspectiva a partir del registro tectónico-sedimentológico del coniaciano al Paleoceno. *Rev. Acad. Colomb. Ciencias Exactas Físicas Nat.* 42 (165), 364–378. doi:10.18257/raccefyn.632

Beardsmore, G. R., and Cull, J. P-. (2001). *Crustal heat flow: A guide to measurement and modelling*. Cambridge, United Kingdom: Cambridge University Press, 324.

Bromhead, A., Sutcliffe, O., Hay, D., and Evans, K. (2017). "Lessons learned from the vaca muerta: An exploration model to aid sweet-spot prediction in the frontier hanifa unconventional resource play in the Middle East," in Paper presented at the SPE/AAPG/SEG Unconventional Resources Technology Conference, Austin, United States, July, 2018.

Caballero, V., Mora, A., Quintero, I., Blanco, V., Parra, M., Rojas, L. E., et al. (2013). "Tectonic controls on sedimentation in an intermontane hinterland basin adjacent to inversion structures: The Nuevo Mundo syncline, Middle Magdalena Valley, Colombia," in *Thick-skin-dominated orogens: From initial inversion to full accretion*. Editors M. Nemcok, A. Mora, and J. Cosgrove (London, United Kingdom: Geological Society, London, Special Publications), 377, 315–342.1.

Casadiego-Quintero, E., and Rios-Reyes, C. A. (2020). Pore structure characteristics and gas storage potential of the cretaceous La Luna Formation, middle Magdalena Valley Basin, Colombia. *Ing. Cienc.* 16 (31), 169–205. doi:10.17230/ingciencia.16.31.8

Ceron, M., Walls, J., and Diaz, E. (2013). "Comparison of reservoir quality from La Luna, gacheta and eagle ford shale formations using digital rock physics," in Presented at AAPG International Conference and Exhibition, Cartagena, Colombia, June, 2013.

Chen, Z., and Jiang, C. (2015). A data driven model for studying kerogen kinetics with application examples from Canadian sedimentary basins. *Mar. Petroleum Geol.* 67, 795–803. doi:10.1016/j.marpetgeo.2015.07.004

Chen, Z., and Jiang, C. (2016). A revised method for organic porosity estimation in shale reservoirs using Rock-Eval data: Example from Duvernay Formation in the Western Canada Sedimentary Basin. *AAPG Bull.* 100 (3), 405–422. doi:10.1306/08261514173

Cooney, P., and Lorente, M. (1997). Implicaciones tectónicas de un evento estructural en el Cretácico Superior (Santoniense-Campaniense) de Venezuela Occiental. Memorias del VIII Congreso Geológico Venezonalo. *Soc. Venez. Geólogos* 1, 195–204.

Cortes, M., Cortes, Y., Higuera, C., García, D., and Maya, L. (2022). "Chapter 16 – regional structure, trap mechanisms, and basin evolution of the Middle Magdalena Basin of Colombia," in *Andean structural styles: A seismic atlas*. Editors G. Zamora, and A. Mora (Amsterdam, Netherlands: Elsevier), 221–226.

Erlich, R. N., Villamil, T., and Keens-Dumas, J. (2003). "Controls on the deposition of Upper Cretaceous organic carbon–rich rocks from Costa Rica to Suriname," in *The circum-gulf of Mexico and the caribbean: Hydrocarbon habitats, basin formation, and plate tectonics: AAPG memoir 79*. Editors C. Bartolini, R. T. Buffler, and J. Blickwede, 1–45.

Etayo-Serna, F. (2019a). "Basin development and tectonic history of the middle Magdalena Valley," in *Estudios geológicos y paleontológicos sobre el Cretácico en la región del embalse del río Sogamoso, Valle Medio del Magdalena, Compilación de los Estudios Geológicos Oficiales en Colombia*. Editor F. Etayo-Serna (Bogota, Columbia; Bogotá: Servicio Geológico Colombiano), 413–423.

Etayo-Serna, F. (2019b). "Formación" simití: Unidad ambigua en la estratigrafía del valle medio del Magdalena," in *Estudios geológicos y paleontológicos sobre el Cretácico en la región del embalse del río Sogamoso, Valle Medio del Magdalena, Compilación de los Estudios Geológicos Oficiales en Colombia*. Editor F. Etayo-Serna (Bogota, Columbia; Bogotá: Servicio Geológico Colombiano), 293–302.

Fertl, W. H., and Rieke, H. H. (1980). Gamma ray spectral evaluation techniques identify fractured shale reservoirs and source-rock characteristics. *J. Petroleum Technol.* 32 (11), 2053–2062. doi:10.2118/8454-PA

Galford, J., Quirein, J., Westacott, D., and Witkowsky, J. (2013). "Quantifying organic porosity from logs," in Presented at SPWLA 54th Annual Logging Symposium, New Orleans, Luisiana, June 2013, 16.

Galvis-Portilla, H., Higuera, I., Cespedes, S., Ballesteros, C., Forero, S., Marfisi, N., et al. (2014). "Regional sequence stratigraphy of the upper cretaceous La Luna Formation in the Magdalena Valley Basin, Colombia," in Paper presented at the SPE/AAPG/SEG Unconventional Resources Technology Conference, Colorado, United States, August 2014, 10.

Gamero-Diaz, H., Miller, C., and Lewis, R. (2013). "sCore: A mineralogy based classification scheme for organic mudstones," in SPE Annual Technical Conference and Exhibition, New Orleans, Louisiana, USA, September 2013.

Gaona-Narvaez, T., Maurrasse, F. J. M., and Etayo-Serna, F. (2013). "Geochemistry, palaeoenvironments and timing of aptian organic-rich beds of the Paja formation (curití, eastern cordillera, Colombia)," in *Isotopic studies in cretaceous research*. Editors A. Bojar, M. Melinte-Dobrinescu, and J. Smit (London, United Kingdom; Geological Society, London, Special Publications), 31–48.1.

García, D., Parra, P., and Sánchez, C. (2001). Modelos de Generación de petróleo en el Valle Medio del Río Magdalena. Internal Report Ecopetrol-ICP. *Piedecuesta* 166, 5. annexes.

García-Delgado, H., and Velandia, F. (2020). Tectonic geomorphology of the serranía de San Lucas (central cordillera): Regional implications for active tectonics and drainage rearrangement in the northern Andes. *Geomorphology* 349, 25. 106914. doi:10.1016/j.geomorph.2019.106914

García-Gonzalez, M., and Carvajal, H. (2006). La supresión de la reflectancia de la vitrinita en las formaciones La Luna y Hondita y sus implicaciones en la exploración de hidrocarburos de las cuencas del VSM y VMM, Colombia. IX Simposio Bolivariano de Exploración Petrolera en las Cuencas Subandinas. https://www.acggp.org/ix-simposio-bolivariano-2006/.7Retrieved from:

Gomez, E., Jordan, T. E., Allmendinger, R. W., Hegarty, K., Kelley, S., and Heizler, M. (2003). Controls on architecture of the late cretaceous to cenozoic southern middle Magdalena Valley Basin. *Colombia Geol. Soc. Am. Bull.* 115 (2), 131–147. doi:10.1130/0016-7606(2003)115<0131:COAOTL>2.0.CO;2

Gomez, E., Jordan, T. E., Allmendinger, R. W., Hegarty, K., and Kelley, S. (2005). Syntectonic cenozoic sedimentation in the northern middle Magdalena Valley Basin of Colombia and implications for exhumation of the northern Andes. *Geol. Soc. Am. Bull.* 117 (5/6), 547–569. doi:10.1130/B25454.1

Gong, C., and Rodriguez, L. (2017). "Challenges in pore pressure prediction for unconventional petroleum systems," in Presented at AAPG Hedberg Conference, The Future of Basin and Petroleum Systems Modeling, California, United States, April 2016.

Gonzalez, R., Suarez, C., Higuera, I., and Rojas, L. (2020). Alternative workflow for three-dimensional basin modeling in areas of structural complexity: Case study from the Middle Magdalena Valley, Colombia. *AAPG Bull.* 104, 1–19. doi:10.1306/0415191612917185

Grauls, D. (1999). Overpressures: Causal mechanisms, conventional and hydromechanical approaches. *Oil Gas Sci. Technol. – Rev. IFP* 54 (6), 667–678. doi:10.2516/ogst:1999056

Guerrero, J., Montes, L., Jaillard, E., and Kammer, A. (2021). Seismic interpretation of the cretaceous unconformities and sequences in the middle Magdalena Valley and the Western margin of the eastern cordillera, Colombia. *Comptes Rendus Géoscience* 353 (1), 155–172. doi:10.5802/crgeos.47

Hantschel, T., and Kauerauf, A. (2009). *Fundamentals of basin and petroleum systems modelling*. Berlin, Germany: Springer-Verlag, 476.

Holgate, F., and Gerner, E. (2010). *OZTemp well temperature data*. Retrieved from: https://researchdata.edu.au/oztemp-well-temperature-data/1215040

Horton, B. K., Anderson, V. J., Caballero, V., Saylor, J. E., Nie, J., Parra, M., et al. (2015). Application of detrital zircon U–Pb geochronology to surface and subsurface correlations of provenance, paleodrainage, and tectonics of the Middle Magdalena Valley Basin of Colombia. *Geosphere* 11 (6), 1790–1811. doi:10.1130/GES01251.1

Ideam (2022). Open weather data. http://dhime.ideam.gov.co/atencionciudadano/. Retrieved from:

Jarvie, D. (2014). Components and processes affecting producibility and commerciality of shale resource systems. *Geol. Acta* 12 (4), 307–325. ALAGO Special Publication. doi:10.1344/GeologicaActa2014.12.4.3

Jimenez, M., Rojas, C., and y Valderrama, Y. (2015). "Initial analysis of hydrocarbon potential in the Tablazo formation; center and northern areas of middle Magdalena Valley, -mmv- Colombia," in Paper presented at the SPE/AAPG/SEG Unconventional Resources Technology Conference, Texas, Unite States, July 2015.

Juliao, T., Suarez-Ruiz, I., Marquez, R., and Ruiz, B. (2015). The role of solid bitumen in the development of porosity in shale oil reservoir rocks of the Upper Cretaceous in Colombia. *Int. J. Coal Geol.* 147-148 (1), 126–144. doi:10.1016/j.coal.2015.07.001

Mews, K., Alhubail, M., and Barati, R. (2019). A review of brittleness index correlations for unconventional tight and ultra-tight reservoirs. *Geosciences* 9 (319), 319. doi:10.3390/geosciences9070319

Mora, C., Cerón, M., Quintero, M., Sanz, C., Rey, C., and Mejia, O. (2018). *Evaluación de recursos en Yacimientos de Roca Generadora (YRG) Formación La Luna, Cuenca Valle Medio del Magdalena, Colombia*. Bogotá, Colombia: Memorias I Cumbre del Petróleo y Gas.

Mora, C., Cordoba, F., Luna, O., Sarmiento, L. F., Rangel, A., Giraldo, N., et al. (1996). "Petroleum systems of the middle Magdalena Valley, Colombia," in AAPG International Conference and Exhibition, Caracas, Venezuela, Bogotá, Colombia, August 1996, 1–7. Memorias de la Cumbre del Petróleo y Gas.

Morales, L. (1958). "The Colombian petroleum industry," in *General geology and oil occurrences of middle Magdalena Valley, Colombia: South America*. Editor L. En: Weeks (Tulsa, Oklahoma: American Association of Petroleum Geologists Special Publication). Habitat of oil.

Parra, M., Mora, A., López, C., Rojas, L. E., and Horton, B. K. (2012). Detecting earliest shortening and deformation advance in thrust belt hinterlands: Example from the Colombian Andes. *Geology* 40 (2), 175–178. doi:10.1130/G32519.1

Passey, Q., Creaney, S., Kulla, J. B., Moretti, F. J., and y Stroud, J. D. (1990). A practical model for organic richness from porosity and resistivity logs. *AAPG Bull.* 74 (12), 1777–1794. doi:10.1306/0C9B25C9-1710-11D7-8645000102C1865D

Pepper, A. S., and Corvi, P. J. (1995). Simple kinetic models of petroleum formation. Part I: Oil and gas generation from kerogen. *Mar. Petroleum Geol.* 12 (3), 291–319. doi:10.1016/0264-8172(95)98381-E

Perez, E., Pachon, Z., Gomez, J., and Marin, P. (2014). "Integrated methodology for laboratory evaluation of Shale Plays cores," in Paper presented at the SPE Latin America and Caribbean Petroleum Engineering Conference, Maracaibo, Venezuela, May 2014.

Piedrahita, J., and Aguilera, R. (2017b). "Models for calculating organic and inorganic porosities in shale oil reservoirs," in Paper presented at the SPE Latin America and Caribbean Petroleum Engineering Conference, Buenos Aires, Argentina, May 2017.

Piedrahita, J., and Aguilera, R. (2017a). *Moveable oil detection in a shale reservoir by integrating simultaneously geochemical, petrophysical and geomechanical models developed from well logs and laboratory test*. Bogotá, Colombia. Paper presented at the Congreso Colombiano del Petróleo.

Ramirez, J., and Aguilera, R. (2014). "Factors controlling fluid migration and distribution in the eagle ford shale," in Paper presented at the SPE/CSUR Unconventional Resources Conference – Canada, Alberta, Canada, September 2014.

Ramón, J. C., Dzou, L., and Giraldo, B. (1997). Geochemical evaluation of the middle Magdalena basin, Colombia. *CT&F-Ciencia, Tecnol. Futuro* 1 (3), 47–66.

Rangel, A., Osorno, J., Ramirez, J., De Bedout, J., Gonzalez, J., and Pabón, J. (2017). Geochemical assessment of the Colombian oils based on bulk petroleum properties and biomarker parameters. *Mar. Petroleum Geol.* 86, 1291–1309. doi:10.1016/j.marpetgeo.2017.07.010

Reyes, H., Montenegro, B., and Gómez, P. (2004). Tectonoestratigrafía y evolución geológica del Valle Inferior del Magdalena. *Bol. De. Geol.* 26 (42), 19–38.

Reyes, M., Kley, J., Mora, A., Bello-Palacios, D., Vargas, A., Carvajal-Torres, J., et al. (2022). "Chapter 15 – La Cira basement-high; middle Magdalena Valley Basin, Colombia," in *Andean structural styles: A seismic atlas*. Editors G. Zamora, and A. Mora (Amsterdam, Netherlands: Elsevier), 207–219.

Rojas, D., Galeano, A., and Sanchez, C. (2013). *First approach for quantifying undiscovered petroleum initially in place on unconventional resources for a new play in the Cretaceous La Luna Formation, at the north of the Middle Magdalena Valley Basin, Colombia*. Bogotá, Colombia: XV Congreso Colombiano del Petróleo, 10. https://www.slideshare.net/marioprince1/first-approach-for-quantifying-undiscovered-petroleum-initially-in-place-on-unconventional-resources-for-a-new-play-in-the-cretaceous-la-luna-formation-at-the-north-of-the-middle-magdalena-valley-basin-colombia.Retrieved from:

Romero-Sarmiento, M. F., Ducros, M., Carpentier, B., Lorant, F., Cacas, M., Pegaz-Fiornet, S., et al. (2013). Quantitative evaluation of TOC, organic porosity and gas retention distribution in a gas shale play using petroleum system modeling: Application to the Mississippian Barnett Shale. *Mar. Petroleum Geol.* 45, 315–330. doi:10.1016/j.marpetgeo.2013.04.003

Sarmiento-Rojas, L. F. (2019). "Cretaceous stratigraphy and paleo-facies maps of northwestern South America," in *Geology and tectonics of northwestern South America. Frontiers in Earth sciences*. Editors F. En Cediel and R. P. Shaw (Berlin, Germany: Springer, Cham), 673–747.

Sarmiento-Rojas, L. F., Van Wess, J. D., and Cloetingh, S. (2001). Mesozoic transtensional basin history of the Eastern Cordillera, Colombian Andes: Inferences from tectonic models. *J. S. Am. Earth Sci.* 21, 383–411. doi:10.1016/j.jsames.2006.07.003

Schmoker, J., and Hester, T. (1983). Organic carbon in bakken formation, United States portion of williston basin. *AAPG Bull.* 67 (12), 2165–2174. doi:10.1306/AD460931-16F7-11D7-8645000102C1865D

Scotese, C. R., Gahagan, L. M., and Larson, R. L. (1988). Plate tectonic reconstructions of the cretaceous and cenozoic ocean basins. *Tectonophysics* 155 (1-4), 27–48. doi:10.1016/0040-1951(88)90259-4

Shurr, G., and Ridgley, J. (2002). "Unconventional shallow biogenic gas systems," in *Unconventional petroleum systems*. Editors B. Law and J. Curtis, 1939–1969. AAPG Bulletin.11.

Slatt, R., McCullough, B., Molinares, C., Baruch, E., and Turner, B. (2015). "Paleotopographic and depositional environment controls on "sweet spot" locations in unconventional resource shales: Woodford and Barnett shale examples: Part 2," in Presented at AAPG Annual Convention & Exhibition, Colorado, United States, June 2015.

Suarez, M., Serrano, M., and Morales, M. (2000). Estilos Estructurales y Potencial de Entrampamiento de la Sección Cretácea, Cuenca del Valle Medio del Magdalena, Colombia. *Presented A. T. VII Simp. Boliv. Exploración Pet. las Cuencas Subandinas*. doi:10.3997/2214-4609-pdb.118.024esp

Suo, C., Peng, S., Chang, S., Duan, R., and Wang, G. (2012). A new calculating method of the curvature to predicting the reservoir fractures. *Procedia Environ. Sci.* 12, 576–582. doi:10.1016/j.proenv.2012.01.320

Terraza-Melo, R. (2019). "Formación La Luna": Expresión espuria en la geología colombiana," in *Estudios geológicos y paleontológicos sobre el Cretácico en la región del embalse del río Sogamoso, Valle Medio del Magdalena, Compilación de los Estudios Geológicos Oficiales en Colombia*. Editor F. Etayo-Serna (Bogota, Colombia: Bogotá: Servicio Geológico Colombiano), 303–362.

Thompson-Butler, W., Peters, K. E., Magoon, L. B., Scheirer, A. H., Moldowan, J. M., Blanco, V. O., et al. (2019). Identification of genetically distinct petroleum tribes in the Middle Magdalena Valley, Colombia. *AAPG Bull.* 103 (12), 3003–3034. doi:10.1306/04101918107

U.S. Energy Information Administration (Eia) (2015). Technically recoverable shale oil and shale gas resources: Northern south America. https://www.eia.gov/analysis/studies/worldshalegas/pdf/Northern_South_America_Columbia_Venezuela_2013.pdf. 30Retrieved from

Vargas-Silva, D. A., Gambús-Ordaz, M., and Calderón-Carrillo, Z. (2019). Assessment of causes of overpressure different from sub-compaction: Application in unconventional reservoir. *CT&F - Cienc. Tecnol. Y Futuro* 9 (2), 5–14. doi:10.29047/01225383.177

Veiga, R., Micucci, E., Cuberes, M., and Bande, A. (2023). "Reservorios no convencionales en Latinoamérica: La Formación La Luna en el Valle Medio del Magdalena-Colombia," in 11th Congreso de Exploración y Desarrollo de Hidrocarburos: Exploración y Sistemas Petroleros, Instituto Argentino del Petróleo y Gas, Argentina, 231–258. Available at: https://www.researchgate.net/publication/370057425_RESERVORIOS_NO_CONVENCIONALES_EN_LATINOAMERICA_LA_FORMACION_LA_LUNA_EN_EL_VALLE_MEDIO_DEL_MAGDALENA-COLOMBIA.

Villamil, T., Arango, C., and Hay, W. W. (1999). "Plate tectonic paleoceanographic hypothesis for Cretaceous source rocks and cherts of northern South America," in *Evolution of the cretaceous ocean-climate system: Boulder, Colorado*. Editors E. Barrera, and C. C. Johnson, 191–202. Geological Society of America Special Paper.

Wang, F., and Gale, J. (2009). Screening criteria for shale-gas systems. *Gulf Coast Assoc. Geol. Soc. Trans.* 59, 779–793.

frontiers | Frontiers in Earth Science

TYPE Original Research
PUBLISHED 18 May 2023
DOI 10.3389/feart.2023.1207033

OPEN ACCESS

EDITED BY
Ruyue Wang,
Sinopec Petroleum Exploration and Production Research Institute, China

REVIEWED BY
Jingshou Liu,
China University of Geosciences Wuhan, China
Jianhua He,
Chengdu University of Technology, China

*CORRESPONDENCE
Zhijun Jin,
jinzj1957@pku.edu.cn

RECEIVED 17 April 2023
ACCEPTED 09 May 2023
PUBLISHED 18 May 2023

CITATION
Liu G, Jin Z, Yang S, Zeng L, He W, Du X, Lu G and Liu G (2023), Distribution pattern of natural fractures in lacustrine shales: a case study of the Fengcheng formation in the Mahu Sag of the Junggar Basin, China.
Front. Earth Sci. 11:1207033.
doi: 10.3389/feart.2023.1207033

Distribution pattern of natural fractures in lacustrine shales: a case study of the Fengcheng formation in the Mahu Sag of the Junggar Basin, China

Guoyong Liu[1], Zhijun Jin[2,3]*, Sen Yang[1], Lianbo Zeng[2,4], Wenjun He[1], Xiaoyu Du[2], Guoqing Lu[4] and Guoping Liu[2]

[1]Research Institute of Exploration and Development, Xinjiang Oilfield Company, PetroChina, Karamay, China, [2]Institute of Energy, Peking University, Beijing, China, [3]State Key Laboratory of Shale Oil and Gas Enrichment Mechanisms and Effective Development, Beijing, China, [4]College of Geosciences, China University of Petroleum (Beijing), Beijing, China

The Lower Permian Fengcheng Formation in the Mahu Sag develops a set of organic-rich alkaline lacustrine shale strata, which is a key area for shale oil exploration and development. As an important storage space and seepage channel for shale reservoirs, natural fractures have an impact on shale oil enrichment, production and development effect. In this study, the types and characteristics of natural fractures were first analyzed using core, thin section and imaging logging data. On this basis, combined with the distribution of fractures in single wells, the vertical distribution law of fractures is discussed. Finally, the planar distribution of fractures is evaluated using different seismic attributes such as coherence, curvature, likelihood, and AVAz. The results showed that three types of fractures are existed, including transformational shear fractures, intraformational open fractures and bed-parallel shear fractures, with intraformational open fractures being the most developed. The development degree of fractures in different layers has obvious differences, mainly controlled by lithology and brittle mineral content. The basalt and tuff are developed in the Feng 1 Member, with low carbonate mineral content, resulting in a relatively low degree of fracture development. The dolomite and argillaceous dolomite are developed in the Feng 2 Member and the Feng 3 Member, with high carbonate mineral content and brittleness, resulting in a high degree of fracture development. Additionally, the closer to the fault, the higher the degree of fracture development. On the plane, the fracture zone develops near the main and secondary faults, with the trend mainly oriented in the E-W direction and approximately parallel to the direction of the faults. The width of the fracture zone is largest in the central and southern part of the study area. These fractures are fault-related and are caused by regional stress fields resulting from the activity of the main-secondary faults.

KEYWORDS

natural fractures, distribution patterns, lacustrine shale, Fengcheng formation, Mahu sag

1 Introduction

Due to the great success of the shale revolution in North America, unconventional oil and gas resources such as shale oil have gradually become the focus of global hydrocarbon exploration and development (Jarvie et al., 2007; Zou et al., 2013; He et al., 2016; 2017; Ghosh et al., 2018; Wang et al., 2019; Jin et al., 2021; Tao et al., 2021). Shale oil refers to petroleum that is stored in organic-rich shale strata, generally requiring special techniques such as horizontal wells and hydraulic fracturing to obtain industrial oil production (Gale et al., 2007; Jin et al., 2021; Tang et al., 2021). Exploration practices have confirmed that multiple sets of organic-rich shale strata exist in the lacustrine basins in China, including the Cretaceous in the Songliao Basin, the Permian in the Junggar Basin, the Triassic in the Ordos Basin, the Jurassic in the Sichuan Basin, and the Paleogene in the Bohai Bay Basin (Zou et al., 2013; Liu et al., 2018; Zhao et al., 2020; Jin et al., 2021; Zhang et al., 2022). Lacustrine shales are characterized by strong heterogeneity, low matrix permeability, high clay mineral content, and large compressibility changes, which constrain the deployment and large-scale development of lacustrine shale oil (Jin et al., 2021).

Previous studies have found that lacustrine shale strata have generally experienced multiple stages of tectonic movement, and the content of brittle minerals can reach over 40%, resulting in the widespread development of natural fractures in shale oil reservoirs (Zou et al., 2013; Jin et al., 2021; Tang et al., 2021). Shale oil reservoirs typically have extremely low matrix porosity and permeability, making it difficult to form an effective fluid flow system and to provide industrial oil flow in natural conditions (Gong et al., 2021; Zhang et al., 2022). Natural fractures, serving as fluid conduits for oil and gas transport from the matrix to the wellbore, can significantly improve reservoir properties and affect shale oil enrichment, production, and the development plan (Gale et al., 2007; Ding et al., 2012; Jarvie, 2012; Mastalerz et al., 2013; Zeng et al., 2016; Wang et al., 2018; Liu et al., 2022b; Yang et al., 2022). Previous researchers have conducted numerous works on the development characteristics, formation mechanisms, and controlling factors of natural fractures in conventional reservoirs, but few have focused on the distribution rules of lacustrine shale reservoirs (Laubach et al., 2004; Laubach and Ward, 2006; Laubach et al., 2019; Gale et al., 2010, 2014; Zeng et al., 2013; Wang et al., 2016a; Wang et al., 2016b; Lyu et al., 2019; Liu et al., 2020a; b; Liu et al., 2021a; Liu et al., 2022a).

In recent years, a set of organic-rich alkaline lake shale strata has developed in the Lower Permian Fengcheng Formation of the Mahu Sag, making it an important exploration area in the Junggar Basin (Tang et al., 2021; Zhi et al., 2021; Xia et al., 2022; Lu et al., 2023). Industrial oil flows from multiple drilling wells have displayed good exploration and development prospects. Previous studies have studied the regional structure, sedimentary background, reservoir lithology, and pore structure of the Fengcheng Formation, indicating that natural fractures are important reservoir spaces in the Fengcheng Formation (Tang et al., 2021; Wang et al., 2021; Zhi et al., 2021). Since the deposition in Permian, the Fengcheng Formation has experienced multi-stage tectonic movements such as Hercynian movement, Indosinian movement, Yanshanian movement and Himalayan movement (Zhou et al., 2019; Wang et al., 2022). In addition, the mixed deposition of terrigenous clast, endogenous carbonate and volcanic materials makes the lithology of the Fengcheng Formation extremely complex (Zhi et al., 2021). A variety of factors lead to the unclear distribution of natural fractures in the Fengcheng Formation, which has strong heterogeneity in the vertical and horizontal directions. Therefore, the study on the distribution pattern of natural fractures in the lacustrine shales of the Fengcheng Formation has important guiding significance for the formulation of subsequent exploration and development plans in the study area.

In this study, the Fengcheng Formation in the Mahu Sag was taken as the research object. Firstly, the fracture development characteristics of the Fengcheng Formation were described using core, imaging logs and thin section data. Then, XRD tests were used to analyze the differences of mineral composition in the Feng 1 Member, Feng 2 Member and Feng 3 Member. On this basis, the vertical pattern of fractures was discussed by characterizing the fracture distribution characteristics of single wells. Finally, the natural fractures identified by different attributes were stacked based on different seismic attributes, including curvature, coherence, likelihood and pre-stack AVAz, and the planar

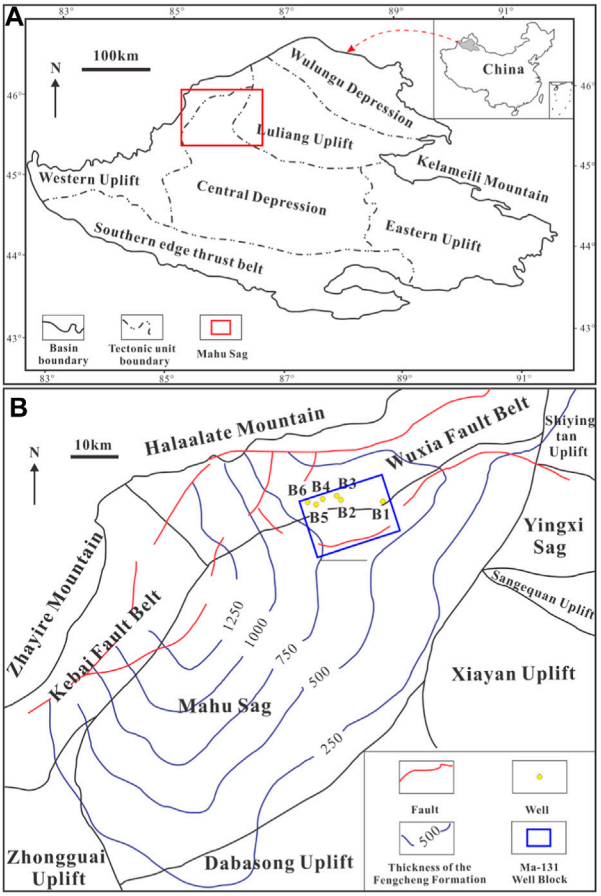

FIGURE 1
(A) Tectonic unit of Junggar Basin. **(B)** Location of the Mahu Sag and Ma-131 Well Block (Modified from Wang et al., 2022).

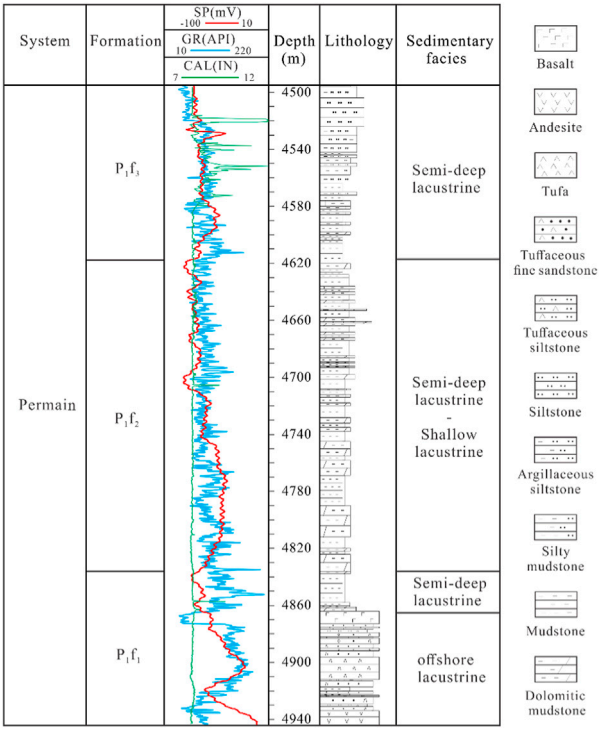

FIGURE 2
Stratigraphic column of the Fengcheng formation in Well B2 in the Mahu Sag.

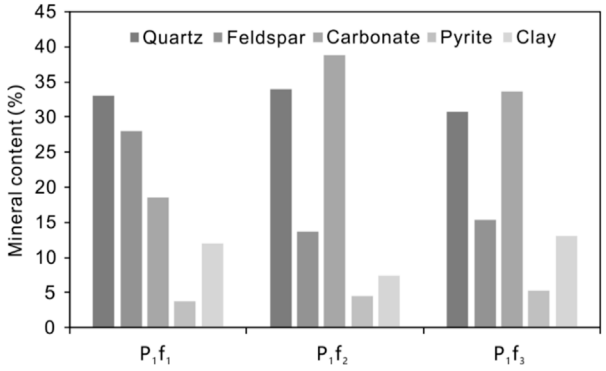

FIGURE 3
Mineral content of P_1f_1, P_1f_2 and P_1f_3 in Well B2 in the Mahu Sag.

distribution pattern of natural fractures was evaluated. The research results will provide a geological basis for the next exploration and development of shale oil reservoirs in the Mahu Sag.

2 Geological setting

The Junggar Basin is a large superimposed petroliferous basin in Northwest China, located in the eastern part of the Kazakhstani Plate, with an area of approximately 13×10^4 km^2 (Xiao et al., 2008; Cao et al., 2020; Tang et al., 2021; Wu et al., 2022). The Mahu Sag is a secondary tectonic unit in the basin, which is the hydrocarbon generation sag with the highest degree of oil and gas enrichment. (Liu et al., 2016; Guo et al., 2021; Tang et al., 2021; Zhi et al., 2021; Wu et al., 2022). The Mahu sag is a Carboniferous-Quaternary sag formed on the pre-Carboniferous fold basement and controlled by multi-period peripheral thrust activities. It is surrounded by the Wuxia Fault Zone, Kebai Fault Zone, and Zhongguai Uplift in the west and the Shiyingtan Uplift, Yingxi Sag, Xiayan Uplift, and Dabasong Uplift in the east (Zhang et al., 2019; Li et al., 2021; Lu et al., 2023). The sag is distributed in the northeast-southwest direction, with an E-W length of about 50 km, a N-S length of about 120 km, and an area of about 5,000 km^2 (Figure 1) (Xia et al., 2020; Zhi et al., 2021). The Mahu 131 Well Block is located in the northern part of the sag, and multiple wells drilled in the area have shown industrial oil flows. The Well B2 achieved a maximum daily oil production of 50 tons from a depth of 4,581–4,850 m, indicating abundant shale oil resources (Zhi et al., 2021; Tang et al., 2023).

The Carboniferous to Cretaceous strata is developed from bottom to top in the sag, among which the Lower Permian Fengcheng Formation develops a set of fan delta-lake sedimentary system, which is a significant regional hydrocarbon source rock (Song et al., 2022; tang et al., 2023). The rock types of the Fengcheng Formation are diverse, including carbonate rocks, clastic rocks and volcanic rocks, reflecting the characteristics of mixed deposition, with a total depositional thickness of 800–1800 m (Zhi et al., 2021; Song et al., 2022). It can be subdivided into three members based on lithologic and electrical characteristics: Feng 1 Member (P_1f_1), Feng 2 Member (P_1f_2), and Feng 3 Member (P_1f_3), each with distinct sedimentary facies (Figure 2 Figure Fig3) (Tang et al., 2021; Wang et al., 2021; Zhi et al., 2021). During the deposition of the Feng 1 Member, the volcanic activity was intense and the supply of terrestrial material was limited, resulting in the development of volcanic clastic rocks. During the Feng 2 Member period, the climate became arid and the salinity of the lake basin increased, leading to the development of dolomitic rocks, dolomitic mudstones, and evaporites. During the sedimentary period of Feng 3 Member, the salinity of the basin decreased, and dolomitic rocks dominated with clastic rocks at the top (Zhang et al., 2018). The various lithologies exhibit a mutually exclusive relationship in different areas, with carbonate sedimentation dominating in the center of the basin, reflecting typical characteristics of a saline lake (Zhang et al., 2018; Zhi et al., 2021).

3 Methods

3.1 X-ray diffraction analysis

XRD was conducted using a German Bruker D8 ADVANCE X-ray diffractometer, completed at the SINOPEC Wuxi Petroleum Geology Research Institute in China. Prior to XRD testing, rock samples were ground into powder with a particle size of 200 mesh. Approximately 10 g of powder was mixed thoroughly with ethanol, and the sample was prepared using a pressing method for testing. Mineral types and mass percentages were calculated by comparing the diffraction peak intensities of standard samples and measuring

the area under the curve of the main peaks of each mineral (Gou et al., 2021). All testing procedures followed the China Oil and Gas Industry Standard SY/T 6010-2018.

3.2 Fracture characterization

In this study, natural fractures of the Permian Fengcheng Formation in the Mahu Sag were studied based on different databases, including cores, thin sections, and imaging logs. The investigated wells are drilled vertically and located on the slope in the northern part of the sag, as shown in Figure 1B. Core observations were conducted at the core library of the PetroChina Xinjiang Oilfield Company. Additionally, thin sections (with a thickness of 30 μm) were prepared to observe the micro-features of the fractures, using a Nikon LV100N POL microscope at the School of Earth and Space Sciences at Peking University. Furthermore, fracture analysis was performed using imaging logs collected by a full-borehole micro-scanner imaging tool (FMI). The drilling employed conductive mud, hence unfilled fractures penetrated by drilling fluids are displayed as dark curves, while fractures filled with minerals are displayed as bright curves due to their high electrical resistivity (Lyu et al., 2019).

3.3 Seismic attribute extraction

Seismic waves propagating in fractured media exhibit anisotropic characteristics in terms of attributes such as amplitude, velocity, attenuation, and travel time, which can be used to predict the development intensity of fractures by analyzing their azimuthal variation (Shen et al., 2002; Liu et al., 2021b). Various seismic attributes have different resolutions and different ability to identify fractures (Wang et al., 2022). Post-stack seismic attributes such as curvature, dip angle, variance, coherence, and azimuth have good identification effects on large-scale fractures, and can identify fractures larger than 1/4 wavelength. Compared to post-stack seismic attributes, likelihood attributes contain dip angle and azimuth information, and pre-stack AVAz retains shot-receiver offset and azimuth information, which have good identification effects on medium and small-scale fractures. In this study, large-scale fractures were first identified using curvature, coherence and likelihood attributes, and then medium and small-scale fractures were identified using pre-stack AVAz attributes. The comprehensive identification result of the Fengcheng Formation fractures in the Mahu sag was obtained by overlaying the results of the two identification methods. In addition, the dominant frequency and bandwidth of the 3D seismic data in the Ma131 Well Block are 25 Hz and 50 Hz, respectively.

4 Results

4.1 Mineral composition

All samples of the Fengcheng Formation are rich in carbonate minerals, quartz, and feldspar, with average contents of 31.6%, 32.6%, and 18.1%, respectively, while the content of clay minerals and pyrite is relatively low, with average contents of 10.5% and 4.6%, respectively. The mineral content in different layers varies to some extent in the vertical direction. In the Feng 1 Member, the content of quartz is the highest, with an average content of 33.0%, followed by feldspar and carbonate minerals, with average contents of 28.1% and 18.6%, respectively. The mineral composition of the Feng 2 Member and the Feng 3 Member is similar, with carbonate minerals being the highest, averaging 38.8% and 33.5%, respectively. The content of quartz is lower with an average of 33.9% and 30.7% respectively. Feldspar is the least abundant, averaging 13.6% and 15.3%, respectively. Therefore, the Feng 2 Member and the Feng 3 Member have similar mechanical properties, which are significantly different from those of the Feng 1 Member.

4.2 Fracture characteristics

Core and thin section observations and imaging log interpretation results show that natural fractures in the Fengcheng Formation are widely developed in the study area. Natural fractures can be classified into three types according to their origin: transformational shear fractures, intraformational open fractures and bed-parallel shear fractures. The transformational shear fractures are generally large in size with a straight fracture surface and a dip angle of nearly 90°. They traverse one or more rock strata boundaries vertically and extend a long distance. In Figure 4A, the height of the transformational shear fractures exceeds 40 cm. The intraformational open fractures develop within the rock strata and are relatively small in size. Their longitudinal extension is significantly restricted by the rock strata boundary, and their vertical extension is short and intersects the rock strata boundary at a high angle. In Figure 4B, the height of the intraformational open fractures is less than 15cm, and it is possible to observe oil seeping out along the fractures. The bed-parallel shear fractures are parallel to the bedding plane with a relatively low dip angle, and their fracture surfaces show scratch marks, steps, and mirror surfaces (Figure 4C). Among the tectonic fractures in the Fengcheng Formation, the intraformational open fractures are the most developed, while transformational shear fractures and bed-parallel shear fractures are relatively less.

According to the degree of mineral cement filling in the fractures, natural fractures can be divided into three types: unfilled, partially filled, and fully filled fractures, and the effectiveness of fractures decreases in that order (Zeng et al., 2013). Most of the fractures observed in the cores are effective fractures, including unfilled fractures (Figures 4B,D) and partially filled fractures (Figure 4E), which can serve as storage space and migration channels for shale oil. Oil is visible in the fractures observed in the cores, and the fluorescence of the fractures under UV light indicates the presence of residual hydrocarbons (Figures 4B,D). The fractures observed in thin sections are mostly filled with minerals, such as quartz, calcite, and reedmergnerite (Figures 4F,G), showing features of cutting through lamination interfaces or mineral particles.

A large number of induced fractures, conductive fractures, resistive fractures and a small number of small faults can be identified in the imaging log images (Figure 5). The induced fractures are a group of parallel and 180° symmetrical high-angle

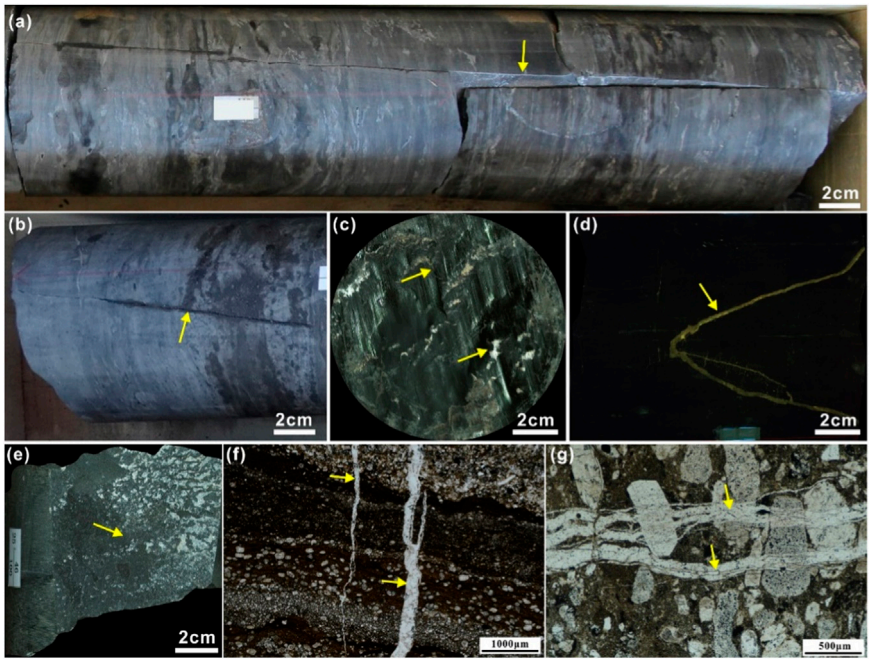

FIGURE 4
Tectonic fractures in the Fengcheng Formation in cores and thin sections in the Mahu Sag. **(A)** Transformational shear fracture, Well B2, 4,752.37 m. **(B)** Intraformational open fracture contains oil, Well B2, 4,722.1 m. **(C)** Bed-parallel shear fracture, Well B2, 4,713.9 m. **(D)** Fluorescence image indicates that fracture contains oil, Well B2, 4,746.47 m. **(E)** High-angle fracture surface is partially filled with mineral, Well B2, 4,872.5 m. **(F)** High-angle fracture is filled with mineral, Well B2, 4,650.3 m. **(G)** High-angle fracture is filled with mineral, Well B2, 4,616.14 m.

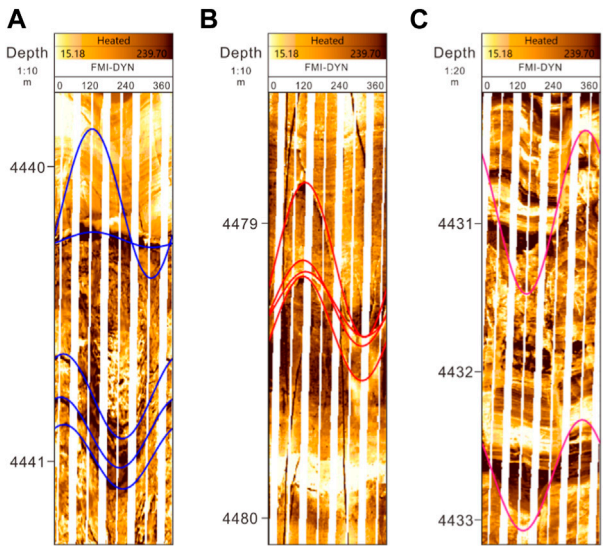

FIGURE 5
Natural fractures in the Fengcheng Formation detected by the borehole image logs in Well B6 in the Mahu Sag. **(A)** Conductive fractures. **(B)** Resistive fractures. **(C)** Small faults.

fractures, and their direction is mainly near E-W, reflecting that the present maximum horizontal principal stress direction is near E-W (Lyu et al., 2019). The conductive fractures appear as dark sinusoidal curves as the open fractures are invaded by drilling mud (Figure 5A). The direction of the conductive fractures is mainly NE-SW, with low dip angles being dominant. Because their orientation is closer to the maximum horizontal principal stress direction, the conductive fractures have large aperture and good effectiveness. The resistive fractures in the Fengcheng Formation are relatively developed, showing bright sinusoidal curves, which are completely filled and having no contribution to the reservoir (Figure 5B). They are mainly in the N-S direction with medium and high dip angles, perpendicular to the direction of the maximum horizontal principal stress, and exhibiting a closure feature. Furthermore, the imaging characteristics of small faults are similar to those of conductive or resistive fractures, with obvious lithological changes or displacement visible (Figure 5C).

4.3 Seismic attribute characteristics

The pink area of the predicted results of the coherence attribute is the low value area, which is the large-scale fracture development zone, distributed in the western, eastern and southern parts of the study area, closer to Well B1 and further away from Wells B2-B5 (Figure 6A). The curvature attribute has a good effect on identifying secondary fractures, with the red area being the area of medium to high values of the curvature attribute, representing secondary fractures, and the blue area being the area of relatively low values, representing fault-related fracture development zones (Figure 6B). The secondary faults are mainly in the near E-W direction, distributed around the primary faults, located in the south and middle of the study area. Wells B1 and B2 are located in the area of high curvature properties, indicating the proximity of Wells

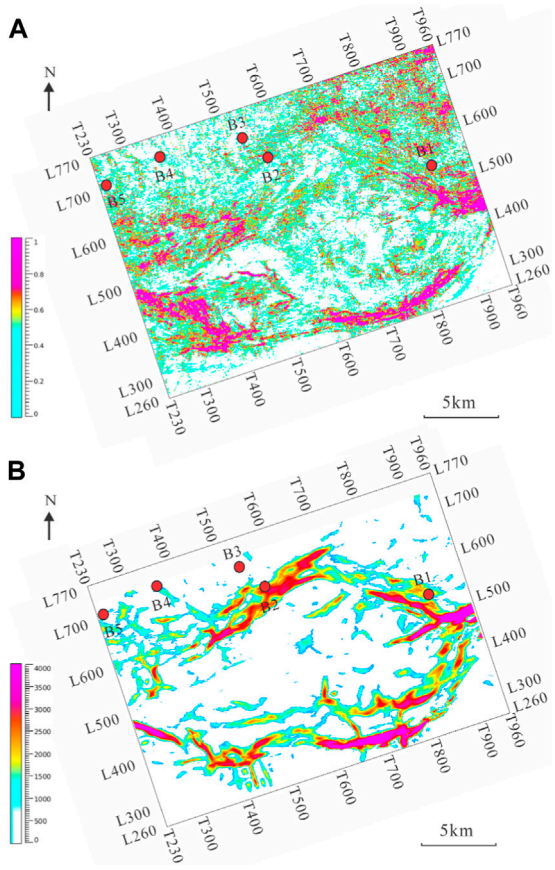

FIGURE 6
Plane distribution of fractue identification results of coherent and curvature seismic attributes. **(A)** Plane distribution of coherent attributes. **(B)** Plane distribution of curvature attributes.

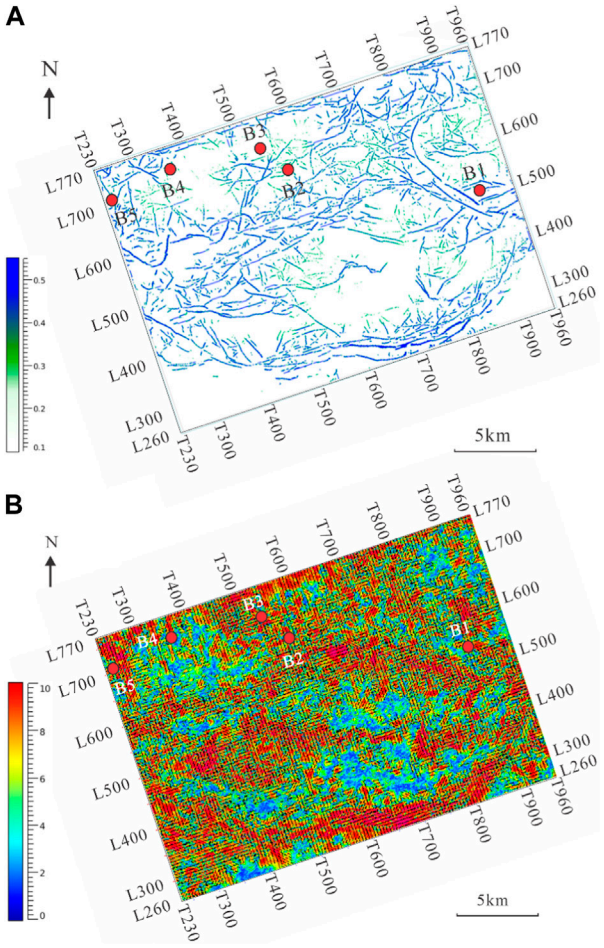

FIGURE 7
Plane distribution of likelihood seismic attributes and AVAZ fracture intensity. **(A)** Plane distribution of likelihood attributes. **(B)** Plane Distribution of AVAZ fracture intensity.

B1 and B2 to the secondary fractures and the development of fault-related fractures.

The Likelihood attribute contains information such as azimuth and dip, and can clearly depict the development of large-scale fractures in the region and accurately detect the boundaries of fracture zones. In the prediction results of the likelihood attribute, the deeper the color (blue), the greater the probability of fractures, and the lighter the color (green, yellow), the smaller the probability of fractures. Because the Likelihood attribute can predict the abnormal information that is not detected in the coherence and curvature attributes, the ability to identify factures is stronger. The results show that large-scale fractures are mainly distributed in the central and northern parts of the study area, as well as the southernmost part, and are more developed near Wells B2 and B1 (Figure 7A).

Small and medium scale fractures are relatively smaller in size but more numerous. In this study, the pre-stack AVAz method was used to predict small and medium scale fractures. The red area near Wells B2 and B3 represents the area with the highest fracture intensity, while the yellow and blue areas represent areas with lower fracture intensity (Figure 7B). Small and medium scale fractures in the Fengcheng Formation have a relatively strong overall development intensity, especially in the northern and central regions, and in the southern part near the main fault, with a predominant orientation parallel to the main fault in the near E-W direction. The northwest direction of Well B2 is the high fracture development area, the area between Wells B2 and B3 is the moderate fracture development area, and the area near Well B4 is the weak fracture development area.

5 Discussion

5.1 Vertical distribution law of fracture

The differences in lithology and mineral composition of shale reservoirs lead to different rock mechanical properties and brittleness, which in turn affects the development of natural fractures in shale (Zeng et al., 2022). According to the imaging log interpretation results of four wells in the study area, including Well B2, Well B3, Well B4, and Well B6, the development of natural fractures in the Fengcheng Formation is obviously controlled by the lithology and mineral composition, and the development degree of fractures varies greatly in different layers. The Feng 1 Member, with a thickness exceeding 100 m and high content of feldspar and quartz., mainly consists of basalt and tuff, as well as small

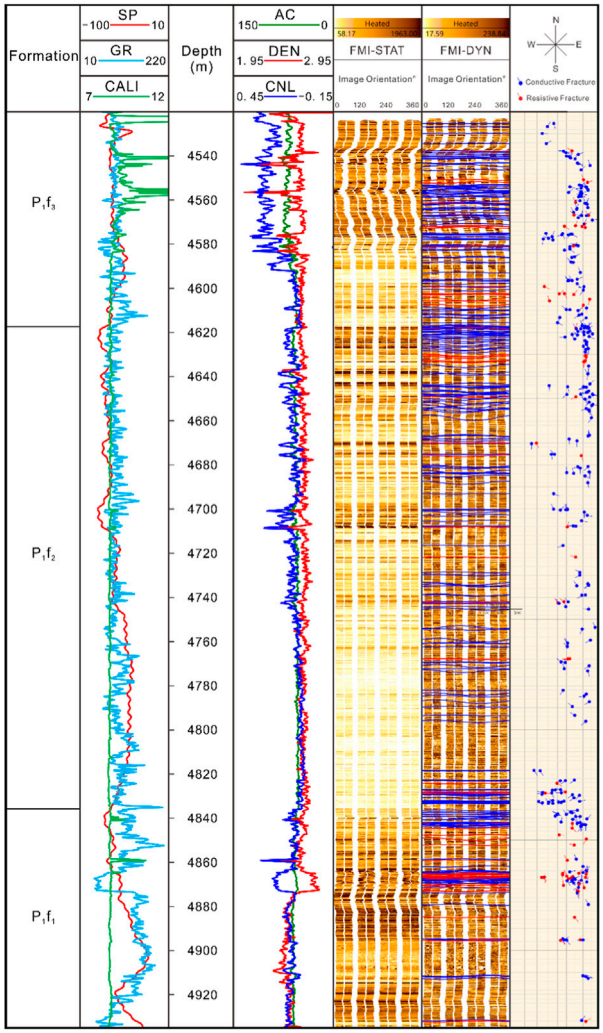

FIGURE 8
Vertical distribution of natural fractures in the Fengcheng Formation in Well B2 in the Mahu Sag.

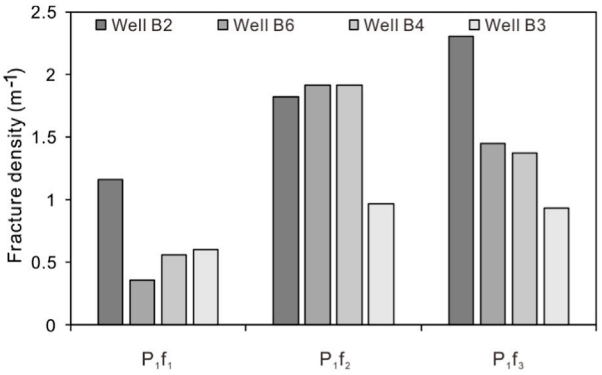

FIGURE 9
Fracture density of P_1f_1, P_1f_2 and P_1f_3 in the Mahu Sag.

amounts of conglomerate, fine sandstone, siltstone, and shale (Figure 2). The Feng 1 Member high-angle fractures is dominated by fractures with high dip angles, and the development degree of fractures with low and medium dip angles is relatively low (Figure 8). The fracture density of the Feng 1 Member in Well B2 is 1.16 m^{-1}. The Feng 2 Member, with a thickness of about 220 m, is mainly composed of argillaceous limestone and shale. The content of carbonate minerals in the Feng 2 Member is high, thus the rock is brittle, and fractures with high and medium dip angles are both developed. The fracture density of the Feng 2 Member in Well B2 is 1.82 m^{-1}. The lithology of the Feng 3 Member is similar to that of the Feng 2 Member, and fractures with high and medium dip angles are also developed. Moreover, a small number of fractures with low dip angles are developed in clastic rocks at the top of Feng 2 Member. The fracture density of the Feng 1 Member in Well B2 is 2.31 m^{-1} (Figure 9). In summary, the Feng 1 Member is mainly composed of volcanic rocks, with low content of carbonate minerals and low brittleness, which leads to low development degree of fracture. The Feng 2 Member and Feng 3 Member are mainly composed of dolomite and argillaceous limestone, with high content of carbonate minerals and higher brittleness, which result in high development degree of fracture (Figure 9). This is because the higher the content of brittle minerals, the greater the brittleness, and fractures will be formed in shale reservoirs when small strains occur under the same tectonic stress (Zeng et al., 2022).

In addition, different orders of faults in the Mahu Sag influence the development of natural fractures in different single wells. The Well B2 is closest to the fault and has the highest degree of fracture development in the Fengcheng Formation, with a fracture density of 1.69 m^{-1}. The fracture development degree of Well B6 and Well B4 is relatively low, with fracture densities of 1.55 m^{-1} and 1.36 m^{-1}, respectively. The Well B3 is the furthest from the fault and the fracture development degree is the lowest, with a fracture density of only 0.74 m^{-1}. This is because there is a fault damage zone near the fault, and the development of natural fractures is affected by the local stress field around the fault. Generally, the closer the distance to the fault, the higher the degree of fracture development (Zeng and Li, 2009; Griffith and Prakash, 2015).

5.2 Plane distribution law of fracture

Due to the fact that different seismic attributes can characterize the distribution of fractures at different scales, superimposing seismic attribute maps of the same layer can be used to analyze the similarities and differences in the distribution patterns of fractures at different scales, and to discuss whether there is any correlation between the origin of fractures at different scales.

Overall, the main and secondary faults of the Fengcheng Formation are distributed in the central and southern parts of the study area, with the trend of near E-W direction.

The zone where large-scale fractures develop is widest in the central and southern parts of the study area, with a predominant trend in the E-W direction and a secondary trend in the S-N direction (Figure 10A). Small and medium scale fractures are well developed in the study area, and their trends are mainly in the E-W and NW-SE directions, which are approximately parallel or obliquely intersected with the large-scale fractures and main-secondary faults (Figure 10B). Locally, the northern part of the study area near Well B4 is a zone of weak fracture development, while the area between Well B3 and Well B1 is a zone of fracture development. The plateau area in the central part of the study area and the southern part near the main-secondary fault zone are both

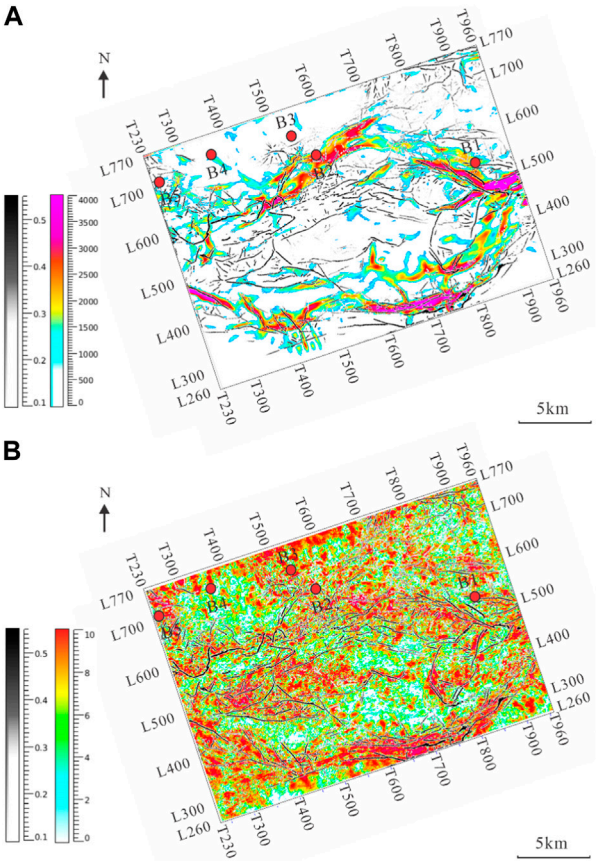

FIGURE 10
Superimposed plane distribution map of pre-stack and post-stack attribute. **(A)** Superimposed plane distribution map of likelihood attribute and curvature attribute. **(B)** Superimposed plane distribution map of pre-stack fracture intensity and likelihood attribute.

areas of large-scale and medium-small-scale fracture development, and the fractures are mostly oriented in the direction of the maximum horizontal principal stress.

Based on the above analysis, large-scale fractures mainly develop near the main-secondary faults and trend approximately parallel to them. They are mainly fault-related fractures resulting from the activity of the main-secondary faults and the effects of regional stress field. Small and medium scale fractures are the most developed in the zone where large-scale fractures develop and nearby, indicating that indicating that they are mainly controlled by fault activity and local stress field during the formation of large-scale fractures.

6 Conclusion

(1) Different types of natural fractures are existed in the Fengcheng Formation of the Mahu Sag, including transformational shear fractures, intraformational open fractures and bed-parallel shear fractures, with intraformational open fractures being the most developed. Moreover, induced fractures, conductive fractures, resistive fractures, and small faults are identified by imaging logs, with good effectiveness of conductive fractures oriented close to the direction of present maximum horizontal principal stress.

(2) There are great differences in the development degree of natural fractures in different layers of Fengcheng formation in the vertical direction. The basalt and tuff are developed in the Feng 1 Member, with low carbonate mineral content and low brittleness, thus the degree of fracture development is relatively low. The dolomite and argillaceous dolomite are developed in the Feng 2 Member and the Feng 3 Member, with high carbonate mineral content and high brittleness, and the degree of fracture development is high. In addition, the closer to the fault, the higher the degree of fracture development in different single wells.

(3) On the plane, the natural fracture development zone is located near the main-secondary faults, with the trend of mainly E-W, approximately parallel to the direction of the faults. The width of the fracture zone is largest in the central and southern part of the study area, and they are fault-related fractures under the action of regional stress fields caused by the activity of the hanging wall and footwall of the main-secondary faults.

Data availability statement

The original contributions presented in the study are included in the article/Supplementary Material, further inquiries can be directed to the corresponding author.

Author contributions

GL, ZJ, and LZ contributed to conception and design of the study. SY and WH organized the database. XD and GL performed the statistical analysis. GL wrote the first draft of the manuscript. XD and GL wrote sections of the manuscript. All authors listed have made a substantial, direct, and intellectual contribution to the work and approved it for publication.

Funding

This research was supported by the National Natural Science Foundation of China (No.42090025), State Key Laboratory of Shale Oil and Gas Enrichment Mechanisms and Effective Development (33550000-22-ZC0613-0336), and CNPC Innovation Found (2023DQ02-0103).

Acknowledgments

We are particularly grateful to the editors and two reviewers for their constructive comments, which will contribute significantly to the improvement of this manuscript.

Conflict of Interest

The authors declare that the research was conducted in the absence of any commercial or financial relationships that could be construed as a potential conflict of interest.

Publisher's note

References

Cao, J., Xia, L., Wang, T., Zhi, D., Tang, Y., and Li, W. (2020). An alkaline lake in the late paleozoic ice age (lpia): A review and new insights into paleoenvironment and petroleum geology. *Earth Sci. Rev.* 202, 103091. doi:10.1016/j.earscirev.2020.103091

Ding, W., Li, C., Li, C., Xu, C., Jiu, K., Zeng, W., et al. (2012). Fracture development in shale and its relationship to gas accumulation. *Geosci. Front.* 3, 97–105. doi:10.1016/j.gsf.2011.10.001

Gale, J. F. W., Lander, R. H., Reed, R. M., and Laubach, S. E. (2010). Modeling fracture porosity evolution in dolostone. *J. Struct. Geol.* 32, 1201–1211. doi:10.1016/j.jsg.2009.04.018

Gale, J. F. W., Reed, R. M., and Holder, J. (2007). Natural fractures in the Barnett Shale and their importance for hydraulic fracture treatments. *AAPG Bull.* 91, 603–622. doi:10.1306/11010606061

Ghosh, S., Galvis-Portilla, H. A., Klockow, C. M., and Slatt, R. M. (2018). An application of outcrop analogues to understanding the origin and abundance of natural fractures in the Woodford Shale. *J. Petroleum Sci. Eng.* 164, 623–639. doi:10.1016/j.petrol.2017.11.073

Gong, L., Wang, J., Gao, S., Fu, X., Liu, B., Miao, F., et al. (2021). Characterization, controlling factors and evolution of fracture effectiveness in shale oil reservoirs. *J. Petroleum Sci. Eng.* 203, 108655. doi:10.1016/j.petrol.2021.108655

Gou, Q., Xu, S., Hao, F., Yang, F., Shu, Z., and Liu, R. (2021). The effect of tectonic deformation and preservation condition on the shale pore structure using adsorption-based textural quantification and 3D image observation. *Energy* 219, 119579. doi:10.1016/j.energy.2020.119579

Griffith, W. A., and Prakash, V. (2015). Integrating field observations and fracture mechanics models to constrain seismic source parameters for ancient earthquakes. *Geology* 43, 763–766. doi:10.1130/g36773.1

Guo, P., Wen, H., Gibert, L., Jin, J., Jiang, Y., and Wang, G. (2021). Controlling factors of high-quality hydrocarbon source rocks developed in lacustrine shallow-water zone of the Junggar Basin, northwestern China. *AAPG Bull.* 105, 2063–2092. doi:10.1306/03122119013

He, J., Ding, W., Jiang, Z., Jiu, K., Li, A., and Sun, Y. (2017). Mineralogical and chemical distribution of the Es3L oil shale in the Jiyang Depression, Bohai Bay Basin (E China): Implications for paleoenvironmental reconstruction and organic matter accumulation. *Mar. Pet. Geol.* 81, 196–219. doi:10.1016/j.marpetgeo.2017.01.007

He, J., Ding, W., Zhang, J., Li, A., Zhao, W., and Dai, P. (2016). Logging identification and characteristic analysis of marine–continental transitional organic-rich shale in the Carboniferous-Permian strata, Bohai Bay Basin. *Mar. Pet. Geol.* 70, 273–293. doi:10.1016/j.marpetgeo.2015.12.006

Jarvie, D. M., Hill, R. J., Ruble, T. E., and Pollastro, R. M. (2007). Unconventional shale-gas systems: The Mississippian Barnett Shale of north-central Texas as one model for thermogenic shale-gas assessment. *AAPG Bull.* 91, 475–499. doi:10.1306/12190606068

Jarvie, D. M. (2012). Shale resource systems for oil and gas: Part 2—shale-oil resource systems. *AAPG Mem.* 97, 89–119. doi:10.1306/13321447M973489

Jin, Z., Zhu, R., Liang, X., and Shen, Y. (2021). Several issues worthy of attention in current lacustrine shale oil exploration and development. *Pet. Explor. Dev.* 48, 1471–1484. doi:10.1016/s1876-3804(21)60303-8

Laubach, S. E., Lander, R. H., Criscenti, L. J., Anovitz, L. M., Urai, J. L., Pollyea, R. M., et al. (2019). The role of chemistry in fracture pattern development and opportunities to advance interpretations of geological materials. *Rev. Geophys.* 57, 1065–1111. doi:10.1029/2019rg000671

Laubach, S. E., Reed, R. M., Olson, J. E., Lander, R. H., and Bonnell, L. M. (2004). Coevolution of crack-seal texture and fracture porosity in sedimentary rocks: Cathodoluminescence observations of regional fractures. *J. Struct. Geol.* 26, 967–982. doi:10.1016/j.jsg.2003.08.019

Laubach, S. E., and Ward, M. E. (2006). Diagenesis in porosity evolution of opening-mode fractures, middle triassic to lower jurassic La boca formation, NE Mexico. *Tectonophysics* 419, 75–97. doi:10.1016/j.tecto.2006.03.020

Li, W., Cao, J., Zhi, D., Tang, Y., He, W., Wang, T., et al. (2021). Controls on shale oil accumulation in alkaline lacustrine settings: Late Paleozoic Fengcheng Formation, northwestern Junggar Basin. *Mar. Pet. Geol.* 129, 105107. doi:10.1016/j.marpetgeo.2021.105107

Liu, G., Chen, Z., Wang, X., Gao, G., Xiang, B., Ren, J., et al. (2016). Migration and accumulation of crude oils from Permian lacustrine source rocks to Triassic reservoirs in the Mahu depression of Junggar Basin, NW China: Constraints from pyrrolic nitrogen compounds and fluid inclusion analysis. *Org. Geochem.* 101, 82–98. doi:10.1016/j.orggeochem.2016.08.013

Liu, G., Zeng, L., Li, H., Ostadhassan, M., and Rabiei, M. (2020a). Natural fractures in metamorphic basement reservoirs in the Liaohe Basin, China. *Mar. Pet. Geol.* 119, 104479. doi:10.1016/j.marpetgeo.2020.104479

Liu, G., Zeng, L., Sun, G., Zu, K., Qin, L., Mao, Z., et al. (2020b). Natural fractures in tight gas volcanic reservoirs and their influences on production in the Xujiaweizi depression, Songliao Basin, China. *AAPG Bull.* 104, 2099–2123. doi:10.1306/05122017169

Liu, J., Chen, P., Xu, K., Yang, H., Liu, H., and Liu, Y. (2022a). Fracture stratigraphy and mechanical stratigraphy in sandstone: A multiscale quantitative analysis. *Mar. Pet. Geol.* 145, 105891. doi:10.1016/j.marpetgeo.2022.105891

Liu, J., Ding, W., Wang, R., Yang, H., Wang, X., and Li, A. (2018). Methodology for quantitative prediction of fracture sealing with a case study of the lower Cambrian Niutitang Formation in the Cen'gong block in South China. *J. Petroleum Sci. Eng.* 160, 565–581. doi:10.1016/j.petrol.2017.10.046

Liu, J., Ding, W., Yang, H., and Liu, Y. (2021a). Quantitative multiparameter prediction of fractured tight sandstone reservoirs: A case study of the yanchang Formation of the Ordos Basin, central China. *SPE J.* 26, 3342–3373. doi:10.2118/205495-pa

Liu, J., Han, L., Shi, L., Chen, S., Lv, W., Zhang, T. G., et al. (2021b). CypB promotes cell proliferation and metastasis in endometrial carcinoma. *Oil Gas Geol.* 42, 747–754. doi:10.1186/s12885-021-08374-7

Liu, J., Mei, L., Ding, W., Xu, K., Yang, H., and Liu, Y. (2022b). Asymmetric propagation mechanism of hydraulic fracture networks in continental reservoirs. *GSA Bull.* 135, 678–688. doi:10.1130/b36358.1

Lu, G., Zeng, L., Dong, S., Huang, L., Liu, G., Ostadhassan, M., et al. (2023). Lithology identification using graph neural network in continental shale oil reservoirs: A case study in Mahu sag, Junggar Basin, western China. *Mar. Pet. Geol.* 150, 106168. doi:10.1016/j.marpetgeo.2023.106168

Lyu, W., Zeng, L., Zhou, S., Du, X., Xia, D., Liu, G., et al. (2019). Natural fractures in tight-oil sandstones: A case study of the upper triassic yanchang Formation in the southwestern Ordos Basin, China. *AAPG Bull.* 103, 2343–2367. doi:10.1306/0130191608617115

Mastalerz, M., Schimmelmann, A., Drobniak, A., and Chen, Y. (2013). Porosity of Devonian and Mississippian New Albany Shale across a maturation gradient: Insights from organic petrology, gas adsorption, and mercury intrusion. *AAPG Bull.* 97, 1621–1643. doi:10.1306/04011312194

Shen, F., Sierra, J., Burns, D. R., and Toksöz, M. N. (2002). Azimuthal offset-dependent attributes applied to fracture detection in a carbonate reservoir. *Geophysics* 67, 355–364. doi:10.1190/1.1468596

Song, Y., Yang, Z., He, W., Gan, R., Zhang, R., Huang, L., et al. (2022). Exploration progress of alkaline lake type shale oil of the permian Fengcheng Formation in Mahu sag, Junggar Basin (in Chinese with English abstract). *China Pet. explor.* 27, 60–72.

Tang, Y., Cao, J., He, W., Guo, X., Zhao, K., and Li, W. (2021). Discovery of shale oil in alkaline lacustrine basins: The late paleozoic Fengcheng Formation, Mahu sag, Junggar Basin, China. *Pet. Sci.* 18, 1281–1293. doi:10.1016/j.petsci.2021.04.001

Tang, Y., He, W., Jiang, Y., Fei, L., Shan, X., Zhao, Y., et al. (2023). Enrichment conditions and exploration direction of Permian saline lacustrine shale oil and gas in Junggar Basin (in Chinese with English abstract). *Acta Pet. Sin.* 44, 125–143.

Tao, K., Cao, J., Hu, W., Zhi, D., Lei, D., Tang, Y., et al. (2021). Petroleum system for the continuous oil play in the lacustrine Lower Triassic, Junggar Basin, China. *AAPG Bull.* 105, 2349–2380. doi:10.1306/07022119211

Wang, R., Ding, W., Zhang, Y., Wang, Z., Wang, X., He, J., et al. (2016a). Analysis of developmental characteristics and dominant factors of fractures in lower cambrian marine shale reservoirs: A case study of niutitang formation in cen'gong block, southern China. *J. Petroleum Sci. Eng.* 138, 31–49. doi:10.1016/j.petrol.2015.12.004

Wang, R., Gu, Y., Ding, W., Gong, D., Yin, S., Wang, X., et al. (2016b). Characteristics and dominant controlling factors of organic-rich marine shales with high thermal maturity: A case study of the lower cambrian niutitang Formation in the cen'gong block, southern China. *J. Nat. Gas. Sci. Eng.* 33, 81–96. doi:10.1016/j.jngse.2016.05.009

Wang, R., Hu, Z., Long, S., Liu, G., Zhao, J., Dong, L., et al. (2019). Differential characteristics of the upper ordovician-lower silurian wufeng-longmaxi shale reservoir and its implications for exploration and development of shale gas in/around the Sichuan Basin. *Acta Geol. Sin. - Engl. Ed.* 93, 520–535. doi:10.1111/1755-6724.13875

Wang, R., Hu, Z., Sun, C., Liu, Z., Zhang, C., Gao, B., et al. (2018). Comparative analysis of shale reservoir characteristics in the wufeng-longmaxi (O3w-S1l) and niutitang (Є1n) formations: A case study of wells JY1 and TX1 in the southeastern Sichuan Basin and its neighboring areas, southwestern China. *Interpretation* 6, SN31–SN45. doi:10.1190/int-2018-0024.1

Wang, S., Wang, G., Huang, L., Song, L., Zhang, Y., Li, D., et al. (2021). Logging evaluation of lamina structure and reservoir quality in shale oil reservoir of Fengcheng Formation in Mahu Sag, China. *Mar. Pet. Geol.* 133, 105299. doi:10.1016/j.marpetgeo.2021.105299

Wang, X., Jin, Z., Chen, G., Peng, M., Huang, L., Wang, Z., et al. (2022). Multi-scale natural fracture prediction in continental shale oil reservoirs: A case study of the Fengcheng Formation in the Mahu sag, Junggar Basin, China. *Front. Earth Sci.* 10. doi:10.3389/feart.2022.929467

Wu, Y., Liu, C., Jiang, F., Hu, T., Lv, J., Zhang, C., et al. (2022). Geological characteristics and shale oil potential of alkaline lacustrine source rock in Fengcheng Formation of the Mahu Sag, Junggar Basin, Western China. *J. Petroleum Sci. Eng.* 216, 110823. doi:10.1016/j.petrol.2022.110823

Xia, L., Cao, J., Stüeken, E. E., Zhi, D., Wang, T., and Li, W. (2020). Unsynchronized evolution of salinity and pH of a permian alkaline lake influenced by hydrothermal fluids: A multi-proxy geochemical study. *Chem. Geol.* 541, 119581. doi:10.1016/j.chemgeo.2020.119581

Xiao, W., Han, C., Yuan, C., Sun, M., Lin, S., Chen, H., et al. (2008). Middle cambrian to permian subduction-related accretionary orogenesis of northern Xinjiang, NW China: Implications for the tectonic evolution of central asia. *J. Asian Earth Sci.* 32, 102–117. doi:10.1016/j.jseaes.2007.10.008

Yang, Z., Wang, X., Ge, H., Zhu, J., and Wen, Y. (2022). Study on evaluation method of fracture forming ability of shale oil reservoirs in Fengcheng Formation, Mahu sag. *J. Petroleum Sci. Eng.* 215, 110576. doi:10.1016/j.petrol.2022.110576

Zeng, L., and Li, X. (2009). Fractures in sandstone reservoirs with ultra-low permeability: A case study of the upper triassic yanchang Formation in the Ordos Basin, China. *AAPG Bull.* 93, 461–477. doi:10.1306/09240808047

Zeng, L., Ma, S., Tian, H., Xue, M., Liu, G., and Lyu, W. (2022). Research progress of natural fractures in organic rich shale (in Chinese with English abstract). *Earth Sci.*, 1–15.

Zeng, L., Su, H., Tang, X., Peng, Y., and Gong, L. (2013). Fractured tight sandstone oil and gas reservoirs: A new play type in the dongpu depression, Bohai Bay Basin, China. *AAPG Bull.* 97, 363–377. doi:10.1306/09121212057

Zhang, C., Liu, D., Jiang, Z., Song, Y., Luo, Q., and Wang, X. (2022). Mechanism for the formation of natural fractures and their effects on shale oil accumulation in Junggar Basin, NW China. *Int. J. Coal Geol.* 254, 103973. doi:10.1016/j.coal.2022.103973

Zhang, G., Wang, Z., Guo, X., Sun, Y., Sun, L., and Pan, L. (2019). Characteristics of lacustrine dolomitic rock reservoir and accumulation of tight oil in the Permian Fengcheng Formation, the Western slope of the Mahu Sag, Junggar Basin, NW China. *J. Asian Earth Sci.* 178, 64–80. doi:10.1016/j.jseaes.2019.01.002

Zhang, Z., Yuan, X., Wang, M., Zhou, C., Tang, Y., Chen, X., et al. (2018). Alkaline-lacustrine deposition and paleoenvironmental evolution in permian Fengcheng Formation at the Mahu sag, Junggar Basin, NW China. *Pet. Explor. Dev.* 45, 1036–1049. doi:10.1016/s1876-3804(18)30107-1

Zhao, W., Hu, S., Hou, L., Yang, T., Li, X., Guo, B., et al. (2020). Types and resource potential of continental shale oil in China and its boundary with tight oil. *Pet. Explor. Dev.* 47, 1–11. doi:10.1016/s1876-3804(20)60001-5

Zhi, D., Tang, Y., He, W., Guo, X., Zheng, M., and Huang, L. (2021). Orderly coexistence and accumulation models of conventional and unconventional hydrocarbons in lower permian Fengcheng Formation, Mahu sag, Junggar Basin. *Pet. Explor. Dev.* 48, 43–59. doi:10.1016/s1876-3804(21)60004-6

Zhou, L., Zhu, J., Song, Y., Lu, P., Qu, J., You, X., et al. (2019). Analysis of fault characteristics and reservoir control in Triassic Baikouquan Formation in central and eastern Mahu depressin (in Chinese with English abstract). *Earth Sci. Front.* 26, 248–261.

Zou, C., Yang, Z., Cui, J., Zhu, R., Hou, L., Tao, S., et al. (2013). Formation mechanism, geological characteristics and development strategy of nonmarine shale oil in China. *Pet. Explor. Dev.* 40, 15–27. doi:10.1016/s1876-3804(13)60002-6

Zeng, L., Lyu, W., Li, J., Zhu, L., Weng, J., Yue, F., et al. (2016). Natural fractures and their influence on shale gas enrichment in Sichuan Basin, China. *J. Nat. Gas Sci. Eng.* 30, 1–9. doi:10.1016/j.jngse.2015.11.048

Xia, L., Cao, J., Bian, L., Hu, W., Wang, T., Zhi, D., et al. (2022). Co-evolution of paleo-environment and bio-precursors in a Permian alkaline lake, Mahu mega-oil province, Junggar Basin: Implications for oil sources. *Science China Earth Sciences* 65, 462–476. doi:10.1007/s11430-021-9861-4

frontiers | Frontiers in Earth Science

TYPE Original Research
PUBLISHED 01 June 2023
DOI 10.3389/feart.2023.1218788

OPEN ACCESS

EDITED BY
Leibo Bian,
Aarhus University, Denmark

REVIEWED BY
Chao Liang,
China University of Petroleum, Huadong, China
Lei Wu,
Zhejiang University, China

*CORRESPONDENCE
Yuanyuan Zhang,
yy-zhang@pku.edu.cn

RECEIVED 08 May 2023
ACCEPTED 22 May 2023
PUBLISHED 01 June 2023

CITATION
Ni M, Zhang Y, Tang Y and He W (2023), Distribution characteristics of organic matter in the Fengcheng Formation in Mahu Sag, Junggar Basin: implications for hydrocarbon generation model in alkaline lacustrine deposition.
Front. Earth Sci. 11:1218788.
doi: 10.3389/feart.2023.1218788

Distribution characteristics of organic matter in the Fengcheng Formation in Mahu Sag, Junggar Basin: implications for hydrocarbon generation model in alkaline lacustrine deposition

Minjie Ni[1], Yuanyuan Zhang[1]*, Yong Tang[2] and Wenjun He[2]

[1]School of Earth and Space Sciences, Peking University, Beijing, China, [2]PetroChina Xinjiang Oilfield Company, Karamay, China

Alkaline lacustrine deposits are known for their high primary productivity, unique aquatic environments, and sedimentary patterns, which are conducive to the formation and preservation of organic matter. Consequently, related source rocks have significant hydrocarbon generation potential. The study of hydrocarbon source rocks in the Fengcheng Formation of the Mahu Sag in the Junggar Basin serves as a good example for understanding organic matter enrichment and hydrocarbon generation characteristics of such alkaline lacustrine deposits source rocks. However, the characteristics of organic matter and hydrocarbon generation model in the source rocks of Fengcheng Formation lack systematic research, thus hindering exploration planning and favorable area selection. In this study, analysis of mineral content based on X-ray diffraction and organic geochemical analysis were employed, along with systematic observations of bio-precursor types under fluorescence microscopy. Based on mineral identification and quantitative statistics, the Fengcheng Formation was classified into three zones according to different alkaline mineral assemblages: an inner zone dominated by sodium carbonate minerals, a transitional zone with higher borosilicate mineral content, and a marginal zone characterized by abundant calcite deposition. The inner zone is characterized by the presence of lamalginite and telalginite, which are influenced by high pH values and changes in water depth, and exhibit high maturity characteristics. The transitional zone exhibits high total organic carbon (TOC) values, with predominantly type I and type II_1 kerogen. Under fluorescence, the main components were observed to be lamalginite and telalginite, with their distribution being influenced by high salinity and ash supply. The marginal zone has relatively lower TOC than the previous two zones, which is dominated by type II_2 kerogens, and contains a certain quantity of terrigenous inertinite supply. The hydrocarbon generation patterns of lamalginite and telalginite are consistent with the bimodal efficient hydrocarbon generation model observed in the source rocks of Fengcheng Formation, revealing the unique hydrocarbon generation model of organic matter in alkaline lacustrine source rocks. This research has significant implications for the exploration strategy of the alkaline lacustrine deposits in the Fengcheng Formation and similar oil- and gas-bearing basins.

KEYWORDS

distribution characteristics, Fengcheng Formation, organic matter, hydrocarbon generation model, alkaline lacustrine deposition

1 Introduction

Alkaline lacustrine deposits are the most productive aquatic environments in the world, with an average productivity level exceeding that of terrestrial aquatic environments by an order of magnitude (Grant et al., 1990; Sorokin et al., 2014). Alkaline lakes with a pH > 9 are a special type of saline lake. In this type of lakes, high CO_2 level causes a rise in pH and various sodium carbonate minerals precipitate by evaporation (Warren, 2016). High pH values in alkaline lakes can activate various nutrient elements and compounds such as Mo, phosphate, and silicate, thereby improving the primary productivity of water bodies (Helz et al., 2011; Li et al., 2021). Therefore, alkaline lacustrine deposits environments are conducive to the deposition of high-quality source rocks (Tänavsuu-Milkeviciene and Frederick Sarg, 2012). Alkaline lacustrine deposits are often associated with oil shales, and their presence typically indicates significant oil and gas resources, as evidenced by previous research on the widespread occurrence of abundant benthic algal mats in the alkaline lacustrine deposits of the Eocene Green River Formation, United States (Horsfield et al., 1994; Katz, 1995; Ruble et al., 2001). These algal mats, which contain lipid-rich components preserved through reactions with inorganic sulfur species produced by bacterial sulfate reduction, represent oil shales with high total organic carbon (TOC) content dominated by type I kerogen (Katz, 1995; Ruble and Philp, 1998; Dyni, 2006). In the contemporaneous Nanxiang Basin of China, the Oligocene Hetaoyuan Formation in the Biyang Sag is characterized by organic-rich shales dominated by type I kerogen (algal mats), with high oil-generating potential and TOC values of up to 8.6%. This suggests that the Hetaoyuan Formation has significant potential for shale oil development (He et al., 2018; Song et al., 2019). In general, the study of alkaline lacustrine deposits source rock holds great significance for oil and gas exploration, particularly in the context of shale oil exploration.

The hydrocarbon source rocks of the Fengcheng Formation in the Mahu Sag of the Junggar Basin are ancient alkaline lacustrine deposits that exhibit source and reservoir characteristics, and are considered a new type of alkaline lacustrine shale oil reservoir (Tang Y. et al., 2021a). Lipid biomarker evidence suggest Fengcheng Formation were stratified in reducing condition and the preserved organic matter of the alkaline lake is dominated by algae and bacteria, with less input from terrigenous plant (Xia et al., 2021). Geochemical and biomarker analyses reveal that the Fengcheng Formation exhibits typical characteristics of high-quality alkaline lacustrine source rocks, with a high abundance of organic matter, favorable types, and strong hydrocarbon-generating potential, enriched with algal organic matter and microbial development (Cao et al., 2020). However, there is a lack of systematic discrimination of the specific types of bio-precursor in source rocks, leading to a lack of systematic research on the issue of low TOC corresponding to relatively high oil and gas reserves. Therefore, it is necessary to strengthen the study of organic matter distribution and formation mechanisms in alkaline lakes, explore the controlling factors of organic matter distribution, and further investigate specific hydrocarbon generation model based on characteristics of organic matter in the Fengcheng Formation.

This study combines mineral observations and quantitative analysis of the Lower Permian Fengcheng Formation in the Mahu Sag to delineate the lateral distribution of different facies and combines it with organic geochemical analysis to conduct qualitative research on hydrocarbon source rocks in different zones. Meanwhile, the identification of bio-precursor types under a fluorescence microscope, in conjunction with the hydrocarbon generation model of the alkaline lake in the Fengcheng Formation, helps improve our comprehensive understanding of organic matter characteristics in the alkaline lacustrine deposits hydrocarbon source rocks of the northwestern margin of the Junggar Basin, and provides new insights for deep exploration in similar basins.

2 Geological background

The Junggar Basin is a large superimposed petroliferous basin in northwest China, and the Mahu Sag is located at the northwestern margin of the Junggar Basin (Figures 1A, B). The Sag is an Early Permian extensional fault-controlled graben (Chen et al., 2010; Han et al., 2010; Han and Zhao, 2018). Mahu Sag is known for its high hydrocarbon accumulation potential and is considered one of the most prolific hydrocarbon source sags in the Junggar Basin (Kuang et al., 2012; Lei et al., 2017). The structural and sedimentary processes of the Mahu Sag during the Permian can be classified into three stages (Tang et al., 2020; Tang W. et al., 2021a; Tang W. et al., 2021b). During the Early Permian, it experienced a tectonic subsidence phase with syn-rift faulting, where the mechanical subsidence rate exceeded the sedimentation rate. The transgressive system tract of the Jiamuhe Formation and Fengcheng Formation transitioned from a fan delta to a deep lacustrine environment, with the lacustrine basin expanding and the fan delta regressing. The sedimentary center and fan delta were distributed along the boundaries of normal faults, forming an important hydrocarbon source rock succession in the Mahu Sag. During the Middle Permian, it entered a post-rifting thermal subsidence phase characterized by the regression system tract of the Xiazijie Formation, Lower Wuerhe Formation, and Upper Wuerhe Formation, along with an expansion of the sedimentary range. The sedimentary environment transitioned from that of a lacustrine to a fan delta, with the lacustrine basin shrinking and the sedimentary center stabilizing in the central part of the Mahu Sag. During this stage, the sedimentation rate exceeded the thermal subsidence rate. During the Late Permian to Early Triassic, there was a tectonic inversion, with the fan delta distributed along the right-lateral strike-slip fault belts of Hongche, Wuxia, and Kebai, and the sedimentary center migrating toward the southeast (Tang W. et al., 2021a). Volcanic rocks and pyroclastic rocks were mainly deposited in

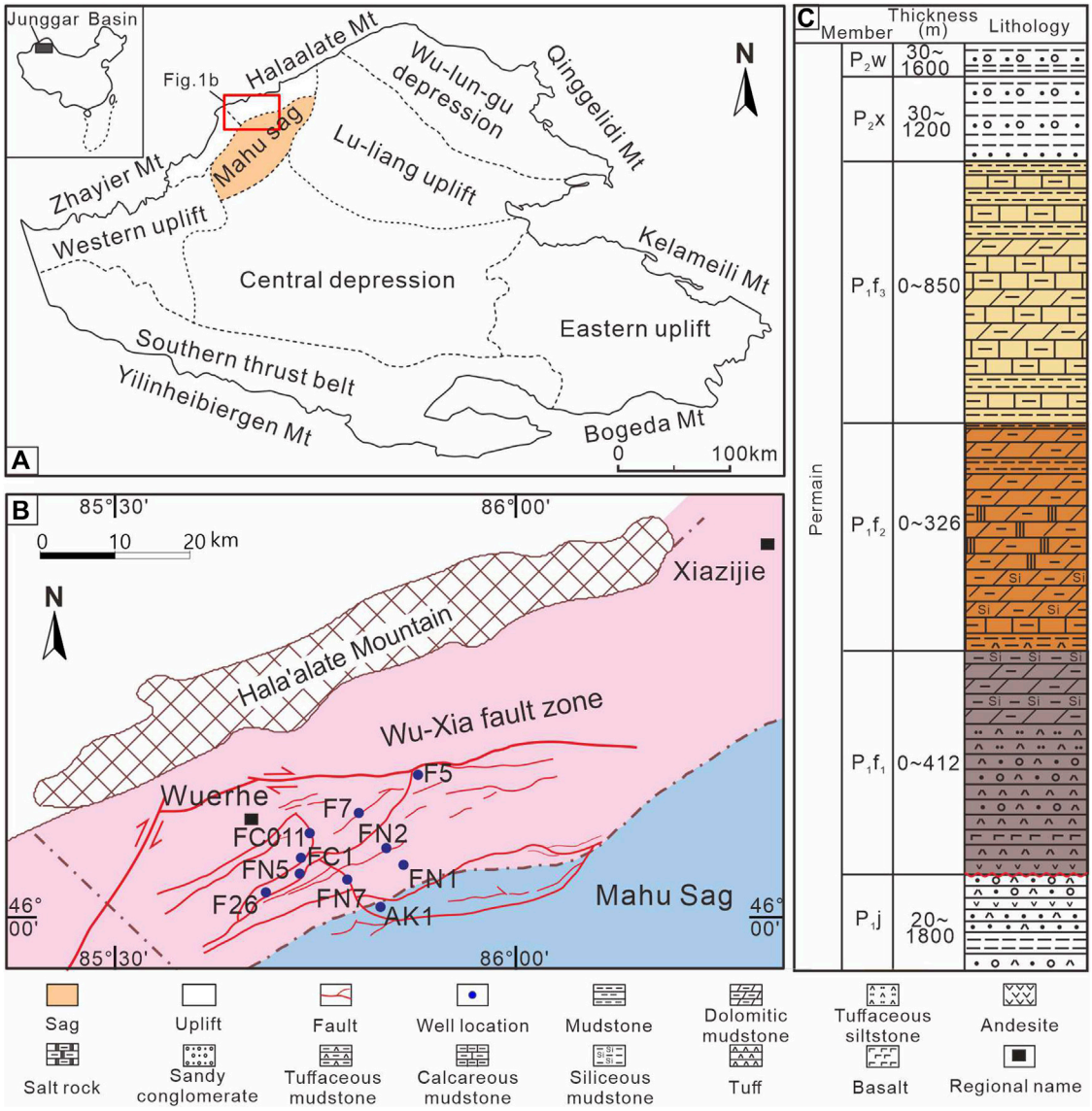

FIGURE 1
Comprehensive geological map of the study area. **(A)** Regional division map of the Junggar Basin. **(B)** Location map of the northern Mahu Sag study area and distribution of faults. **(C)** Stratigraphic profile of the Fengcheng Formation in the Mahu Sag. P_1j = Jiamuhe Formation, P_1f_1 = the Lower Member, P_1f_2 = the Middle Member, P_1f_3 = Upper Member, P_2x = Xiazijie Formation, P_2w = Wuerhe Formation.

the northeast of the Mahu sag. Conglomerate and coarse-grained sandstone are mainly distributed near the boundary faults, and finer sandstones and mudstones are dominated away from the boundary faults (Yu et al., 2018a; Zhi et al., 2021).

The lacustrine facies of the Fengcheng Formation in the Lower Permian are considered the oldest known alkaline lacustrine deposits discovered in China to date, and they are recognized as high-quality hydrocarbon source rocks (Cao et al., 2015; Cao et al., 2020). These sediments form an important foundation for the extensive oilfield in the northwest margin of the Junggar Basin. The Fengcheng Formation is abundant in oil and gas resources, with developed source and reservoir beds, characterized by self-generated and self-reservoired properties (Kuang et al., 2012; Lei et al., 2017). The sedimentary rock composition is complex, with thin and interbedded layers exhibiting strong rhythmicity, and is considered a new type of lacustrine shale oil reservoir (Zhi et al., 2019; Tang Y. et al., 2021c), possessing significant potential for shale oil production. The distribution range of shale oil reservoirs in the Mahu Sag is controlled by high-quality source rocks with alkaline lacustrine deposits, which forms the foundation of the entire oil and gas system in the Mahu Sag.

The formation of alkaline lacustrine source rocks in the Fengcheng Formation of the Mahu Sag is believed to have occurred in a high-salinity, closed-basin lacustrine environment influenced by deep-seated hydrothermal and volcanic activities. This environment is characterized by abundant alkaline minerals and exhibits complex and variable lithology and mineral

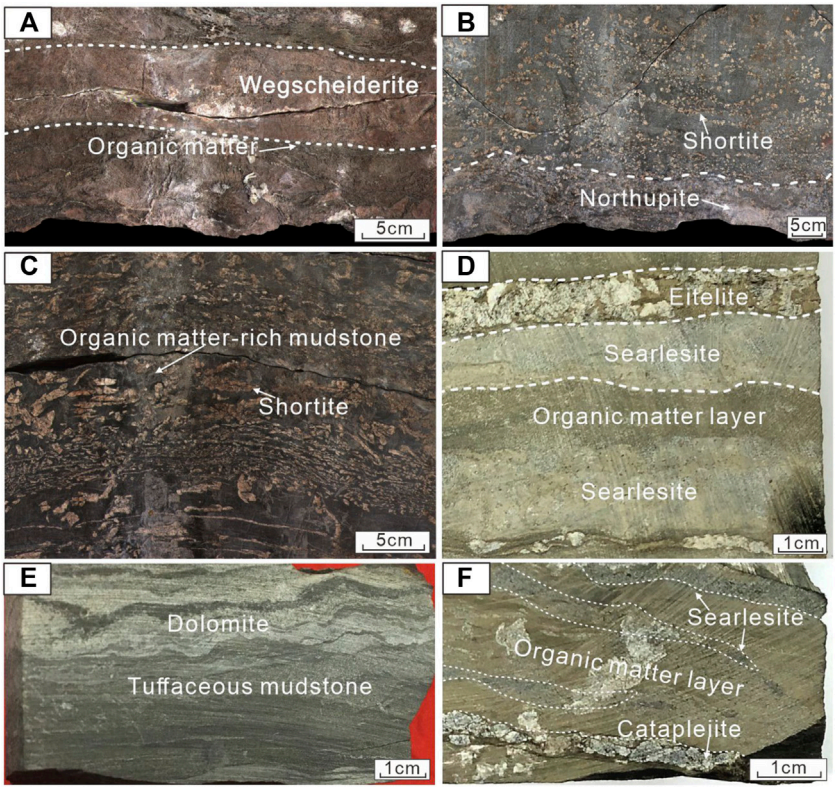

FIGURE 2
Photographs of core samples. **(A)** The top and bottom parts of the wegscheiderite bearing layer are mudstones, with a high organic content in the transition layer. The wegscheiderite content in the mudstone layer is low, dominated by shortite and northupite, well FN5, P_1f_2. **(B)** The upper mudstone layer is mainly composed of shortite, while the lower layers have an increased content of northupite and reedmergnerite, well FN5, P_1f_2. **(C)** Shortite in hand specimens exhibits various shapes, and there is a substantial amount of special organic matter developed in the mudstone matrix, well FN5, P_1f_2. **(D)** White eitelite and searlesite occur in layered distribution, and there are clusters of searlesite in the brown-yellowish-white dolomitic mudstone below, which is rich in organic matter, well F26, P_1f_3. **(E)** Deposition of tuffaceous and dolomitic mudstone, well F26, P_1f_3. **(F)** A significant amount of organic matter with yellow-green color is developed in the dolomitic mudstone, and alkaline mineral searlesite clusters and characteristic mineral catapleite are also developed, well F26, P_1f_3.

composition (Zhang Y. et al., 2018). Based on different lithofacies combinations and sedimentary environments, the Fengcheng Formation is classified into three units from bottom to top: Lower Member (P_1f_1), Middle Member (P_1f_2), and Upper Member (P_1f_3) (Figure 1C). The lower part of the Lower Member (P_1f_1) is predominantly composed of coarse clastic rocks, organic-rich mudstones, interbedded dolomitic mudstones, intermediate to mafic volcanic rocks, tuffaceous rocks, and welded tuff rocks, whereas the upper part is mainly composed of organic-rich mudstones and tuffaceous interbeds. The Middle Member (P_1f_2) is mainly composed of organic-rich shale, mudstone, dolomitic mudstone, and siltstone, with abundant alkaline minerals present, such as wegscheiderite, shortite, eitelite, northupite, reedmergnerite, and searlesite (Zhang Y. et al., 2018). The lower part of the Upper Member (P_1f_3) is dominated by mudstones and interbedded dolomitic mudstones, while the upper part is characterized by terrigenous clastic sedimentary rocks. Extensive geochemical studies indicate that the paleoclimatic conditions of the Lower Member shifted from semi-arid to humid, while the Middle Member transitioned from humid to arid, and the Upper Member reverted back to a semi-arid climate (Cao et al., 2015; Zhang Z. et al., 2018).

3 Sample and experimental methods

Based on observations and descriptions of core samples from 10 wells in the study area (Figures 2A–F), we selected 80 samples from the Permian Fengcheng Formation for organic matter and related analyses.

First, the samples were cut into blocks of suitable size, and the cut samples were subjected to multiple polishing processes to obtain regular thin sections (30 μm) and probe sections (35–40 μm) for optical observation, and specific polished thin sections for fluorescence. The remaining samples were ground to approximately 200 mesh using an agate mortar and pestle for whole-rock mineral analysis using X-ray diffraction, measurement of TOC content, and rock pyrolysis experiments.

Initially, the minerals in the thin sections were preliminarily identified under a microscope. Then, 80 powder samples containing various types of minerals were selected for X-ray diffraction (XRD) analysis. The samples were analyzed using a D8 Advance X-ray diffractometer with an incident slit width of 0.3 mm and a detector slit width of 8 mm. The scanning angle (2θ) was set from 4.5° to 50° with a step size of 0.02° and a scanning time of 0.5 s per step. Data processing was carried out using Jade 6.5 software.

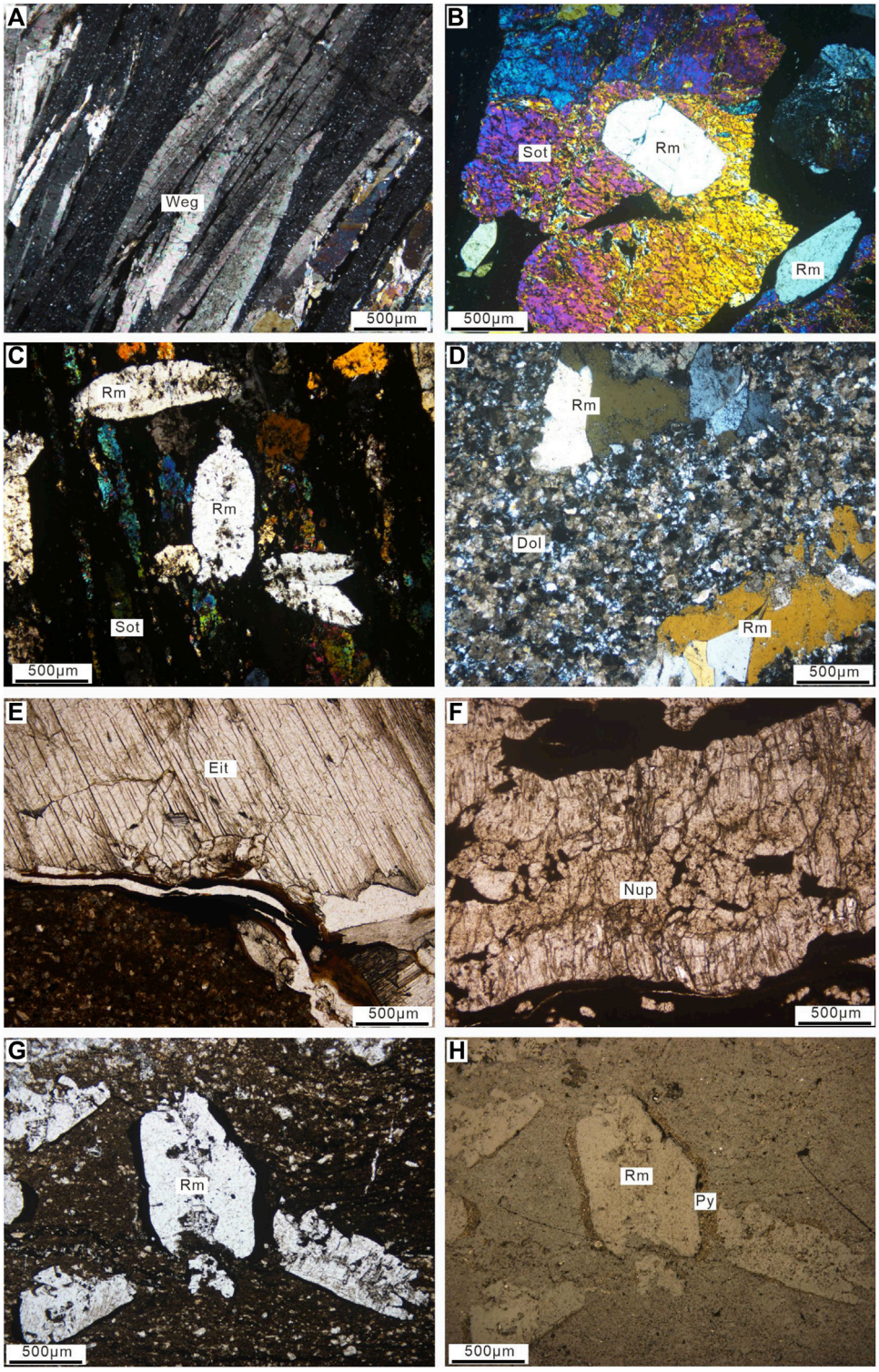

FIGURE 3
(A) Columnar crystals of wegscheiderite in a pure alkali layer, which appear colorless and exhibit high-grade white interference color under cross-polarized light, well FN5, P_1f_2. **(B)** In the alkaline mineral-rich mudstone, the anhedral shortite contains euhedral reedmergnerite, as observed under cross-polarized light, well FN7, P_1f_2. **(C)** Reedmergnerite cross-cuts the shortite, as observed under cross-polarized light, well AK1, P_1f_1. **(D)** Anhedral reedmergnerite crystals are developed in the dolomitic mudstone, as observed under cross-polarized light, well FN1, P_1f_1. **(E)** Vein-like crystals of eitelite are present in the dolomitic mudstone, as observed under plane-polarized light, well F26, P_1f_3. **(F)** Aggregates of anhedral northupite crystals are found in the alkaline mineral-rich mudstone, as observed under plane-polarized light, well FN5, P_1f_2. **(G)** and **(H)** Fine-grained pyrite is accumulated around the subhedral reedmergnerite crystals in the dolomitic mudstone, with **(G)** observed under plane-polarized light and **(H)** observed under reflected light, well FN2, P_1f_2. Abbreviations: Weg, Wegscheiderite, Sot, Shortite, Rm, Reedmergnerite, Dol, Dolomite, Eit, Eitelite, Nup, Northupite, Py, Pyrite.

The TOC and rock pyrolysis analyses were conducted on 80 samples. The 200-mesh powder samples were soaked in diluted HCl (5%) for 24 h, centrifuged, dried to remove inorganic carbon, and then continuously washed with distilled water until neutral. The samples were analyzed using a LECO CS-230 C–S analyzer. The milled samples were subjected to rock pyrolysis analysis using a Rock-Eval six pyrolysis instrument, and the main test results included S1 (free hydrocarbons), S2 (pyrolyzed hydrocarbons), and Tmax, which represents the maximum heating temperature at the peak of S_2. Finally, the hydrogen index (HI) was calculated using the formula HI = S_2/TOC × 100, and the oxygen index (OI) was calculated as OI = S_3/TOC × 100.

A Nikon E200 microscope with a ×50 oil-immersion objective lens was used to conduct reflectance and fluorescence microscopic observations on 75 fluorescence slides, following the methods described by Taylor et al. (1998). The types of organic matter were determined based on the morphology, reflectance, and fluorescence colors of the organic material, following the classification scheme provided by ICCP (1994, 1998, and 2001), as outlined by Pickel et al. (2017).

The selected thin sections and bulk samples were observed, imaged, and analyzed using a FEI Quanta 650 FEG field-emission scanning electron microscope equipped with an Oxford INCA X-MAX50 250+ X-ray energy-dispersive spectrometer. The acceleration voltage was set at 15–20 kV, the beam current was 5 nA, and the working distance was approximately 10 mm.

4 Results

4.1 Alkaline minerals and their distribution characteristics

Based on the lithological characteristics observed from drilling core samples and thin section analysis, it is evident that the northern part of the Mahu Sag is characterized by the presence of abundant alkaline minerals, including laminar, thinly laminar, spotted, cloud-like, and pure alkali layers. Based on lithofacies and mineralogical analysis, the alkaline minerals in the Fengcheng Formation of the Mahu Sag can be classified into four categories: sodium carbonate, sodium silicate, characteristic, and common minerals. The sodium carbonate minerals mainly include shortite ($Na_2Ca_2(CO_3)_3$), wegscheiderite ($Na_2CO_3{\cdot}3NaHCO_3$), northupite ($Na_3Mg(CO_3)_2Cl$), and eitelite ($Na_2Mg(CO_3)_2$). Wegscheiderite occurs as thick layers ranging from several centimeters to tens of centimeters (Figures 2A, 3A), and is often associated with low quantities of nahcolite, trona, and other minerals. Shortite is primarily distributed in the Lower and Middle members, occurring as banded or massive aggregates in mudstones, some of which are intergrown with spotted northupite crystals (Figure 3F). Eitelite is mainly distributed in the transitional zone between the pure alkaline layer (wegscheiderite layer) and mud layers, mostly occurring in layers with a thickness of 0.1–5 cm (as shown in Figure 3E). Moreover, a low quantity of eitelite crystals also occurs in a subhedral to anhedral distribution in layers enriched with wegscheiderite. Sodium borosilicate minerals refer to sodium-rich silicate minerals that form in alkaline lacustrine environments, primarily distributed along the margin of the Mahu Slope near the Wuxia Fault Belt. These minerals are often associated with sodium carbonate minerals, and include reedmergnerite, searlesite, and leucosphenite. In the mudstone interbeds with dolomitic mudstone, reedmergnerite and searlesite coexist, forming horizontal laminations, vein-like bodies, and lenses (Figures 3B–D, G, H). The characteristic minerals in these deposits include relatively minor quantities of burbankite, catapleiite, leucosphenite, and aegirine. Common minerals include dolomite, ankerite, and pyrite. Dolomite and ankerite are widely distributed, occurring in the slope and sag areas of the Fengcheng region. The morphology of dolomite and ankerite in the Fengcheng Formation can be categorized as rosette-like, spotted aggregates, and euhedral grains (Figure 3D). Framboids pyrite and layered pyrite at the bottom of the wegscheiderite layer are also observed in the core samples, as well as coarse-grained euhedral pyrite occurring in reedmergnerite or quartz veins.

Based on observations from thin sections, scanning electron microscopy (SEM), energy-dispersive X-ray spectroscopy (EDS) data, and XRD analysis, the distribution of alkaline minerals and common minerals in the Fengcheng Formation exhibits a clear and systematic pattern. Based on the mineral assemblages observed on the plane, the alkaline lacustrine deposits of the Fengcheng Formation can be classified into three zones: 1) inner zone, 2) transitional zone, and 3) marginal zone. The inner zone is located in the center of the sag, with major well locations such as AK1, FN5, and FN7 (with the lithologic column of well FN5 shown in Figure 4). Based on results of the XRD analysis, the inner zone is characterized by the presence of sodium carbonate minerals (the sodium carbonate content is up to 79%), with the mineral assemblage dominated by wegscheiderite and shortite. Meanwhile, common minerals such as calcite and dolomite are not well developed in the inner zone. The transitional zone is characterized by a mineral assemblage of sodium borosilicate minerals, including reedmergnerite and searlesite, with significantly higher content than the inner and marginal zones (the sodium borosilicate content is up to 49%). Additionally, calcite and dolomite start to appear in the transitional zone, with dolomite being more abundant than calcite. Wells F26, FN2, FC011, FN1, and FN4 are located within the transitional zone (Figure 4). In the marginal zone, there is a significant increase in the abundance of calcite, which is much higher than in the inner and transitional zones (the content of calcite is up to 27%). At the same time, sodium carbonate minerals are largely absent in the marginal zone and the content of reedmergnerite and searlesite is very small. Wells F5, F7, and MY1 are located in the marginal zone. There is a regular variation in mineral content from the inner zone to the marginal zone, with a gradual decrease in sodium carbonate minerals from the center to the margin. The highest contents of reedmergnerite and searlesite are observed in the transitional zone, while calcite is absent in the inner zone and reaches its highest content in the marginal zone. The content of felsic minerals is positively correlated with the abundance of clastic rocks in sedimentary rocks such as mudstone and dolomitic mudstone, which exhibit a decrease in mineral content from the inner zone to the marginal zone (Figure 5A). Therefore, the

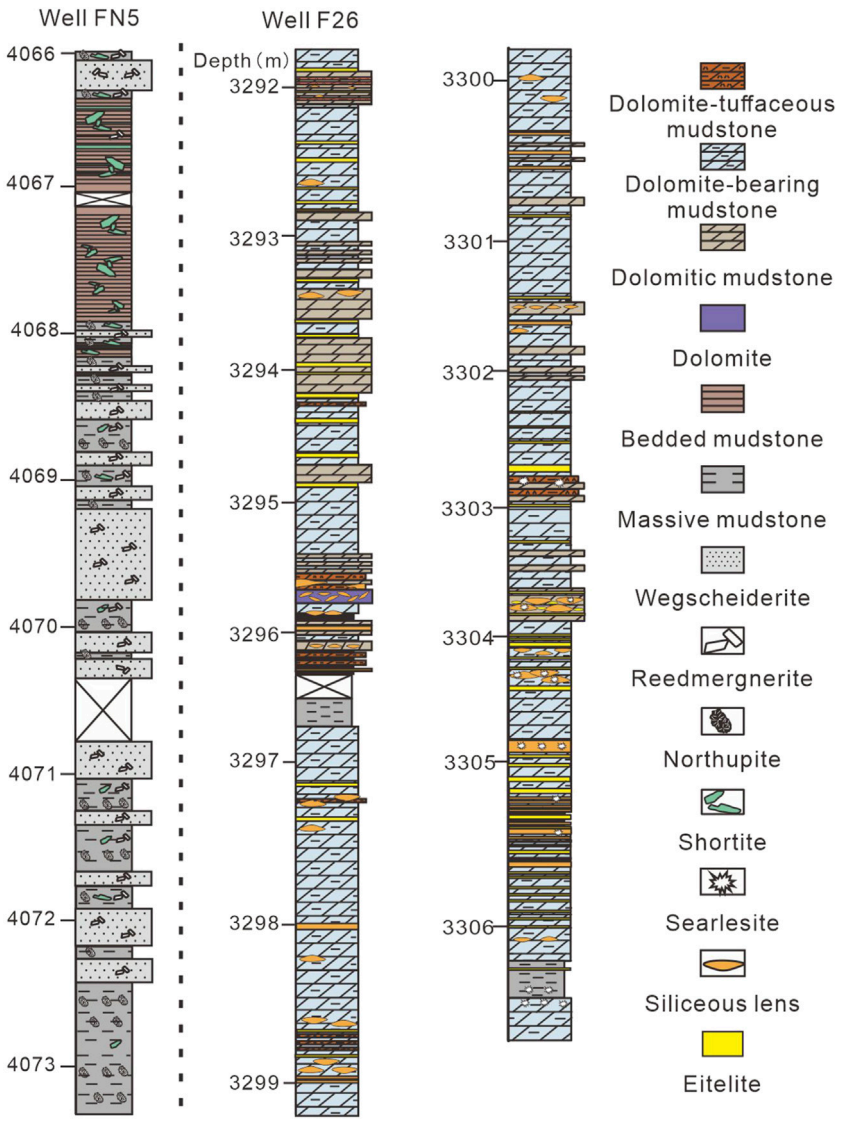

FIGURE 4
Lithological columnar diagrams for wells FN5 and F26 (well locations shown in Figure 1).

plane distribution of the Fengcheng Formation can be classified into three zones based on changes in mineral composition. At the same time, clay mineral content also exhibits a certain distribution pattern. From the inner zone to the marginal zone, the content of illite–smectite mixed layers increases while the content of illite decreases (Figure 5B). In the inner zone, the content of illite is the highest, with some samples reaching 100%.

4.2 Organic geochemical characteristics

Based on the results summarized from previous studies (Chen et al., 2016; Gao et al., 2018; Xiao et al., 2021; He et al., 2022; Hou et al., 2022), the TOC content of the source rocks in the Fengcheng Formation ranges from 0.03% to 4.17%, with an average of 0.96%. The S_1+S_2 values of the source rocks range from 0.15 mg/g to 29.56 mg/g, with an average of 5.63 mg/g. Overall, the source rock samples from the Fengcheng Formation exhibit characteristics of high organic matter abundance (TOC >1.0%) and high hydrocarbon generation potential (S_1+S_2 > 6.0 mg/g) (Figure 6A). Most of the samples are classified as moderate to high-quality source rocks. High-quality source rocks constitute 40% and are characterized by a predominance of sapropelic type organic matter, indicating a high hydrocarbon generation potential. Results of the classification of kerogen types based on the Van Krevelen diagram indicate that the dominant kerogen types in the shale of the Fengcheng Formation are type II_2 and type II_1(Welte and Tissot, 1984), with minor occurrences of type I and type III kerogens (Figure 6B). Among these, type I and type II_1 kerogens exhibit the highest oil-prone characteristics and have relatively high residual hydrocarbon generation potential in the shale. The organic matter of the Fengcheng Formation shale sample in the

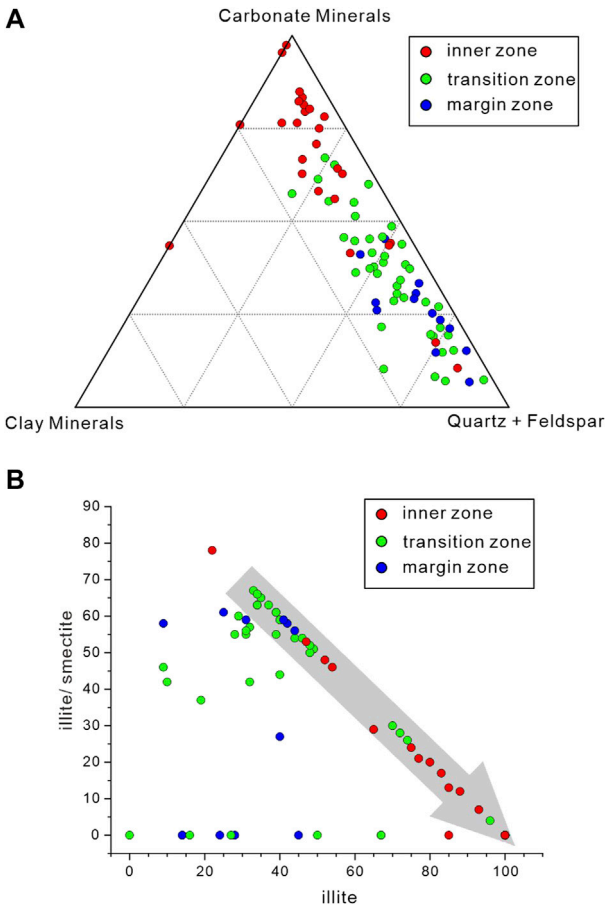

FIGURE 5
(A) Classification of mineral species using the triangular diagram in the Fengcheng Formation. **(B)** Correlation between illite and illite-smectite layers in the clay minerals of the Fengcheng Formation.

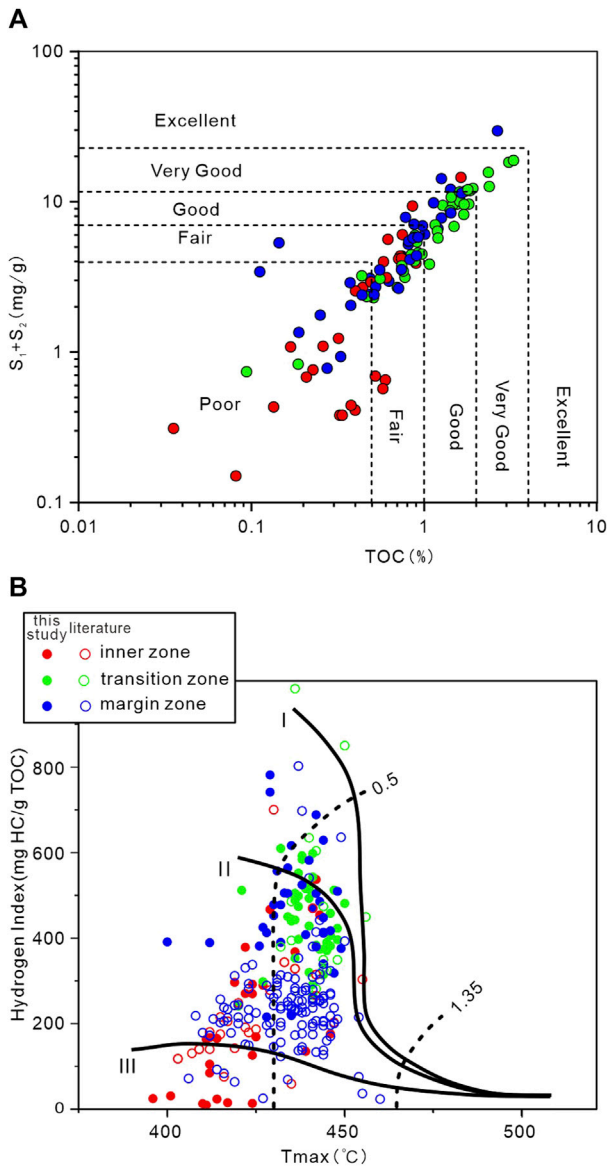

FIGURE 6
(A) Correlation between TOC content and hydrocarbon generation potential in the shale of the Fengcheng Formation. The base map is based on studies by Mukhopadhyay et al. (1995) and Peters et al. (1994). **(B)** Classification of organic matter types in the Fengcheng Formation. (Data are sourced from Chen et al., 2016; Gao et al., 2018; He et al., 2022; Xiao et al., 2021).

study area is generally in the low maturity to mature stage (Figure 6B), with Ro range of 0.56%–1.14% and an average of 0.80%. This indicates that the organic matter has reached the mature stage. In summary, the shale of the Fengcheng Formation is a good quality source rock, with high organic matter abundance, favorable oil generation potential, and overall maturity.

4.3 Types of organic matter

A large number of organic matters, including bacteria, algae and higher plants, were observed in the alkaline lacustrine deposits of the Fengcheng Formation. Bacteria, mainly spherical microorganisms, are seldomly observed in the marginal zone, and not discussed in this study. Algae contain both telalginite and lamalginite, which developed throughout the entire region. Most higher plants are distributed in the marginal zone in the form of inertinites.

4.3.1 Inner zone

The organic matter in the inner zone of the Fengcheng Formation is primarily composed of algal material, including well-preserved telalginite and lamalginite algal (Figure 7). These exhibit typical yellow and yellow-green fluorescence. Because the wegscheiderite layer in the inner zone is interbedded with mudstone layers, where shortite, eitelite, and northupite are developed, and reedmergnerite is developed throughout (FN5 in Figure 4). Under microscopic observation, organic matter is rarely present in the wegscheiderite layer. In the transition layer between the wegscheiderite layer and the mudstone layer, a large number of lamalginites are developed, which undergo deformation due to the later compression of reedmergnerite (Figure 7A). Specific morphological telalginites

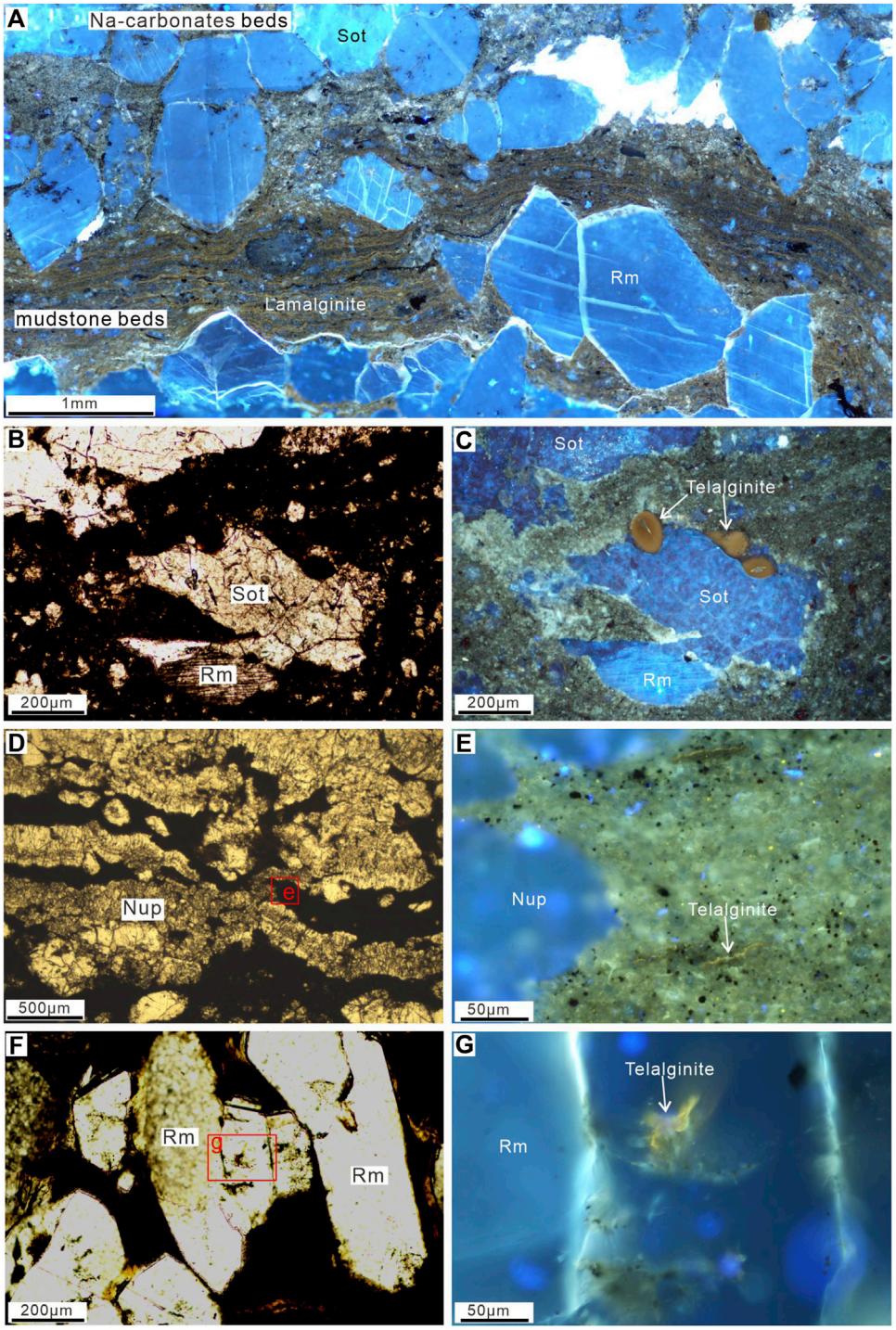

FIGURE 7
Microscopic photographs of organic matter in the inner zone. **(A)** The transition layer between the wegscheiderite and mudstone layers shows abundant lamalginite, which have been compressed by later-stage reedmergnerite minerals. Observed under fluorescence microscopy. **(B)** and **(C)** Specific types of telalginite coexisting with shortite minerals in mudstone. **(B)** Plane-polarized light, **(C)** Fluorescence microscopy. **(D)** Northupite minerals develop in the mudstone layer, with telalginite preserved between the minerals. **(E)** Enlarged view of the telalginite preserved in the mudstone layer, shown in **(D)**. Displayed in orange-yellow color. Observed under fluorescence microscopy. **(F)** Well-preserved telalginite in the searlesite in dolomitic mudstone. Plane-polarized light microscopy. **(G)** Enlarged view of the telalginite shown in **(F)** under fluorescence microscopy. Nup, Northupite; Sot, Shortite; Rm, Reedmergnerite.

are also developed in the shortite of the mudstone layer (Figures 7B, C), with a diameter of approximately 50–100 μm. Telalginite is found in muddy rocks coexisting with northupite and shortite (Figures 7D, E). Well-preserved yellow-green fluorescent telalginites are also found in reedmergnerite crystals (Figures 7F, G).

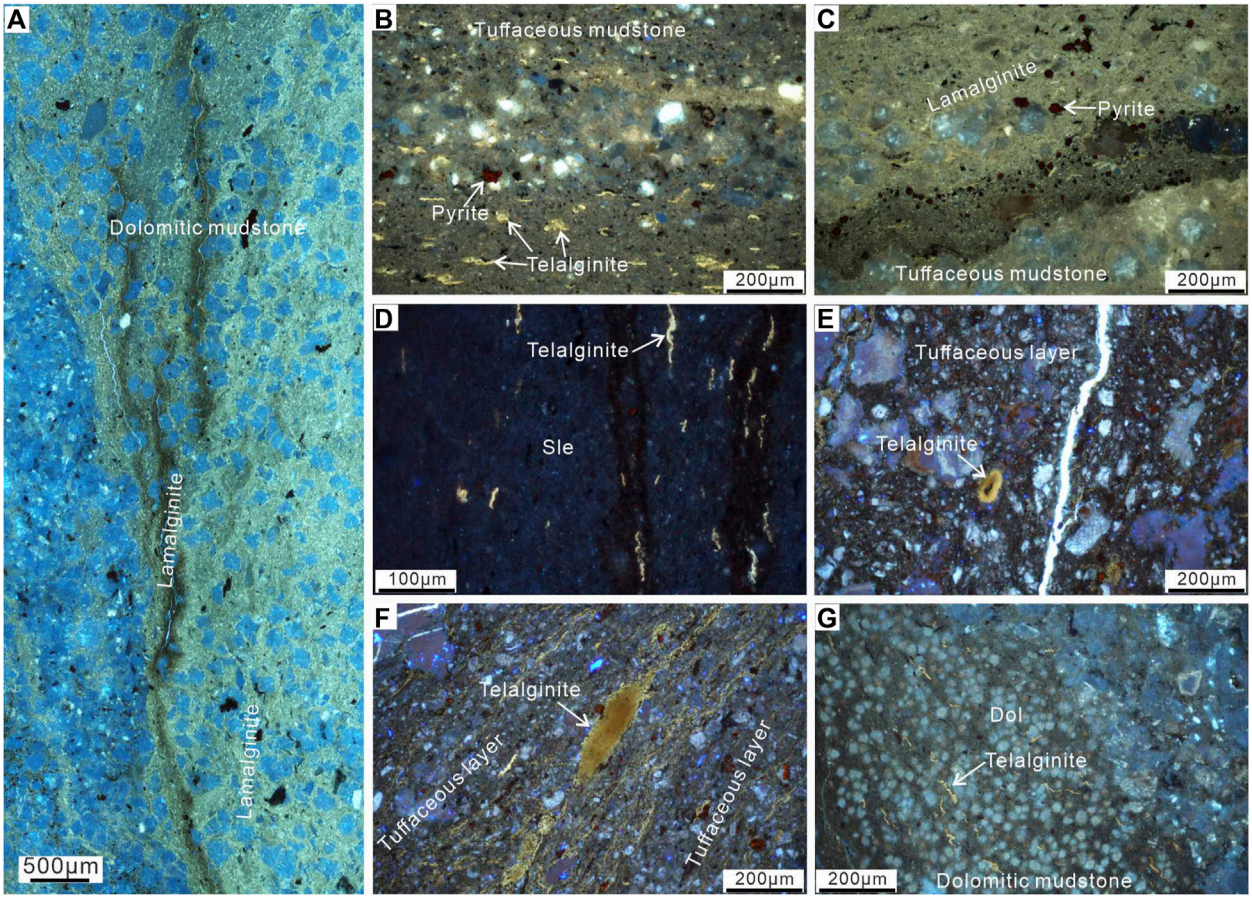

FIGURE 8
Microscopic photographs of organic matter in the transitional zone. **(A)** Lamalginite in dolomitic mudstones. Observed under fluorescence microscopy. **(B)** Abundant development of telalginite in tuffaceous layers. Observed under fluorescence microscopy. **(C)** Lamalginite preserved in tuffaceous mudstone. **(D)** Well-preserved telalginite in searlesite. Observed under fluorescence microscopy. **(E)** Telalginite in tuffaceous layers, observed under fluorescence microscopy. **(F)** Agglomerated telalginite in tuffaceous layers, observed under fluorescence microscopy. **(G)** Telalginite in the matrix surrounding dolomite. Observed under fluorescence microscopy. Dol, Dolomite; Rm =, Reedmergnerite; Sle, Searlesite.

4.3.2 Transitional zone

The lithology of the transitional zone in the Fengcheng Formation is complex. The main lithologies identified include dolomitic tuffaceous mudstones and dolomite-bearing mudstone. Reedmergnerite and searlesite are abundantly developed, while secondary minerals such as shortite, northupite, and eitelite are also present, with scarce occurrence of wegscheiderite (as shown in Figure 4, FN26). Abundant lamalginites are also observed in the dolomitic mudstone of the transitional zone (Figure 8A), exhibiting yellow-green fluorescence under the microscope. Telalginites are also present in the muddy matrix between dolomite grains (Figure 8G). In the dolomite containing tuffaceous mudstone, both telalginite and lamalginite are extensively developed (Figures 8B, C, E), with some forming clustered aggregates (Figure 8F). The transitional zone is characterized by the symbolic mineral, reedmergnerite, which shows a certain distribution relationship with organic matter. Well-preserved telalginites are found in the nodules of searlesite (Figure 8D). Residual telalginites are also observed in the vein-like fractures of reedmergnerite, exhibiting strong deformation due to compression. Aggregates of telalginite and fine-grained sedimentary pyrite are observed on the edge of poorly crystallized reedmergnerite.

4.3.3 Marginal zone

The marginal zone of the Fengcheng Formation has a relatively low total organic carbon content, and telalginite are a major component of the bio-precursor. Abundant, well-preserved telalginite are developed in the mudstone layers, showing intact structures (Figures 9A, C, E), and exhibiting deformation due to compression (Figure 9A). The fluorescence color of the telalginite is relatively dark, appearing orange-red under fluorescence microscopy (Figures 9C–E). In addition, numerous inertinite macerals can be identified (Figures 9B, F). Similar to the vitrinite group, the inertinite group in shale is present in the form of dispersed particles within the mineral matrix (Figure 9B). Cell structures can be preserved in the maceral components of the fusinite and semifusinite groups.

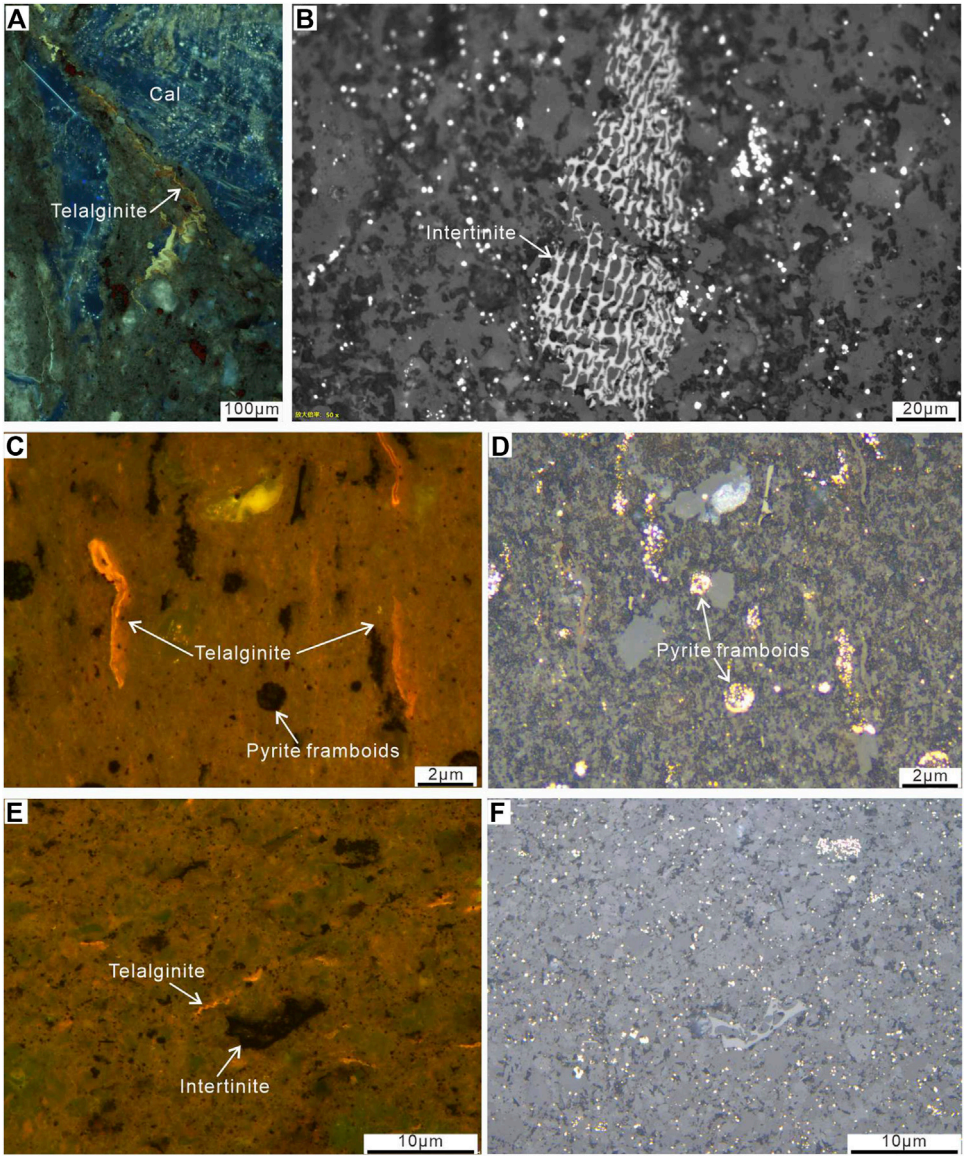

FIGURE 9
Microscopic photographs of organic matter in the margin zone. **(A)** Telalginite developed in mudstone surrounding calcite, deformed due to compression. Observed under fluorescence microscopy. **(B)** Well-preserved inertinite distributed in the clastic matrix, observed under reflected light microscopy. **(C)** and **(D)** Co-occurrence of distinctively shaped telalginite and framboids pyrite. **(C)** Observed under fluorescence microscopy, **(D)** observed under reflected light microscopy. **(E)** and **(F)** Co-occurrence of telalginite and inertinite. **(E)** Observed under fluorescence microscopy, **(F)** observed under reflected light microscopy. Cal, Calcite.

5 Discussion

5.1 Characteristics of organic geochemical zonation

The distribution of alkaline lacustrine source rocks in the Mahu Sag of the Fengcheng Formation is stable, with a cumulative thickness exceeding 200 m, providing a solid material basis for hydrocarbon generation (Zhi et al., 2016; Bai et al., 2022). The abundance of organic matter of the source rocks is mainly evaluated through parameters such as TOC, petroleum generation potential (PG = $S_1 + S_2$), and HI in rock pyrolysis (Welte and Tissot, 1984; Peters, 1986). Based on results of previous studies on mineral zoning, we also conducted zone-specific analysis of organic geochemical data. Results from the marginal zone show that the TOC content of the source rocks ranges from 0.11% to 2.67%, with an average of 1.16%, predominantly composed of type II_2 kerogen. In the transitional zone, the TOC content varies from 0.09% to 3.30%, with an average of 1.89%, dominated by types I and II_1 kerogens. The inner zone exhibits a TOC content ranging from 0.03% to 1.64%, with an average of 0.76%. Types II_1 and I kerogens are mainly oil-prone, and during the mature stage, the generated gas is predominantly of the oil type gas (Figure 6B).

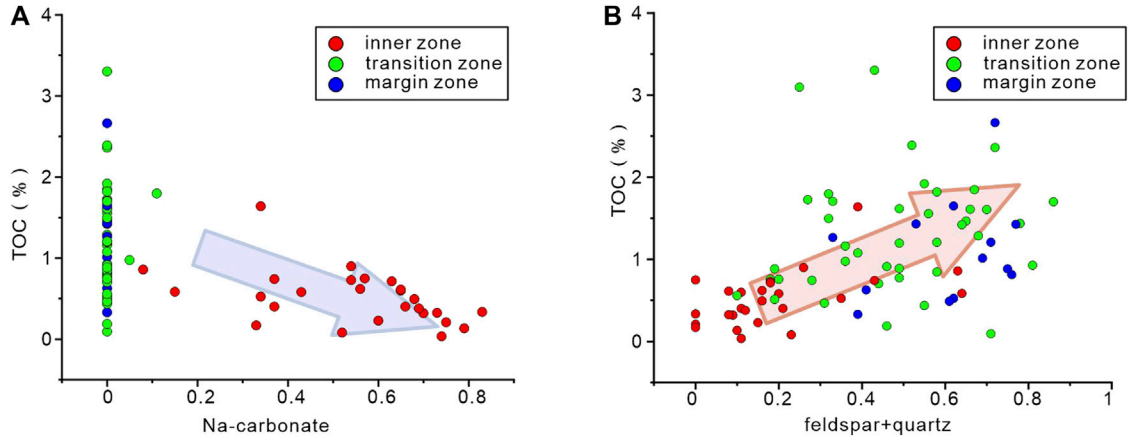

FIGURE 10
(A) Correlation between contents of sodium carbonate minerals and TOC. **(B)** Correlation between contents of felsic mineral and TOC.

As mentioned earlier, the sedimentation in alkaline lake is influenced by climate changes characterized by alternating cold-dry and warm-wet periods, resulting in fluctuations in lacustrine water salinity. The interbedding of evaporite rocks such as dolomite and trona with organic-rich mudstones (oil shales) during wet periods (Figure 4), reflecting seasonal fluctuations in lacustrine water levels and salinity changes. During humid periods, there is a significant proliferation of algal organisms that develop into algal mats (Namsaraev et al., 2018). These mats can become buried and lithified, eventually forming an important constituent of source rocks known as kerogen. Mudstones and other clastic rocks are primarily composed of felsic minerals, and significant bio-precursor such as algae are mainly developed within these rocks. The previous analysis revealed a positive correlation between TOC content and abundance of felsic minerals. However, the presence of sodium carbonate minerals has a negative impact on TOC content, indicating that organic matter development is not significant in environments with high alkalinity (Figure 10A). Therefore, in this study, we have excluded the content of sodium carbonate minerals in the samples to investigate the correlation between organic matter and lithological components outside the sodium carbonate mineral (Figure 11). The specific calculation of total organic carbon normalization (TOC_n) is based on the results of XRD data. The original whole rock organic carbon content is divided by the content of residual minerals excluding sodium carbonates. Normalization results show that the TOC_n content is higher in the inner and transitional zones than in the marginal zone. Therefore, we can conclude that during the intermittent period of evaporite mineral deposition, which corresponds to a relatively wet period, a high quantity of organic matter was deposited in the inner and transitional zones of the alkaline lacustrine deposits in the Fengcheng Formation. This depositional environment was more conducive to the development of high-quality algae. The Green River Formation in the Piceance Basin during the Eocene Epoch is a typical deep lacustrine deposit, that is, rich in organic matter. It exhibits a mixed lacustrine sedimentary system with carbonate-siliceous and evaporitic facies, and the variation in organic matter abundance is primarily controlled by climate-induced changes in lacustrine water level during the Eocene Epoch (Tänavsuu-Milkeviciene and Frederick Sarg, 2012). During the lowstand phase, productivity was low, while during the highstand phase of rising lacustrine waters, the average organic abundance was higher. Simultaneously, weak freshwater inflow and high salinity in the Eocene Hetaoyuan Formation of the Biyang Sag promoted water column stratification, creating stable chemoclines and anoxic environments in the bottom water. The combination of relatively higher nutrient concentrations in saline water and abundant CO_3^{2-} ions under alkaline conditions may have resulted in high primary productivity in the high-salinity lacustrine (Tan et al., 2019). In the Mahu Sag, the Fengcheng Formation is characterized by distinct lithofacies that represent different sedimentary environment patterns, including shallow lacustrine margin, slope, lacustrine

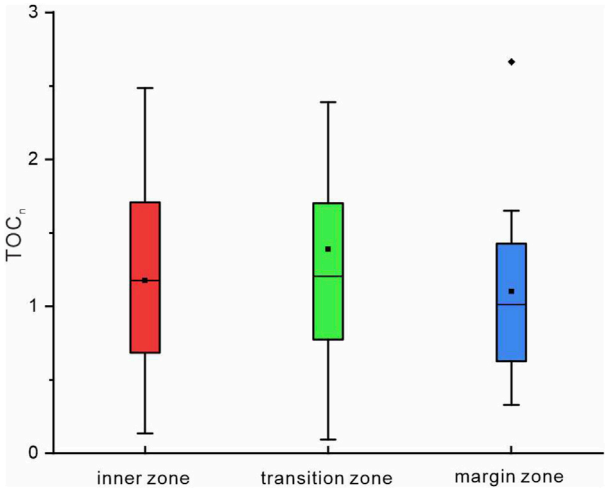

FIGURE 11
Box plot of normalized total organic carbon content (TOC_n), after excluding the contribution of sodium carbonate minerals.

center, and steep slope margin. Lacustrine level fluctuations have a significant impact on shallow saline lacustrine systems, resulting in complex sedimentary environments (Yu et al., 2019). In summary, the distribution of organic matter in the ancient alkaline lacustrine deposits of the Fengcheng Formation is controlled by the sedimentary environment of the waterbody. During the period of alkaline mineral development, evaporation of the lacustrine water is at its maximum, resulting in a shallow water depth. During the humid period, as the lacustrine water level rises, the inner zone of the lacustrine develops deep lacustrine facies sedimentation, with a mixture of alkaline minerals and clastic minerals. The relatively high productivity and reducing environment of the alkaline lacustrine deposits during this period result in the deposition of abundant organic matter in the Fengcheng Formation, similar to the observation of extensive algal mats and microbial communities in the alkaline lakes of East Africa (Grant and Jones, 2016).

5.2 Controls on the distribution of organic matter

As hydrologic closure is one of the necessary conditions for the formation of alkaline lacustrine deposits, the evolution process involving the evaporation and concentration of alkaline lacustrine water is controlled by the composition of inflowing water ions in a closed hydrological system. The hydrological characteristics of alkaline lacustrine deposits and the precipitation of sodium carbonate in alkaline lacustrine deposits both indicate that the evolution path of alkaline lacustrine water is characterized by initial higher concentrations of bicarbonate ions compared to calcium and magnesium ions. As the lacustrine water continues to get concentrated, calcium and magnesium ions will preferentially precipitate, leading to the formation of calcite, dolomite, and magnesite in the mudflats at the margins of the lacustrine. As the evaporation and concentration of water increases, saline groundwater infiltrates into the central of the lacustrine basin, and sodium-calcium carbonate minerals precipitate in the pores. Eventually, the lacustrine water further concentrates into salt pans and naturally occurring alkaline minerals, such as sodium carbonate minerals (Hardie and Eugster, 1970). Therefore, the presence of alkaline minerals in alkaline lacustrine deposits can reflect changes in the sedimentary environment of the waterbody (Gärtner and Witkamp, 2007; Jagniecki et al., 2013; Jia et al., 2015; Yu et al., 2019; Getenet et al., 2023). Accordingly, the types of minerals found in different zones of the Fengcheng Formation can be used to infer changes in paleoenvironmental conditions within each respective zone. Previous research has revealed that the distribution of salinity and pH of the Fengcheng Formation in the Mahu Sag follows a certain pattern in the planar. Calculations based on indicators such as Z-values, Y/Ho ratios, oxygen isotopes, and nitrogen isotopes, which represent paleosalinity and paleo-pH values, have shown that pH decreases from the center to the margin, while salinity initially increases and then decreases (Yu et al., 2018a; Xia et al., 2020).

Previous analyses have shown that algae thrive in nutrient-rich brackish surface waters, which results from the mixing of fresh and salt waters (Goodarzi et al., 2022). Vertical variations in salinity are observed in the well FN5 in the inner zone of the Fengcheng Formation (Yu et al., 2018b). Abundant algal is found in the wegscheiderite layer with high pH and the transitional mud layers with high salinity, indicating that the lamalginite in the Fengcheng Formation developed extensively during the transition phase between evaporative and humid periods. The fluorescent color of the telalginite is darker, some displaying yellow to orange-red. In the inner zone of the Fengcheng Formation, at depths exceeding 4,000 m, which is considered a highly mature stage of hydrocarbon generation, the telalginite exhibit darker colors. This confirms that the inner zone is at a higher level of maturity, with significant hydrocarbon generation from the bio-precursor, while the lamalginite is well preserved due to protection by salt minerals (Cao et al., 2015). Compared to the inner zone, transitional zone has lower pH and higher salinity. Previous research has determined that the development of telalginite is associated with environments characterized by a relatively higher salinity than lamalginite, which is consistent with the distribution of organic matter in the Fengcheng Formation (Liu S. et al., 2022). This indicates that the type and distribution of organic matter in the Fengcheng Formation are influenced by the salinity and pH of the waterbody. The inertinite in the marginal zone is derived from terrestrial organic matter and exhibit minimal hydrocarbon generation potential, typically classified as type III kerogen (Liu B. et al., 2022). Inertinite is believed to have originated from pre-sedimentation wildfires or oxidation events, and even in early stages of maturation, they exhibit high reflectance values.

Based on a comprehensive analysis of lithofacies mineralogy, organic geochemistry, and fluorescence microscopy observations in the Mahu Sag, the organic matter distribution in the source rocks of Fengcheng Formation exhibits distinct characteristics on the plane, which are influenced by various factors. The inner zone of the alkaline lacustrine deposit is characterized by abundant and diverse alkaline minerals, complex lithofacies, and interbedding of evaporite minerals and mud layers, indicating significant fluctuations in the lacustrine surface water level. In the inner zone of the alkaline lacustrine deposit, which experiences high evaporation during dry periods, a local environment with high pH is formed. This leads to the abundant precipitation and deposition of wegscheiderite, resulting in the formation of wegscheiderite layers. The wegscheiderite layers have very low TOC content and are largely devoid of lamalginite, with predominantly prokaryotic bacteria. Subsequently, during wet periods, the lacustrine water level gradually rises and the water depth increases. During the transitional period, abundant lamalginite develop which adapted to the high pH alkaline waterbody. This algal is similar to the algal mats that formed during the Eocene rapid environmental changes, as well as the algal mats found in the high TOC oil shales of the Green River Formation (Boucsein and Stein, 2009; Tänavsuu-Milkeviciene et al., 2017). In later stages, the lamalginite undergoes bending and deformation due to the crystallization of well-preserved reedmergnerite. Even in the mudstone layers with low content of wegscheiderite formed during the rising phase of waterbody, developed characteristic assemblages of alkaline minerals that indicate high pH values during the deposition period. Lamalginite is not well-developed in the muddy matrix, and instead, matured telalginite forms mainly (Figures 7B–G Figures 7B–G, 10E), accompanied by relatively high TOC content. During this period, the bottom of the deep lacustrine environment in the central sag is

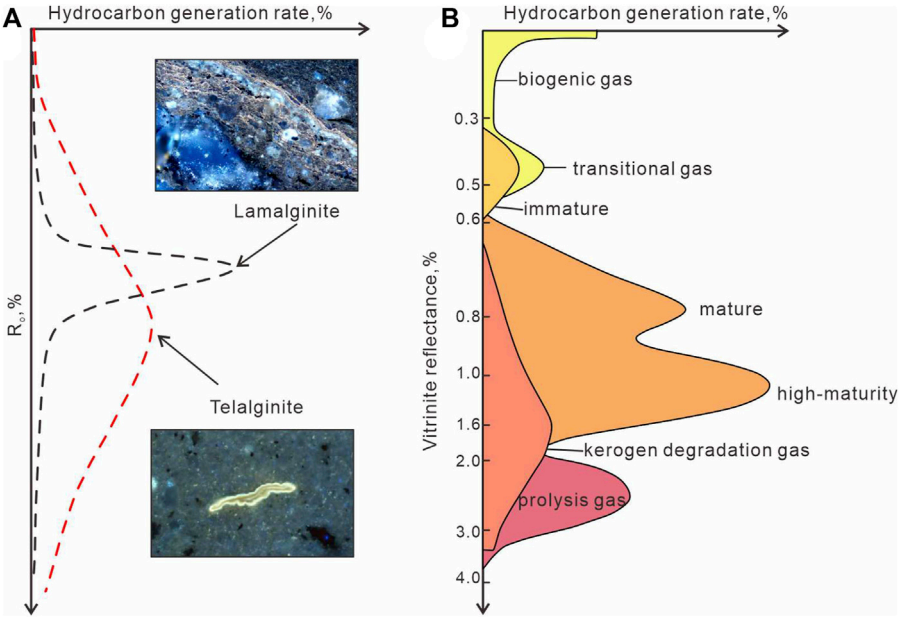

FIGURE 12
(A) Pattern of hydrocarbon generation in source rock rich in telalginite and lamalginite (Modified by Liu et al., 2023) **(B)** Bimodal high-efficiency hydrocarbon generation model in the Fengcheng Formation of the Mahu Sag (Modified by Tang Y. et al., 2021b).

predominantly characterized by reducing conditions (Tang W. et al., 2021b), which contribute to the preservation of organic matter. Previous studies have suggested that upwelling of deep hydrothermal fluids along faults in the sag center may have provided nutrient elements for the development of organic matter (Wang et al., 2020).

The transitional zone mainly comprises dolomitic mudstone, mudstone, and dolomite bearing tuffaceous mudstone. The occurrence of characteristic alkaline minerals indicates that the waterbody is still in an alkaline environment, with a relatively higher salinity than in the inner zone, supporting the development of halophilic and alkaliphilic algal. Lamalginite and telalginite are abundant in the transitional zone (Figures 8, 10F). Petrological, organic, and inorganic geochemical analyses indicate that lamalginite develop in low salinity environments, while telalginite forms are associated with high salinity environments (Liu S. et al., 2022). The content of telalginite in the transitional zone of the Fengcheng Formation is significantly higher than that in the inner zone, reflecting higher salinity conditions during the depositional period. The presence of tuffaceous mudstone reflects the input of abundant nutrients from peripheral volcanism, which in turn promotes the bloom of algae. The relatively high salinity and alkalinity of the waterbody provide favorable conditions for the development of algae. Together with tuffaceous materials, they control the characteristics of high TOC content and high productivity in the transitional zone of the alkaline lacustrine deposit. The abundant occurrence of siliceous layers, such as searlesite and reedmergnerite, also plays a protective role in preserving organic matter, preventing later destruction.

In the marginal zone, the TOC is relatively lower than that in the inner and transitional zones, and the development of sodium carbonate alkaline minerals is limited, with only a low quantity of reedmergnerite present. The pH of the water in the marginal zone is lower, and the salinity is relatively low. Due to the proximity to the lacustrine margin, the sedimentary environment is disturbed by debris, which disrupts the reducing conditions for organic matter preservation, resulting in only the partial development of telalginite (Figures 9, 10C). However, near the source, abundant and well-preserved inertinite are found, providing a significant contribution to the sedimentation of the Fengcheng Formation. Despite this, in some well locations close to volcano, there is still a significant development of telalginite, likely due to the input of abundant nutrients from volcanic eruptions.

5.3 Exploration of hydrocarbon generation model in the Fengcheng Formation

The Lower Permian source rocks of Fengcheng Formation are alkaline lacustrine deposition, characterized by abundant algal and bacteria and high hydrocarbon generation potential. The source rocks have entered the oil window and are generally in a mature to highly mature stage, containing oil and gas in different evolutionary stages of low mature, mature, and high mature. The thermal evolution of the Fengcheng Formation shale is positively correlated with burial depth, with the hydrocarbon generation threshold of depth ≥3,500 m or deeper (Zhi et al., 2016). Shales at burial depths exceeding 4,000 m are typically mature source rocks. In the central area of the Mahu Sag where burial depths exceed 5,000 m, the source rocks have reached a high level of maturity (Wang et al., 2018). Particularly noteworthy is the presence of a bimodal high-efficiency hydrocarbon generation model with peaks in both “maturity” and “high maturity” (Figure 12B), with a hydrocarbon generation potential nearly twice that of traditional lacustrine source rocks (Tang Y. et al.,

2021a). In this study on the organic matter of source rocks in the Fengcheng Formation, it was found that the bio-precursor is mainly composed of lamalginite in the inner and transitional zones, as well as telalginite in the inner, transition, and marginal zones. Lamalginite source rock displays a much narrower distribution of activation energies than telalginite source rocks, which effectively narrows down the main stages of hydrocarbon generation (Figure 12A). In addition, the concentration of activation energy distribution in the high-value interval for lamalginite indicating the characteristics of the relatively lagging hydrocarbon generation of lamalginite (Liu et al., 2023). The hydrocarbon generation characteristics of different stages of algal are consistent with the bimodal hydrocarbon generation model of the Fengcheng Formation, indicating that both telalginite and lamalginite are the main bio-precursor in the alkaline lacustrine deposits rocks of the Fengcheng Formation. The inner zone of the sag in the alkaline and lacustrine sedimentary rocks of the Fengcheng Formation, buried to >4,000 m, preserves well-preserved lamalginite in the transitional layer of the core in the inner zone, protected by characteristic alkaline minerals, which have been preserved during the burial process. The telalginite in the mud layers exhibit a darker fluorescence color (Figure 7E), indicating a higher maturity. When the thermal maturity of the source rock reaches 1.05%, abundant hydrocarbons are generated, with an increase in illite content from illite–smectite layers. Previous analysis indicated that telalginite in oil shales can generate a significant quantity of hydrocarbons and organic acids under temperature conditions, and these organic acids promote the transformation of smectite to illite. This greatly enhances the catalytic activity of illite, resulting in an increased hydrocarbon generation rate (Xu et al., 2022). In the cores of the Fengcheng Formation, there is a negative correlation between illite content and illite–smectite (Figure 5B). The highest illite content is observed in the inner zone, indicating higher maturity than the transition and marginal zones. Overall, the source rock of the Fengcheng Formation in the Mahu Sag exhibit unique characteristics owing to its alkaline lacustrine deposition features. The findings of this study on the organic matter of the Fengcheng Formation in the Mahu Sag provide important insights and guidance for the effective evaluation of source rocks and the selection of exploration targets in shale oil reservoirs and sweet spots.

6 Conclusion

(1) The distribution of alkaline minerals and common minerals in the Fengcheng Formation exhibits distinct patterns on a plane. Based on the characteristics of mineral assemblages, the alkaline lacustrine deposits of the Fengcheng Formation can be classified into three zones: the inner zone, transitional zone, and marginal zone. The inner zone is characterized by the dominant presence of sodium carbonate minerals, with a mineral assemblage consisting mainly of wegscheiderite and shortite. The transitional zone is characterized by a mineral assemblage of sodium borosilicate minerals, including reedmergnerite and searlesite, with significantly higher abundances than the inner and marginal zones.

(2) Organic geochemical data indicate that the source rocks of Fengcheng Formation in the Mahu Sag are generally moderate to high quality, with high TOC content and maturity ranging from mature to high mature. The inner zone exhibits a relatively high TOC_n content after normalization, along with the presence of types II_1 and I kerogen. In contrast, the marginal zone has a relatively lower TOC content than the inner zone and transitional zone, with type II2 kerogen being predominant.

(3) The transitional layer between the wegscheiderite layer and the alkaline mineral-rich mudstone layer in the inner zone of the Fengcheng Formation contains well-preserved lamalginite, and the telalginite with higher maturity developed in the muddy layer. The transitional zone develops telalginite that are more adaptable to high salinity. Transitional zoneAdditionally, the tuffaceous material in the transitional zone has provided abundant nutrient elements, promoting the bloom of lamalginite. The presence of searlesite has not only protected the organic matter from subsequent degradation, but also prevented further damage. In the marginal zone, the pH of the waterbody decreased, resulting in the limited development of telalginite, accompanied by the input of inertinite from terrestrial sources.

(4) The development and distribution of organic matter in different zones of the Fengcheng Formation in the Mahu Sag are controlled by multiple factors. In the inner zone, the alkaline-tolerant algal are primarily influenced by water depth and pH variations, with possible nutrient input from deep hydrothermal fluids. In the transitional zone, the organic matter is controlled by the combined effects of water salinity, pH, and allochthonous nutrient supply. In the marginal zone, the distribution of organic matter is mainly influenced by proximal sedimentary input, low pH, and low salinity of the depositional water. The distinct differences in hydrocarbon generation efficiency between telalginite and lamalginite source rocks are evident. Telalginite are capable of early hydrocarbon generation, aligning with the bimodal high-efficiency hydrocarbon generation model observed in the Fengcheng Formation of the Mahu Sag.

Data availability statement

The original contributions presented in the study are included in the article/Supplementary Material, further inquiries can be directed to the corresponding author.

Author contributions

MN: writing—original draft, data processing. YZ: supervision, conceptualization; funding acquisition writing—review and editing. YT: resources. WH: resources. All authors contributed to the article and approved the submitted version.

Funding

This research is supported by Natural Science Foundation of China (NSFC) Project given to Zhaojie Guo (No. 42090021) and to ZY (42272157).

Conflict of interest

Authors TY and HW were employed by the company PetroChina Xinjiang Oilfield Company.

The remaining authors declare that the research was conducted in the absence of any commercial or financial relationships that could be construed as a potential conflict of interest.

Publisher's note

References

Bai, Y., Wang, F., Niu, Z., Jin, K., Li, P., Xu, D., et al. (2022). Hydrocarbon generation kinetics of source rocks of permian Fengcheng Formation in Mahu sag,Junggar Basin. *Lithol. Reserv.* 34, 116–127. doi:10.12108/yxyqc.20220411

Boucsein, B., and Stein, R. (2009). Black shale formation in the late Paleocene/early Eocene Arctic Ocean and paleoenvironmental conditions: New results from a detailed organic petrological study. *Mar. Petroleum Geol.* 26, 416–426. doi:10.1016/j.marpetgeo.2008.04.001

Cao, J., Lei, D., Li, Y., Tang, Y., AbulimitChang, Q., and Wang, T. (2015). Ancient high-quality alkaline lacustrine source rocks discovered in the lower permian Fengcheng Formation, Junggar Basin. *Acta Pet. Sin.* 36, 781–790.

Cao, J., Xia, L., Wang, T., Zhi, D., Tang, Y., and Li, W. (2020). An alkaline lake in the late paleozoic ice age (lpia): A review and new insights into paleoenvironment and petroleum geology. *Earth-Science Rev.* 202. doi:10.1016/j.earscirev.2020.103091

Chen, J.-F., Han, B.-F., Ji, J.-Q., Zhang, L., Xu, Z., He, G.-Q., et al. (2010). Zircon U–Pb ages and tectonic implications of paleozoic plutons in northern west junggar, north xinjiang, China. *Lithos* 115, 137–152. doi:10.1016/j.lithos.2009.11.014

Chen, Z., Liu, G., Wang, X., Gao, G., Xiang, B., Ren, J., et al. (2016). Origin and mixing of crude oils in Triassic reservoirs of Mahu slope area in Junggar Basin, NW China: Implication for control on oil distribution in basin having multiple source rocks. *Mar. Petroleum Geol.* 78, 373–389. doi:10.1016/j.marpetgeo.2016.09.022

Dyni, J. R. (2006). *Geology and resources of some world oil-shale deposits*. Reston, VA: USGS. doi:10.3133/sir29955294

Gao, G., Yang, S., Ren, J., Zhang, W., and Xiang, B. (2018). Geochemistry and depositional conditions of the carbonate-bearing lacustrine source rocks: A case study from the early permian Fengcheng Formation of well FN7 in the northwestern Junggar Basin. *J. Petroleum Sci. Eng.* 162, 407–418. doi:10.1016/j.petrol.2017.12.065

Gärtner, R. S., and Witkamp, G.-J. (2007). Mixed solvent reactive recrystallization of trona (sodium sesqui-carbonate) into soda (sodium carbonate anhydrate). *Hydrometallurgy* 88, 75–91. doi:10.1016/j.hydromet.2007.03.006

Getenet, M., Otálora, F., Emmerling, F., Al-Sabbagh, D., and García-Ruiz, J. M. (2023). Mineral precipitation and hydrochemical evolution through evaporitic processes in soda brines (East African Rift Valley). *Chem. Geol.* 616. doi:10.1016/j.chemgeo.2022.121222

Goodarzi, F., Hosseininejad, S., Pedersen, P. K., Gentzis, T., and Sanei, H. (2022). Characterization of immature oil shales from the cretaceous second white specks Formation in saskatchewan and manitoba, Canada. *Mar. Petroleum Geol.* 143. doi:10.1016/j.marpetgeo.2022.105774

Grant, W. D., and Jones, B. E. (2016). "Bacteria, archaea and viruses of soda lakes," in *Soda lakes of East Africa*. Editor M. Schagerl (Cham: Springer International Publishing), 97–147.

Grant, W. D., Mwatha, W. E., and Jones, B. E. (1990). Alkaliphiles: Ecology, diversity and applications. *FEMS Microbiol. Lett.* 75, 255–269. doi:10.1016/0378-1097(90)90536-Y

Han, Y., and Zhao, G. (2018). Final amalgamation of the tianshan and junggar orogenic collage in the southwestern central asian orogenic belt: Constraints on the closure of the paleo-asian ocean. *Earth-Science Rev.* 186, 129–152. doi:10.1016/j.earscirev.2017.09.012

Han, B. F., Guo, Z. J., Zhang, Z. C., Zhang, L., Chen, J. F., and Song, B. (2010). Age, geochemistry, and tectonic implications of a late Paleozoic stitching pluton in the North Tian Shan suture zone, Western China. *Geol. Soc. Am. Bull.* 122, 627–640. doi:10.1130/b26491.1

Hardie, L. A., and Eugster, H. P. (1970). The evolution of closed basin brines. *Mineral. Soc. Spec. Pap.* 3, 273–290.

He, T., Lu, S., Li, W., Tan, Z., and Zhang, X. (2018). Effect of salinity on source rock Formation and its control on the oil content in shales in the Hetaoyuan Formation from the Biyang depression, Nanxiang Basin, central China. *Energy fuels.* 32, 6698–6707. doi:10.1021/acs.energyfuels.8b01075

He, W., Sun, Z., Qian, M., Yang, Z., Li, Z., Leng, J., et al. (2022). Evaluation of the oil-bearing properties of shale and shale oil mobility in the Fengcheng Formation in the Mahu sag, Junggar Basin, northwest China: A case study of well maye-1. *Geofluids* 2022, 1–16. doi:10.1155/2022/6206645

Helz, G. R., Bura-Nakić, E., Mikac, N., and Ciglenečki, I. (2011). New model for molybdenum behavior in euxinic waters. *Chem. Geol.* 284, 323–332. doi:10.1016/j.chemgeo.2011.03.012

Horsfield, B., Curry, D. J., Bohacs, K., Littke, R., Rullkötter, J., Schenk, H. J., et al. (1994). Organic geochemistry of freshwater and alkaline lacustrine sediments in the Green River Formation of the washakie basin, Wyoming, USA. *Org. Geochem.* 22, 415–440. doi:10.1016/0146-6380(94)90117-1

Hou, M., Qu, J., Zha, M., Swennen, R., Ding, X., Imin, A., et al. (2022). Significant contribution of haloalkaliphilic cyanobacteria to organic matter in an ancient alkaline lacustrine source rock: A case study from the permian Fengcheng Formation, Junggar Basin, China. *Mar. Petroleum Geol.* 138. doi:10.1016/j.marpetgeo.2022.105546

Jagniecki, E. A., Jenkins, D. M., Lowenstein, T. K., and Carroll, A. R. (2013). Experimental study of shortite ($Na_2Ca_2(CO_3)_3$) formation and application to the burial history of the wilkins peak member, Green River basin, Wyoming, USA. *Geochim. Cosmochim. Acta* 115, 31–45. doi:10.1016/j.gca.2013.04.005

Jia, B., Wen, H., Li, Y., Liu, Y., and Wang, T. (2015). Fluid inclusions in the salt minerals from the permian Fengcheng Formation in the urho region, Junggar Basin, xinjiang. *Sediment. Geol. Tethyan Geol.* 34, 33–42.

Katz, B. J. (1995). "The Green River shale: An Eocene carbonate lacustrine source rock," in *Petroleum source rocks*. Editor B. J. Katz (Berlin, Heidelberg: Springer Berlin Heidelberg), 309–324.

Kuang, L., Tang, Y., Lei, D., Chang, Q., Ouyang, M., Hou, L., et al. (2012). Formation conditions and exploration potential of tight oil in the Permian saline lacustrine dolomitic rock, Junggar Basin, NW China. *Petroleum Explor. Dev.* 39, 700–711. doi:10.1016/s1876-3804(12)60095-0

Lei, D., Chen, G., Liu, H., Li, X., Tao, K., and Cao, J. (2017). Study on the forming conditions and exploration fields of the Mahu giant oil (gas) province, Junggar Basin. *Acta Geol. Sin.* 91, 1604–1619.

Li, C., Guo, P., Ke, X., and Ma, Y. (2021). Genesis of high-quality source rocks in volcano-related alkaline lakes and implications for the exploration and development of shale oil and gas. *OIL GAS Geol.* 42. doi:10.11743/ogg20210616

Liu, B., Mastalerz, M., and Schieber, J. (2022a). SEM petrography of dispersed organic matter in black shales: A review. *Earth-Science Rev.* 224. doi:10.1016/j.earscirev.2021.103874

Liu, S., Gao, G., Jin, J., Gang, W., and Xiang, B. (2022b). Source rock with high abundance of C28 regular sterane in typical brackish-saline lacustrine sediments: Biogenic source, depositional environment and hydrocarbon generation potential in Junggar Basin, China. *J. Petroleum Sci. Eng.* 208. doi:10.1016/j.petrol.2021.109670

Liu, S.-J., Gao, G., Gang, W.-Z., Xiang, B.-L., and Wang, M. (2023). Differences in geochemistry and hydrocarbon generation of source-rock samples dominated by telalginite and lamalginite: A case study on the permian saline lacustrine source rocks in the jimusaer sag, NW China. *Petroleum Sci.* 20, 141–160. doi:10.1016/j.petsci.2022.08.034

Mukhopadhyay, P. K., Wade, J. A., and Kruge, M. A. (1995). Organic facies and maturation of Jurassic/Cretaceous rocks, and possible oil-source rock correlation based on pyrolysis of asphaltenes, Scotian Basin, Canada. *Org. Geochem.* 22, 85–104. doi:10.1016/0146-6380(95)90010-1

Namsaraev, Z. B., Gorlenko, V. M., and Buryukhaev, S. P. (2018). Successional changes in the microbial community of the alkaline lake khilganta during the dry season. *Microbiology* 87, 591–596. doi:10.1134/s0026261718040124

Peters, K. E., Cassa, M. R., Magoon, L. B., and Dow, W. G. (1994). *Applied source rock geochemistry, the petroleum system—From source to trap*. American Association of Petroleum Geologists.

Peters, K. E. (1986). Guidelines for evaluating petroleum source rock using programmed Pyrolysis1. *AAPG Bull.* 70, 318–329. doi:10.1306/94885688-1704-11d7-8645000102c1865d

Pickel, W., Kus, J., Flores, D., Kalaitzidis, S., Christanis, K., Cardott, B. J., et al. (2017). Classification of liptinite – ICCP system 1994. *Int. J. Coal Geol.* 169, 40–61. doi:10.1016/j.coal.2016.11.004

Ruble, T. E., and Philp, R. P. (1998). *Stratigraphy, depositional environments and organic geochemistry of source-rocks in the Green River petroleum system*. Utah: Uinta Basin.

Ruble, T. E., Lewan, M. D., and Philp, R. P. (2001). New insights on the Green River petroleum system in the Uinta basin from hydrous pyrolysis experiments. *AAPG Bull.* 85, 1333–1371. doi:10.1306/8626cab9-173b-11d7-8645000102c1865d

Song, Y., Li, S., and Hu, S. (2019). Warm-humid paleoclimate control of salinized lacustrine organic-rich shale deposition in the Oligocene Hetaoyuan Formation of the Biyang Depression, East China. *Int. J. Coal Geol.* 202, 69–84. doi:10.1016/j.coal.2018.11.016

Sorokin, D. Y., Berben, T., Melton, E. D., Overmars, L., Vavourakis, C. D., and Muyzer, G. (2014). Microbial diversity and biogeochemical cycling in soda lakes. *Extremophiles* 18, 791–809. doi:10.1007/s00792-014-0670-9

Tan, Z., Lu, S., Li, W., Zhang, Y., He, T., Jia, W., et al. (2019). Climate-driven variations in the depositional environment and organic matter accumulation of lacustrine mudstones: Evidence from organic and inorganic geochemistry in the Biyang depression, Nanxiang Basin, China. *Energy fuels.* 33, 6946–6960. doi:10.1021/acs.energyfuels.9b00595

Tänavsuu-Milkeviciene, K., and Frederick Sarg, J. (2012). Evolution of an organic-rich lake basin - stratigraphy, climate and tectonics: Piceance Creek basin, Eocene Green River Formation. *Sedimentology* 59, 1735–1768. doi:10.1111/j.1365-3091.2012.01324.x

Tänavsuu-Milkeviciene, K., Sarg, J. F., and Bartov, Y. (2017). Depositional Cycles and Sequences In An Organic-Rich Lake Basin: Eocene Green River Formation, Lake Uinta, Colorado and Utah, U.S.A. *J. Sediment. Res.* 87, 210–229. doi:10.2110/jsr.2017.11

Tang, W., Zhang, Y., Pe-Piper, G., Piper, D. J. W., Guo, Z., and Li, W. (2020). Soft-sediment deformation structures in alkaline lake deposits of Lower Permian Fengcheng Formation, Junggar Basin, NW China: Implications for syn-sedimentary tectonic activity. *Sediment. Geol.* 406. doi:10.1016/j.sedgeo.2020.105719

Tang, W., Zhang, Y., Pe-Piper, G., Piper, D. J. W., Guo, Z., and Li, W. (2021a). Permian rifting processes in the NW Junggar Basin, China: Implications for the post-accretionary successor basins. *Gondwana Res.* 98, 107–124. doi:10.1016/j.gr.2021.06.005

Tang, W., Zhang, Y., Pe-Piper, G., Piper, D. J. W., Guo, Z., and Li, W. (2021b). Permian to early Triassic tectono-sedimentary evolution of the Mahu sag, Junggar Basin, Western China: sedimentological implications of the transition from rifting to tectonic inversion. *Mar. Petroleum Geol.* 123. doi:10.1016/j.marpetgeo.2020.104730

Tang, Y., Cao, J., He, W.-J., Guo, X.-G., Zhao, K.-B., and Li, W.-W. (2021a). Discovery of shale oil in alkaline lacustrine basins: The Late Paleozoic Fengcheng Formation, Mahu Sag, Junggar Basin, China. *Petroleum Sci.* 18, 1281–1293. doi:10.1016/j.petsci.2021.04.001

Tang, Y., Cao, J., He, W., Shan, X., Liu, Y., and Zhao, K. (2021b). Development Tendency of Geological Theory of Total Petroleum System: Insights From the Discovery of Mahu Large Oil Province. *Xinjiang Pet. Geol.* 42, 1–9. doi:10.7657/xjpg20210101

Tang, Y., He, W., Bai, Y., Zhang, X., Zhao, J., Yang, S., et al. (2021c). Source Rock Evaluation and Hydrocarbon Generation Model of a Permian Alkaline Lakes—A Case Study of the Fengcheng Formation in the Mahu Sag, Junggar Basin. *Minerals* 11. doi:10.3390/min11060644

Taylor, G. H., Teichmüller, M., Davis, A., Diessel, C., Littke, R., and Robert, P. (1998). *Organic petrology*. Berlin, Stuttgart: Gebrüder Borntraeger.

Wang, X., Wang, T., and Cao, J. (2018). Basic Characteristics and Highly Efficient Hydrocarbon Generation of Alkaline-Lacustrine Source Rocks in Fengcheng Formation of Mahu Sag. *Xinjiang Pet. Geol.* 39, 9–15. doi:10.7657/XJPG20180102

Wang, T., Cao, J., Carroll, A. R., Zhi, D., Tang, Y., Wang, X., et al. (2020). Oldest preserved sodium carbonate evaporite: Late Paleozoic Fengcheng Formation, Junggar Basin, NW China. *GSA Bull.* 133, 1465–1482. doi:10.1130/b35727.1

Warren, J. K. (2016). *Evaporites: A geological compendium*. Springer Berlin Heidelberg, 1813. doi:10.1007/978-3-319-13512-0

Welte, D., and Tissot, P. (1984). *Petroleum formation and occurrence*. Springer. doi:10.1007/978-3-642-87813-8

Xia, L., Cao, J., Stüeken, E. E., Zhi, D., Wang, T., and Li, W. (2020). Unsynchronized evolution of salinity and pH of a Permian alkaline lake influenced by hydrothermal fluids: A multi-proxy geochemical study. *Chem. Geol.* 541. doi:10.1016/j.chemgeo.2020.119581

Xia, L., Cao, J., Hu, W., Zhi, D., Wang, T., and Li, E. (2021). Coupling of paleoenvironment and biogeochemistry of deep-time alkaline lakes: A lipid biomarker perspective. *Earth-Science Rev.* 213. doi:10.1016/j.earscirev.2020.103499

Xiao, Z., Chen, S., Liu, C., Lu, Z., Zhu, J., and Han, M. (2021). Lake basin evolution from early to Middle Permian and origin of Triassic Baikouquan oil in the Western margin of Mahu Sag, Junggar Basin, China: Evidence from geochemistry. *J. Petroleum Sci. Eng.* 203. doi:10.1016/j.petrol.2021.108612

Xu, J., Peng, S., Bai, Y., Cheng, X., Xu, Y., Liang, C., et al. (2022). Controlling Factors and Evolution of Oil Shale Quality in the Upper Cretaceous, Songliao Basin: Implications from Thermal Simulations. *ACS Earth Space Chem.* 6, 704–713. doi:10.1021/acsearthspacechem.1c00348

Yu, K., Cao, Y., Qiu, L., and Sun, P. (2018a). The hydrocarbon generation potential and migration in an alkaline evaporite basin: The Early Permian Fengcheng Formation in the Junggar Basin, northwestern China. *Mar. Petroleum Geol.* 98, 12–32. doi:10.1016/j.marpetgeo.2018.08.010

Yu, K., Cao, Y., Qiu, L., Sun, P., Jia, X., and Wan, M. (2018b). Geochemical characteristics and origin of sodium carbonates in a closed alkaline basin: The Lower Permian Fengcheng Formation in the Mahu Sag, northwestern Junggar Basin, China. *Palaeogeogr. Palaeoclimatol. Palaeoecol.* 511, 506–531. doi:10.1016/j.palaeo.2018.09.015

Yu, K., Cao, Y., Qiu, L., and Sun, P. (2019). Depositional environments in an arid, closed basin and their implications for oil and gas exploration: The lower Permian Fengcheng Formation in the Junggar Basin, China. *AAPG Bull.* 103, 2073–2115. doi:10.1306/01301917414

Zhang Y, Y., Li, W., and Tang, W. (2018). Tectonic setting and environment of alkaline lacustrine source rocks in the Lower Permian Fengcheng Formation of Mahu Sag. *Xinjiang Pet. Geol.* 39, 1. doi:10.7657/xjpg20180106

Zhang Z, Z., Yuan, X., Wang, M., Zhou, C., Tang, Y., Chen, X., et al. (2018). Alkaline-lacustrine deposition and paleoenvironmental evolution in Permian Fengcheng Formation at the Mahu sag, Junggar Basin, NW China. *Petroleum Explor. Dev.* 45, 1036–1049. doi:10.1016/s1876-3804(18)30107-1

Zhi, D., Cao, J., Xiang, B., Qin, Z., and Wang, T. (2016). Fengcheng Alkaline Lacustrine Source Rocks of Lower Permian in Mahu Sag in Junggar Basin: Hydrocarbon Generation Mechanism and Petroleum Resources Reestimation. *Xinjiang Pet. Geol.* 37, 1. doi:10.7657/xjpg20160501

Zhi, D., Tang, Y., Zheng, M., Xu, Y., Cao, J., Ding, J., et al. (2019). Geological characteristics and accumulation controlling factors of shale reservoirs in Fengcheng Formation, Mahu sag, Junggar Basin. *China Pet. Explor.* 24, 615–623. doi:10.3969/j.issn.1672-7703.2019.05.008

Zhi, D., Tang, Y., He, W., Guo, X., Zheng, M., and Huang, L. (2021). Orderly coexistence and accumulation models of conventional and unconventional hydrocarbons in Lower Permian Fengcheng Formation, Mahu sag, Junggar Basin. *Petroleum Explor. Dev.* 48, 38–51. doi:10.11698/PED.2021.01.04

frontiers | Frontiers in Earth Science

TYPE Original Research
PUBLISHED 05 July 2023
DOI 10.3389/feart.2023.1232418

OPEN ACCESS

EDITED BY
George Kontakiotis,
National and Kapodistrian University of Athens, Greece

REVIEWED BY
Yong Zhou,
China University of Petroleum, China
Juye Shi,
China University of Geosciences, China

*CORRESPONDENCE
Yuanyuan Zhang,
yy-zhang@pku.edu.cn

RECEIVED 31 May 2023
ACCEPTED 21 June 2023
PUBLISHED 05 July 2023

CITATION
Tang Y, He W, Wang R, Ren H, Jin Z, Yang Z and Zhang Y (2023), Cyclostratigraphy of Lower Permian alkaline lacustrine deposits in the Mahu Sag, Junggar basin and its stratigraphic implication.
Front. Earth Sci. 11:1232418.
doi: 10.3389/feart.2023.1232418

Cyclostratigraphy of Lower Permian alkaline lacustrine deposits in the Mahu Sag, Junggar basin and its stratigraphic implication

Yong Tang[1], Wenjun He[1], Ran Wang[1], Haijiao Ren[1], Zhijun Jin[2], Zhuang Yang[2,3] and Yuanyuan Zhang[2,3]*

[1]PetroChina Xinjiang Oilfield Company, Karamay, Xinjiang, China, [2]Institute of Energy, Peking University, Beijing, China, [3]School of Earth and Space Sciences, Peking University, Beijing, China

The Lower Permian Fengcheng Formation of the Mahu Sag is one of the most potentially petroliferous sequences in China, and its unique alkaline lacustrine deposits provide important information on the paleoclimate and paleoenvironment of the early Permian. However, because of the complexity of the heterogeneous lithology and sedimentary facies in lacustrine deposits, the lateral correlation of lithofacies becomes challenging. Using cyclostratigraphy, we conducted a detailed astronomical cycle analysis of the Lower Permian Fengcheng Formation in the northern Mahu Sag, established an astronomical time scale, and constructed an isochronous sedimentary framework by collating the cycles of the different wells. Nine 405-kyr long-eccentricity cycles in the Fengcheng Formation were identified, and absolute astronomical time scales were established with the anchored point at ~300 Ma in the Lower member of the Fengcheng Formation. Based on the identification of lithofacies, the spatio-temporal variation in the lithofacies within the Fengcheng Formation was reconstructed. The astronomical time scale has proven to be reliable, and the lithofacies distribution within the isochronal framework is effective for investigating the spatial variation of lithofacies in alkaline lacustrine deposits. Favorable dolomitic mudstones developed in the central and transitional zones, corresponding to the three long-eccentricity cycles in the middle member of the Fengcheng Formation. Tuffaceous mudstones with high potential mainly developed in the lower member of the Fengcheng Formation in the marginal zone of the Mahu Sag. This study demonstrates an approach that can be used to study lithofacies in lacustrine deposits.

KEYWORDS

Fengcheng Formation, lacustrine deposit, cyclostratigraphy, lithofacies identification, isochronal framework

1 Introduction

With its great exploration potential, lacustrine shale oil has been considered a critical strategic target for increasing hydrocarbon production in China (Jin et al., 2021). Shale oil exploration is primarily associated with saline or brackish lacustrine basins (Hu et al., 2022). Alkaline lacustrine deposits develop in extremely salinized lakes and are prone to host high-

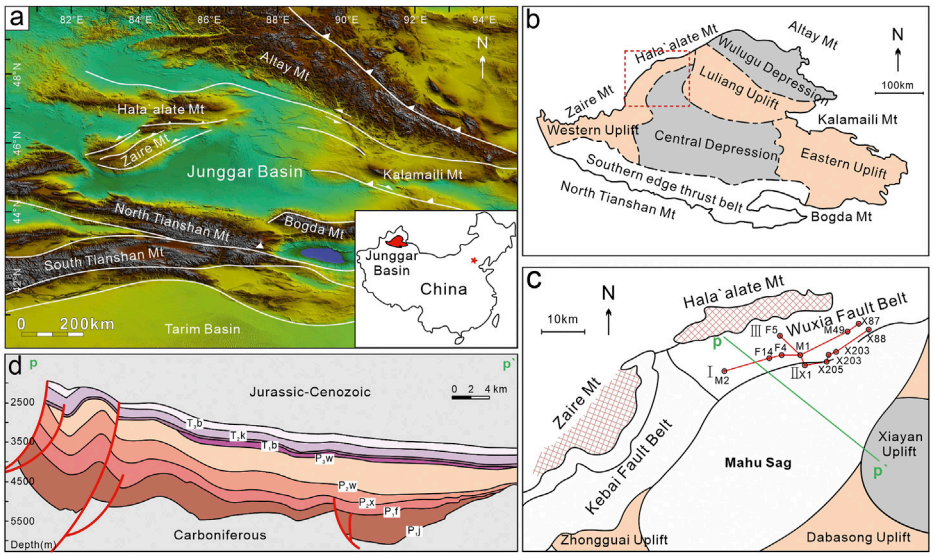

FIGURE 1
(A) Location of the Junggar Basin and regional geological map of the Junggar Basin and adjacent regions. **(B)** The first-order six structural units of the Junggar Basin and the location of Mahu sag (red dotted frame). **(C)** Simplified geological map of the Mahu sag with well locations. **(D)** Stratigraphic framework of the Permian to Triassic based on the seismic profiles (modified from Liang et al., 2020). The location of the profile is shown in green line pp' in Figure 1C.

quality oil shales (Zhi et al., 2019; Tang Y et al., 2021). The formation of such an alkaline lake is jointly controlled by favorable paleoclimatic, paleotectonic, and paleogeographic conditions (Cao et al., 2020). Alkaline lakes have been proven to be favorable environments for organic matter accumulation and preservation and have been recognized as having high hydrocarbon (Burton et al., 2014; Xia et al., 2022). Therefore, alkaline lacustrine deposits are of great environmental and economic significance in paleoclimatic reconstruction and shale oil exploration (e.g., Smith and Carroll, 2015; Yu et al., 2019) and are characterized by the deposition of alkaline minerals (sodium carbonate minerals) and fine-grained organic-rich sediments (Warren, 2010; Pecoraino et al., 2015). However, the joint controlling factors in the formation of alkaline lakes, rapid facies changes, and variable depositional processes complicate the lithofacies in alkaline lakes, making it challenging to determine the distribution of favorable lithofacies (Li et al., 2019b).

Most known alkaline lake deposits are Eocene or younger in age (Warren, 2010; Wang T et al., 2020), whereas the Lower Permian Fengcheng Formation of the Junggar Basin is the most ancient well-preserved alkaline lacustrine deposit, which recorded crucial paleoclimate information of the Permian era and is considered a favorable archive of the Late Pale Ice Age (LPIA) (Montañez and Poulsen, 2013; Cao et al., 2020). Understanding the distribution of lithofacies in the Fengcheng Formation is fundamental for further paleoclimatic studies. The lack of an isochronal lithofacies framework hinders the lateral lithofacies correlation. Astronomical analysis of sedimentary sequences has been applied widely to find global signals recorded in strata and investigate the sedimentary responses to paleoclimate change of astronomy forcing, based on the Milankovitch theory (Hinnov, 2000; Hinnov, 2013; Sha et al., 2015), in order to establish the isochronal framework. Recently, ~405 kyr long-eccentricity cycles were recognized in the Late Permian strata (Huang et al., 2020), extending the astronomical time scale to the Paleozoic era.

In this study, we aimed to establish an astronomical time scale (ATS) for targeted sequences of the Fengcheng Formation and to reconstruct the sedimentary isochronal framework of the Fengcheng Formation in the Mahu Sag by lateral comparison among different wells. In combination with lithofacies identification, this study explored the lithofacies distribution of the alkaline lacustrine Fengcheng Formation in northern Mahu Sag, demonstrating an approach that can be used for the study of lithofacies in lacustrine deposits.

2 Geological background

Located in northwestern China, covering an area of approximately 134,000 km^2, the triangular-shaped Junggar Basin is a large petroliferous superimposed basin, in the southern part of the Central Asian Orogenic Belt (CAOB), which is bounded by the Altay Mountain (Mt.) to the north, the Kalamaili Mt. to the east, the Zaire-Hala'alate Mts. at the northwestern margin, and the North Tianshan-Bogda Mts. to the south (Figure 1A). As an intraplate superimposed basin, the Junggar Basin has experienced multistage intraplate deformation after the final amalgamation of the Paleo-Asian Ocean (PAO) (Zhang et al., 2013; Han and Zhao, 2018; Liu et al., 2017, 2019; Zhang et al., 2016). The Junggar Basin consists of six first-order structural units: Wulungu Depression, Luliang Uplift, Central Depression, West Junggar, Northern Tianshan Overthrust Belt, and East Uplift (Figure 1B). The Mahu Sag is located in the northwestern region of the Central Depression (Figure 1C) and is surrounded by the Zhongguai and Dabasong Uplifts to the south and the Zaire and Hala'alate mountains in the northwest margin,

along which form three NE-SW trending dextral strike-slip faults (Yu et al., 2016; Tang W et al., 2021).

The Mahu Sag developed on the basement of a Paleozoic remnant ocean basin in West Junggar, and the filling process of the remnant ocean basin lasted until the Late Carboniferous (Chen et al., 2013). With the closure of the remnant ocean, the Mahu Sag transformed from marine to terrestrial sedimentation (Li et al., 2015) and evolved into a rift basin during the Permian (Tang W et al., 2021) (Figure 1D). The Lower Permian Fengcheng Formation of the Mahu Sag is considered an ancient alkaline lacustrine deposit (Cao et al., 2015) and has been demonstrated to be a set of fan-lacustrine sedimentary systems (Tang W et al., 2021). With thinning to the southeast (Figure 1D), the Fengcheng Formation is divided into three members with different lithological associations from bottom to top. The lower member (P_1f_1) is transitional with underlying volcanic units, dominated by dark gray mudstone, but contains a few tuffaceous mudstones and mafic-intermediate volcanic rocks. The middle member (P_1f_2) is characterized by alternating beds of evaporite and dolomitic mudstone and contains parts of other lithofacies, such as calcareous mudstone and dolomitic siltstone. Evaporites are dominated by sodium carbonates, which are formed under extremely alkaline water conditions (Yu et al., 2018; Jiang et al., 2023). The upper member (P_1f_3) is dominated by alternating beds of mudstone and siltstone, representing a phase in which salinity decreases and the input of terrestrial detrital sediments gradually increases, following the middle member (Yu et al., 2018; Wang T et al., 2020; Guo et al., 2021).

The Fengcheng Formation in the Mahu Sag is divided into three lateral areas (Cao et al., 2020; Ni et al., 2023), namely, a central zone with substantial deposition of sodium carbonate minerals and dolomitic mudstone, a transitional zone dominated by alternating dolomitic mudstone and siltstone, and a marginal zone dominated by siltstone and coarser sandstone, and quite a few volcanics, which correspond to the lateral changes of the fan-lacustrine sedimentary system.

3 Data and methods

3.1 Logging data

A number of geophysical log series have been utilized in the effort to recover long, continuous, and high-resolution stratigraphy signals (Hinnov, 2000; Li et al., 2019a). Natural Gamma Ray (NGR) logging data have been widely applied in sedimentology and stratigraphy, based on the radiogenic isotope uranium, thorium, and potassium content within sediments. Generally, K consists of minerals such as clays, mica, and feldspar; U and Th commonly exist in minerals such as clays, feldspar, and several heavy minerals; and U is also relatively concentrated in organic matter (Schnyder et al., 2006; Wang M et al., 2020). A high GR is generally attributed to fine-grained facies, such as mudstone and siltstone, whereas a low GR is related to coarser facies such as sandstone (Cantalejo and Pickering, 2015; Li et al., 2019a). Because all the above are associated with relative clay abundance, which is sensitive to environmental and climatic change, NGR log data of outcrops and drill wells are valuable tools for cyclostratigraphy and effective proxies for paleoclimate analysis (Huang et al., 2021). In addition, caliper and resistivity well logging data were utilized to assist in lithologic identification due to the different intrinsic physical and electric features of sodium carbonates and common rock-forming minerals.

In this study, the NGR profiles of the Fengcheng Formation from four wells, M1, F4, X202, and X203, in the northern Mahu Sag were used to conduct cyclostratigraphy analysis. Stratigraphic cyclicity and paleoclimate quasi-periodicity changes of astronomical forcing could be recognized, horizontal comparison of the astronomical time scale (ATS) performed, and even the establishment of a sedimentary isochronal framework of the whole sag could be conducted. Among the four wells, M1 and F4 were close to each other and approached to the depocenter, and X202 and X203 were close to the lake margin (Figure 1C). The vertical thickness of the four well profiles of the Fengcheng Formation was approximately 300–400 m, and the sampling rate of all the NGR profiles was 0.125 m. Then logging data from 12 wells widespread in the northern the Mahu Sag were used for lithological identification, from which three lateral profiles of the Fengcheng Formation were established in this study.

3.2 Time series analysis methods

Firstly, raw NGR data was screened from the perturbation of events and detrended. Then the spectral analysis of the detrended NGR was conducted to find periodic or quasi-periodic components. The data series in the depth domain were transformed into time domain by astronomical tuning in order to extract potential 405-kyr eccentricity cycles.

3.2.1 Pretreatment of raw NGR data

Climate proxy variations consist of long-terms, 10^3–10^6 year-scale orbital (eccentricity, obliquity, and precession) cycles, in addition to being punctuated by isolated events of sedimentary perturbation, such as storm, flooding, and volcanism, so-call sedimentary noises (Hinnov, 2013; Li et al., 2018a), which are more intense and frequent in lacustrine than marine. Therefore, quantitative cyclostratigraphic analysis should differentiate astronomical signals from spectral noise (Huang et al., 2020). Before the time series analysis, obvious isolated event perturbations were removed from the raw NGR data. Volcanism was the most widespread sedimentary perturbation event in the Fengcheng Formation of the northern Mahu Sag, particularly in M1, X202, and X203. Tuff layers and tuffaceous mudstone, characterized by their unusually high NGR values, were recorded in the sections, resulting in the prominent deviations in time series analysis. Then the screened NGR data from the Fengcheng Formation were detrended by subtracting a 35% weighted average to remove long-term trends (Li et al., 2019a).

3.2.2 Spectral analysis and tuning

Spectral analysis is primarily used to recognize periodic or quasi-periodic components in a data series (Li et al., 2019a). Prior to analysis, the NGR data were analyzed using multi-taper method (MTM) spectral estimator with robust red noise models, which could achieve an optimal trade-off between frequency resolution

TABLE 1 Summary of criterion of the identification of lithofacies based on the logging data (adapted from Qian et al. (2022)).

CAL	NGR	Rt	CNL	Litho
<10	>69	15<Rt<80	>0.16	Calcareous Mudstone
	>69	80<Rt<1500	>0.16	Dolomitic Mudstone
	100 ≤ Gr ≤ 130	Rt<80	<0.16	Dolomitic Mudstone
	<69	Rt<15	>0.16	Silty Mudstone
	>69	Rt<15	>0.16	Mudstone
		>1500	0.09<CNL<0.16	Muddy Dolomite
	<130	1500<Rt<2000	<0.09	Silty Dolomite
		>2000	<0.09	Dolomite
	<69	15<Rt<80	>0.16	Calcareous Siltstone
	<100	Rt<80	<0.16	Calcareous Siltstone
	<69	80<Rt<1500	>0.16	Dolomitic Siltstone
		<80	<0.16	Siltstone
	>150			Tuffaceous Mudstone
>10	>69	>1500	>0.09	Sodium carbonate-bearing Mudstone
	<69	>1500	>0.09	Sodium carbonate-bearing Mudstone
>16			>0.3	Sodium Carbonate

and statistical confidence for uniformly spaced time series. Evolutionary spectral analysis was applied to the NGR data to detect the evolution of frequencies through succession, by setting a specific sliding window and a step to detect the targeted frequencies according to the spectral characteristics of the well. Filtering is an efficient way to isolate specific frequency components (according to the results of spectral analysis) in a data series, and frequencies with high significance levels may be related to Milankovitch forcing frequencies. All analysis steps were conducted using *Acycle* v2.0 software (Li et al., 2019a). Astronomical tuning is a necessary step when original data, usually in the depth domain, must be transformed into the time domain. A filter signal from the data series can be used to reconstruct the age model by assigning the maximum (or minimum) depth of each filtered series to a time value that is generally obtained from radioisotopic dating (Li et al., 2019a). The absolute astronomical time scale was constructed by anchoring the floating ATS to the U-Pb age of widespread volcanic rocks in the lower member of the Fengcheng Formation at ~300 Ma (Li et al., 2023), which was taken as the anchored point for the absolute time scale in this study.

3.2.3 Evolutional correlation coefficient

The *Acycle v2.0* software includes tools for simultaneously testing the astronomical forcing of paleoclimate data series and mean sedimentation rate with a correlation coefficient (COCO) approach, with an extension for testing the evolution of the sedimentation rate (eCOCO) along the data series (Li et al., 2018b; Li et al., 2019a). The NGR data were analyzed using the COCO approach to find the most likely sedimentation rate and the eCOCO approach to test the evolution of the sedimentation rate along the data series with a given sliding window and step. ρ (correlation coefficient), H_0 significance level, and number of contributing astronomical frequencies are three key indices for evaluating the availability and significance level of the simulated results (Li et al., 2018b). The sedimentation rate most likely corresponded to the highest correlation coefficient (ρ). A null hypothesis (H_0), that no astronomical frequencies existed, was adopted in the data series, which helped determine whether astronomical forcing existed (Li et al., 2018b). All analysis steps were conducted using *Acycle v2.0* software (Li et al., 2019a).

3.3 Lithofacies identification based on logs data

Based on the log data and drill core samples, lithofacies' identification was performed for 12 wells (Figure 1C). We summarized the distinct lithofacies of the Fengcheng Formation based on the different characteristics of the logging data. Combined with a previous study (Qian et al., 2022), there are three remarkable indices from the logging data to distinguish several different lithofacies (Table 1). 1) Caliper (CAL) is a log index used to measure the size change of the borehole. In general, rocks of different physical natures respond differently to the pressure generated from drilling and the breakout of the well wall increasing in size, whereas the standard borehole size is approximately 9 cm. In the Fengcheng Formation, lithofacies bearing sodium carbonate minerals have a prominent feature: the caliper (CAL) log index is higher than 9, which distinguishes it from other lithofacies. 2) Natural Gamma Ray (NGR) is a reliable index for detecting clay content in different lithofacies, which can help

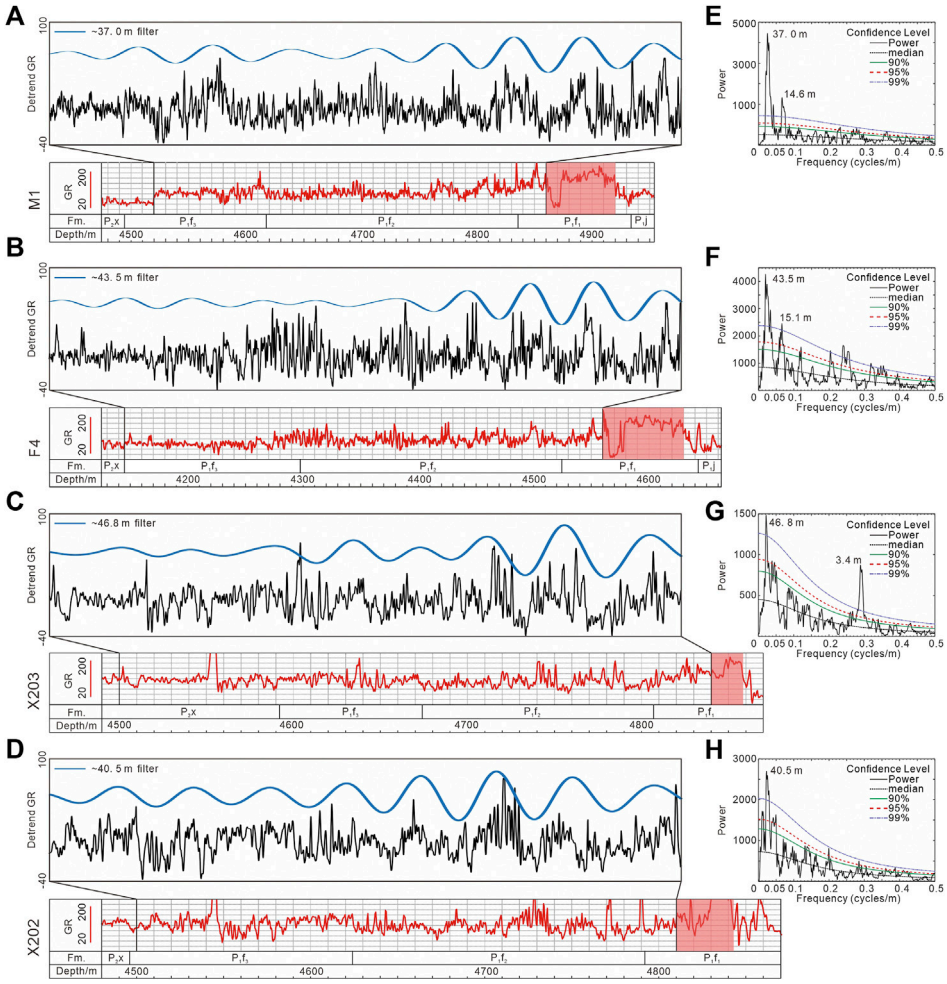

FIGURE 2
Spectral analysis and filter outputs of four wells: M1, F4, X203, and X202 **(A–D)**. Raw NGR data (red curve) and standardized NGR data (black curve) after pretreatment of detrending and removing event perturbations and filter outputs (blue wave line) by isolating specific frequency. **(E–H)** The main filtered cycles with more than 99% confidence level of four sections were calculated and identified by the 2π multi-taper method (MTM) spectral estimator. The red shades in **(A–D)** represent the widespread and simultaneous volcanism in the lower member of Fengcheng Formation, which is as an anchored point for absolute time scale in this study.

distinguish mudstone from siltstone at a value of approximately 69 GAPI. 3) Resistivity (Rt) is a logs index used to measure the resistivity of the original strata, which could help to distinguish "calcareous" lithofacies from those of "dolomitic." In general, "calcareous" is classified with an Rt value of 15–80 Ωm, while "dolomitic" is identified with a value higher than 80 Ωm. Detailed integrated logging characteristics of the different lithofacies are listed in Table 1.

4 Results

4.1 Times series analysis

The 2π multitaper (MTM) power spectrum of 4-wells NGR series shows significant peaks above 99% confidence level at wavelengths of 37.0 m, 14.6 m for M1, 43.5 m, 15.1 m for F4 and 46.8 m, 3.4 m for X203, and 40.5 m for X202 respectively (Figure 2). Then Low-pass Gaussian filters were used to recognize and isolate the low-frequency and secular trend components though the entire NGR series, and the filter outputs of specific frequencies for targeted series intervals were shown above the detrended NGR curves (Figure 2). Nine cycles were identified in the Fengcheng Formation of F 4; those of the other wells were at least eight.

The correlation coefficient (COCO) approach can help estimate the most likely sedimentation rate, and the studied section and two representative wells, M1 and X203, were applied to this COCO approach. Three potential sedimentation rates at 3.5 cm/kyr, 9–12 cm/kyr, and 14–15 cm/kyr of M1 have null hypothesis (H_0) significant levels of less than 0.01, indicating the null hypothesis of no astronomical signal can be rejected at a 1% (H_0 value < 2–10). In other words, the significance level of the presence of an astronomical signal was 99%, but the sedimentation rate at 9–12 cm/kyr yields correlation coefficient values higher than 0.4, which were generally higher than those of the other two sedimentation rates (Figure 3A). Together, these two indices indicate that the most likely sedimentation rate of

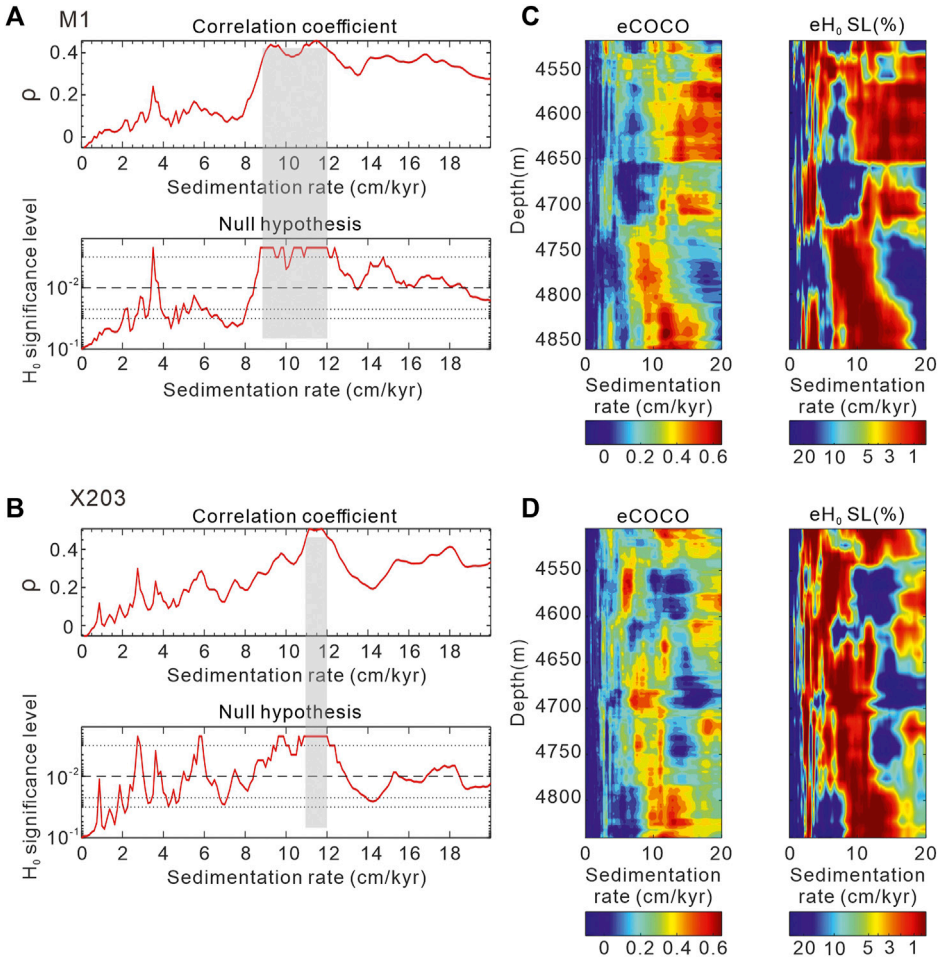

FIGURE 3
Sedimentation rate estimations of the Fengcheng Formation of wells M1 and X203 based on COCO and eCOCO analysis. **(A,B)** With the highest correlation coefficient value and smallest null hypothesis (H_0) significance level, the most likely sedimentation rates are 9–12 cm/kyr and 11–12 cm/kyr for M1 and X203 respectively. **(C,D)** Changes in sedimentation rates along the sections of both wells were demonstrated with the evolutional correlation coefficient (eCOCO) map and the evolutional null hypothesis significance level map.

M1 varies between 9 and 12 cm/kyr. The results of the COCO analysis of well X203 showed that the most likely sedimentation rate varies between 11 and 12 cm/kyr (Figure 3B). The evolutional correlation coefficient (eCOCO) and evolutional null hypothesis significance level (eH_0SL) maps show the change of the sedimentation rate through the data series (Figures 3C, D); a relatively stable sedimentation rate at 10–15 cm/kyr is significantly identified in the lower part of the targeted section with upwards reducing to 9–10 cm/kyr slowly, and at the top of the targeted section, the sedimentation rates are significantly increased to about 15 cm/kyr.

4.2 Astronomical tuning and floating astronomical time scale

Based on both the filtered outputs of the NGR data series and the corresponding estimation of the most likely sedimentation rate, a simple calculation can be conducted by dividing the wavelength of the filtered output by the sedimentation rate, which generates the duration time of a single cycle. Taking wells M1 and X203 as examples, with filtered outputs of 37 m/cycle and 46.8 m/cycle and sedimentation rates of 9–12 cm/kyr and 11–12 cm/kyr, the duration time of a single cyclicity is generated ranging between 308–412 kyr and 390–468 kyr respectively, and almost the same duration ranges were obtained from the other two NGR log data. Numerical models indicate that the ~405 kyr long-eccentricity cycles can be recognized through the Late Permian (Wu et al., 2013). Collectively, we tuned these filtered outputs extracted from several NGR data series by fixing the duration time of every single cycle to a 405 kyr long-eccentricity (Figure 4) and yield a ~3.6 Ma long floating astronomical time scale of (ATS) for the Fengcheng Formation in the northern Mahu Sag.

5 Discussion

5.1 Astrochronology of the Fengcheng Formation

An absolute astronomical time scale (ATS) can be constructed by anchoring a floating ATS to the absolute time (Li et al., 2019a).

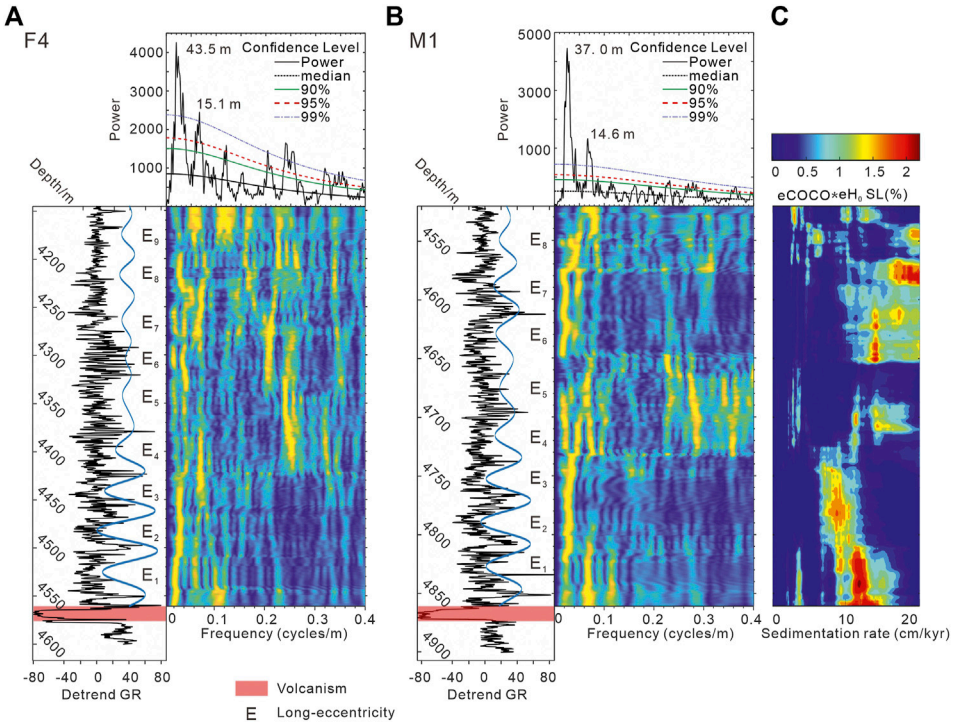

FIGURE 4
Astronomical tuning and astronomical time scale of wells F4 and M1. **(A)** F4, Tuning the cycle 43.5 m by fixing its duration to 405-kyr long-eccentricity (blue wave line), and anchoring the floating astronomical time scale at the widespread volcanism event (red shade) to establish the absolute time scale. Evolutional power spectra (colored plot) calculated using an 80-m running window. 2π MTM power spectrum is also shown on the top. **(B)** M1, different cycle thickness (37.0 m) but with the same duration time 405-kyr long-eccentricity, indicating the different sedimentation rates from F4 in Fengcheng formation. **(C)** evolution sedimentation rate map with eCOCO*eH$_0$SL values indicating the most likely sedimentation rates' estimation with the presence of astronomical forcing.

Widespread volcanism in the lower Fengcheng Formation of the northern Mahu Sag was discovered by identification of the lithofacies based on log data series, marked by a combination of basalt and an underlying tuff layer, which are characterized by unusually low GR and unusually high GR values, respectively (Figures 2, A,B). The absolute astronomical time scale was constructed by anchoring the floating ATS to the U-Pb age of volcanism (~300 Ma) in the lower member of the Fengcheng Formation (Li et al., 2023). The common anchored time of the ATS and the same duration of cycles form an established isochronal framework of the northern Mahu Sag, by calibrating the beginning of the time series and the long-eccentricity cycles of adjacent wells.

Frequency ratio is a common approach to test whether the observed cycles in data series were formed by astronomical forcing (Hinnov, 2000). Except for the 405-kyr long eccentricity cycle, no other prominent astronomical cycles were discovered in the spectral analysis, such as short-eccentricity, obliquity, and precession (Figure 4). Therefore, we cannot use frequency ratios to calibrate the long eccentricity to tune other astronomical cycles. The results of the time series analysis show that the long-eccentricity cycles are remarkable in the lower part of the targeted Fengcheng Formation (Figures 4A, B), but upward ambiguous cycle signals complicate the interval, and the long-eccentricity cycle signals become less certain (with depth of 4300–4400 m of F4 in Figure 4A and 4650–4730 m for M1 in Figure 4B), which indicates more intense sedimentary perturbations. Based on both the evolutionary spectral analysis and the evolutionary sedimentation rate map of M1 well (Figure 4), the intervals with clear and robust astronomical cycle signals have sedimentation rate estimations with stable variation and a high significance level. The sedimentation rate in the upper part of the Fengcheng Formation was higher than that in the lower part, as indicated by the estimation of the eCOCO*eH$_0$SL map (Figure 4C).

5.2 Sedimentary isochronal framework and spatial variation of lithofacies

Based on the absolute astronomical time scale of 12 wells in the northern Mahu Sag and the criterion of lithofacies' identification, a sedimentary isochronal framework involving the absolute time scale, distribution, and variation of lithofacies was constructed (Figure 5). Although the Fengcheng Formation has been recognized as having a heterogeneous lithology and sedimentary facies (Tang Y et al., 2021), this sedimentary isochronal framework provides an approach for investigating and describing the distribution and spatial variation of lithofacies.

Three crossing profiles were constructed within an isochronal framework to demonstrate the variation in lithofacies in the northern Mahu Sag. The two NE-SW trending profiles show variation in the lithofacies along the provenance direction (Figures 5A, B), and the NW-SE trending profile shows lithofacies' variation subvertical to the provenance direction

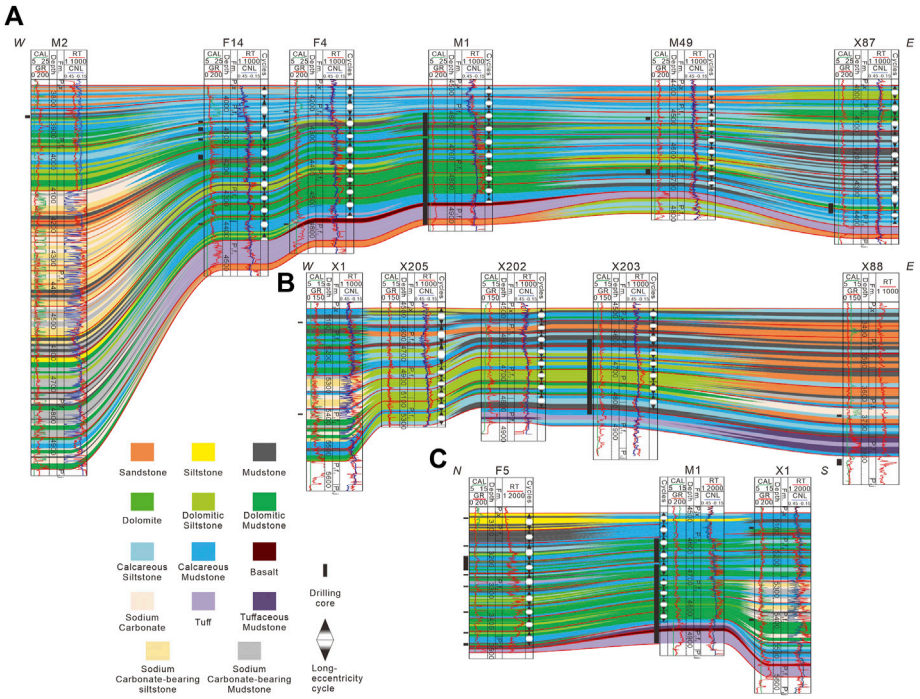

FIGURE 5
Distribution of lithofacies within the astronomical isochronal framework of profile I **(A)**, II **(B)**, and III **(C)**, see the profile location in Figure 1C.

(Figure 5C). According to profile I, widespread volcanism occurred in the lower member of the Fengcheng Formation in the northern Mahu Sag and upward, the lithofacies were principally composed of calcareous and dolomitic mudstone and siltstone. The distinct facies change from the marginal fan to the central deep lake, especially in the middle member of the Fengcheng Formation. For example, in the M2 well, the facies changed from calcareous mudstone or siltstone in the marginal fan to dolomitic mudstone in the central deep lake environment and a large mass of sodium carbonate minerals emerged in the middle member of the Fengcheng Formation. In the upper Fengcheng Formation, the lithofacies consist of calcareous mudstone and siltstone, with small amounts of dolomitic mudstone and siltstone. The coarser grain size from the lower member to the upper member indicates a trend of the lake level gradually becoming shallower, especially the remarkable facies change in wells F14, F4, and M1 (Figure 5A), corresponding to the change in the sedimentation rate of the evolutional correlation coefficient analysis (Figure 4). In addition, the lateral variations in lithofacies showed favorable continuity within the framework, which is consistent with the astronomical time scale. Profile II has a similar trend with profile I from the marginal to the central zone but reveals more distinct facies changes. In the middle member of the Fengcheng Formation, an apparent change in lithofacies from sandstone interbedded with mudstone to dolomitic siltstone is displayed, and the lithofacies upward become more complex, indicating more intense sedimentary perturbations. Well X1 in the central zone of the Mahu Sag also shows the accumulation of sodium carbonate minerals under deep lacustrine conditions.

Profile III demonstrates a direction vertical to the trend of profiles I and II, and reveals different variations of lithofacies' characteristics. The lithofacies in profile III (Figure 5C) gradually changed vertically from dolomitic mudstone chiefly to interbedded dolomitic and calcareous mudstone and transformed into calcareous mudstone chiefly in the upper member. The lateral distribution of lithofacies revealed better continuity and stability than in profiles I and II. There are no prominent changes in lithofacies in the lower and middle parts of the Fengcheng Formation. However, there is a remarkable terrigenous supply from the NW to SE, as shown by the F5 well in the upper member of the Fengcheng Formation (Figure 5C), indicating that the lake level became shallow and sedimentary perturbations gradually intensified.

Among the three profiles, the lithofacies' identification results were consistent with the absolute astronomical time scale. In other words, based on the cyclostratigraphy, the correlation of lithofacies of the alkaline lacustrine deposits can be established. Therefore, the ATS is reliable and the lithofacies' distribution within the isochronal framework is effective for investigating the spatial variation of lithofacies of alkaline lacustrine deposits in the northern Mahu Sag, providing a reference for understanding the sedimentation process. Lateral continuity and variation contribute to the search for favorable intervals in the lithofacies. Dissolved pores in dolomites and microfractures associated with laminae can greatly contribute to the pore volume of dolomitic mudstones. Tuffaceous mudstones have plenty of dissolved pores in feldspars. Therefore, dolomitic and tuffaceous mudstones have been shown to have better resource potential (Tang et al., 2022). Dolomitic mudstones developed in the central and transitional zones corresponding to three long-eccentricity cycles in the middle member of the Fengcheng Formation. Tuffaceous mudstones are mainly developed in the lower member of the Fengcheng Formation in the marginal zone of the Mahu Sag. The factors controlling the lithofacies' distribution should be further investigated

in the future. This study goes beyond the demonstration of variations in lithofacies in Lower Permian alkaline lacustrine deposits through a cyclostratigraphy study and attempts to establish an approach to demonstrate lithofacies' framework in lacustrine deposits.

6 Conclusion

The alkaline lacustrine deposits of the Fengcheng Formation in the northern Mahu Sag record the sedimentary response of paleoclimatic change to astronomical forcing. Based on cyclostratigraphic analyses of the NGR, nine 405-kyr long-eccentricity cycles in the Fengcheng Formation were identified, and the absolute astronomical time scales could be established with the anchored point at ~300 Ma in the Lower member of the Fengcheng Formation. By calibrating the ATSs of different wells, an isochronal framework of the Fengcheng Formation was constructed for the northern Mahu Sag.

Combined with the identification of lithofacies from logging data, the lithofacies' correlation of alkaline lacustrine deposits was well established. The ATS is reliable and the distribution of the lithofacies within the isochronal framework is effective for investigating the spatial variation in the lithofacies of the alkaline lacustrine deposits in the northern Mahu Sag. Favorable lithofacies with high potential are well demonstrated in the spatio-temporal lateral lithofacies' framework. This study demonstrates an approach that can be used in the study of lithofacies in lacustrine deposits.

Data availability statement

The original contributions presented in the study are included in the article/supplementary material, further inquiries can be directed to the corresponding author.

Author contributions

YT resources and project administration; WH resources and project administration; RW resources; HR resources; ZJ project administration; ZY writing—original draft and data processing. YZ supervision, conceptualization, writing, review, and editing. All authors contributed to the article and approved the submitted version.

Funding

This research is supported by the Natural Science Foundation of China (NSFC) Project given to Prof. Zhaojie Guo (No. 42090021).

Conflict of interest

Authors YT, WH, RW, and HR were employed by PetroChina Xinjiang Oilfield Company.

The remaining authors declare that the research was conducted in the absence of any commercial or financial relationships that could be construed as a potential conflict of interest.

Publisher's note

References

Burton, D., Woolf, K., and Sullivan, B. (2014). Lacustrine depositional environments in the green river formation, uinta basin: Expression in outcrop and wireline logs. *AAPG Bull.* 98 (9), 1699–1715. doi:10.1306/03201413187

Cantalejo, B., and Pickering, K. T. (2015). Orbital forcing as principal driver for fine-grained deep-marine siliciclastic sedimentation, Middle-Eocene Ainsa Basin, Spanish Pyrenees. *Paleogeogr. Paleoclimatol. Paleoecol.* 421, 24–47. doi:10.1016/j.palaeo.2015.01.008

Cao, J., Lei, D. W., Li, Y. W., Tang, Y., Abulimit, Chang, Q. S., et al. (2015). Ancient high-quality alkaline lacustrine source rocks discovered in the lower permian Fengcheng Formation, Junggar Basin. *Acta Pet. Sin.* 36 (07), 781–790. (in Chinese with English Abstract). doi:10.7623/syxb201507002

Cao, J., Xia, L., Wang, T., Zhi, D., Tang, Y., and Li, W. (2020). An alkaline lake in the late paleozoic Ice age (LPIA): A review and new insights into paleoenvironment and petroleum geology. *Earth-Sci. Rev.* 202, 103091. doi:10.1016/j.earscirev.2020.103091

Chen, S., Guo, Z., Pe-Piper, G., and Zhu, B. (2013). Late Paleozoic peperites in West Junggar, China, and how they constrain regional tectonic and palaeoenvironmental setting. *Gond. Res.* 23, 666–681. doi:10.1016/j.gr.2012.04.012

Guo, P., Wen, H., Gibert, L., Jin, J., Wang, J., and Lei, H. (2021). Deposition and diagenesis of the Early Permian volcanic-related alkaline playa-lake dolomitic shales, NW Junggar Basin, NW China. *Mar. Pet. Geol.* 123, 104780. doi:10.1016/j.marpetgeo.2020.104780

Han, Y., and Zhao, G. (2018). Final amalgamation of the tianshan and junggar orogenic collage in the southwestern central asian orogenic belt: Constraints on the closure of the paleo-Asian ocean. *Earth-Sci. Rev.* 186, 129–152. doi:10.1016/j.earscirev.2017.09.012

Hinnov, L. A. (2013). Cyclostratigraphy and its revolutionizing applications in the Earth and planetary sciences. *Geol. Soc. Am. Bull.* 125 (11-12), 1703–1734. doi:10.1130/b30934.1

Hinnov, L. A. (2000). New perspectives on orbitally forced stratigraphy. *Annu. Rev. Earth Planet. Sci.* 28, 419–475. doi:10.1146/annurev.earth.28.1.419

Hu, S., Bai, B., Tao, S., Bian, C., Zhang, T., Chen, Y., et al. (2022). Heterogeneous geological conditions and differential enrichment of medium and high maturity continental shale oil in China. *Pet. Explor. Dev.* 49 (2), 257–271. doi:10.1016/s1876-3804(22)60022-3

Huang, H., Gao, Y., Jones, M. M., Tao, H., Carroll, A. R., Ibarra, D. E., et al. (2020). Astronomical forcing of Middle Permian terrestrial climate recorded in a large paleolake in northwestern China. *Paleogeogr. Paleoclimatol. Paleoecol.* 550, 109735. doi:10.1016/j.palaeo.2020.109735

Huang, H., Gao, Y., Ma, C., Niu, L., Dong, T., Tian, X., et al. (2021). Astronomical constraints on the development of alkaline lake during the carboniferous-permian period in north pangea. *Glob. Planet. Change.* 207, 103681. doi:10.1016/j.gloplacha.2021.103681

Jiang, C., Wang, G., Song, L., Huang, L., Wang, S., Zhang, Y., et al. (2023). Identification of fluid types and their implications for petroleum exploration in the shale oil reservoir: A case study of the Fengcheng Formation in the Mahu sag, Junggar Basin, northwest China. *Mar. Pet. Geol.* 147, 105996. doi:10.1016/j.marpetgeo.2022.105996

Jin, Z., Zhu, R., Liang, X., and Shen, Y. (2021). Several issues worthy of attention in current lacustrine shale oil exploration and development. *Pet. Explor. Dev.* 48 (6), 1471–1484. doi:10.1016/s1876-3804(21)60303-8

Li, D., He, D., Qi, X., and Zhang, N. (2015). How was the carboniferous balkhash–West Junggar remnant ocean filled and closed? Insights from the well tacan-1 strata in the tacheng basin, NW China. *Gond. Res.* 27 (1), 342–362. doi:10.1016/j.gr.2013.10.003

Li, M., Hinnov, L. A., Huang, C., and Ogg, J. G. (2018a). Sedimentary noise and sea levels linked to land-ocean water exchange and obliquity forcing. *Nat. Commun.* 9 (1), 1004. doi:10.1038/s41467-018-03454-y

Li, M., Hinnov, L., and Kump, L. (2019a). Acycle: Time-series analysis software for paleoclimate research and education. *Comput. Geosciences* 127, 12–22. doi:10.1016/j.cageo.2019.02.011

Li, M., Kump, L. R., Hinnov, L. A., and Mann, M. E. (2018b). Tracking variable sedimentation rates and astronomical forcing in Phanerozoic paleoclimate proxy series with evolutionary correlation coefficients and hypothesis testing. *Earth Planet. Sci. Lett.* 501, 165–179. doi:10.1016/j.epsl.2018.08.041

Li, M., Ma, X. X., Jiang, Q. G., Li, Z. M., Pang, X. Q., Zhang, C. T., et al. (2019b). Enlightenment from formation conditions and enrichment characteristics of marine shale oil in north America. *Pet. Geol. Recovery Effic.* 26 (01), 13–28. (in Chinese with English Abstract). doi:10.13673/j.cnki.cn37-1359/te.2019.01.002

Li, W., Zhang, Y., He, W., and Tang, Y. (2023). Subaqueous felsic volcanic sequence and its contribution to the ancient alkaline lacustrine deposits in the Mahu Sag, Junggar Basin, NW China. *Geol. J.* 2023, 4812. doi:10.1002./gj.4812

Liang, Y., Zhang, Y., Chen, S., Guo, Z., and Tang, W. (2020). Controls of a strike-slip fault system on the tectonic inversion of the Mahu depression at the northwestern margin of the Junggar Basin, NW China. *J. Asian Earth Sci.* 198, 104229. doi:10.1016/j.jseaes.2020.104229

Liu, B., Han, B.-F., Chen, J.-F., Ren, R., Zheng, B., Wang, Z.-Z., et al. (2017). Closure time of the junggar-balkhash ocean: Constraints from late paleozoic volcano-sedimentary sequences in the barleik mountains, West Junggar, NW China. *Tectonics* 36 (12), 2823–2845. doi:10.1002/2017tc004606

Liu, Y., Wang, X., Wu, K., Chen, S., Shi, Z., and Yao, W. (2019). Late Carboniferous seismic and volcanic record in the northwestern margin of the Junggar Basin: Implication for the tectonic setting of the West Junggar. *Gond. Res.* 71, 49–75. doi:10.1016/j.gr.2019.01.013

Montañez, I. P., and Poulsen, C. J. (2013). The late paleozoic Ice age: An evolving paradigm. *Annu. Rev. Earth Planet. Sci.* 41 (1), 629–656. doi:10.1146/annurev.earth.031208.100118

Ni, M., Zhang, Y., Tang, Y., and He, W. (2023). ·Distribution characteristics of organic matter in the Fengcheng Formation in Mahu sag, Junggar Basin: Implications for hydrocarbon generation model in alkaline lacustrine deposition. *Front. Earth Sci.* 11. doi:10.3389/feart.2023.1218788

Pecoraino, G., D'Alessandro, W., and Inguaggiato, S. (2015). The other side of the coin: Geochemistry of alkaline lakes in volcanic areas. *Volcan. Lakes* 2015, 219–237. doi:10.1007/978-3-642-36833-2_9

Qian, Y., Zou, Y., Zhao, X., Chang, Q., He, W., and Huang, L. (2022). Full core analysis and petroleum geological significance of permian Fengcheng Formation in well-MY1, Mahu sag. *Petroleum Reserv. Eval. Dev.* 12 (1), 204–214. (in Chinese with English Abstract). doi:10.13809/j.cnki.cn32-1825/te.2022.01.018

Schnyder, J., Ruffell, A., Deconinck, J.-F., and Baudin, F. (2006). Conjunctive use of spectral gamma-ray logs and clay mineralogy in defining late Jurassic–early Cretaceous palaeoclimate change (Dorset, U.K). *Paleogeogr. Paleoclimatol. Paleoecol.* 229 (4), 303–320. doi:10.1016/j.palaeo.2005.06.027

Sha, J., Olsen, P. E., Pan, Y., Xu, D., Wang, Y., Zhang, X., et al. (2015). Triassic-Jurassic climate in continental high-latitude Asia was dominated by obliquity-paced variations (Junggar Basin, Urumqi, China). *Proc. Natl. Acad. Sci. U. S. A.* 112 (12), 3624–3629. doi:10.1073/pnas.1501137112

Smith, M. E., and Carroll, A. R. (2015). *Stratigraphy and paleolimnology of the green river formation*. western USA: Springer.

Tang, W., Zhang, Y., Pe-Piper, G., Piper, D. J. W., Guo, Z., and Li, W. (2021). Permian to early triassic tectono-sedimentary evolution of the Mahu sag, Junggar Basin, Western China: Sedimentological implications of the transition from rifting to tectonic inversion. *Mar. Pet. Geol.* 123, 104730. doi:10.1016/j.marpetgeo.2020.104730

Tang, Y., Cao, J., He, W. J., Guo, X. G., Zhao, K. B., and Li, W. W. (2021). Discovery of shale oil in alkaline lacustrine basins: The late paleozoic Fengcheng Formation, Mahu sag, Junggar Basin, China. *Pet. Sci.* 18, 1281–1293. doi:10.1016/j.petsci.2021.04.001

Tang, Y., He, W., Zheng, M., Chang, Q., Jin, Z., and Li, J. (2022). Shale lithofacies and its effect on reservoir formation in Lower Permian alkaline lacustrine Fengcheng Formation, Junggar Basin, NW China. *Front. Earth Sci.* 10. doi:10.3389/feart.2022.930890

Wang, M., Chen, H., Huang, C., Kemp, D. B., Xu, T., Zhang, H., et al. (2020). Astronomical forcing and sedimentary noise modeling of lake-level changes in the Paleogene Dongpu Depression of North China. *Earth Planet. Sci. Lett.* 535, 116116. doi:10.1016/j.epsl.2020.116116

Wang, T., Cao, J., Carroll, A. R., Zhi, D., Tang, Y., Wang, X., et al. (2020). Oldest preserved sodium carbonate evaporite: Late paleozoic Fengcheng Formation, Junggar Basin, NW China. *GSA Bull.* 133 (7-8), 1465–1482. doi:10.1130/b35727.1

Warren, J. K. (2010). Evaporites through time: Tectonic, climatic and eustatic controls in marine and nonmarine deposits. *Earth-Science Rev.* 98 (3-4), 217–268. doi:10.1016/j.earscirev.2009.11.004

Wu, H., Zhang, S., Hinnov, L. A., Jiang, G., Feng, Q., Li, H., et al. (2013). Time-calibrated Milankovitch cycles for the late permian. *Nat. Commun.* 4, 2452. doi:10.1038/ncomms3452

Xia, L., Cao, J., Jin, J., Xiang, B., Ma, W., and Wang, T. (2022). Response of nitrogen isotopes to paleo-environment and organic carbon accumulation in a Late Paleozoic alkaline lake, Junggar Basin. *Chem. Geol.* 602, 120884. doi:10.1016/j.chemgeo.2022.120884

Yu, K., Cao, Y., Qiu, L., and Sun, P. (2019). Depositional environments in an arid, closed basin and their implications for oil and gas exploration: The lower Permian Fengcheng Formation in the Junggar Basin, China. *AAPG Bull.* 103 (9), 2073–2115. doi:10.1306/01301917414

Yu, K., Cao, Y., Qiu, L., Sun, P., Jia, X., and Wan, M. (2018). Geochemical characteristics and origin of sodium carbonates in a closed alkaline basin: The lower permian Fengcheng Formation in the Mahu sag, northwestern Junggar Basin, China. *Paleogeogr. Paleoclimatol. Paleoecol.* 511, 506–531. doi:10.1016/j.palaeo.2018.09.015

Yu, Y., Wang, X., Rao, G., and Wang, R. (2016). Mesozoic reactivated transpressional structures and multi-stage tectonic deformation along the Hong-Che fault zone in the northwestern Junggar Basin, NW China. *Tectonophysics* 679, 156–168. doi:10.1016/j.tecto.2016.04.039

Zhang, X., Zhao, G., Sun, M., Eizenhöfer, P. R., Han, Y., Hou, W., et al. (2016). Tectonic evolution from subduction to arc-continent collision of the Junggar ocean: Constraints from U-Pb dating and Hf isotopes of detrital zircons from the North Tianshan belt, NW China. *Geol. Soc. Am. Bull.* 128 (3-4), 644–660. doi:10.1130/b31230.1

Zhang, Y., Pe-Piper, G., Piper, D. J. W., and Guo, Z. (2013). Early Carboniferous collision of the Kalamaili orogenic belt, North Xinjiang, and its implications: Evidence from molasse deposits. *Geol. Soc. Am. Bull.* 125 (5-6), 932–944. doi:10.1130/b30779.1

Zhi, D. M., Tang, Y., Zheng, M. L., Xu, Y., Cao, J., Ding, J., et al. (2019). Geological characteristics and accumulation controlling factors of shale reservoirs in Fengcheng Formation, Mahu sag, Junggar Basin. *China Pet. explor.* 24 (05), 615–623. (in Chinese with English Abstract). doi:10.3969/j.issn.1672-7703.2019.05.008

frontiers | Frontiers in Earth Science

TYPE Original Research
PUBLISHED 06 July 2023
DOI 10.3389/feart.2023.1218215

OPEN ACCESS

EDITED BY
Ruyue Wang,
SINOPEC Petroleum Exploration and Production Research Institute, China

REVIEWED BY
Shuai Yin,
Xi'an Shiyou University, China
Mengdi Sun,
Northeast Petroleum University, China

*CORRESPONDENCE
Yuqiang Jiang,
xnsyjyq3055@126.com

RECEIVED 06 May 2023
ACCEPTED 26 June 2023
PUBLISHED 06 July 2023

CITATION
Fang R, Jiang Y, Sun S, Luo Y, Qi L, Dong D, Lai Q, Luo Y and Jiang Z (2023), Controlling factors of organic matter accumulation and lacustrine shale distribution in Lianggaoshan Formation, Sichuan Basin, SW China.
Front. Earth Sci. 11:1218215.
doi: 10.3389/feart.2023.1218215

Controlling factors of organic matter accumulation and lacustrine shale distribution in Lianggaoshan Formation, Sichuan Basin, SW China

Rui Fang[1,2], Yuqiang Jiang[1,2]*, Shasha Sun[3], Yao Luo[4], Lin Qi[5], Dazhong Dong[3], Qiang Lai[5], Yuzhuo Luo[6] and Zengzheng Jiang[7]

[1]School of Geosciences and Technology, Southwest Petroleum University, Chengdu, China, [2]The Unconventional Reservoir Evaluation Department, PetroChina Key Laboratory of Unconventional Oil and Gas Resources, Chengdu, China, [3]PetroChina Research Institute of Petroleum Exploration and Development, Beijing, China, [4]Southwest Geophysical Exploration Branch of China Petroleum Group Dongfang Geophysical Exploration Co., Ltd., Chengdu, China, [5]Geology Exploration and Development Research Institute, CNPC Chuanqing Drilling Engineering Co., Ltd., Chengdu, China, [6]Northeastern Sichuan Oil and Gas District, PetroChina Southwest Oil and Gas Field Company, Dazhou, China, [7]Sichuan Geotech Science and Technology Ltd., Company, Chengdu, China

The lacustrine shale, represented by the Lianggaoshan Formation, is widely distributed in oil and gas basins of China and will be a key target for unconventional hydrocarbon exploration in the future. Due to the complexity of geological conditions, the distribution of lacustrine shale and the mechanism of organic matter (OM) enrichment show significant differences between different basins. In this study, seismic interpretation, core observation, high-frequency geochemical analysis and other methods are integrated to reveal factors controlling lacustrine shale distribution and OM accumulation in lacustrine shale. The results suggest that six bottom-to-top organic-rich shale intervals are identified within the Lianggaoshan Formation due to lake-basin migration. The migration process of depocenters controls the planar distribution of lacustrine organic-rich shale. The organic-rich lacustrine shale within 1st Member and 2nd Member is characterized by relatively high paleoproductivity and dysoxic condition. The lacustrine organic-rich shale of the upper to the top of 3rd Member is characterized by relatively low paleoproductivity, relatively high terrestrial input, and dysoxic condition. Paleoproductivity and preservation condition caused by lake-level rise are generally the major influencing factor of organic matter accumulation in 1st Member and 2nd Member organic-rich shale. The input of terrestrial OM, and the condition of preservation caused by rapid deposition are the major factors controlling OM accumulation in 3rd Member of Lianggaoshan Formation.

KEYWORDS

Jurassic, lacustrine shale, lake-basin, organic matter enrichment, Lianggaoshan Formation, Sichuan Basin

Introduction

Organic matter (OM) in fine-grained sedimentary rock (such as shale) is not only an important carrier of reservoir space and hydrocarbon occurrence, but also the material basis for hydrocarbon formation (Ross and Bustin, 2009; Fu et al., 2019; Zou, 2019; Fu et al., 2021). Its content is closely related to oil and gas production in both conventional and unconventional reservoirs (Zou et al., 2013; Zou et al., 2019; Li et al., 2022; Li et al., 2023). The OM enrichment in fine-grained sedimentary rock has important guiding significance for the prediction and evaluation of hydrocarbon "sweet spots" (Qiu and Zou, 2020a; Qiu and Zou, 2020b). The OM enrichment in shale is a complex physical-chemical process, which is affected by paleoclimate condition, paleoredox condition, paleosalinity, regional tectonic background, sediment transport process, hydrothermal activity, volcanic activity, gravity flow deposition (Deng et al., 2019; Liang et al., 2020; Liu et al., 2020; Gu et al., 2022a; Gu et al., 2022b; Lei et al., 2023). The impact of various paleo-environmental factors such as major geological events (water hypoxia events, biological extinction events) (Murphy et al., 2000), and the mechanisms (favorable or unfavorable) of different environmental conditions affecting OM can be summarized into three types of elements: input, preservation, and dilution of OM. The OM input mainly includes net primary productivity of endogenous seawater (or lake water) (excluding respiratory consumption by producers themselves) and inflow of terrestrial OM accompanied by debris (Lei et al., 2023). The preservation of organic matter mainly refers to the amount of input OM remaining on the sediment surface (after degradation and before sedimentation), which is mainly related to the redox characteristics of bottom water (Tribovillard et al., 2006). Dilution of OM mainly refers to the dilution of the molar concentration of OM by the input amount and input rate (or authigenic carbonate yield) of terrestrial debris (Deng et al., 2019).

The successful development of marine shale oil benefits by countries represented by the United States has triggered a wave of unconventional hydrocarbon exploration and development worldwide (Wang et al., 2016a; Wang et al., 2016b; Wang et al., 2018; Jiang et al., 2022). In recent years, the practical experience of marine shale oil has been continuously applied to the geological studies of lacustrine shale hydrocarbon resources (Lu et al., 2012). Major breakthroughs in shale oil have been achieved in several sedimentary basins in western and northern China (Hu D. et al., 2021; Hu Z. et al., 2021; He et al., 2022; Cai et al., 2023; Lai et al., 2023).

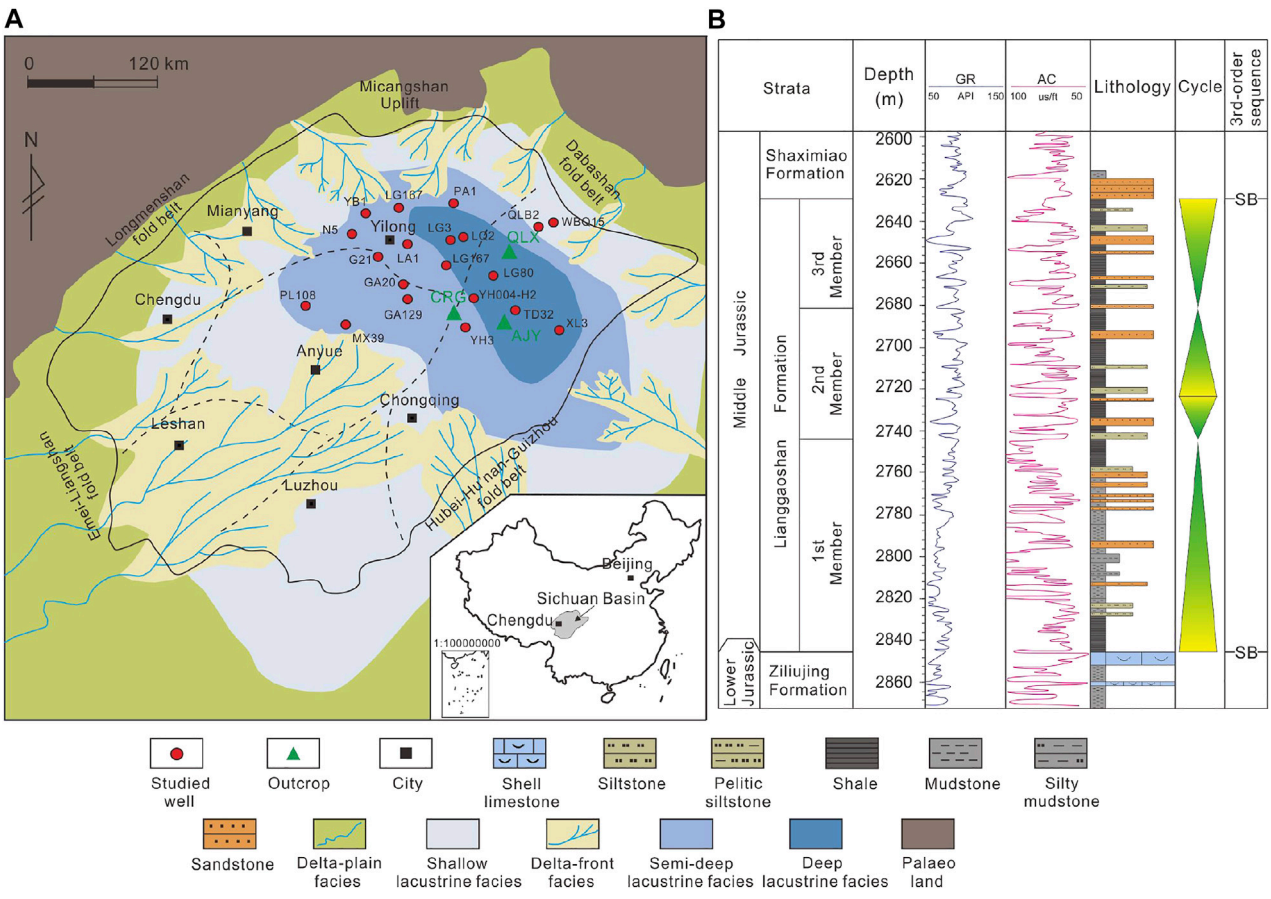

FIGURE 1
(A) Paleogeography of Lianggaoshan Fm. in Sichuan Basin. **(B)** Stratigraphic column of Jurassic Lianggaoshan Fm. in Sichuan Basin. SB, sequence boundary.

TABLE 1 Sedimentary facies division of Lianggaoshan Fm. in Sichuan Basin.

Facies	Subfacies	*In-situ* facies
Delta	Delta front	Underwater distributary channel
		Underwater natural levee
		Mouth bar
		Distal bar
	Delta plain	Natural levee
		Distributary channel
		Floodplain
Lake	Shallow lake	Shell shoal
		Sand bar
		Mud flat
	Semi-deep lake	Lacustrine mud

Breakthroughs have been obtained in the exploration of lacustrine shale hydrocarbons of the Middle Jurassic Lianggaoshan Fm. from Pingchang and Fuling areas of the Sichuan Basin since 2017 (Hu D. et al., 2021; Hu Z. et al., 2021; Cheng et al., 2023), demonstrating a good prospect for unconventional hydrocarbon exploration within the Lianggaoshan Formation. However, due to the significant differences in geological background between different basins and different environmental conditions during the development of lacustrine shale, there is significant uncertainty in its application, which poses great difficulties for exploration and development.

Based on seismic interpretation, core observation, high-frequency geochemical analysis and other methods, this study aims to reveal the lake-basin migration in the sedimentary process of Lianggaoshan Formation, characterizes the paleoenvironment of organic-rich shale, discusses the control of paleoclimate, redox properties of water bodies, paleoproductivity, and paleosalinity on organic matter enrichment, and reveals the relationship between the distribution of lacustrine shale, organic matter enrichment, and the sedimentary process of Lianggaoshan Formation.

Geological setting

The Sichuan Basin is located in southwestern China. During the sedimentary period of the Early Jurassic Ziliujing Formation (Fm.) to the Middle Jurassic Lianggaoshan Fm., the vast majority of this Basin belongs to the delta-lake sedimentary system (Figure 1A). The provenance of Lianggaoshan Fm., can be divided into three types: Type I, Type II and Type III, which reflects that the nature of parent rock has changed from igneous rock to metamorphic rock and sedimentary rock. The provenance areas correspond to the Micangshan area, northern margin of Yangtze plate, and Dabashan area respectively (Cheng et al., 2023). After the completion of Lianggaoshan Fm., sedimentation, the basin was converted into a river sedimentary system in internal conversion during the Middle Jurassic Shaximiao Fm., sedimentation period

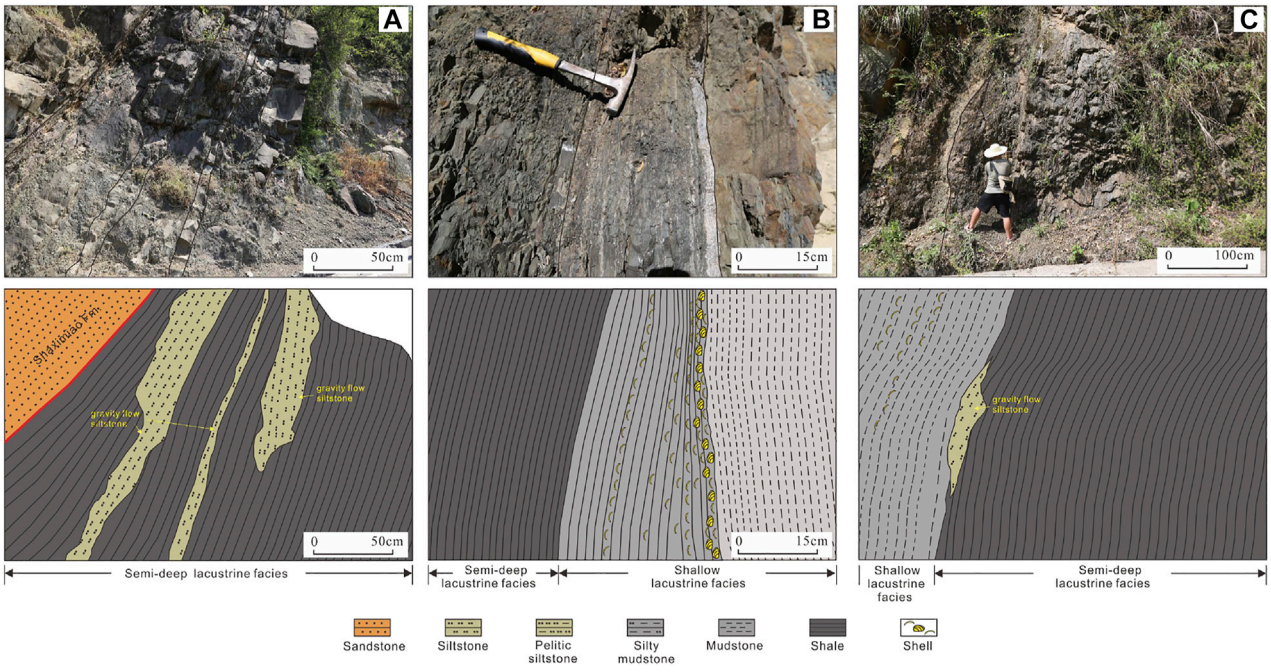

FIGURE 2
Typical lithological combinations and sedimentary facies types of Lianggaoshan Fm. in outcrops. **(A)** Gravity flow siltstone in black shale of semi-deep lake, QLX Outcrop, 3rd Member. **(B)** Black shale formed in semi-deep lake and grey mudstone formed in shallow lake, CRG Outcrop, 1st Member. **(C)** Shallow lacustrine grey mudstone and semi-deep lacustrine black shale, AJY Outcrop, 2nd Member.

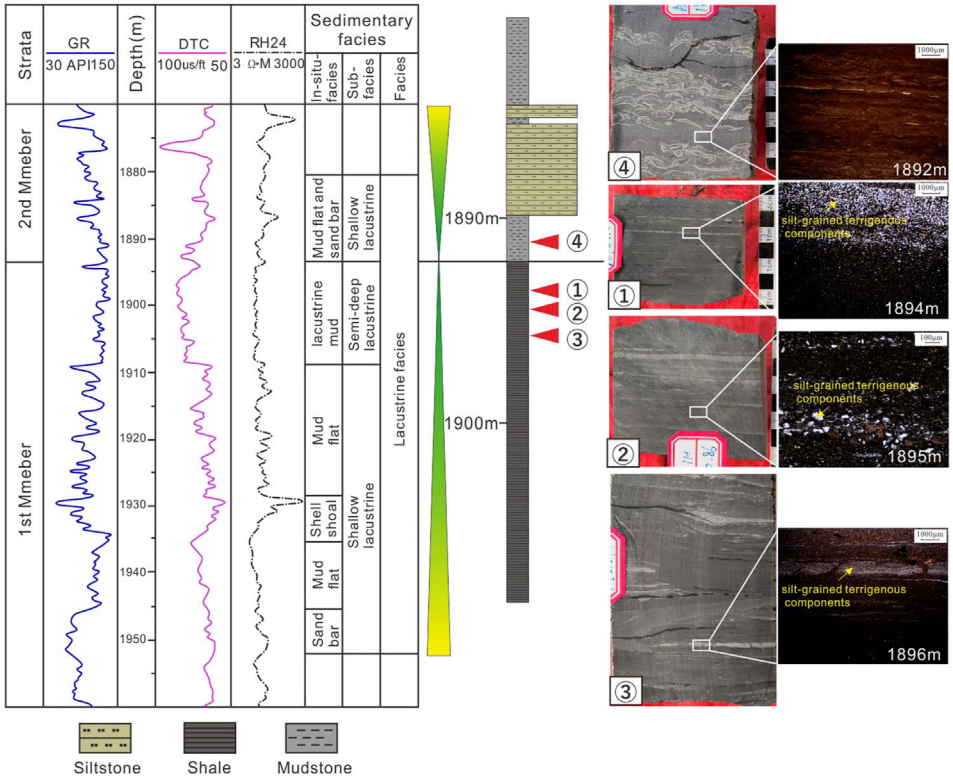

FIGURE 3
Development characteristics of lacustrine organic-rich shale in 1st Member of Lianggaoshan Fm., (based on Well HQ1).

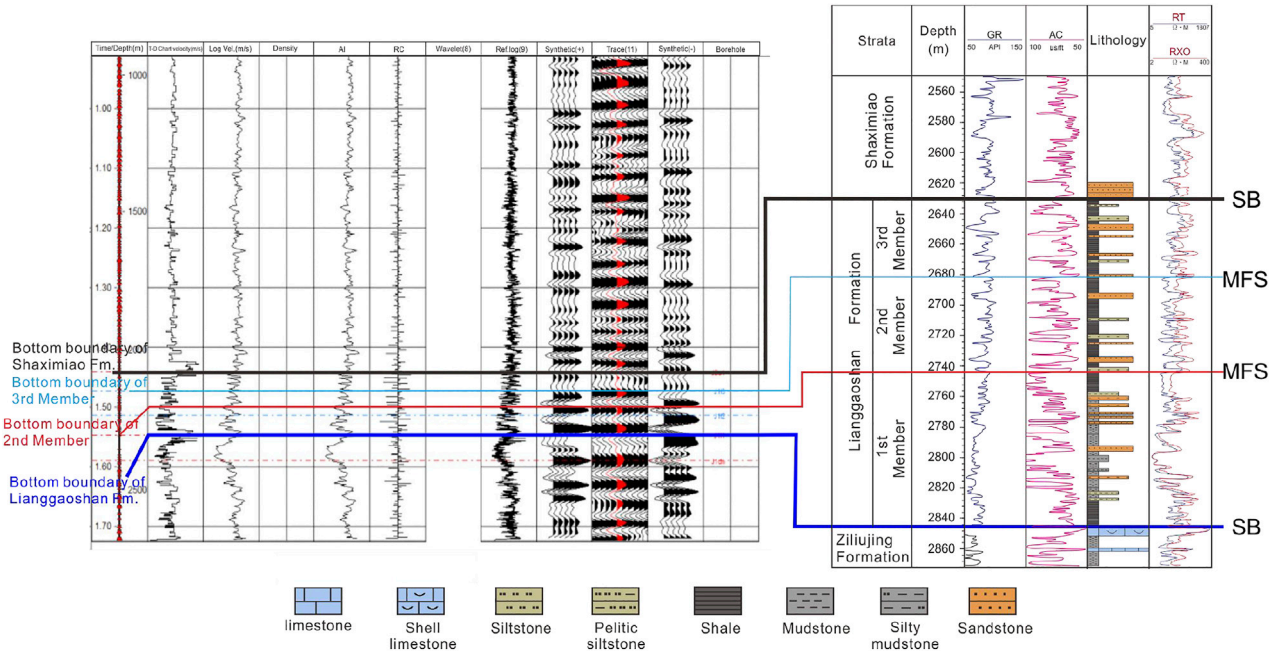

FIGURE 4
Synthetic seismogram of Jurassic system in Well LG3. MFS, maximum flooding surface; SB, sequence boundary.

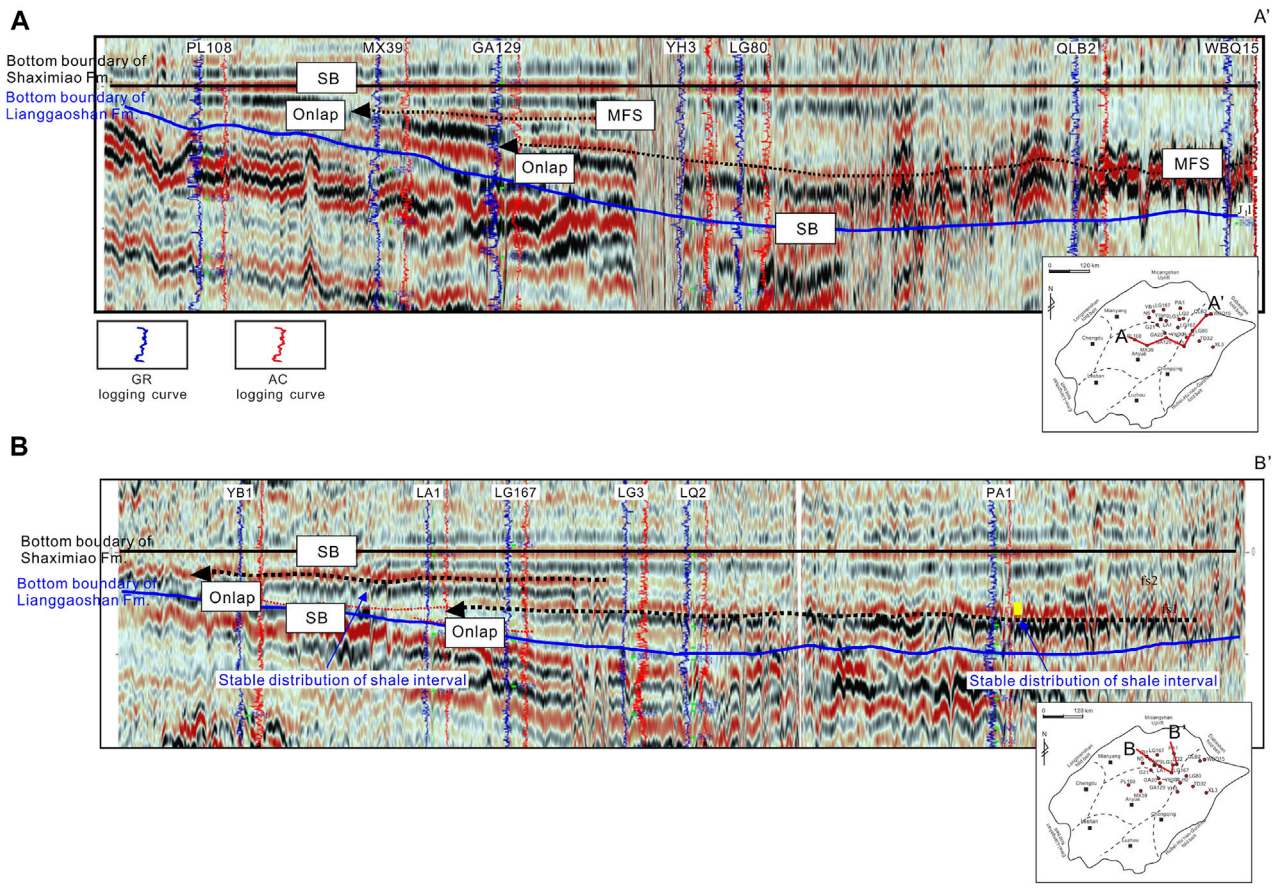

FIGURE 5
Seismic section showing maximum flooding surface (MFS) and sequence boundary (SB) in Lianggaoshan Formation. **(A)** Well PL108-MX39-GA129-YH3-LG80-QLB2-WBQ15. **(B)** Well YB1-LA1-LG167-LG3-LQ2-PA1.

(Cheng et al., 2023; Hu et al., 2023). The Lianggaoshan Fm., forms a separate third-order sequence, with a sequence boundary between the underlying and upper strata (Figure 1B). The Lianggaoshan Fm., belongs to the Middle Jurassic Aalenian to Bajocian Stage in terms of geological age (Huang, 2019), with a total thickness ranging from 100 to 260 m. The stratigraphic thickness gradually decreases from northeast to southwest. According to the characteristics of rock assemblages and cyclicity, the Lianggaoshan Fm., is divided into three segments: 1st Member, 2nd Member, and 3rd Member (Figure 1B).

Samples and methods

First, four Shaximiao Formation mudstone/shale samples and 28 Lianggaoshan shale samples obtained from coring wells were processed into 25 mm × 25 mm rock sample. Then, these rock samples were made into 0.03 mm thick thin-sections. Before the observation of petrology characteristics, the thin-sections shall be pretreated with mixed solution of alizarin red-S and potassium ferrocyanide.

The rock type and microscopic characteristics of thin-sections were observed through a Carl Zeiss polarizing microscope. The remaining samples were ground to 200 mesh powder by a mortar for elemental content detection. The main elements were tested using the Axios PW4400 X-ray fluorescence spectrometer, while the trace elements (TE) were tested using the Thermo X Series 2 plasma mass spectrometer. Corresponding analysis accuracy of both was below 5%. The TOC value was obtained using the American LECO CS-230 infrared sulfur and carbon analyzer, and pyrolysis parameters such as S_1, S_2, and T_{max} were obtained using the OGE-II rock pyrolysis analyzer.

Classification and characteristics of sedimentary facies

The main sedimentary facies types of Lianggaoshan Fm. include delta and lacustrine facies (Hu et al., 2023). The delta facies are mainly composed of delta front and delta plain subfacies (Cheng et al., 2023). The lake facies can be subdivided into shallow lake and semi-deep lake subfacies (Table 1). The semi-deep lake subfacies are mainly characterized by black shale (Figure 2A), and siltstone bodies of gravity flow origin are developed inside. The shallow lake subfacies are mainly characterized by gray mudstone (Figure 2B), and shell fossils can be observed internally (Figures 2B, C). The delta

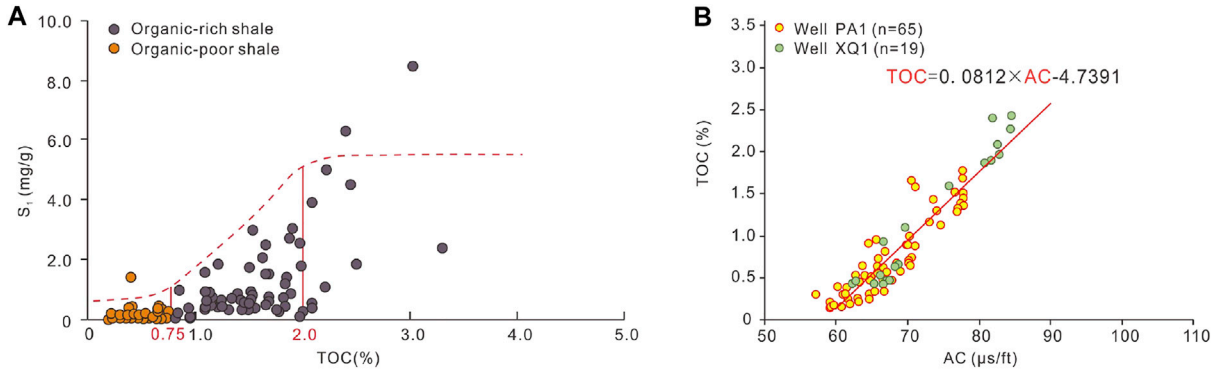

FIGURE 6
Correlations between different indicators. **(A)** TOC-S_1 diagram for Lianggaoshan lacustrine shale. **(B)** AC-TOC diagram for Lianggaoshan lacustrine shale.

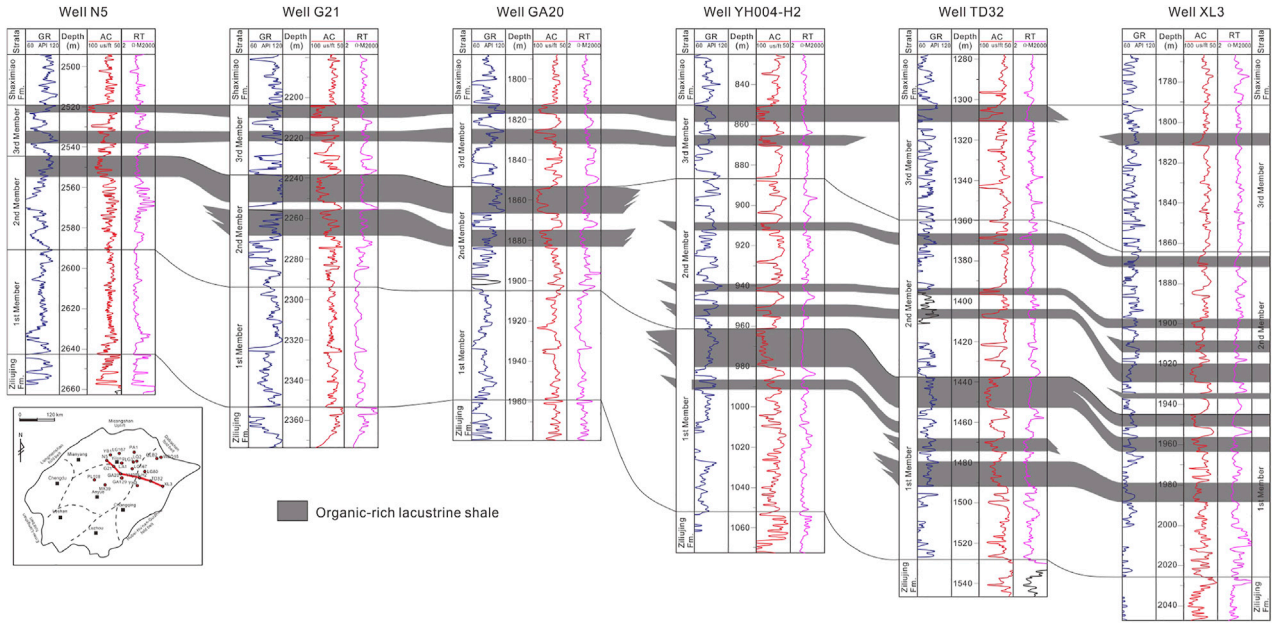

FIGURE 7
Cross-section showing distribution of Lianggaoshan organic-rich lacustrine shale.

facies does not affect the development of lacustrine shale, so this study will not discuss it.

Sedimentary evolution of lacustrine facies

Variation of lake level and sequence division

The frequent migration of continental lake-basins and the rise and fall of lake-levels make it difficult to apply traditional system tract classification methods due to the unclear system tract characteristics of lake-basin sequence stratigraphy (Cheng et al., 2023). Previous studies based on outcrop observation received that the Lianggaoshan lake-basin underwent a complete cycle of lacustrine transgression-lacustrine extension, which was divided into a 3rd-order sequence. Using seismic data, sequence boundary (SB) and maximum flooding surface (MFS) can be identified, which is easy to operate in the actual work of sequence stratigraphy and is convenient for analysis and research (Figure 4). Therefore, using the lacustrine transgression-lacustrine extension system tract division can more intuitively understand the evolution process of lake-basin and explain the filling pattern of sedimentary sequences.

During the sedimentary period of the Lianggaoshan Fm., the tectonic setting was relatively stable and it was a large depression

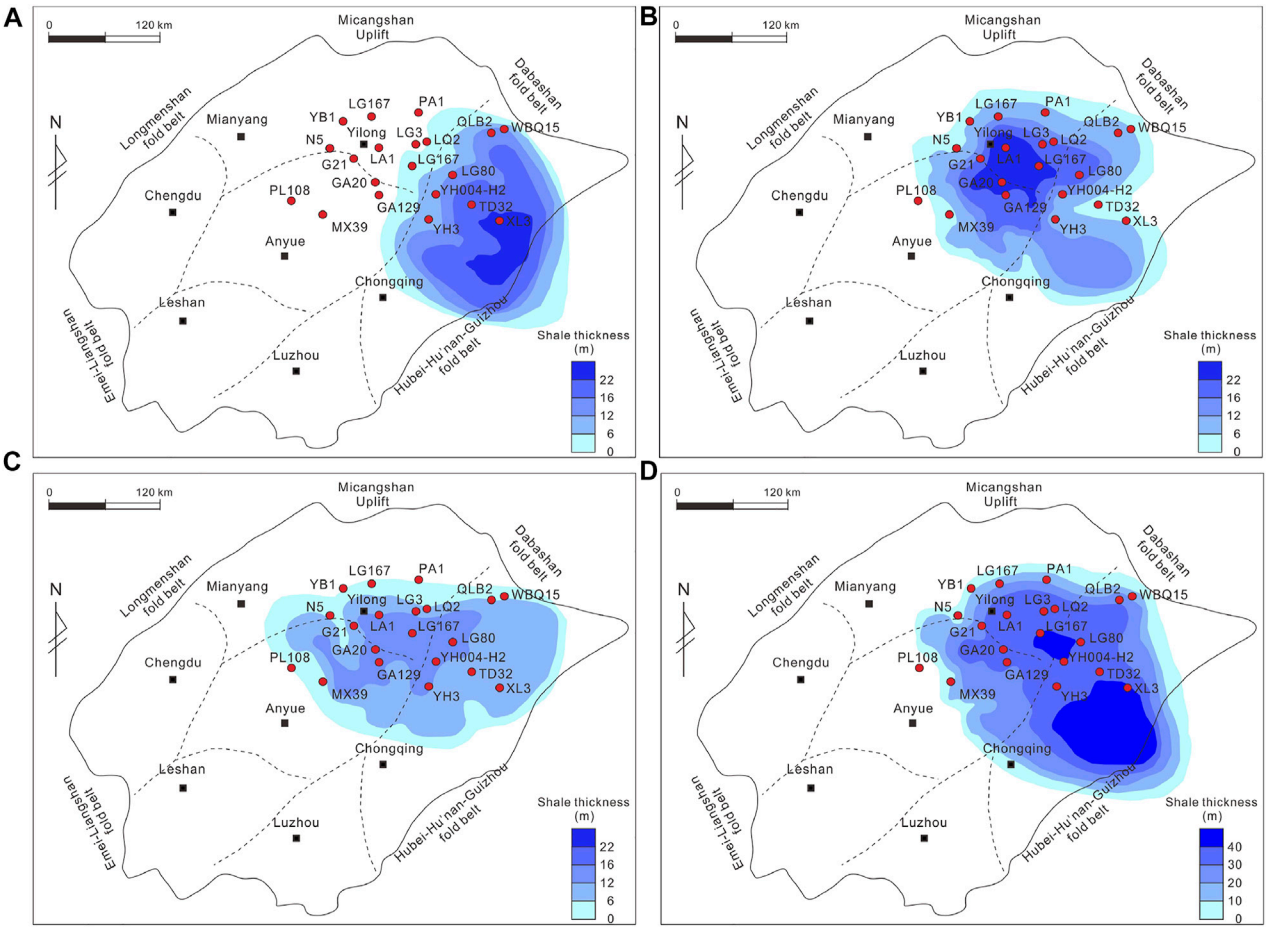

FIGURE 8
Contour plot showing distribution of Lianggaoshan lacustrine organic-rich shale. **(A)** Lianggaoshan 1st Member. **(B)** Lianggaoshan 2nd Member. **(C)** Lianggaoshan 3rd Member. **(D)** Lianggaoshan Formation.

lake-basin (Bai et al., 2022; Cheng et al., 2023). The top boundary of Lianggaoshan Fm. is bounded by black grey mudstone/shale and sandstone at the bottom of Shaximiao Formation. The logging curve features upward that GR changes from box high value to toothed medium low value, acoustic curve changes from high value to low value, and resistivity changes from box low value to toothed high value. This interface is a typical lithologic discontinuity (Figure 2A). The shale at the bottom of the Lianggaoshan Fm. is in integrated contact with the limestone of the underlying Ziliujing Fm., which is also a lithological discontinuous surface (Figure 1B). These two lithological mutation surfaces serve as 3rd-order sequence boundary (SB), and the division of sequence boundary in the Lianggaoshan Fm. is widely accepted and recognized, without controversy. Petrology characteristics of maximum flooding surface (MFS): it is located in the position where the maximum lake transgression reaches in the sequence, which is the boundary between lacustrine transgression system tract and extension system tract, and is characterized by retrogradation cycles (or parasequence sets) turning into progradation or aggradation cycles (or parasequence sets). The Lianggaoshan Fm. MFS is shown as the upper part of a large section of black shale on the core (Figure 3). This section of shale is characterized by deep color and laminated structure. The continuous thickness of the shale interval is 12–25 m, and pyrite grains can be seen, which reflects the sedimentary environment of strong reduction, and does not contain or have less scale debris (Figure 3). MFS in the study area is relatively easy to identify, mainly manifested as straight or toothed high GR, high acoustic time difference, and low electrical resistance characteristics (Figure 4). Among them, the acoustic time difference is affected by the lower velocity of black shale, and the high value of the box shaped is obvious.

Evolution and migration of lake-basin

This study uses the maximum flooding surface (MFS) and spatial distribution of shale/mudstone to analyze the migration and evolution of Lianggaoshan lake-basin. The sedimentary period corresponding to MFS results in widespread distribution of lacustrine mudstone/shale. This widely distributed set of lacustrine mudstone/shale is prone to forming continuous strong reflection coaxial lines on seismic sections, often serving as a marker layer that can be traced throughout the entire study area. In the presence of a lower hyperplane, the lower hyperplane serves as the

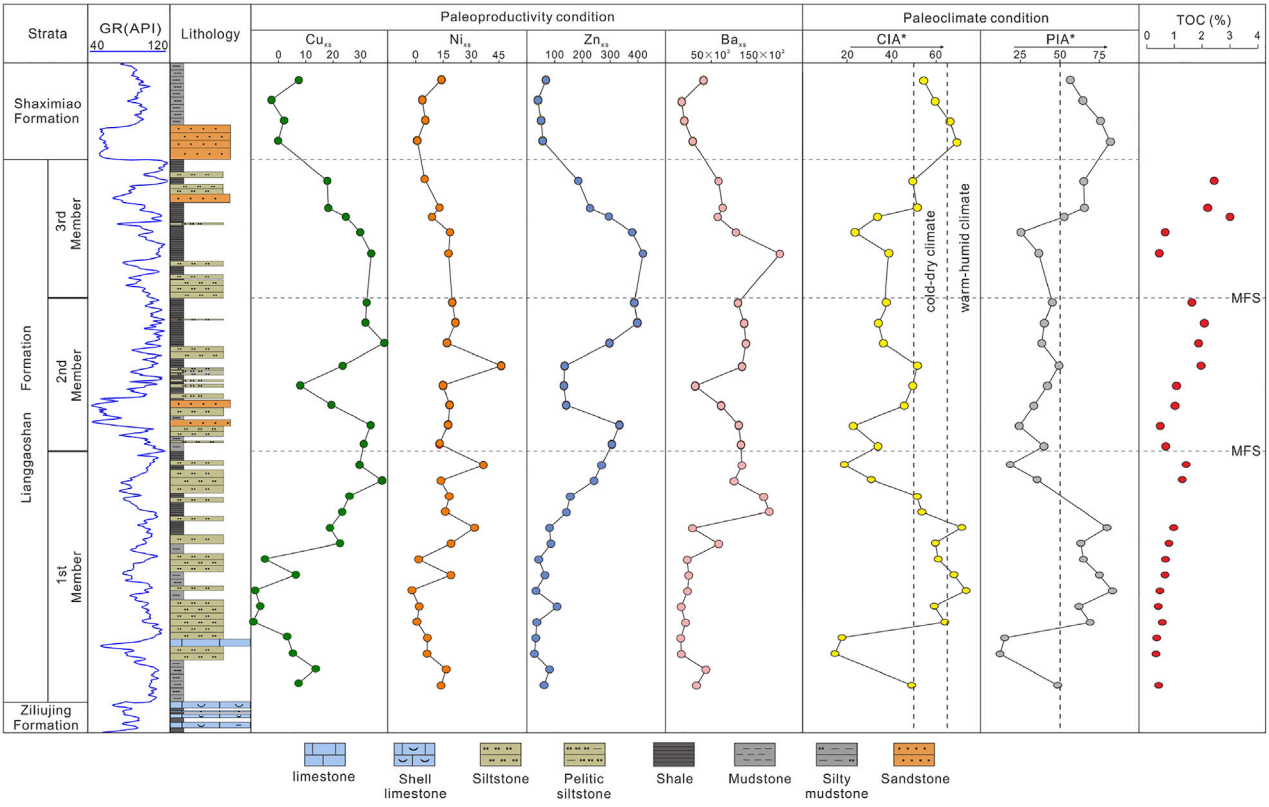

FIGURE 9
Paleoproductivity condition and paleoclimate for the Lianggaoshan Formation.

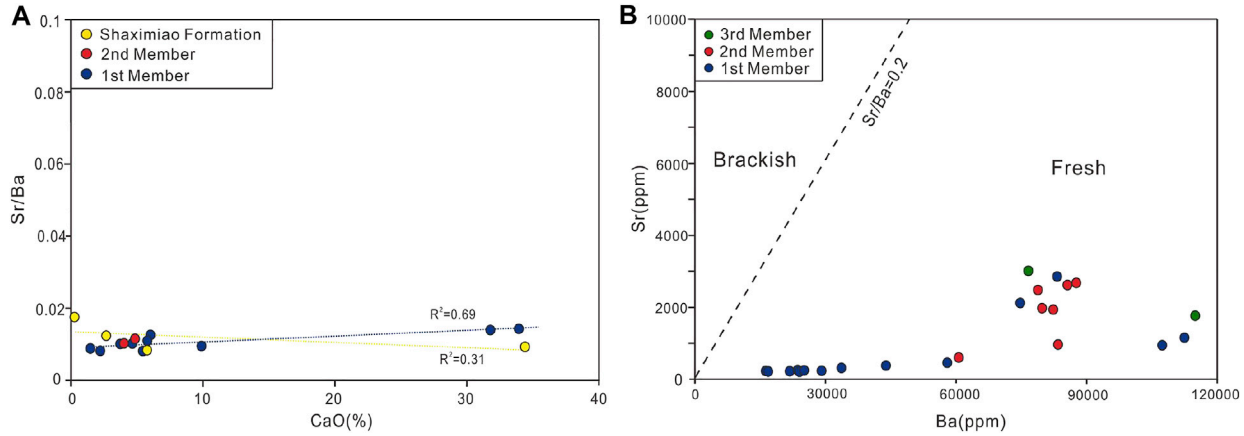

FIGURE 10
(A) Cross-plot of Sr/Ba ratios and CaO concentration for Lianggaoshan lacustrine shale. **(B)** Cross-plot of Ba content and Sr content for Lianggaoshan lacustrine shale.

MFS; in the absence of a undersurface, the MFS can be determined based on the characteristics of the farthest point of the undersurface or strong reflection on the seismic sections. The seismic response characteristics of the MFS inside the Lianggaoshan Fm. are obvious. Affected by the high-speed sandstone at the top, the mudstone/shale at the top of the MFS exhibits continuous and stable strong trough reflections. Figure 5 shows that the MFS of the two periods formed continuous strong reflections on the seismic section, which can be

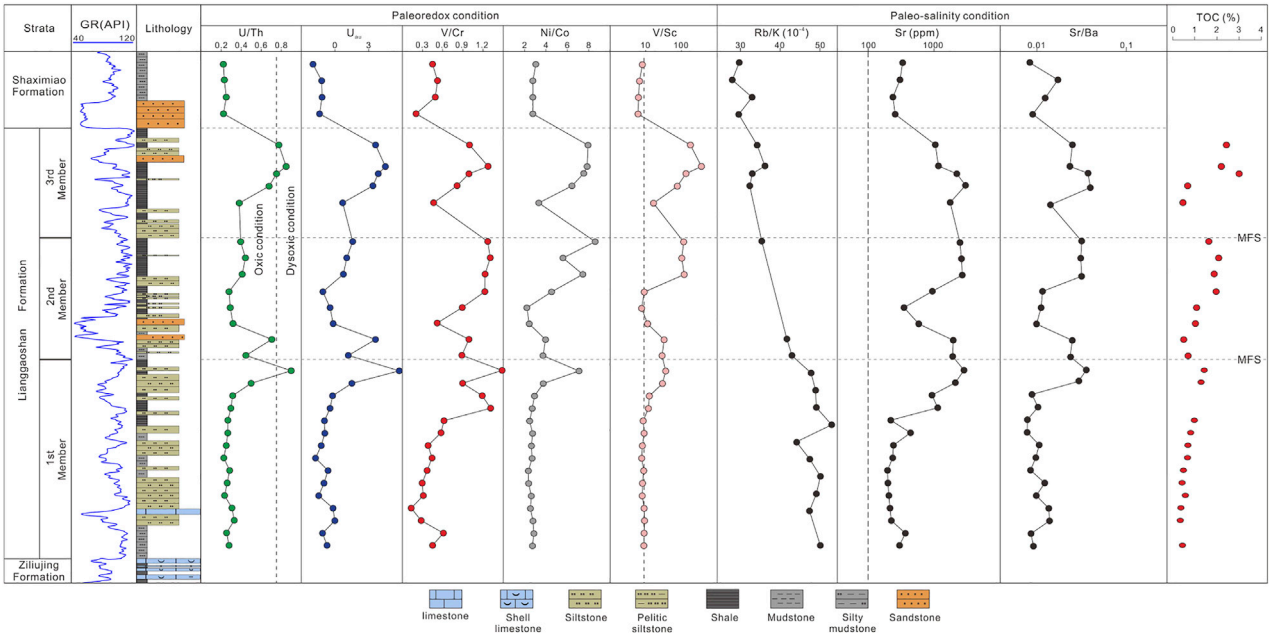

FIGURE 11
Paleoredox condition and paleo-salinity for the Lianggaoshan Formation.

continuously compared and traced in Central, Northern, and Eastern Sichuan Basin. These MFSs are characterized by onlaping sequence boundary (SB) between Lianggaoshan and Ziliujing Formation.

This study utilized the classification method of lacustrine organic-rich shale proposed by Lu et al. (2012). In the TOC range of less than 0.75%, the S_1 value of lacustrine shale is in the low range. As the TOC content increases, S_1 rapidly increases, suggesting that the oil content is rapidly increasing and entering the median range. Subsequently, when the TOC content exceeds 2%, the oil content of Lianggaoshan shale reaches saturation, and the S_1 value reaches equilibrium and hardly rises, entering the high value stage (Figure 6A). Therefore, the TOC lower limit value of Lianggaoshan lacustrine organic-rich shale is 0.75%. Based on the identification and classification criteria of continuous thickness greater than 3 m and logging TOC greater than 0.75% (Figure 6B), the organic-rich shale thickness and spatial distribution in each member of the Liangshan Formation are tracked and compared horizontally.

The spatial distribution characteristics of Lianggaoshan organic-rich shale suggest that six stages of shale are developed from bottom to top (Figure 7), representing multiple migration stages of Lianggaoshan lake-basin. Within Lianggaoshan Fm., the lake-basin within 1st Member formed the 1st to 3rd stage shale, and the depocenter of the lake-basin gradually expanded from the Southeastern to the Central Sichuan Basin (Figure 8A). The lake-basin within 2nd and 3rd Member formed the 4th to 6th stage shale (Figure 7). At this time, the depocenter of the lake-basin is located in the Central Sichuan Basin (Figure 8B). Shale thickness corresponding to MFS of 1st Member reaches maximum in Southeastern Sichuan Basin, with a thickness of 18 m. The depocenter of the lake-basin at the MFS of 2nd Member is near Central Sichuan Basin, with a maximum shale thickness of 14 m (Figure 8B). The organic-rich shale thickness corresponding to the upper 3rd Member is relatively thin (Figure 8C), with a maximum of about 7 m, but the distribution range is relatively large (Figure 8D).

Environmental conditions

Paleo-productivity proxies

The content of life elements (P, Ba, Mo, Cu, Zn, Ni, etc.) can be used as indicators of paleo-productivity (Schoepfer et al., 2015; Gu et al., 2022a; Lei et al., 2023). The selection of paleo-productivity indicators can not only promote plankton development, but also be less susceptible to diagenesis, debris input, and water redox conditions, or can distinguish and correct these effects. Previously, P and Ba were commonly used to reflect the primary productivity of lake water bodies (Deng et al., 2019; Qiu et al., 2022). However, reducing the environment can hinder the accumulation of P and Ba and affect the accuracy of paleo-productivity assessment based on the content of these elements. To avoid the impact of terrigenous debris, Element$_{xs}$ (Cu_{xs}, Ni_{xs}, Zn_{xs}, and Ba_{xs}) can be applied as an indicator of paleo-productivity in lacustrine sediments (Lei et al., 2023). From the trend of vertical variation of TOC, organic-rich shale is developed between the upper part of the 1st and 2nd Member and MFS. Within these intervals (Figure 9), the paleo-productivity indicators (Cu_{xs}, Ni_{xs}, Zn_{xs}, and Ba_{xs}) increase dsignificantly, indicating that the increase in paleo-productivity exhibits positive effects on organic matter enrichment. The upper 3rd Member also develops organic-rich shale, but the paleo-

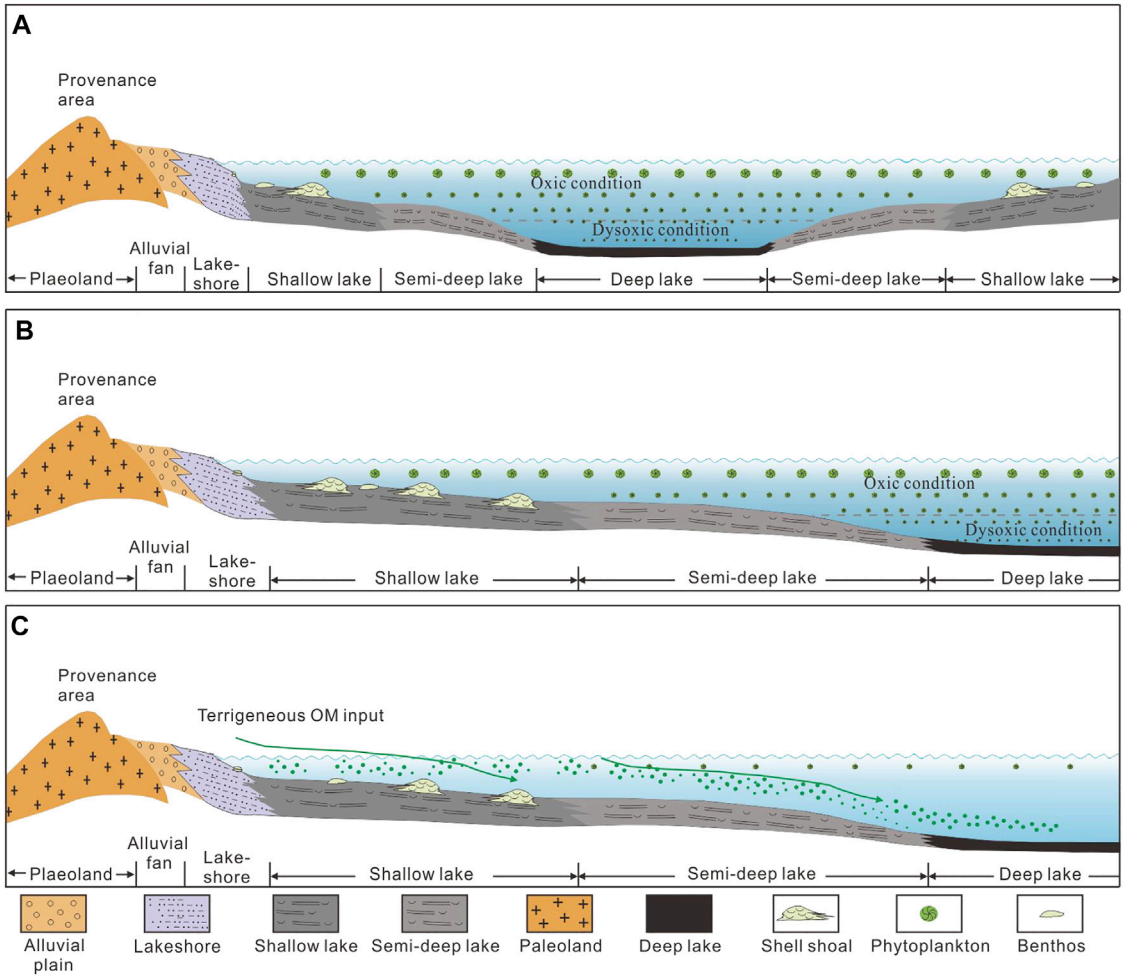

FIGURE 12
Pattern diagram of organic matter enrichment process for the Lianggaoshan Formation. **(A)** 1st Member of Lianggaoshan Formation. **(B)** 2nd Member of Lianggaoshan Formation. **(C)** 3rd Member of Lianggaoshan Formation.

productivity does not have a significant control over the enrichment of organic matter in this interval (Figure 9).

Paleo-climate condition

Climate influences the sedimentary characteristics and organic matter accumulation within the lake-basin by controlling exogenic processes and controlling input of terrestrial sediments. CIA* (Chemical Index of Alteration) and PIA* are classic indicators for assessing paleo-climate (Price et al., 2003; Deng et al., 2019). Higher CIA* and PIA* generally indicate a humid climate, which is conducive to the input of terrigenous debris dominated by weathering (Nesbitt and Young, 1982). The CIA* value for upper part of 1st and 2nd Member is lower than 50, suggesting very low chemical weathering degree (Bai et al., 2015). The CIA* value for upper part of the 3rd Member is between 50 and 65 (Figure 9), suggesting a relatively low chemical weathering degree (Bai et al., 2015). It appears that the paleo-climate of upper part of 3rd Member is more conducive to the input of terrestrial debris than 1st and 2nd Member. The longitudinal variation trend of PIA* exhibits similarity to that of CIA*, reflecting the same characteristics of climate change.

Paleoredox condition

The redox level of bottom water is a key factor in the burial and preservation of OM, and paleoredox-sensitive elements (Mo, U, Ni, V, Cu, Mn, etc.) are commonly used in the reconstruction of paleoredox conditions in lacustrine environments (Algeo and Liu, 2020; Bennett and Canfield, 2020; Algeo and Rowe, 2021). This study used the bimetallic ratio to evaluate the redox condition of lacustrine bottom water. Results indicate that compared to other intervals, the reducibility of the organic-rich interval is significantly stronger. V/Cr, Ni/Co, and V/Sc exhibit high values within the organic-rich interval. The value of U/Th is distributed within the dysoxic condition range within the organic-rich interval. It is suggested that the upper parts of 1st, 2nd and 3rd Member are deposited in a dysoxic condition that is favorable for OM preservation.

Paleosalinity

Ba and Sr were proved to be two indicator elements sensitive to paleosalinity (Deng et al., 2019; Gu et al., 2022a; Gu et al., 2022b). Before using Sr/Ba to evaluate paleosalinity, it is first necessary to remove the adverse effects of carbonate rocks on the data (Gu et al., 2022a; Gu et al., 2022b). The test results of Lianggaoshan lacustrine shale indicate that the vast majority of samples have a CaO content below 10%, which can exclude the interference of carbonate rocks on paleosalinity characterization (Figure 10A). During Lianggaoshan deposition, the paleo-salinity of lake water tends to be freshwater (Figure 10B). However, Sr/Ba ratios significantly increase in the range of organic rich shale, suggesting that an increase in paleo-salinity is beneficial for improving paleo-productivity and thus for enrichment of OM (Figure 11).

Factors of lacustrine organic matter enrichment

During the 1st Member of Lianggaoshan, high biological productivity provided a material basis for lacustrine organic-rich shale (Figure 12A). After formation, the OM immediately entered the burial process. Only when the rate of OM accumulation exceeds the decomposition rate can OM enrichment be caused (Burdige, 2007; Lash and Blood, 2014; Lei et al., 2023). Although the lake-basin is relatively close to the provenance area during 1st Member deposition, but the paleo-climate during this period was not conducive to terrestrial OM input, but due to the large-scale lake-level rise, a dysoxic condition favorable for the preservation of OM was formed at the lake-basin bottom. With the uplift of Dabashan, the distance between the lake basin and the source area becomes farther, which is not conducive to the input of terrestrial OM during 2nd Member deposition. The other conditions controlling OM enrichment in 2nd Member are the same as those of the 1st Member (Figure 12B). During the 3rd Member, paleo-productivity was unable to form a large amount of lacustrine OM. The distance between the lake-basin and the provenance area is also unfavorable for terrestrial OM input. However, due to the favorable paleo-climate for chemical weathering during this period, a large amount of terrestrial organic matter entered the lake-basin (Figure 12C), and a high sedimentation rate can also shorten the time for OM to be oxidized in lake-basin, allowing for rapid deposition and burial of OM, which can also form a dysoxic condition conducive to OM preservation.

Conclusion

1) During Lianggaoshan Fm. deposition, the lake-basin underwent multiple migrations. The multiple migrations of the lake-basin formed six stages of organic-rich shale from bottom to top within the Lianggaoshan Formation. During the deposition of Lianggaoshan Fm. 1st Member, the depocenter of the lake-basin gradually expanded from the southeastern Sichuan Basin to the Central Sichuan Basin. During the deposition of 2nd and 3rd Members, the depocenter of the lake-basin is located in the Central Sichuan Basin. The migration process of depocenters controls the planar distribution of lacustrine organic-rich shale.
2) The Lianggaoshan lacustrine organic-rich shale is distributed from the upper to the top of each member. The OM enrichment during the upper to the top of 1st Member and 2nd Member is controlled by relatively high paleo-productivity and preservation under dysoxic conditions. Organic matter enrichment during upper 3rd Member deposition is controlled by terrestrial input and dysoxic conditions. The dysoxic conditions corresponding to the upper 1st-2nd Member are caused by lake-level rise, while the dysoxic conditions corresponding to the upper 3rd Member are caused by rapid burial.

Data availability statement

The raw data supporting the conclusion of this article will be made available by the authors, without undue reservation.

Author contributions

RF contributed as the major author of the paper. SS, YJ, and DD conceived the project. YaL contributed as rock sample collectors. LQ, QL, and ZJ are responsible for analyzing the data measured in these experiments. All authors contributed to the article and approved the submitted version.

Funding

The research was supported by the National Natural Science Foundation of China (Grant No. 42272171) and Science and Technology Cooperation Program of CNPC–SWPU Innovation Alliance (Grant No. 2020CX020104).

Conflict of interest

Authors RF and YJ were employed by PetroChina Key Laboratory of Unconventional Oil and Gas Resources. Authors SS and DD were employed by PetroChina Research Institute of Petroleum Exploration and Development. Author YaL was employed by Southwest Geophysical Exploration Branch of China Petroleum Group Dongfang Geophysical Exploration Co., Ltd. Authors LQ and QL were employed by CNPC Chuanqing Drilling Engineering Co., Ltd. Author YuL was employed by PetroChina Southwest Oil and Gas Field Company. Author ZJ was employed by Sichuan Geotech Science and Technology Ltd., Company.

Publisher's note

References

Algeo, T. J., and Liu, J. (2020). A re-assessment of elemental proxies for paleoredox analysis. *Chem. Geol.* 540, 119549. doi:10.1016/j.chemgeo.2020.119549

Algeo, T. J., and Rowe, H. (2021). Paleoceanographic applications of trace-metal concentration data. *Chem. Geol.* 324–325, 6–18. doi:10.1016/j.chemgeo.2011.09.002

Bai, H., Yang, X., Xiong, Y., Guan, X., Xu, X., Si, G., et al. (2022). Determination of Lianggaoshan Formation lake strandline and favorable tight oil and gas areas in the central Sichuan Basin. *Nat. Gas. Ind.* 42 (2), 40–49. doi:10.3787/j.issn.1000-0976.2022.02.005

Bai, Y., Liu, Z., Sun, P., Liu, R., Hu, X., Zhao, H., et al. (2015). Rare Earth and major element geochemistry of Eocene fine-grained sediments in oil shale- and coal-bearing layers of the Meihe Basin, Northeast China. *J. Asian Earth Sci.* 97 (97), 89–101. doi:10.1016/j.jseaes.2014.10.008

Bennett, W. W., and Canfield, D. E. (2020). Redox-sensitive trace metals as paleoredox proxies: A review and analysis of data from modern sediments. *Earth Sci. Rev.* 204, 103175. doi:10.1016/j.earscirev.2020.103175

Burdige, D. J. (2007). Preservation of organic matter in marine sediments: Controls, mechanisms, and an imbalance in sediment organic carbon budgets? *Chem. Rev.* 107, 467–485. doi:10.1021/cr050347q

Cai, G., Gu, Y., Fu, Y., Jiang, Y., Wei, Z., Wang, Z., et al. (2023). Pore system classification of Jurassic Da'anzhai Member lacustrine shale: Insight from pore fluid distribution. *Energy Explor. Exploitation* 41 (3), 900–921. doi:10.1177/01445987231154613

Cheng, D., Zhang, Z., Hong, H., Zhang, S., Qin, C., Yuan, X., et al. (2023). Sedimentation and provenance and the basin-mountain relationship of the jurassic Lianggaoshan Formation in eastern Sichuan Basin. SW China. *Petroleum Explor. Dev.* 50 (2), 262–272. doi:10.11698/PED.20220412

Deng, T., Li, Y., Wang, Z. J., Yu, Q., Dong, S., Yan, L., et al. (2019). Geochemical characteristics and organic matter enrichment mechanism of black shale in the Upper Triassic Xujiahe Formation in the Sichuan basin: Implications for paleoweathering, provenance and tectonic setting. *Mar. Petroleum Geol.* 109, 698–716. doi:10.1016/j.marpetgeo.2019.06.057

Fu, Y., Jiang, Y., Dong, D., Hu, Q., Lei, Z., Peng, H., et al. (2021). Microscopic pore-fracture configuration and gas-filled mechanism of shale reservoirs in the Western Chongqing area, Sichuan Basin,China. *Petroleum Explor. Dev.* 48 (5), 1063–1076. doi:10.1016/s1876-3804(21)60091-5

Fu, Y., Jiang, Y., Wang, Z., Hu, Q., Xie, J., Ni, G., et al. (2019). Non-connected pores of the longmaxi shale in southern Sichuan Basin of China. *Mar. Petroleum Geol.* 110, 420–433. doi:10.1016/j.marpetgeo.2019.07.014

Gu, Y., Hu, D., Wei, Z., Liu, R., Hao, J., Han, J., et al. (2022b). Sedimentology and geochemistry of the upper permian linghao formation marine shale, central nanpanjiang basin, SW China. *Front. Earth Sci.* 10, 914426. doi:10.3389/feart.2022.914426

Gu, Y., Li, X., Qi, L., Li, S., Jiang, Y., Fu, Y., et al. (2022a). Sedimentology and geochemistry of the lower permian shanxi formation Shan 2^3 submember transitional shale, eastern ordos basin, north China. *Front. Earth Sci.* 10, 859845. doi:10.3389/feart.2022.859845

He, W., He, H., Wang, Y., Cui, B., Meng, Q., Guo, X., et al. (2022). Major breakthrough and significance of shale oil of the jurassic Lianggaoshan Formation in well ping'an 1 in northeastern Sichuan Basin. *China Pet. Explor.* 27 (1), 40–49. doi:10.3969/j.issn.1672-7703.2022.01.004

Hu, D., Li, Z., Wei, Z., Duan, J., Miao, Z., Pan, L., et al. (2023). Breakthrough in oil and gas exploration of Jurassic channel sandstone in Well Bazhong 1HF in northern Sichuan Basin and its significance. *Nat. Gas. Ind.* 43 (3), 1–11. doi:10.3787/j.issn.1000-0976.2023.03.001

Hu, D., Wei, Z., Liu, R., Wei, X., Chen, F., and Liu, Z. (2021a). Enrichment control factors and exploration potential of lacustrine shale oil and gas: A case study of jurassic in the fuling area of the Sichuan Basin. *Nat. Gas. Ind.* 41 (8), 1–8. doi:10.1016/j.ngib.2021.08.012

Hu, Z., Wang, R., Liu, Z., Liu, G., Feng, D., Yang, Z., et al. (2021b). Lin28a is essential for synaptic plasticity in dentate granule cells and spatial memory. *Earth Sci. Front.* 1, 261–266. doi:10.1007/s12264-020-00591-7

Huang, D. (2019). Jurassic integrative stratigraphy and timescale of China. *Sci. China Earth Sci.* 62 (1), 223–255. doi:10.1007/s11430-017-9268-7

Jiang, C., Zhang, H., Zhou, Y., Gan, H., Pu, J., Jiang, Y., et al. (2022). Paleogeomorphic characteristics of wufeng—longmaxi formation and its influence on development of high-quality shale in dazu area, Western chongqing. *J. Central South Univ. Technol.* 53 (9), 3628–3640. doi:10.11817/j.issn.1672-7207.2022.09.026

Lai, Q., Qi, L., Chen, S., Ma, S., Zhou, Y., Fang, P., et al. (2023). Resercoir space characteristics and pore structure of Jurassic Lianggaoshan Formation lacustrine shale reservoir in Sichuan Basin, China: Insights into controlling factors. *Front. Earth Sci.* 11, 1133413. doi:10.3389/feart.2023.1133413

Lash, G. G., and Blood, D. R. (2014). Organic matter accumulation, redox, and diagenetic history of the Marcellus Formation, southwestern Pennsylvania, Appalachian basin. *Mar. Petroleum Geol.* 57, 244–263. doi:10.1016/j.marpetgeo.2014.06.001

Lei, W., Chen, D., Liu, Z., and Cheng, M. (2023). Paleoenvironment-driven organic matter accumulation in lacustrine shale mixed with shell bioclasts:A case study from the Jurassic Da'anzhai member, Sichuan Basin (China). *J. Petroleum Sci. Eng.* 220, 111178. doi:10.1016/j.petrol.2022.111178

Li, J., Li, H., Yang, C., Ren, X. H., and Li, Y. D. (2023). Geological characteristics of deep shale gas and their effects on shale fracability in the Wufeng–Longmaxi Formations of the southern Sichuan Basin, China. *Lithosphere* 1, 4936993. doi:10.2113/2023/4936993

Li, J., Li, H., Yang, C., Wu, Y. J., Gao, Z., and Jiang, S. L. (2022). Geological characteristics and controlling factors of deep shale gas enrichment of the Wufeng-Longmaxi Formation in the southern Sichuan Basin, China. *Lithosphere 2022* S12, 4737801. doi:10.2113/1970/4737801

Liang, H., Xu, G., Xu, F., Yu, Q., Liang, J., and Wang, D. (2020). Paleoenvironmental evolution and organic matter accumulation in an oxygen-enriched lacustrine basin: A case study from the laizhou bay sag, southern bohai sea (China). *Int. J. Coal Geol.* 217, 103318. doi:10.1016/j.coal.2019.103318

Liu, J., Cao, J., Hu, G., Wang, Y., Yang, R., and Liao, Z. (2020). Water-level and redox fluctuations in a Sichuan Basin lacustrine system coincident with the Toarcian OAE. *Palaeogeogr. Palaeoclimatol. Palaeoecol.* 558, 109942. doi:10.1016/j.palaeo.2020.109942

Lu, S., Huang, W., Chen, F., Li, J., Wang, Min., Xue, Haitao., et al. (2012). Classification and evaluation criteria of shale oil and gas resources:Discussion and application. *Petroleum Explor. Dev.* 39 (2), 268–276. doi:10.1016/s1876-3804(12)60042-1

Murphy, A. E., Sageman, B. B., Hollander, D. J., Lyons, T. W., and Brett, C. E. (2000). Black shale deposition and faunal overturn in the devonian appalachian basin: Clastic starvation, seasonal water-column mixing, and efficient biolimiting nutrient recycling. *Paleoceanography* 15, 280–291. doi:10.1029/1999PA000445

Nesbitt, H., and Young, G. (1982). Early proterozoic climates and plate motions inferred from major element chemistry of lutites. *Nature* 299 (5885), 715–717. doi:10.1038/299715a0

Price, J. R., and Velbel, M. A. (2003). Chemical weathering indices applied to weathering profiles developed on heterogeneous felsic metamorphic parent rocks. *Chem. Geol.* 202, 397–416. doi:10.1016/j.chemgeo.2002.11.001

Qiu, Z., and He, J. (2022). Depositional environment changes and organic matter accumulation of Pliensbachian-Toarcian lacustrine shales in the Sichuan basin, SW China. *J. Asian Earth Sci.* 232, 105035. doi:10.1016/j.jseaes.2021.105035

Qiu, Z., and Zou, C. (2020a). Controlling factors on the formation and distribution of "sweet-spot areas" of marine gas shales in South China and a preliminary discussion on unconventional petroleum sedimentology. *J. Asian Earth Sci.* 194, 103989. doi:10.1016/j.jseaes.2019.103989

Qiu, Z., and Zou, C. (2020b). Unconventional petroleum sedimentology: Connotation and prospect. *Acta Sedimentol. Sin.* 38, 1–29. doi:10.14027/j.issn.1000●0550.2019.116

Ross, D. J. K., and Bustin, R. M. (2009). The importance of shale composition and pore structure upon gas storage potential of shale gas reservoirs. *Mar. Petroleum Geol.* 26, 916–927. doi:10.1016/j.marpetgeo.2008.06.004

Schoepfer, S. D., Shen, J., Wei, H., Tyson, R. V., Ingall, E., and Algeo, T. J. (2015). Total organic carbon, organic phosphorus, and biogenic barium fluxes as proxies for paleomarine productivity. *Earth Sci. Rev.* 149, 23–52. doi:10.1016/j.earscirev.2014.08.017

Tribovillard, N., Algeo, T. J., Lyons, T., and Riboulleau, A. (2006). Trace metals as paleoredox and paleoproductivity proxies: An update. *Chem. Geol.* 232 (1/2), 12–32. doi:10.1016/j.chemgeo.2006.02.012

Wang, R., Ding, W., Zhang, Y., Wang, Z., Wang, X., He, J., et al. (2016b). Analysis of developmental characteristics and dominant factors of fractures in lower cambrian marine shale reservoirs: A case study of niutitang formation in cen'gong block, southern China. *J. Petroleum Sci. Eng.* 138, 31–49. doi:10.1016/j.petrol.2015.12.004

Wang, R., Gu, Y., Ding, W., Gong, D., Yin, S., Wang, X., et al. (2016a). Characteristics and dominant controlling factors of organic-rich marine shales with high thermal maturity: A case study of the lower cambrian niutitang formation in the cen'gong block, southern China. *J. Nat. Gas Sci. Eng.* 33, 81–96. doi:10.1016/j.jngse.2016.05.009

Wang, R., Hu, Z., Sun, C., Liu, Z., Zhang, C., Gao, B., et al. (2018). Comparative analysis of shale reservoir characteristics in the wufeng-longmaxi (O_3w-S_1l) and niutitang (ϵ_1n) formations: A case study of the wells JY1 and TX1 in southeastern Sichuan Basin and its periphery, SW China. *Interpretation* 6 (4), SN31–SN45. doi:10.1190/int-2018-0024.1

Zou, C., Zhang, G., Yang, Z., Tao, S., Hou, L., Zhu, R., et al. (2013). Geological concepts, characteristics, resource potential and key techniques of unconventional hydrocarbon: On unconventional petroleum geology. *Petroleum Explor. Dev.* 40 (4), 385–399. doi:10.11698/PED.2013.04.01

Zou, C., Zhu, R., Chen, Z., Ogg, J. G., Wu, S., Dong, D., et al. (2019). Organic-matter-rich shales of China. *Earth Sci. Rev.* 189, 51–78. doi:10.1016/j.earscirev.2018.12.002

frontiers | Frontiers in Earth Science

TYPE Original Research
PUBLISHED 10 August 2023
DOI 10.3389/feart.2023.1207994

OPEN ACCESS

EDITED BY
Ruyue Wang,
SINOPEC Petroleum Exploration and Production Research Institute, China

REVIEWED BY
Kun Zhang,
Southwest Petroleum University, China
Kuizhou Li,
Chengdu University of Technology, China

*CORRESPONDENCE
Shaomin Zhang,
zhangsm19@petrochina.com.cn
Xiangye Kong,
kongxiangyecup@163.com
Jinliang Gao,
jinliang0205@126.com

RECEIVED 18 April 2023
ACCEPTED 31 May 2023
PUBLISHED 10 August 2023

CITATION
Bai R, Zhang S, Hong H, Qin C, Li Y, Cai C, Kong X, Li N, Lei D, Lei X, Wang C, Jin T, Gao J and Tang W (2023), Source-reservoir rock assemblages and hydrocarbon accumulation models in the Middle-Lower Jurassic of eastern Sichuan Basin, China.
Front. Earth Sci. 11:1207994.
doi: 10.3389/feart.2023.1207994

Source-reservoir rock assemblages and hydrocarbon accumulation models in the Middle-Lower Jurassic of eastern Sichuan Basin, China

Rong Bai[1], Shaomin Zhang[1]*, Haitao Hong[1], Chunyu Qin[1], Yucong Li[1], Changhong Cai[1,2], Xiangye Kong[3]*, Nan Li[1], Dong Lei[4], Xin Lei[4], Changyong Wang[4], Tao Jin[1], Jinliang Gao[5]* and Wenbin Tang[4]

[1]Exploration and Development Research Institute of PetroChina Southwest Oil and Gas Field Company, Chengdu, China, [2]Shale Gas Evaluation and Exploitation Key Laboratory of Sichuan Province, Chengdu, China, [3]College of Geosciences, China University of Petroleum Beijing, Beijing, China, [4]Institute of Sedimentary Geology, Chengdu University of Technology, Chengdu, China, [5]PetroChina Research Institute of Petroleum Exploration and Development, Beijing, China

The eastern Sichuan Basin in China holds vast potential for oil and gas exploration in the Lower-Middle Jurassic strata. However, the geological characteristics and hydrocarbon accumulation patterns of this region remain largely unclear. During the deposition period of the Lower-Middle Jurassic strata, the eastern Sichuan is characterized by the formation of multiple sets of source, reservoir, and caprock assemblages through depositing lake-delta-fluvial deposits, which have great exploration potential. The Jurassic source rocks in eastern Sichuan are mainly developed in the Dongyuemiao Member, Da'anzhai Member, and Liangshan Formation. These source rocks have a total organic carbon (TOC) content greater than 1 and a varying range of organic matter maturity, with a Ro value of 0.8–2.0. The kerogen in these source rocks is primarily type II, with a smaller proportion being type III. A range of reservoir rocks can be found in the Jurassic strata of eastern Sichuan, with sandstone reservoirs being predominantly found in the Liangshan Formation, Shaximiao Formation, and Zhenzhuchong Member. Shale reservoirs are mostly present in the Dongyuemiao, Da'anzhai, Liangshan, and Maanshan Members, and there is a limited distribution of limestone reservoirs in the Da'anzhai Member and Dongyuemiao Formation. The arrangement of source rocks and reservoir rocks in eastern Sichuan has led to the formation of three types of reservoir-forming combinations, including lower generation and upper storage, self-generation and self-storage, and composite. Sandstone reservoirs are typically of lower generation and upper storage, shale reservoirs are primarily of self-generation and self-storage, and limestone reservoirs are mostly composite. The exploration of Jurassic oil and gas in eastern Sichuan should prioritize "layer and area selections." The Da'anzhai, Dongyuemiao, and Liangshan shale reservoirs should be the primary exploration targets, with the semi-deep lake deposits in the syncline area being the most favorable. The degree of fracture development in the exploration area also has a significant impact on the shale oil and gas content. The Liangshan Formation and Shaximiao Formation sandstone reservoirs can serve as secondary exploration targets, with anticline areas that have better sealing conditions being more favorable. Limestone

reservoirs have limited distribution, and exploration areas with high and steep fractures are relatively more advantageous.

KEYWORDS

continental shale, exploration potential, jurassic, eastern sichuan, sichuan basin

1 Introduction

Over the past few years, the continued expansion and deepening of oil and gas exploration has resulted in the discovery of oil and gas reservoirs in the Jurassic strata of the Sichuan Basin, such as the Da'anzhai Member, Lianggaoshan Formation, Shaximiao Formation, and others (Chen, 1990; Wang et al., 2012; Xiao et al., 2018; Yang et al., 2019; Wang et al., 2021), indicating a positive outlook for crude oil exploration in the region. Despite this, the exploration and development of oil and gas in the eastern Sichuan Basin has primarily focused on deep marine strata, while continental strata exploration remains relatively underdeveloped, particularly with regard to the Jurassic oil and gas geological characteristics. In the Wanzhou-Fuling area, the sandstone of the Shaximiao Formation and the shale of the Da'anzhai Member have already produced industrial oil and gas after drilling in the Wubaochang area (Wang et al., 2012; Yang et al., 2019). Furthermore, the application of vertical well fracturing in the sandstone of the Lianggaoshan Formation in the old Tiandong 002-X18 well has also produced industrial gas flow. Additionally, Wells Taiye 1 and Fuye 10HF, which were tested in the shale of the Lianggaoshan Formation and the Dongyuemiao Member, respectively (Wang et al., 2018; Hu et al., 2021; Shu et al., 2021), have produced medium-high yield industrial oil and gas, indicating the promising exploration potential of the Jurassic lacustrine strata in the eastern Sichuan Basin. Despite these developments, research into the Jurassic strata in the eastern Sichuan Basin is still relatively limited, and there is a lack of systematic studies on stratigraphic development characteristics, sedimentary systems and evolution, and oil and gas systems. This significantly limits future exploration decisions. Therefore, it is imperative to investigate the oil and gas geological characteristics of the Jurassic in the eastern Sichuan Basin, identify favorable zones and layers, and provide technical support and understanding for oil and gas exploration in the area.

2 Geological setting

The Sichuan Basin underwent foreland basin evolution during the Late Triassic, which was primarily controlled by the differential thrust nappe tectonic activities of surrounding orogenic belts (Guo, 1996; Chen et al., 2019). The period after the Late Triassic was the main period of construction for the current landform and tectonic basin of the Sichuan Basin (Liu et al., 2011; Wang et al., 2022). The late Indosinian movement resulted in varying degrees of erosion of the Upper Triassic Xujiahe Formation (Wu et al., 2013). The Early Jurassic Luzhou-Huayingshan uplift subsided, and the Weiyuan uplift began to form, creating a depression area in western-central and northeastern Sichuan, and an uplift area in southeastern Sichuan (Sun et al., 2012; Xu et al., 2016). The Early Jurassic Zhenzhuchong Member is dominated by vertical progradation sequences of river and lake facies, influenced by the early nappe structure. During the sedimentary period of the Ma'anshan Member, the Songpan-Ganzi Plateau in the western margin of the basin continued to uplift, leading to the formation of coarse-grained braided river-fan delta deposits, while central Sichuan saw extensive shallow lake beach-bar deposits. The Da'anzhai Member was characterized by weak tectonic activity of the basin margin, steady subsidence, and weak source supply, resulting in the largest lake in the Early Jurassic (Li, 2014). During the sedimentary period of the Lianggaoshan Formation, the Micang Mountain-Daba Mountain region in the northern margin of the basin was undergoing intense tectonic activity, which provided a vast number of clastic materials. At the same time, the southeastern margin's Xuefeng uplift was a stable source of sediment. This resulted in the dominance of a delta-semi-deep lake sedimentary system in the basin (Yang, 2014).

The Late Early Cretaceous period saw the formation of a series of northeast-southwest trending, high-steep structural belts in the eastern Sichuan region as a result of the continuous compression of the Xuefeng-Jiangnan ancient land in the southeast and the Micang-Daba Mountains in the north (Zou et al., 2015). These belts consist of alternating complex anticlines and synclinoriums that form barrier folds (Figure 1). The uplift of the anticline area on a large scale and its subsequent strong denudation processes have made it a favorable site for conventional oil and gas exploration (Yuan et al., 2014). In contrast, the syncline area is more suitable for unconventional oil and gas exploration.

3 Source rock characteristics

The Jurrasic source rocks in eastern Sichuan are primarily found in the Dongyuemiao Member, Da'anzhai Member, and Lianggaoshan Member of the Lower Jurassic Ziliujing Formation. These formations experienced typical lake transgression events during sedimentation, leading to the widespread development of shale and thus the high organic matter content.

Over 70% of the shale samples had a TOC greater than 1%, with more than 10% of the samples measuring TOC greater than 2%. The average TOC of the samples with TOC greater than 1% was 1.70%, which represents the highest organic matter abundance. The organic carbon content of dark shale in the Da'anzhai Member was mainly concentrated in the range of 1%–2%, with 57% of the samples measuring TOC greater than 1%, averaging 1.51%. The distribution of TOC was relatively concentrated, but with a relatively small range of high values. The organic matter abundance of shale in the Lianggaoshan Formation was relatively low, with the average TOC of 1% samples measuring 1.65%. Silty mudstone in the Lianggaoshan Formation had a relatively low TOC content and weak hydrocarbon generation potential. The measured TOC content of mudstone samples from the Zhenzhuchong Member

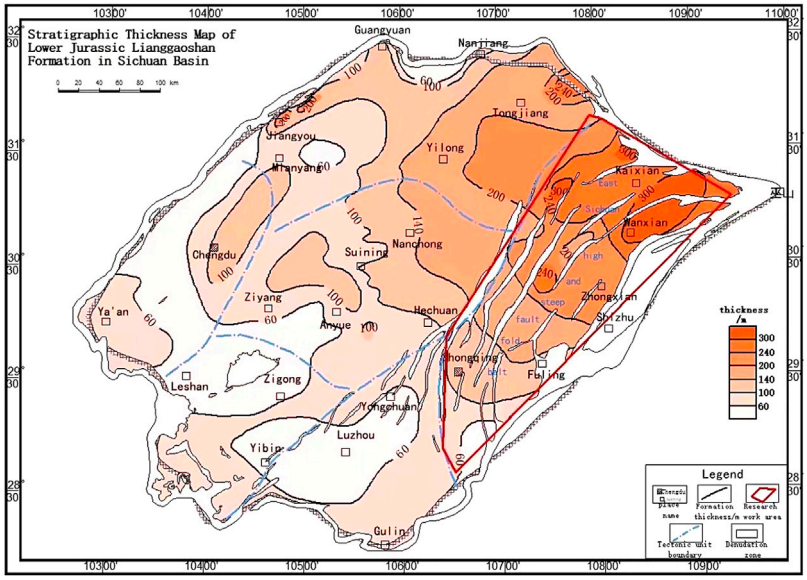

FIGURE 1
Geographical location and main structural features of the eastern Sichuan Basin.

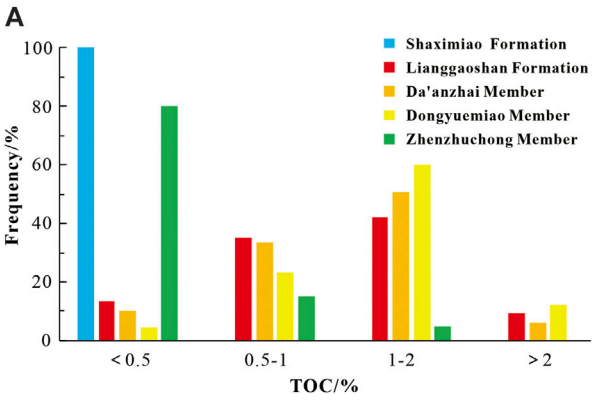

B

Formation	Sample number	TOC(%)			
		< 0.5	0.5-1	1-2	> 2
Shaximiao Formation	3	100 %	0 %	0 %	0 %
Lianggaoshan Formation	225	13 .33 %	35 .11 %	42 .22 %	9 .33 %
Da'anzhai Member	180	10 .00 %	33 .33 %	50 .56 %	6 .11 %
Dongyuemiao Member	90	4 .44 %	23 .33 %	60 .00 %	12 .22 %
Zhenzhuchong Member	20	80 .00 %	15 .00 %	5 .00 %	0 %

FIGURE 2
TOC distribution characteristics of Jurassic mudstone in the eastern Sichuan Basin: **(A)** TOC distribution diagram and **(B)** statistical table of mudstone samples from different layers of the Jurassic in eastern Sichuan.

of the Ziliujing Formation and Shaximiao Formation was mostly less than 0.5%, making them non-hydrocarbon source rocks. Although the number of measured samples from the Zhenzhuchong Member and Shaximiao Formation was relatively small, it can be concluded that the organic matter abundance of mudstone in these formations in eastern Sichuan was generally low and did not meet the standards of a source rock based on the characteristics of most cores, which were mainly variegated, purplish red, and gray-green. The high-quality source rocks of the Dongyuemiao Member, Da'anzhai Member, and Lianggaoshan Formation accounted for over 60% of the total, followed by general source rocks. Nonsource rocks were a relatively small proportion, with the nonsource rocks of the Lianggaoshan Formation shale accounting for the highest proportion.

As shown in Figure 3, the areas with high organic matter content (TOC ≥ 1%) in Lower Jurassic source rocks in eastern Sichuan are mainly located in the Kaixian-Liangping-Zhongxian-Fuling region. The organic matter enrichment areas in the three mudstone shale formations are distinct. The Dongyuemiao Member has a high TOC content in the Kaixian-Liangping-Zhongxian area (Figure 2A), with TOC values exceeding 1.3% and a thickness of approximately 15–30 m (Figure 2B). The quality of shale in the Da'anzhai Member is relatively poor in the eastern Sichuan, with high TOC areas mainly located in the Yilong-Quxian-Liangping area and TOC values ranging from 1.2% to 1.6% (Figure 3A). In the central Sichuan area, the semideep-deep lake facies are more developed, leading to an increase in the TOC of the shale (Figure 3B). The Gaoshan Formation shales are developed in the eastern Sichuan Basin, and the source rocks with the highest organic matter content are primarily located in the Kaixian and Liangping areas, with an average TOC of over 1.3% (Figure 3C).

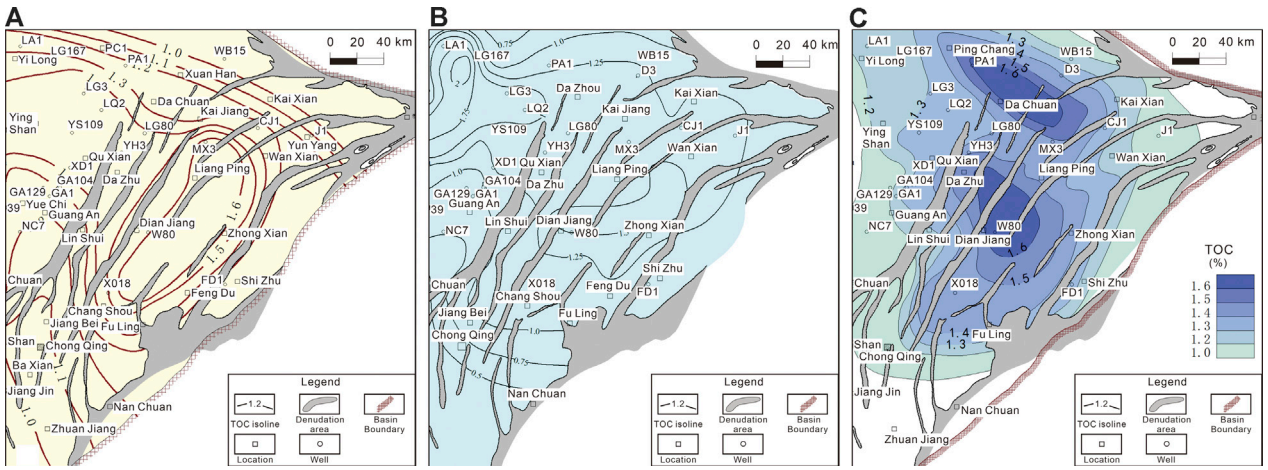

FIGURE 3
TOC contour map of main source rocks of the Lower Jurassic in the eastern Sichuan Basin. **(A)** Dongyuemiao shale. **(B)** Da'anzhai shale. **(C)** Lianggaoshan shale.

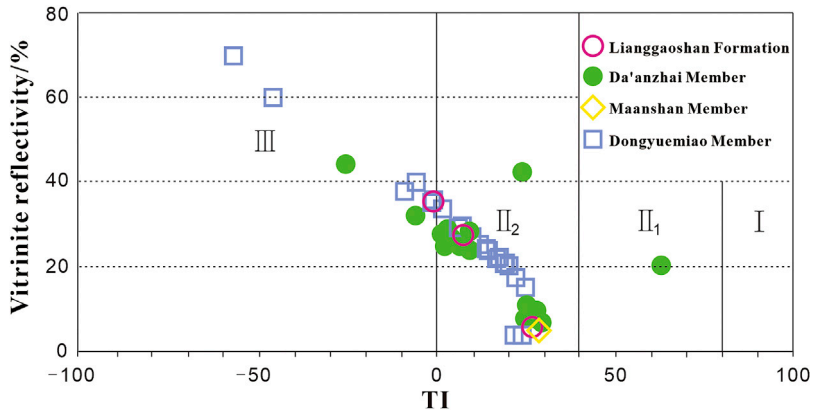

FIGURE 4
Kerogen types of Jurassic source rocks in the eastern Sichuan Basin (partial data from the literature: Deng, 2016)

Microscopic analysis of kerogen indicates that the organic matter in eastern Sichuan mudstone is dominated by humic amorphous and vitrinite, with very low filamentous content. The kerogen type is mainly type II2, with small amounts of type III and type II1, and type I kerogen is absent (Figure 4). Ro of Lower Jurassic source rocks in eastern Sichuan is between 0.8% and 2%, indicating that the source rocks have reached the hydrocarbon generation threshold and are in the mature to high mature stage. The Dongyuemiao Member has the highest Ro, ranging from 1.2% to 1.6%, and is in the mature to high mature stage, with the main products being condensed gas. The Gaoshan Formation has the lowest Ro, mainly between 0.8% and 1.4%, and is in the peak oil generation to early gas generation stage, with oil generation still being dominant. The Da'anzhai Member has a moderate Ro, ranging from 0.9% to 1.5%, and is in the peak oil-gas generation stage.

4 Reservoir characteristics

A variety of reservoir rock types developed in the Jurassic in eastern Sichuan. The Zhenzhuchong Member of the Ziliujing Formation and the Shaximiao Formation are mainly of sandstone reservoirs, while Dongyuemiao Member and Da'anzhai Member are mainly of shale and carbonate reservoirs. The sandstone and shale reservoirs of the Lianggaoshan Formation also exhibit a certain degree of development (Figure 5).

4.1 Sandstone reservoirs

In eastern Sichuan, the Zhenzhuchong Member, Lianggaoshan Member, and Shaximiao Member of the Ziliujing Formation display different degrees of sandstone development. However, the

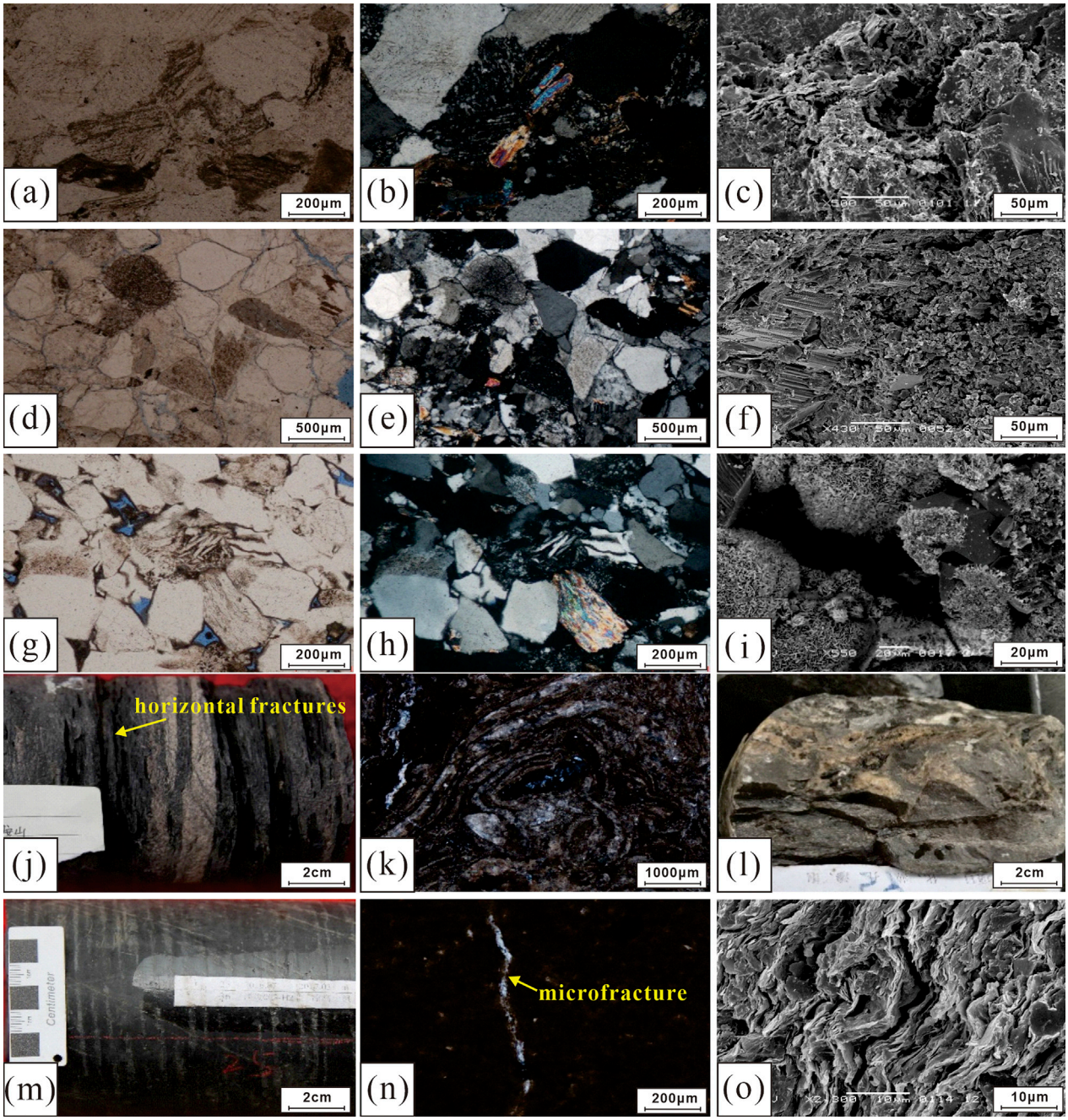

FIGURE 5
Characteristics of the Jurassic reservoir rocks in the eastern Sichuan Basin. **(A–C)** Medium-grained lithic feldspar sandstone, containing granite, granitic gneiss debris, authigenic kaolinite filling intergranular pores, with a small amount of residual intergranular pores, Well Wubaoqian 20, 3531.21 m, Zhenzhuchong Member. Panel a is the pore-casted thin section (–), panel b is the pore-casted thin section (+), and panel c is the scanning electron microscope photograph. **(D–F)** Coarse lithic feldspathic sandstone, with granite debris, laumontite filling cemented intergranular pores, sporadic secondary dissolution pores, extremely developed microfractures, Well Wubaoqian 006-H1, 1807.5 m, Shaximiao Formation. Panel d is pore-casted thin section (–), panel e is pore-casted thin section (+), and panel f is scanning electron microscope photograph. **(G–I)** Medium-grained lithic sandstone, chlorite rim cementation, well-preserved primary intergranular pores, Well Tiandong 021-X8, 1792.4 m, Lianggaoshan Formation. Panel g is pore-casted thin section (–), panel h is pore-casted thin section (+), and panel i is scanning electron microscope photograph. **(J)** Gray black shell-bearing shale, developed horizontal fractures, filled with calcite veins, Well Yunan 012-X8, 2664.5 m, Da'anzhai Member. **(K)** The shell layer in mudstone with secondary dissolved pores and filled with asphalt, Well Yunan 012-X8, 2465.22 m, Da'anzhai Member. **(L)** Bioclastic limestone, development of high-angle fractures, along the fracture development of dissolved pores and caves, filling asphalt, 750.13 m, Da'anzhai Member. **(M)** Gray black mudstone, Well Yangdu 003-H2, 2017 m, Lianggaoshan Formation. **(N, O)** Gray mudstone, developed bedding fracture, 2017.77 m, Lianggaoshan Formation.

characteristics of the sandstone reservoirs vary greatly in different strata. The Zhenzhuchong Member has relatively dense sandstone reservoirs, with fewer effective pores (Figures 5A, B) observed in the pore-casted thin sections (Figures 5A, B), and no obvious apparent pores are found. SEM analysis reveals that there is a small amount of residual intergranular pores filled with authigenic kaolinite

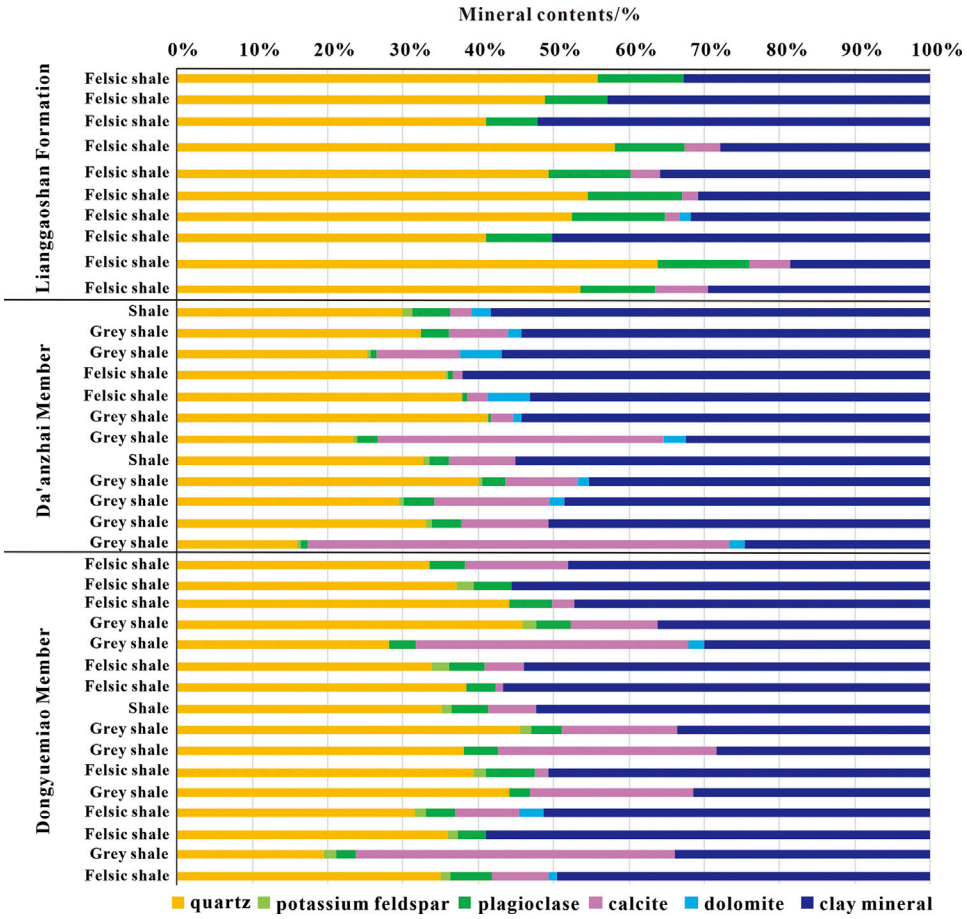

FIGURE 6
Content of minerals in Jurassic mudstones in eastern Sichuan.

(Figure 5C), which mainly consist of micropores. The Shaximiao Formation sandstone has a high content of cements such as laumontite and calcite (Figures 5D, E). The type of intergranular pore reservoir space mainly consists of microcracks (Figure 5D), with a small amount of residual intergranular pores (Figure 5F) and feldspar dissolution pores. The sandstone of the Gaoshan Formation has an obvious early chlorite rim cementation, which has a significant inhibitory effect on compaction and cementation. The primary intergranular pores in this kind of reservoir are well preserved (Figures 5G–I), resulting in high porosity.

4.2 Shale reservoirs

Shale reservoirs are most developed in the Da'anzhai Member, Dongyuemiao Member, and Lianggaoshan Formation. X-ray diffraction analysis shows that the Jurassic shale in eastern Sichuan is dominated by clay minerals, and the quartz content is generally high. Among them, the quartz contents of the Dongyuemiao Member and Lianggaoshan Formation are relatively high, and the quartz content of the Da'anzhai Member is slightly lower. The contents of carbonate minerals such as calcite and siderite are high, and the Dongyuemiao Member and Da'anzhai Member have the highest contents. The feldspar content is 3.5%–14.1%, with no significant differences between layers (Figure 6). The content of Jurassic felsic brittle minerals in eastern Sichuan is generally between 30% and 60%, which is lower than that in typical marine shale (Wang et al., 2015).

Certain shell layers are developed in the Da'anzhai Member and the Dongyuemiao Member shale. The thickness of the shell layer varies from 0.2 cm to 10 cm, forming a thin layer of shale with the shell layer or the combination of the shell layer and the shale layer. A large number of horizontal fractures are developed, and some of the fractures are filled with calcite veins (Figure 5J). Under the microscope, secondary dissolved pores are developed in the common shell layer and calcite veins, and asphalt is partially filled (Figure 5K). Additionally, the scanning electron microscope reveals numerous intergranular pores and clay mineral intergranular pores, with few organic pores. The dark shale in the Gaoshan Formation displays well-developed horizontal bedding (as seen in Figure 5M), and is often interspersed with silty thin layers and occasional shell layers. Pore-casted thin sections and scanning electron microscopy analysis indicate the presence of microfractures (Figure 5N, Figure 3). The matrix pores are dominated by inorganic pores such as residual intergranular pores, dissolution pores, and clay mineral intercrystal pores.

4.3 Limestone reservoirs

Bioclastic limestone and shell limestone are the main forms of reservoirs. The calcareous cementation of such rocks is generally strong, and dissolution is only in areas with high-angle fracture development (Figure 5L). The reservoir space primarily consists of cracks and secondary dissolution pores, and the limestone with undeveloped cracks is dense.

5 Hydrocarbon accumulation characteristics

Three sets of Lower Jurassic source rocks are developed in the eastern Sichuan Basin, which are matched with different types of reservoir rocks to form various types of reservoir-forming assemblages, including lower generation and upper storage type, self-generation and self-storage type, and composite type.

5.1 Lower generation and upper storage reservoir-forming assemblage

In this type of reservoir-forming assemblage, the source rock is located in the lower part, while the reservoir is directly on the source rock or separated from the source rock. Oil and gas migrate upward through faults and fractures, filling the sand body to form oil and gas reservoirs (Fusen and Tinghu, 2007; Kong et al., 2021). This type of reservoir-forming assemblage is common in the upper part of the Shaximiao Formation and Lianggaoshan Formation in eastern Sichuan, forming lithologic and lithologic-structural reservoirs (Xu et al., 2021). This type of reservoir-forming assemblage is mainly formed in sedimentary facies such as underwater distributary channels and beach bar sand in delta fronts. Due to the development of high and steep structures in eastern Sichuan, the Shaximiao Formation and Lianggaoshan Formation have different degrees of denudation. At the same time, the synclinal area has less denudation but more developed faults. Therefore, the quality of caprock and preservation conditions is the key to determining whether such reservoirs are destroyed.

5.2 Self-generation and self-storage reservoir-forming assemblage

The mud shales of the Dongyuemiao Member, Da'anzhai Member, and Lianggaoshan Formation serve as both source rocks and oil and gas reservoirs, which have the characteristics of source-reservoir homogeneity. The discovered Fuling Gas Field and Jiannan Gas Field belong to this type of reservoir combination (Zhou et al., 2012; Zhou et al., 2013). Shale oil and gas exploration practices show that the main occurrence location of these reservoirs is in syncline areas. The distribution of shale oil and gas is largely influenced by factors such as the abundance, type, and maturity of organic matter. To achieve industrial production, oil and gas reservoirs often require fracturing and other technical means, making the type and content of brittle minerals critical factors. The brittle minerals in the Da'anzhai and Dongyuemiao Members are primarily composed of quartz and feldspar, with calcite present mainly in the form of shells, followed by cement. However, the influence of calcite on brittleness is still unclear and different from that of marine shale. Additionally, the development of fractures plays a significant role in enhancing the enrichment and availability of shale oil and gas.

5.3 Composite reservoir-forming assemblage

Most limestone reservoirs belong to this type of reservoir-forming assemblage, where high-angle fractures connect to the lower source rocks. This allows for oil and gas to enter the limestone reservoirs from the upper and lower Xujiahe Formation, and even deeper marine strata, through fractures. Adjacent mud shales also have the potential to supply hydrocarbons to the limestone reservoirs. The source of oil and gas in these cases can be complex and classified as a composite accumulation combination. Such oil and gas reservoirs are typically dense and have locally developed dissolution pores. In addition to having necessary conditions, such as hydrocarbon sources and reservoirs, it is also important to have a certain level of fracture development to increase reservoir connectivity and create effective channels for oil and gas migration. However, it should be noted that based on current research, the development of these reservoirs in the Jurassic of the eastern Sichuan is relatively limited and only found in the Da'anzhai Member and Dongyuemiao Member limestones in Wells W081-H1 and Yuntan 1.

6 Exploration direction

The complexity of the Jurassic source-reservoir-cap assemblage and oil and gas reservoir types in eastern Sichuan requires different exploration approaches for different hydrocarbon accumulation configurations. The reconstruction of the sedimentary environment, source rocks, reservoir conditions, structural features, and trap development should be emphasized differently.

(1) Sandstone reservoirs: The Lianggaoshan Formation and Shaximiao Formation should be the primary target layers. The exploration area selection should take into account the development of source rocks in the Dongyuemiao Member, Da'anzhai Member, and Lianggaoshan Formation. Structural-lithologic traps should be the preferred option for exploration, but the caprock development and trap preservation conditions should also be considered in the selection process.
(2) Shale oil and gas reservoirs: The Da'anzhai Member, Dongyuemiao Member, and Lianggaoshan Formation should be the primary exploration targets. The evaluation of the hydrocarbon generation conditions of these strata is crucial, as shale oil and gas reservoirs are mainly of self-

generation and self-storage. Research should also focus on the development of fractures, especially horizontal fractures. The exploration mode for continental shale oil and gas, such as the Da'anzhai Member and Dongyuemiao Member, cannot be replicated from that of marine shale gas. The evaluation of continental shale oil and gas should pay more attention to the reconstruction of sedimentary microfacies and sedimentary water properties. The syncline area is still a relatively favorable location for shale oil and gas.

(3) Core observations and drilling in eastern Sichuan have shown that the fracture development degree has a significant impact on the distribution of Jurassic oil and gas reservoirs, particularly shale oil and gas. High-angle fractures are well developed in the Da'anzhai Member and Dongyuemiao Member of Wells Qiuwo 081-H1 and Yuntan 1. Shell limestone and bioclastic limestone with developed fractures have significant dissolution and asphalt filling. Almost all of the observed core gas outbursts in Well Yuntan 1 are located in high-angle fractures, indicating that the degree of fracture development, especially high-angle fractures, may be an important factor affecting the productivity of oil and gas in shale and limestone reservoirs.

Data availability statement

The original contributions presented in the study are included in the article/Supplementary Material, further inquiries can be directed to the corresponding authors.

Author contributions

RB and SZ: Conceptualization, Methodology, Writing-Original Draft. HH: Data curation, Supervision. CQ and YL: Supervision. CC and XK: Formal analysis. NL and DL: Investigation. XL and CW: Validation. TJ and JG: Resources. WT: Software.

Conflict of interest

Authors RB, SZ, HH, CQ, YL, CC, NL, and TJ were employed by PetroChina Southwest Oil and Gas Field Company.

Author JG was employed by PetroChina Research Institute of Petroleum Exploration and Development.

The remaining authors declare that the research was conducted in the absence of any commercial or financial relationships that could be construed as a potential conflict of interest.

Publisher's note

All claims expressed in this article are solely those of the authors and do not necessarily represent those of their affiliated organizations, or those of the publisher, the editors and the reviewers. Any product that may be evaluated in this article, or claim that may be made by its manufacturer, is not guaranteed or endorsed by the publisher.

References

Chen, Z., Li, W., Wang, Lining, Lei, Y., Yang, G., Zhang, B., et al. (2019). Structural geology and favorable exploration prospect belts in northwestern Sichuan Basin, SW China. *Petroleum Explor. Dev.* 46 (2), 413–425. doi:10.1016/s1876-3804(19)60022-4

Chen, Z. (1990). Jurassic hydrocarbon exploration in east Sichuan. *Oil Gas Geol.* 11, (03), 304–312.

Deng, Y. (2016). *Study on shale gas enrichment law in Da'anzhai member of Lower Jurassic in eastern Sichuan*. Chengdu, China: Chengdu University of Technology.

Fusen, X., and Tinghu, M. (2007). Exploration and development of Shaximiao formation gas reservoir in Wubaochan structure, Northeast Sichuan. *Nat. Gas. Ind.* 163 (05), 4–7.

Guo, Z., Deng, K., and Han, Y. (1996). *Formation and evolution of Sichuan Basin*. Beijing, China: Geological Publishing House.

Hu, D. F., Zhihong, W., and Ruobing, L. (2021). Major breakthrough of shale oil and gas in well taiye 1 in bashansi syncline in the sichuan basin and its significance. *China pet. Explor.* 21.

Kong, X., Zeng, J., Tan, X., Ding, K., Luo, Q., Wang, Q., et al. (2021). Natural tectonic fractures and their formation stages in tight reservoirs of Permian Lucaogou Formation, Jimsar Sag, southern Junggar Basin, NW China. *Mar. Petroleum Geol.* 133, 105269. doi:10.1016/j.marpetgeo.2021.105269

Li, Y., and He, D. (2014). Evolution of tectonic-depositional environment and prototype basins of the Early Jurassic in Sichuan Basin and adjacent areas. *Acta Pet. Sin.* 35 (2), 219–232.

Liu, S., Deng, B., and Li, Z. (2011). Basin mountain structure and oil and gas distribution - a case study of Sichuan Basin. *Acta Petrol. Sin.* 27 (03), 621–635.

Shu, Z., Zhou, L., Li, X., Liu, H., Zeng, Y., Xie, H., et al. (2021). Geological characteristics of gas condensate reservoirs and their exploration and development prospect in the Jurassic continental shale of the Dongyuemiao Member of Ziliujing Formation, Fuxing area, eastern Sichuan Basin. *Oil Gas Geol.* 42 (1), 212–223.

Sun, W., Liu, S., and Han, K. (2012). Yanshanian paleotectonic development and its influence on oil and gas in Sichuan Basin. *J. Chengdu Univ. Technol. Nat. Sci. Ed.* 39 (01), 70–75.

Wang, R., Hu, Z., and Liu, J. (2018). Comparative analysis of characteristics and controlling factors of fractures in marine and continental shales: A case study of the lower cambrian in cengong area,northern guizhou province. *Oil Gas Geol.* 39.

Wang, R., Hu, Z., and Long, S. (2022). Reservoir characteristics and evolution mechanisms of the upper ordovician wufeng-lower silurian longmaxi shale,Sichuan Basin. *Oil Gas Geol.* 43 (02), 353–364.

Wang, R., Hu, Z., and Zhou, T. (2021). Characteristics of fractures and their significance for reservoirs in Wufeng-Longmaxi shale,Sichuan Basin and its periphery. *Oil Gas Geol.* 42 (06), 1295–1306.

Wang, S., Hu, S., and Dong, D. (2012). Jurassic in eastern Sichuan - a new tight oil and gas field in Sichuan Basin. *Nat. Gas. Ind.* 32 (12), 22–29+125.

Wang, S., Dong, D., Wang, Y., Li, X., Huang, J., and Guan, Q. (2015). Comparative study on geological characteristics of marine shale gas between China and the United States. *Nat. Gas. Geosci.* 26 (09), 1666–1678.

Wu, Y., Zhang, T., and Tao, S. (2013). Sequence stratigraphic analysis of sedimentary sand bodies in deep-water Lake Basin - a case study of Jurassic in Sichuan. *Acta Sedimentol. Sin.* 31 (05), 798–806.

Xiao, J., and Xiangfeng, W. (2018). Difference of accumulation conditions between Fuling marine shale gas and Yuanba-Xinglongchang lacustrine shale gas. *Nat. Gas Explor. Dev.* 41 (04), 8–17.

Xu, A., Hu, S., Wang, Z., Bo, D., Li, M., Lu, W., et al. (2016). Sedimentary mode and reservoir distribution of the Cambrian carbonate & evaporate paragenesis system in the Sichuan Basin. *Nat. Gas. Ind. B* 3 (5), 418–427. doi:10.1016/j.ngib.2017.02.003

Xu, Y., Dai, Z., Hu, X., Xu, Z., and Dan, L. I. (2021). Geochemical characteristics and geological significance of Shaximiao Formation in northeastern Sichuan Basin: A case study from Wubaochang area. *Lithol. Reserv.* 33 (01), 209–219.

Yang, s. (2014). *Sedimentary evolution and facies controlled reservoir prediction of Jurassic in Sichuan Basin*. Chengdu, China: Chengdu University of Technology.

Yang, Y., and Huang, D. (2019). Geological characteristics and new understandings of exploration and development of Jurassic lacustrine shale oil and gas in the Sichuan Basin. *Nat. Gas. Ind.* 39 (6), 22–33.

Yang, Y., Huang, D., Yang, G., Li, Y., Dai, H., and Rong, B. (2019). Geological conditions to form lacustrine facies shale oil and gas of Jurassic Daanzhai Member in Sichuan Basin and exploration directions. *Nat. Gas Explor. Dev.* 42 (02), 1–12.

Yuan, Y., Lin, J., and Cheng, X. (2014). Late yanshanian himalayan denudation in western hubei and eastern chongqing. *Chin. J. Geophys.* 57 (09), 2878–2884.

Zhou, D., and Jiao, F. (2012). Evaluation and prediction of shale gas sweet spots: A case study in jurassic of jiannan area, Sichuan Basin. *PETROLEUM Geol. Exp.* 34 (2).

Zhou, D., Jiao, F., Guo, X., Guo, D., and Zhihong, W. (2013). Geological characteristics of lower jurassic shale oil and gas in fuling area, southeast sichuan. *Oil Gas Geol.* 34 (04), 450–454.

Zou, Y., Duan, J., and Zhao, Y. (2015). Structural characteristics and evolution of high and steep fault fold belt in eastern Sichuan. *Acta Geol. Sin.* 89 (11), 2046–2052.

frontiers | Frontiers in Earth Science

TYPE Original Research
PUBLISHED 28 December 2023
DOI 10.3389/feart.2023.1231694

OPEN ACCESS

EDITED BY
Ruyue Wang,
SINOPEC Petroleum Exploration and Production Research Institute, China

REVIEWED BY
Wenqiang Tang,
Chengdu University of Technology, China
Wei Dang,
Xi'an Shiyou University, China
Yahao Huang,
Yangtze University, China

*CORRESPONDENCE
DaWei Cheng,
chengdawei123@petrochina.com.cn
ChunYu Qin,
qinchy_0416@163.com
Wenbin Tang,
wbtang@cdut.edu.cn,
tangwenbin100@163.com

RECEIVED 30 May 2023
ACCEPTED 25 August 2023
PUBLISHED 28 December 2023

CITATION
Hong H, Qin C, Zhang S, Zhang Z, Wang X, Li N, Cheng D and Tang W (2023), Early–middle Jurassic source to sink evolution and its tectonic significance in the northeastern Sichuan Basin. *Front. Earth Sci.* 11:1231694. doi: 10.3389/feart.2023.1231694

Early–middle Jurassic source to sink evolution and its tectonic significance in the northeastern Sichuan Basin

HaiTao Hong[1,2], ChunYu Qin[1,2]*, ShaoMin Zhang[1,2], ZhiJie Zhang[3], XiaoJuan Wang[1,2], Nan Li[1,2], DaWei Cheng[3]* and Wenbin Tang[4]*

[1]PetroChina Southwest Oil and Gas Field Company, Chengdu, China, [2]Research Institute of Exploration and Development, PetroChina Southwest Oilfield Company, Chengdu, China, [3]PetroChina Research Institute of Petroleum Exploration and Development, Beijing, China, [4]State Key Laboratory of Oil and Gas Reservoir Geology and Exploitation, Institute of Sedimentary Geology, Chengdu University of Technology, Chengdu, China

This paper discusses the sedimentary environment and source supply in the sedimentary area and their coupling relationship through a detailed description of the deposits from the Ziliujing Formation to Shaximiao Formation of the Lower–Middle Jurassic on the Tieshan section in the Dazhou City, northeastern Sichuan Province, through sedimentary characterization, determination of the paleocurrent direction, analysis of heavy minerals, and detrital zircon U–Pb dating. The results show that the Zhenzhuchong Member is sufficiently supplied with detrital sediments and is dominantly composed of fluvial-delta deposits. The Dongyuemiao Member—the first member of the Lianggaoshan Formation—is dominated by lacustrine deposits, with the detrital supply increased initially in the early Lianggaoshan. The second member of the Lianggaoshan Formation suggests a significant increase in detrital supply, with shrunken lake basin and changed paleocurrent direction. The Shaximiao Formation reveals a complete disappearance of the lake basin in the northern Sichuan Basin. The comprehensive analysis on source supply indicates that the change in source property is apparently coupled with the change in the sedimentary environment, both controlled by orogenesis around the basin. It is inferred from the zircon age distribution that the changes in the sedimentary environment and source supply during the late Ziliujing period and the middle and late Lianggaoshan period resulted from the uplifting of the Micangshan Mountain, Dabashan Mountain, and Qinling Mountain, respectively.

KEYWORDS

heavy mineral composition, zircon U–Pb age, paleocurrent direction, Micangshan Mountain, Dabashan Mountain

1 Introduction

The sedimentary basin and orogenic belt are two basic tectonic units in the upper continental crust. They can be studied as a whole to explore the collisional orogeny and its influence on sedimentation processes and environment change from the perspective of geotectonic geology and sedimentology.

The northern margin of the Sichuan Basin is adjacent to the Dabashan and Micangshan structural belts to the north, separated from the EW-trending Qinling orogenic belt, and

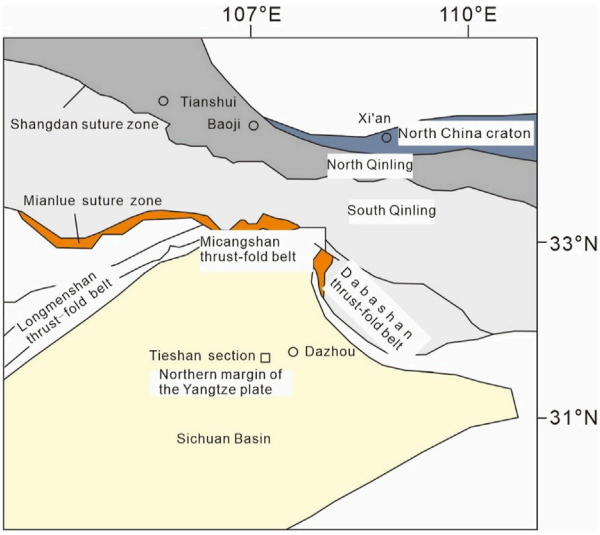

FIGURE 1
Structural sketch of tectonic belts from the northern margin of the Yangtze plate to the North China plate and location of the target section.

bordered by the Songpan–Ganzi and Longmenshan orogenic belts to the west and the Xuefengshan fold belt to the east. It acts as an intersection between multiple structural belts. The Indosinian collision between the Yangtze plate and the North China plate led to a tectonic evolution from the passive continental margin in the northern margin of the Upper Yangtze into the Late Triassic–Early Cretaceous foreland thrust-fold belt and its corresponding foreland basin. The sediments in the northern margin of the Sichuan Basin record the tectonic history of its adjacent orogenic belts. They are ideal for identifying the coupling relationships between the northern margin of the Sichuan Basin and its adjacent orogenic belts.

Many studies have been conducted on the tectonic evolution of sedimentary basin–orogenic belt systems in the northern margin of the Sichuan Basin, including structural interpretation of seismic sections (He et al., 2020), zircon U–Pb dating (Li et al., 2010; Li et al., 2012; Li et al., 2018), and sedimentary environment analysis and paleocurrent direction determination (Qu et al., 2009). However, these studies usually adopted a single method to interpret the tectonic evolution but rarely dealt with sediment–structure coupling; moreover, the interpretation results are different significantly from method to method. On the basis of previous achievements, this paper attempts to explore the uplifting stages of orogenic belts around the basin and their tectonic–sedimentary response relations, through a detailed dissection of field outcrops and the comparison of sedimentary environments and source supply in different periods within the basin.

2 Geological setting

The northeastern Sichuan Basin, i.e., the northeastern margin of the Sichuan Basin, is located in the part transiting from the present-day Qinling orogenic belt to the Sichuan Basin (Figure 1). The Qinling orogenic belt, in the north of the Sichuan Basin, is characteristically composed of three plates and two suture zones. Fu (2016) from north to south, the North China plate, the Qinling micro-plate, and the Yangtze plate are separated by the Shangdan suture zone (Xinyang–Shucheng fault) in the north and the Mianlue suture zone (Xiangfan–Guangji Fault) in the south (Zhang et al., 2001; Wang et al., 2019; Cai, 2020). Structurally, the northeastern Sichuan Basin is connected to the Qinling orogenic belt through the Dabashan thrust-fold belt to the north and the Micangshan thrust-fold belt to the northwest. The northeastern Sichuan foreland basin is a product of the isostatic adjustment induced by huge load of the overthrust sheets under the extrusion stress regime when the South China plate collided with the Qinling micro-plate and North China plate during the late Indosinian and the Central Sichuan land mass subducted into the land beneath the Qinling Mountain in the Yangtze area during the Yanshanian (Li et al., 2012). During the Middle–Late Triassic, along with the closing of the Mianlue Ocean and the emergence of the Qinling orogenic belt, marine sedimentation in the major part of the Sichuan Basin ended and the continental clastic sediments began to deposit in the Late Triassic Xujiahe Formation. The Jurassic continental clastic sediments in the basin, from bottom to top, are composed of the Lower Jurassic Ziliujing Formation (J_1z), which is subdivided into the Zhenzhuchong, Dongyuemiao, Maanshan, and Daanzhai members, the Middle Jurassic Lianggaoshan Formation (J_2l) (also known as the Qianfoya Formation and Xintiangou Formation due to sedimentary facies variation within the basin) and Shaximiao Formation (J_2s), and the Upper Jurassic Suining Formation (J_3s) and Penglaizhen Formation (J_3p) (Yang et al., 2022).

2.1 Sample testing methods

Heavy mineral analysis and isotope dating analysis were conducted on 12 siltstone and fine sandstone samples taken from six intervals in the Dongyuemiao Member, the Daanzhai Member, and the first, second, and third members of Lianggaoshan Formation and the Shaximiao Formation.

Identification and content measurement of heavy minerals and LA-ICPMS zircon U–Pb dating were completed in the State Key Laboratory of Continental Dynamics, Northwest University. The heavy minerals of the rock samples were quantitatively identified and separated by using a binocular microscope and a magnetic separator, through the procedures of screening, rough elutriation, high-intensity magnetic separation, electromagnetic separation, fine elutriation, packaging, and mineral separation. Then, the types of heavy minerals in each sample were statistically determined and the weight ratio of each heavy mineral was calculated. On this basis, the LA-ICP-MS U–Pb dating was performed on the selected zircon grains from some samples. A PVC ring was put on the glass slide, where complete and typical zircon grains were glued with double-faced adhesive tape, and then injected with fully mixed epoxy resin and hardener. The samples were separated from the glass slide when the epoxy resin was solidified fully and then polished until a smooth plane came out. Before measurements, the samples were washed with HNO_3 with a volume percentage of 3% to remove contaminations on the surface. An integration of ICP-MS and the laser ablation system was used for LA-ICPMS zircon U–Pb dating, with a laser beam spot of 32 μm in diameter, 6 Hz, single

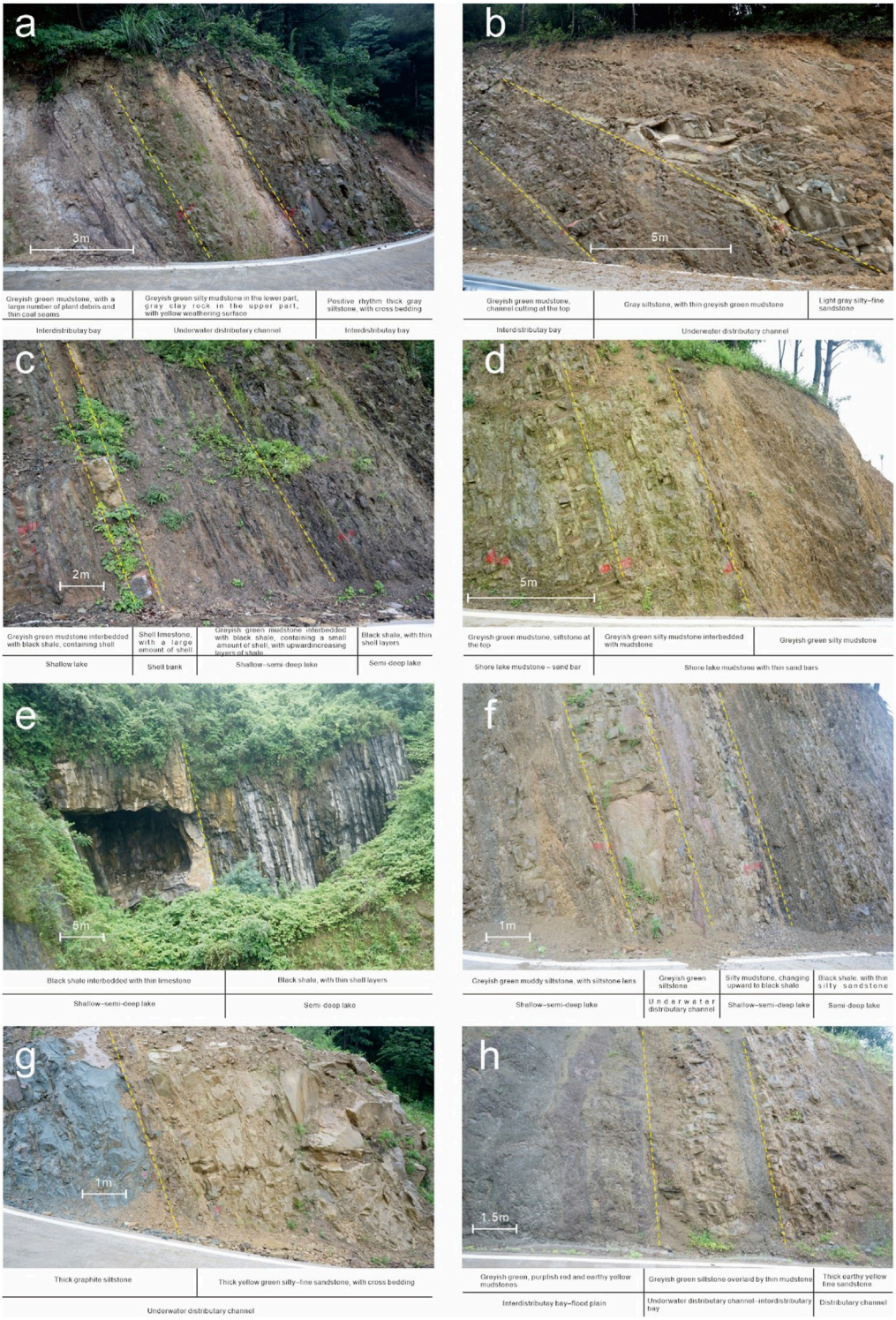

FIGURE 2
Interpretation of the sedimentary environment of intervals on the Tieshan section. **(A, B)** Zhenzhuchong Member, **(C)** Dongyuemiao Member, **(D)** Maanshan Member, **(E)** Daanzhai Member, **(F, G)** Lianggaoshan Formation, and **(H)** Shaximiao Formation.

point ablation, and helium as the carrier gas. Zircon 91500 was measured every five sample points, and standard glass NIST610 and Plesovice zircon were measured every 10 sample points. Each analysis incorporated a background acquisition of 20–30 s (gas blank), followed by 50 s of data acquisition from the sample. ICPMSDataCal was used for offline processing of these analysis data (Liu et al., 2008; Liu et al., 2010a; Liu et al., 2010b). Zircon 91500 served as an external standard for isotope fractionation

correction in the zircon U–Pb dating. Zircon U–Pb concordia diagram mapping and weighted average age calculation were performed by using Isoplot/Ex_ver3 (Ludwig, 2003). The standard deviation of single measurement of the U–Th–Pb isotope ratio, age, and trace elements of zircon was 1σ.

3 Results

3.1 Sedimentary characterization and paleocurrent direction determination

Nearly E–W compression occurred in the eastern Sichuan Basin after the Cretaceous, forming the present SN-trending high and steep fold belt. The Jurassic outcrop in the core of the fold belt provides an ideal stratigraphic section for this study. On the Tieshan section (107.36° E and 31.21° N) to the west of Dazhou City (Figure 1), the strata from the top of the Upper Triassic Xujiahe Formation to the bottom of the Middle Jurassic Shaximiao Formation, with a total thickness of 20 m, are well exposed along a new road through mountains, without any hiatus and huge fault. This study carries out a fine centimeter-scale description of the Tieshan section and records the lithology, color, thickness, sedimentary structure, macroscopic paleontological fossils, and lithofacies superposition of the Lower–Middle Jurassic strata. On this basis, the sedimentary structures indicative of the paleocurrent direction are measured.

On the Tieshan section, the members of the Lower Jurassic Ziliujing Formation exhibit distinctly different sedimentary characteristics with clear interfaces between them. The Zhenzhuchong Member at the bottom is 219 m thick and mainly composed of medium–thin layers of siltstone, grayish-green muddy siltstone, silty mudstone, mudstone, and gray clay rock. It is dominated by delta front facies, and it develops multiple thick layers of underwater distributary channel deposits with trough cross-bedding and parallel beddings, where the deposits of interdistributary bay are mainly fine in grain size with plant debris and coal streaks. The light-gray fine quartz sandstone at the bottom of the Zhenzhuchong Member acts as a parallel unconformity with the underlying gray fine lithic sandstone at the top of the Upper Triassic Xujiahe Formation (Figure 2).

The top of the Zhenzhuchong Member is dominated by light-grayish-green muddy siltstone, and the appearance of black–gray mudstone marks the beginning of the Dongyue Member. The Dongyue Member is 42 m thick and generally lithologically fine. It is mainly composed of medium layers of siltstone, light-gray limestone, black–gray shell-bearing shale, and mudstone. It is believed to be deposited in a shallow–semi-deep lake paleo-environment, where the shallow lake sediments include multiple sand bars and low-energy shell banks, and the semi-deep lake sediments are dominated by low-energy thick shales.

Gray shale is deposited at the top of the Dongyuemiao Member and is covered by gray muddy siltstone at the bottom of the Maanshan Member. The Maanshan Member is 40 m thick and composed of greyish-green mudstone with thin layers of siltstone. It is identified as the deposits of shore lake facies, which include mudflat, beach, and other microfacies.

The appearance of greyish-green shell-bearing silty mudstone followed by the greyish-green mudstone of the Maanshan Member represents the beginning of the Daanzhai Member. The Daanzhai Member is approximately 100 m thick and mainly composed of gray shell limestone and black–gray shell-bearing shale. It is identified as the product of the shallow–semi-deep lake paleo-environment.

After the deposition of gray shell limestone in the Maanshan Formation ended, the Lianggaoshan Formation began with the deposition of thick gray siltstone. The Lianggaoshan Formation is 257 m thick and mainly consists of medium layers of siltstone, greyish-green silty mudstone, mudstone, black–gray shale, and mudstone. It is identified as the deposits of delta front–shallow lake–semi-deep lake facies. The delta front subfacies generally includes multiple underwater distributary channel sand bodies, which are mainly distributed in the upper, lower, and middle parts. According to the latest stratigraphic division proposed by PetroChina Southwest Oil & Gas Field Company, the Lianggaoshan Formation is subdivided into the first, second, and third members from the bottom to top (J_2l_1, J_2l_2, and J_2l_3) roughly by the bottom boundaries of three thick channel sand bodies. J_2l_1 develops the shallow lake deposits in the middle, including shallow lake mudstone, distal sand bar, and beach bar, and is dominated by semi-deep lake shale, shallow lake mud flat, and beach bar at the top. With a significantly increased amount of sand bodies than J_2l_2, J_2l_3 is mainly composed of the shore-shallow lake beach bar, delta front channel, and distal sand bar, with thin layers of lacustrine black and black–gray mudstones.

The Lianggaoshan Formation and Shaximiao Formation are successively deposited, with indistinct boundaries. In this study, the variegated mudstone is considered as the boundary between them. Siltstones alternated with purplish-red/earthy-yellow mudstone and greyish-green mudstone at the bottom of Shaximiao Formation suggest a paleo-environment near the water–atmosphere interface. They are identified as the deposits of delta front–delta plain subfacies. The purplish-red mudstones dominating the middle and upper parts are mainly the deposits of delta plain subfacies, with thick–medium layers of channel fine sandstones (Figures 2, 3).

3.2 Determination of the paleocurrent direction

The Middle–Lower Jurassic deposits in the Tieshan section are generally fine grained. Few indicative sedimentary structures indicative of the paleocurrent direction have been observed, mainly including asymmetric ripples on the surface of sandstone, flute casts at the bottom, and cross-bedding in sandstones. The paleocurrent direction is determined to provide a basis for clarifying the provenance direction, and further research is needed to provide more data. The Zhenzhuchong Member at the bottom indicates the S–W paleocurrent direction (Figures 2, 3). As dominated by shales, the Dongyuemiao and Maanshan members have not provided data for the determination of the paleocurrent direction. The Daanzhai Member indicates that there were multiple paleocurrent directions, including west, south, and southwest, with southwest in dominance (Figures 2, 3). Fluvial sand bodies are deposited at the bottom of the Lianggaoshan Formation (J_2l_1), and the measured paleocurrent directions are dominantly southwest, the same as the Daanzhai

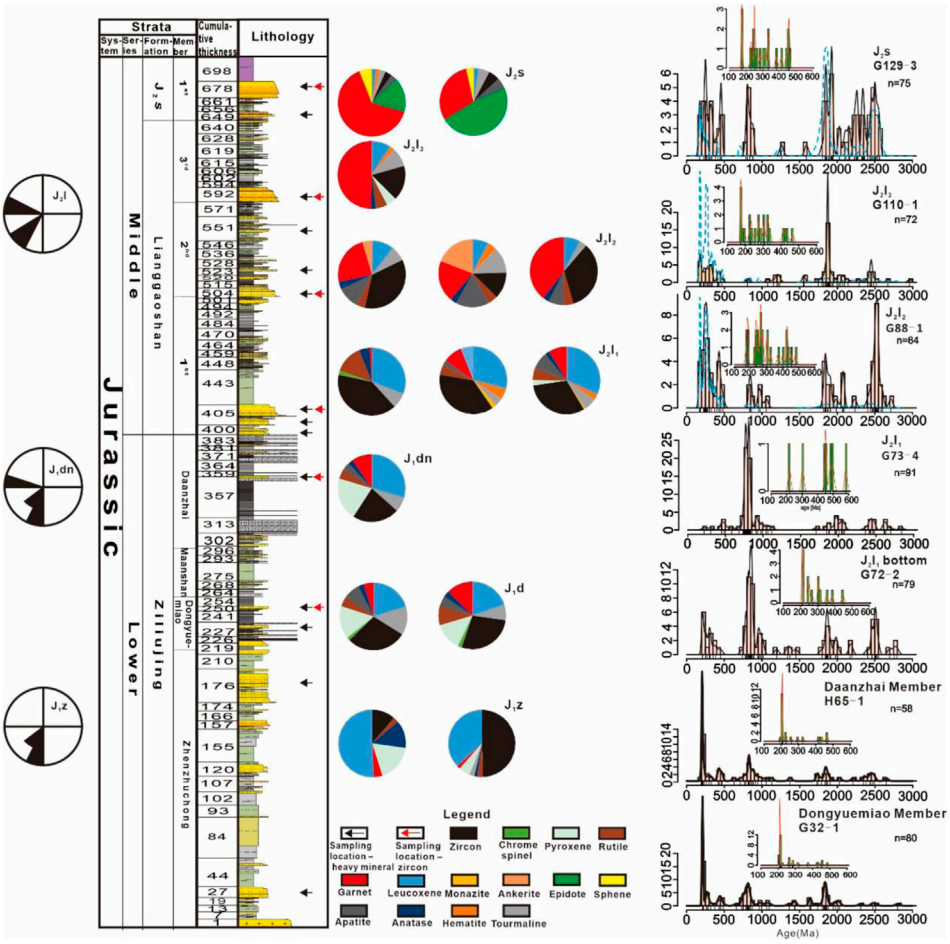

FIGURE 3
Analysis results of paleocurrent direction, lithology, heavy mineral composition, and detrital zircon U–Pb age in the Tieshan section.

Member. The paleocurrent directions measured began to change to southwest and west in the J_2l_2 and J_2l_3 periods, respectively.

3.3 Analysis of heavy minerals

According to the types and proportions of heavy mineral assemblages, a total of five samples from the Zhenzhuchong Member, Dongyuemiao Member, and Daanzhai Member of the Ziliujing Formation show similar characteristics of heavy mineral assemblages. The heavy minerals that account for high proportions include leucoxene, zircon, and pyroxene, and the secondary minerals include rutile, tourmaline, apatite, anatase, and garnet (Figure 2). Differences are also observed between intervals, mainly in the content of secondary minerals. For example, the contents of tourmaline and apatite in the Zhenzhuchong Member are significantly lower than those in the overlying intervals.

Seven samples from the Lianggaoshan Formation are distinct in the heavy mineral assemblage. Three samples from J_2l_1 have similar heavy mineral assemblages that are dominated by leucoxene and zircon, with tourmaline, rutile, apatite, anatase, and garnet (Figure 2).

Four samples from J_2l_2 and J_2l_3 show similar heavy mineral assemblages that are dominated by zircon and garnet, with leucoxene, tourmaline, apatite, rutile, and ankerite (Figure 2).

Two samples from the bottom of J_2l_1 present similar heavy mineral assemblages that are dominated by epidote and garnet, with a small amount of apatite, zircon, tourmaline, and sphene (Figure 2).

3.4 Zircon U–Pb dating

Sample G32-1 from the Dongyuemiao Member of the Ziliujing Formation provided a total of 80 zircon concordia ages, which are divided into five groups (Figure 2). The first group consists of 31 ages in the range of 208–493 Ma. The second group consists of 23 ages in the range of 660–1,098 Ma. The third group consists of three ages in the range of 1,363–1,436 Ma. The fourth group consists of 19 ages in the range of 1,633–2019 Ma. The fifth group consists of four ages in the range of 2,302–2,910 Ma.

Sample H65-1 from the Dongyuemiao Member of the Ziliujing Formation provided a total of 58 zircon concordia ages, which are divided into five groups (Figure 2). The first group is composed of 22 ages in the range of 192–468 Ma. The second group is composed

of 10 ages in the range of 628–1,050 Ma. The third group has only one age of 1,369 Ma. The fourth group is composed of eight ages in the range of 1714–1960 Ma. The fifth group is composed of seven ages in the range of 2,166–2,629 Ma.

Sample G72-2 from the bottom of the Lianggaoshan Formation provided a total of 79 zircon concordia ages, which are divided into seven groups (Figure 2). The first group has 13 ages in the range of 210–447 Ma. The second group has 33 ages in the range of 740–1,046 Ma. The third group has five ages in the range of 1,191–1,450 Ma. The fourth group has 12 ages in the range of 1796–1975 Ma. The fifth group has two ages in the range of 2,140–2,186 Ma. The sixth group has 11 ages in the range of 2,403–2,523 Ma. The seventh group has three ages in the range of 2,697–2,799 Ma.

Sample G73-4 from J_2l_1 provided a total of 91 zircon concordia ages, which are divided into five groups (Figure 2). The first group consists of two ages in the range of 218–303 Ma. The second group consists of five ages in the range of 451–583 Ma. The third group consists of 59 ages in the range of 680–1,123 Ma. The fourth group consists of 13 ages in the range of 1,697–2066 Ma. The fifth group consists of 12 ages in the range of 2,346–2,896 Ma.

Sample G88-1 from J_2l_2 provided a total of 73 zircon concordia ages, which are divided into five groups (Figure 2). The first group has 25 ages in the range of 170–480 Ma. The second group has six ages in the range of 835–1,060 Ma. The third group has 13 ages in the range of 1817–2,220 Ma. The fourth group has 19 ages in the range of 2,397–2,712 Ma. The fifth group has one age of 3,193 Ma.

Sample G110-1 from J_2l_3 provided a total of 72 zircon concordia ages, which are divided into 7 groups (Figure 2). The first group has 22 ages in the range of 173–465 Ma. The second group has one age of 809 Ma. The third group has five ages in the range of 1,076–1,233 Ma. The fourth group has two ages in the range of 1,543–1,553 Ma. The fifth group has 31 ages in the range of 1709–2085 Ma. The sixth group has nine ages in the range of 2,275–2,447 Ma. The seventh group has two ages in the range of 2,654–2,870 Ma.

Sample G129-3 from J_2s_1 provided a total of 75 zircon concordia ages, which are divided into five groups (Figure 2). The first group consists of 20 ages in the range of 173–461 Ma. The second group consists of eight ages in the range of 785–883 Ma. The third group consists of one age of 1,287 Ma. The fourth group has one age of 1,588 Ma. The fifth group consists of 45 ages in the range of 1779–2,587 Ma.

3.5 Comprehensive source analysis

The results of heavy mineral assemblages and zircon U–Pb ages indicate that the northeastern Sichuan Basin has experienced three distinct changes in source supply during the deposition from the Ziliujing Formation to the Shaximiao Formation. They are divided by S_1 (from the end of J_1z to the beginning of J_2l), S_2 (from the end of J_2l_1 to the beginning of J_2l_2), and S_3 (from the end of J_2l to the beginning of J_2s). From above to below S_1, the deposition of the Lianggaoshan Formation started, when the pyroxene content decreased remarkably in mineral assemblages, a small amount of monazite and hematite began to appear, and the proportion of zircons at the Neoproterozoic age began to increase by significant percentages and reached its maximum in the middle of J_2l_1. From above to below S_2, the deposition of J_2l_2 started, when the proportion of garnet increased obviously and the proportion of leucoxene decreased; zircons at the Neoproterozoic age reduced remarkably and almost disappeared in J_2l_3, and the zircons at the Paleoproterozoic and Archean ages increased significantly at the appearance of the Yanshanian zircons (170 Ma). From above to below S_3, the deposition of Shaximiao Formation started, when zircons decreased significantly, epidote and sphene began to be detected, rutile content significantly decreased, zircons at the Neoproterozoic age increased again, and zircons at the Paleoproterozoic and Archean ages continued to increase with a more dispersed distribution.

4 Zircon U–Pb age distribution in potential provenance

The results of paleocurrent direction determination show that the provenances are mainly distributed in the Qinling orogenic belt to the north of the study area. Along with the progress of orogenic chronology, petrographic composition and formation age of each tectonic unit within the Qinling orogenic belt have been gradually clarified (Figure 4). The southern margin of the North China craton mainly has outcrops of the Taihua and Dengfeng groups in the Neoarchean basement, the Paleoproterozoic Angou Group, and the Middle Proterozoic Xionger Group volcanic rocks (Zhang et al., 2000). Three major tectonothermal events occurred in the Early Neoarchean period (2.7–2.9 Ga), Late Neoarchean period (2.2–2.5 Ga), and Middle Paleoproterozoic period (1.8–2.1 Ga) (Zhai et al., 2000). Since the Meso-Cenozoic, a large number of granites formed by the collision between the South China plate and the North China plate have been distributed extensively in the southern margin of the North China plate and the east of the North Qinling orogenic belt. Their zircon ages are mainly concentrated in the Indosinian (~278 Ma) and the Late Caledonian (~463 Ma), and few in the Late Neoproterozoic (~906 Ma) (Figure 5A).

From north to south, the Kuanping Group Complex, Erlangping Group Complex, Qinling Group Complex, Songshugou ophiolite fragment, and Danfeng Group Complex are outcropped successively in the North Qinling orogenic belt. The Kuanping Group Complex was formed during the Neoproterozoic–Early Paleozoic, the Erlang Group Complex was formed in the Early Paleozoic, the Qinling Group Complex was deposited in the Early Neoproterozoic, the Songshugou ophiolite was formed by the Mesoproterozoic tectonic emplacement, and the Danfeng Group Complex was developed in the Late Neoproterozoic (Shi et al., 2013; Dong et al., 2016). Four peaks, 2.4–2.6 Ga (Neoarchean), approximately 850–950 Ma, approximately 744 Ma, and 450–350 Ma (Early Paleozoic), are shown in the distribution of detrital zircon ages of the North Qinling orogenic belt (Figure 5B).

The South Qinling orogenic belt is geologically composed of the Neoarchean–Paleoproterozoic crystalline basement, the Meso-Neoproterozoic transitional basement, and the Paleozoic and Lower–Middle Triassic deposits. Oblique collision between

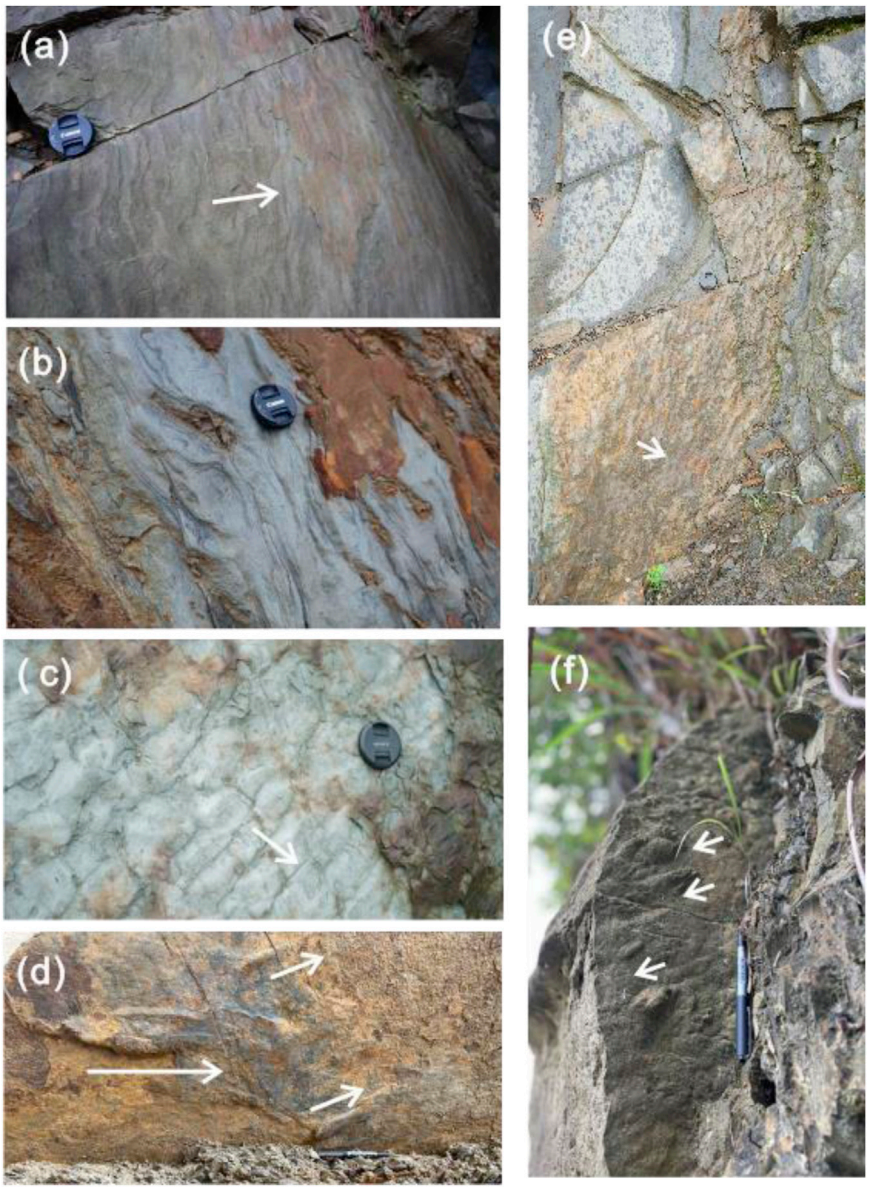

FIGURE 4
Indicated paleocurrent directions. **(A)** Asymmetrical ripple marks in the Zhenzhuchong Member; **(B)** small-scale cross-bedding in the Zhenzhuchong Member; **(C, E)** asymmetrical ripple marks at the bottom of the Daanzhai Member; and **(D, F)** marks on the bottom of the thick fluvial sand body in J_2l_2. The white arrows indicate the flow direction.

the Yangtze plate and the North China plate occurred during the Indosinian, when a large amount of syncollisional volcanic rocks were developed along the Mianlue suture zone, ranging between 206 Ma and 220 Ma in age (Sun et al., 2000; Hu et al., 2004), and granites were developed extensively in Caoping, Zhashui Yangba, and Foping areas with ages peaking at 216 Ma. At the same time, the zircons at the Late Caledonian–Early Hercynian age (~443 Ma) and the Late Neoproterozoic age (~751 Ma) were distributed sporadically in the northern margin of the South Qinling. The Meso-Neoproterozoic transitional basement composed of volcanic–sedimentary rock series is the principal part of the South Qinling basement and is represented by the Wudang Group and Yunxi Group, as well as the Bikou Group, in the west (Ling et al., 2002; Li et al., 2003). The Yudongzi Group of the Neoarchean basement is sporadically exposed near the Lueyang–Ningqiang area and was formed around 2.7 Ga ago (Zhang et al., 2005; Zhang et al., 2010). Zhang et al. (2001) believed that the uplifting of Mianlue suture zone and South Qinling orogenic belt during the Middle–Late Hercynian–Indosinian, when the collisional orogeny of the Qinling–Dabieshan orogenic belt ended, provided abundant sediments to the foreland basin (Figure 5C).

The northern margin of the Yangtze plate mainly refers to the part adjacent to the South Qinling orogenic belt in the south of the Mianlue–Chengkou–Fangxian–Xiangguang Fault, including the Hannan and Micangshan uplifts in the northern margin of

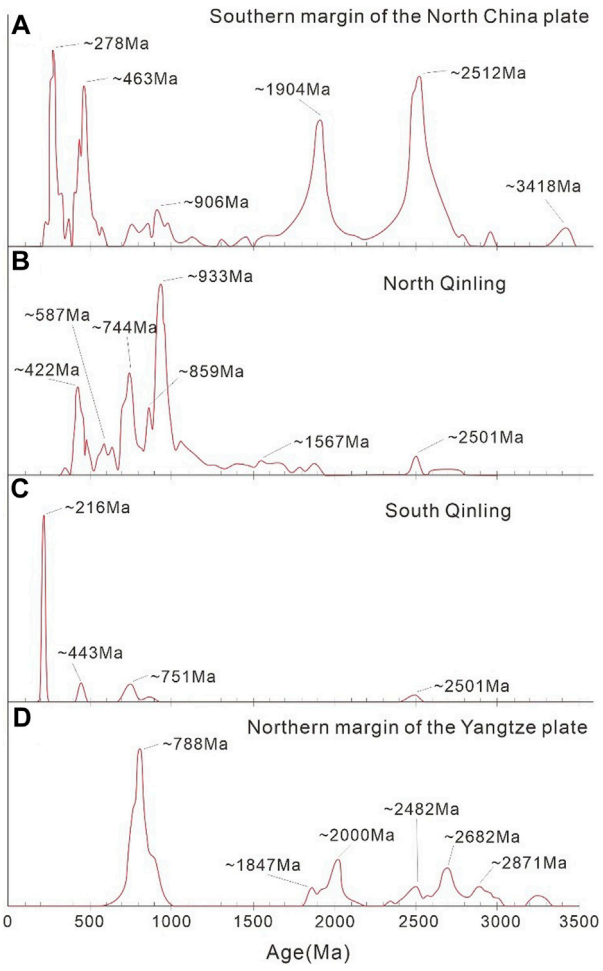

FIGURE 5
Zircon U–Pb age distribution in potential provenance (modified from the work of Qian (2015)).

the Sichuan Basin, where a small amount of Archean basement (e.g., Kongling and Honghe groups) and a large number of Neoproterozoic basement are mainly exposed. Volcanic rocks were barely developed since the Phanerozoic and have three major peaks of zircon age, i.e., ~2,682 Ma, ~2000 Ma, and ~788 Ma (Diwu et al., 2012). Pre-Sinian magmatic and metamorphic rocks are dominantly exposed in the Hannan area, and the Neoproterozoic basic–intermediate-acid intrusive rocks widely exposed near the Xixiang–Hanzhong area are known as the "Hannan Complex." Its formation age was reported as 837–800 Ma (Zhang et al., 2000; Zhao et al., 2006; Zhao et al., 2008; Geng, 2010). Zircon U–Pb dating provides ages of 778 ± 5 Ma for tonalites in the Wudumen composite granite within the Hannan Complex and 840–820 Ma for volcanic rocks of the Sunjiahe Formation in the Hannan area, suggesting a close association between formation of the magmatic rocks and break-up of Rodinia Supercontinent (Dong et al., 2011; Dong et al., 2012). The Proterozoic metamorphic rocks and polyphasic intrusive magmatites and their surrounding Paleozoic and Mesozoic sedimentary rocks are the major part of the Micangshan Mountain (Figure 5D).

5 Comprehensive source analysis

The identified paleocurrent direction from the Zhenzhuchong Member suggests the principal provenance as the North Qinling orogenic belt to the north. The identified multiple paleocurrent directions from the Dongyuemiao and Daanzhai members indicate an input of sediments from multiple directions. Consistent heavy mineral assemblages and highly similar distribution of zircon U–Pb ages were observed within the Ziliujing Formation. The zircon ages are mainly in the range of 205–210 Ma, followed by 750–850 Ma, and few in the ranges of 400–500 Ma, 1700–19000 Ma, and 2,400–2,500 Ma. This zircon age distribution is highly similar to that in the South Qinling area, so the South Qinling is inferred as a provenance for the Ziliujing Formation. A small amount of zircons at the Early Paleozoic and Neoproterozoic ages probably came from the Dabashan Mountain, Hannan area, and Micangshan Mountain on the pathway from the South Qinling to the sedimentary area (Sun, 2014). It reveals low-amplitude uplifting of the Dabashan and Hannan–Micangshan occurred during the Ziliujing period, providing a small amount of sediments to the sedimentary area. Zircon ages of the North Qingling have not been detected, indicating that the South Qingling had been uplifted during this period, which hindered the sediment supply from the North Qinling.

From J_1z to J_2l^1, zircons at the Late Triassic age reduced and those at the Neoproterozoic age increased gradually. The zircon age distribution in the middle of J_2l_1 shows a high consistency to that in the northern margin of the Yangtze craton. Based on the indications of the paleocurrent direction that the sediments mainly came from the north and the Neoproterozoic zircons are currently exposed in the Hannan area and Micangshan Mountain, it is speculated that the Hannan area and Micangshan Mountain that were rapidly uplifted during this period have gradually become the major provenances for the sedimentary area and have hindered the source supply from the South Qingling to the north until the early Lianggaoshan period. Moreover, a small amount of the Early Paleozoic zircons are inferred to originate from the Dabashan Mountain.

In the J_2l_2 period, the paleocurrent direction changed to W–WS from S–SW. Compared with the older formations, J_2l_2 shows a different zircon age distribution. Specifically, the zircons younger than the Mesoproterozoic show a significantly increased proportion and have a greater number than all of the zircons at the Neoproterozoic age, which corresponds to the basement formation stage of the North China plate, Yangtze plate, and Qinling orogenic belt. In addition, a few young zircons at ages (170–180 Ma) approximate to the synsedimentary age appear. Despite having a small number (only 3–5 in each sample), these young zircons have been detected in high concentrations in three samples, confirming the credibility of analysis results. By comparison, it is shown that the zircon ages of $J_2l_{2\text{-}3}$ in the study area and in the Lianghekou area reported by Qian (2015) are centralized in same ranges; however, they have significant differences in their proportions. It is also indicated that the provenance of $J_2l_{2\text{-}3}$ consists of at least two parts: one is composed of relatively younger zircons formed after 400 Ma, and the other is made up of older zircons at age of 400–2,500 Ma. It is speculated the younger zircons came from the South Qinling in the north, and those of older age were transported from the northwest. The older zircons have been recorded in neither the North Qinling

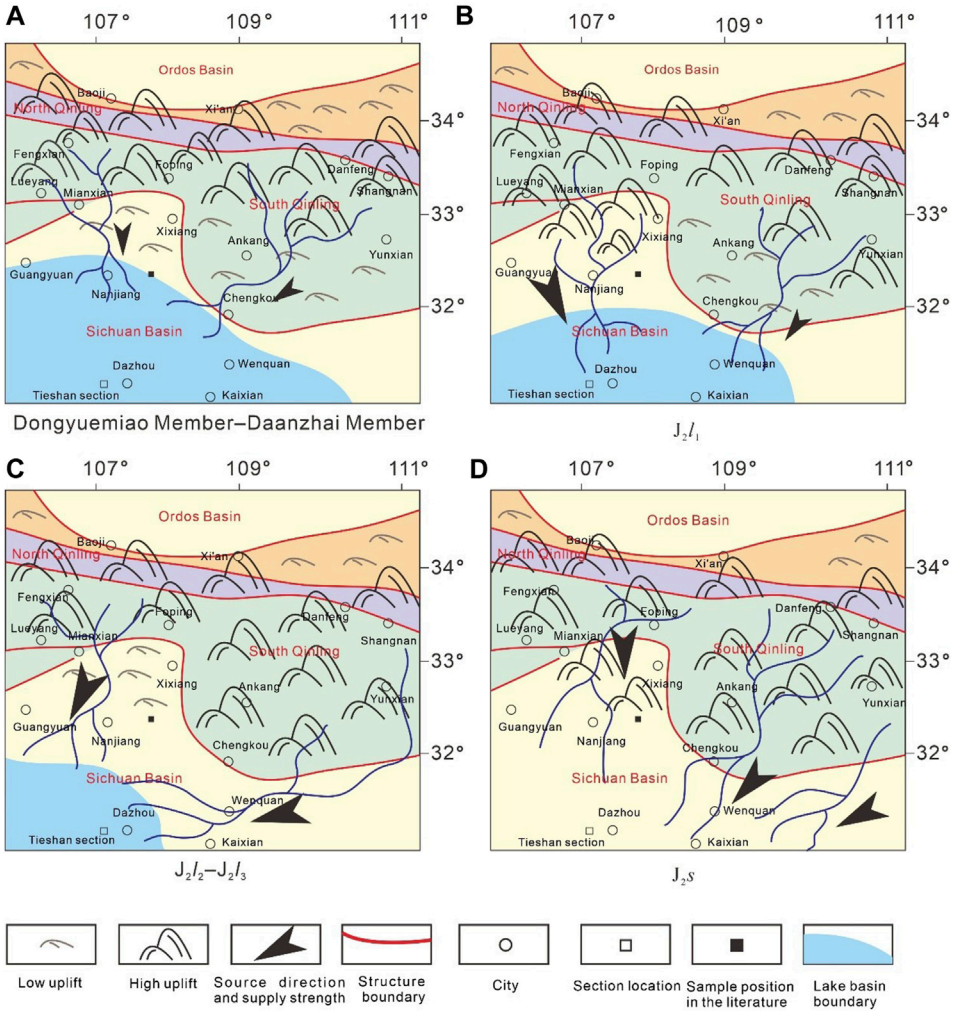

FIGURE 6
Variation in the Middle–Lower Jurassic sedimentary area and provenance in the northeastern Sichuan Basin.

nor the South Qinling, only in the North China plate, resulting in significant controversy on their source. For example, provenance of the Archean–Paleoproterozoic zircons was reported as the ancient basement of the Qingling orogenic belt by Li et al. (2010), was speculated to be the northern margin of the South China plate by Qian (2015), and was indicated as the Paleozoic–Early Mesozoic sedimentary rocks by Li et al. (2018). These zircons show similar age distribution to the southern margin of the North China plate. However, it was impossible for erosion products of the North China plate to break through the barrier formed by the fore-arc accretionary wedges generated by subduction and collision between plates during the Archean–Paleoproterozoic. Therefore, it is concluded that the zircons are mainly from the earlier sedimentary rocks mingled with zircons in the basement of the Qingling orogenic belt. According to the emergence of young zircons and increase of old zircons in this period, an inference could be drawn that the Qingling orogenic belt experienced strengthened tectonic movement during J_2l_2. Consequently, a larger number of old layers and basement rocks cropped out and suffered erosion. In the meanwhile, the rapid uplifting of the Dabashan Mountain allowed an input of sediments in the north from the northeast of the basin and generated a major influence on the northeastern Sichuan Basin and a significantly decreased impact on the northern part of the central Sichuan Basin. Moreover, the remarkably reduced amount of the Neoproterozoic zircons and their gradually decreasing trend from J_2l_2 to J_2l_3 suggest that the Hannan area and Micangshan Mountain have experienced another tectonic stabilization after short-term uplifting followed by deposition of the Ziliujing Formation. Due to long-term denudation, the Hannan area and Micangshan Mountain provided gradually reducing sediments to the sedimentary area.

Zircon age distributions in both the lower J_2s_1 and $J_2l_{2\text{-}3}$ are similar and comparatively more dispersive than other formations. It could be explained by their more complex source and the possible combined contribution of multiple sources. Another increase in the proportion of the Early Paleozoic zircons indicates that the Hannan area and Micangshan Mountain were uplifted again, leading to an increased proportion of the sediments provided by it to the sedimentary area. A comparison of detrital zircons in the Shaximiao Formation between the study area and in the

Kaixian–Wenquan area that was reported by Li et al. (2010) shows similar age distributions. However, the Neoproterozoic zircons have been barely detected in the former, suggesting that the sediments from the Micangshan Mountain failed to extend into Kaixian–Wenquan.

6 Uplifting stages of adjacent orogenic belts and their influence on sedimentary evolution

Along with the closing of the Qingling Ocean, the Sichuan Basin evolved from a marine basin into a continental basin during the Middle–Late Triassic. The sedimentary center migrated from the western Sichuan Basin to the Micangshan Mountain and Dabashan Mountain in the northern Sichuan Basin in the Jurassic (Cheng, 2014). The results of this study indicate that the Early–Middle Jurassic provenance of the northeastern Sichuan Basin mainly includes the northern margin of Yangtze plate and the Qinling orogenic belt and excludes the source supply from the North Qinling orogenic belt. It suggests that tectonic uplifting of the South Qingling orogenic belt occurred in the Early Jurassic. Tectonic activities within the northeastern Sichuan Basin caused the unconformity contact between the Triassic and the Jurassic, and the subsequent uplifting and denudation continued until the Early Jurassic, when the deposition of the Zhenzhuchong Member ended. The subsequent tectonic stabilization allowed a change from fluvial-delta facies with strong sediments supply to lacustrine facies in the northeastern Sichuan Basin (Figure 6A).

There is still a relatively large controversy on the uplifting period of the Micangshan Mountain in the northern Sichuan Basin. According to the distribution of continental sequences, it is generally believed that the Micangshan Mountain experienced large-scale uplifting in the Late Triassic and another intensive uplifting under the action of the Longmenshan Mountains and Qingling Mountains in the Early Jurassic; after that, slow uplifting continued until overthrusting occurred during the Himalayan (Guo, 1996; Liu et al., 2003). Based on the internal unconformities in the Triassic strata, Shen et al. concluded that the Micangshan Mountain had developed thrust belts in the Early Triassic, and the front of thrust belts had reached the present front of the foreland thrust belt (Shen et al., 2010). The recent apatite fission track analysis and zircon (U–Th)/He dating indicate that the Micangshan Mountain experienced rapid uplifting and relative large-scale erosion in the late Early Cretaceous and another rapid uplifting at 20–15 Ma. The apatite fission track data of the Micangshan structural belt show that it is generally younger than the Sichuan Basin in the north and reflect that uplifting of the thrust belt and uplifting of the basin are not synchronous processes, with the former occurring earlier. The Micangshan Mountain was dominated by sedimentation due to generally weak tectonic effect before the Cretaceous, experienced intensive intracontinental deformation and mainly finalized structurally during the Cretaceous, and has been uplifted as a whole since the Late Eocene. Through dating the zircons from clastic rocks in front of the Micangshan Mountain, Li et al. analyzed the change in source supply of the southern margin of the Micangshan Mountain since the Late Triassic. It was speculated that the Hannan–Micangshan area experienced uplifting and erosion in the Late Triassic, followed by piggy-back uplifting to the south of the South Qingling orogenic belt in the Early Jurassic, which continued to the Late Jurassic; during the Early Cretaceous, the front of the Micangshan Mountain accepted sediments from multiple provenances along with intensive orogenic movement within the peripheral orogenic belts of the Sichuan Basin (Li et al., 2018). He et al. reported two stages in the tectonic evolution of the Micangshan Mountain: the late Early Cretaceous–early Late Cretaceous slip deformation and the Neogene large-scale uplifting (He et al., 2020). According to the results of this study, it is considered that the Micangshan Mountain was not exposed dramatically in the Early Jurassic but was probably uplifted slightly and stabilized tectonically again after one stage of rapid uplifting (Figure 6B). As it lasted for a short time, the uplifting mainly provided a large amount of clastic sediments to the study area but failed to change its characteristic dominance of lacustrine sediments.

Many scholars have worked a lot on the tectonic evolution of the Dabashan Mountain. Xie regarded the Dabashan Mountain as the product of superposition of two stages of tectonic processes: the earlier stage is the Indosinian collision orogenesis in the south of the South Qinling (230–200 Ma), which is the dominant controlling tectonic event; and the later stage is the Late Indosinian–Early Yanshanian extensional collapse and the intracontinental orogenesis in the Middle–Late Yanshanian (165–100 Ma) (Xie et al., 2014). He et al. divided the tectonic evolution of Dabashan Mountain into four stages: 1) during the Middle–Late Triassic, the northern Dabashan Mountain was formed and the southern Dabashan Mountain was still located in the subsidence center; 2) during the Late Triassic to Early Jurassic, the northern Dabashan Mountain mainly experienced thrusting and was uplifted as a whole; 3) during the late Early Cretaceous, the northern Dabashan Mountain was fully formed, and the southern Dabashan Mountain began to thrust, resulting in a wide and gentle anticline cropped out; and 4) during the Paleogene, the southern Dabashan Mountain started to suffer a strong deformation (He et al., 2020). The results of this study indicate that the Dabashan Mountain experienced low-amplitude uplifting during the Early Jurassic and rapid uplifting during J_2l_2 (Figure 6C). The rapid uplifting of Qinling and Dabashan Mountains supplied a large amount of sediments to the basin and also changed their input direction, and the extensive shrinkage of lake basin in the northeastern Sichuan Basin changed the sedimentary facies characterized by the lacustrine deposits in dominance that have been formed since the end of Zhenzhuchong Member deposition.

A large-scale tectonic compression in the Qingling orogenic belt during the deposition of the Shaximiao Formation further uplifted the Dabashan and Micangshan mountains, which provided a significant amount of sediments to the foreland basin, and lake basins disappeared completely in the northeastern Sichuan Basin (Figure 6D).

7 Conclusion

The strata from the Ziliujing Formation to the bottom of the Shaximiao Formation on the Tieshan section and the northwestern Sichuan Basin suggest the paleocurrent direction generally as NE–SW.

(1) The Zhenzhuchong Member is sufficiently supplied with detrital sediments and is dominantly composed of fluvial-delta deposits. The Dongyuemiao Member–J_1l_1 is dominated by lacustrine

deposits. An enhanced source supply has been detected from the end of Daanzhai Member to J_1l_1. Since the initial deposition of J_1l_2, the detrital supply increased and lake shrinkage occurred. The detrital supply reached its maximum during the deposition of the Shaximiao Formation when the lake basin disappeared completely in the northern Sichuan Basin.

(2) The heavy mineral assemblages and zircon U–Pb ages indicate that the northeastern Sichuan Basin has experienced three distinct changes in source supply, respectively, between the Ziliujing period and the Lianggaoshan period, between J_2l_1 and J_2l_2, and between the Lianggaoshan period and the Shaximiao period. The latter two are the most distinct.

(3) The sediments of the Ziliujing Formation were mainly sourced from the South Qingling, and the source supply from the Hannan and Micangshan Mountain increased rapidly during the J_2l^2 deposition. The source properties were complicated when the Shaximiao Formation was deposited, with the combined contribution of multiple provenances detected.

(4) Changes in the sedimentary environment and source supply are responses to tectonic activities. The three changes in the study area correspond to the uplifting of the Micangshan Mountain, the uplifting of the Dabashan Mountain, and the overall uplifting of the Qinling orogenic belt, respectively. Along with the three phases of tectonic uplifting, lake basins gradually shrank and finally disappeared completely in the northeastern Sichuan Basin.

Data availability statement

The datasets presented in this study can be found in online repositories. The names of the repository/repositories and accession number(s) can be found in the article/Supplementary Material.

Author contributions

HH: Conceptualization, Methodology, Writing-Original Draft. CQ: Conceptualization, Methodology, Writing-Original Draft. SZ: Data curation, Supervision. ZZ: Supervision. XW: Supervision. NL: Formal analysis. DC: Investigation. WT: Validation.

Funding

This research was supported by the Natural Science Foundation of China (NSFC) Project (No. 42202188), and TW was supported by the Sichuan Science and Technology Program (No. 2023NSFSC1986).

Conflict of interest

HH, CQ, SZ, XW, and NL were employed by PetroChina Southwest Oil and Gas Field Company, PetroChina Southwest Oilfield Company. ZZ and DC were employed by PetroChina Research Institute of Petroleum Exploration and Development.

The remaining author declares that the research was conducted in the absence of any commercial or financial relationships that could be construed as a potential conflict of interest.

The reviewer WT declared a shared affiliation with the authors WT, XK to the handling editor at time of review.

Publisher's note

All claims expressed in this article are solely those of the authors and do not necessarily represent those of their affiliated organizations, or those of the publisher, the editors, and the reviewers. Any product that may be evaluated in this article, or claim that may be made by its manufacturer, is not guaranteed or endorsed by the publisher.

References

Cai, R. (2020). Detrital records of the eastern qinling indosinian orogenic processes: sedimentology and sedimentary provenance analysis of the middle triassic-early jurassic successions in zigui basin. PhD dissertation. Beijing: China University of Geosciences.

Cheng, L. X. (2014). Sedimentary response within orogenic movement of basin edge during late triasiic to jurassic in eastern and northern sichuan, China. PhD dissertation. Chengdu, China: Chengdu University of Technology.

Diwu, C. R., Sun, Y., Zhang, H., Wang, Q., Guo, A. L., and Fan, L. G. (2012). Episodic tectonothermal events of the western north China craton and North Qinling orogenic belt in central China: constraints from detrital zircon U-Pb ages. *J. Asian Earth Sci.* 47 (3), 107–122. doi:10.1016/j.jseaes.2011.07.012

Dong, Y. P., Liu, X. M., Santosh, M., Chen, Q., Zhang, X. N., Li, W., et al. (2012). Neoproterozoic accretionary tectonics along the northwestern margin of the Yangtze block, China: constraints from zircon U-Pb geochronology and geochemistry. *Precambrian Res.* 196-197, 247–274. doi:10.1016/j.precamres.2011.12.007

Dong, Y. P., Liu, X. M., Santosh, M., Zhang, X. N., Chen, Q., Yang, C., et al. (2011). Neoproterozoic subduction tectonics of the northwestern Yangtze block in South China: constrains from zircon U-Pb geochronology and geochemistry of mafic intrusions in the hannan massif. *Precambrian Res.* 189, 66–90. doi:10.1016/j.precamres.2011.05.002

Dong, Y. P., Yang, Z., Liu, X. M., Sun, S. S., Li, W., Cheng, B., et al. (2016). Mesozoic intracontinental orogeny in the qinling mountains, central China. *Gondwana Res.* 30 (1), 144–158. doi:10.1016/j.gr.2015.05.004

Fu, J. H. (2016). *Late paleozoic-mesozoic basin evolution in the longmenshan-dabashan region and its tectonic implications*. Thesis (Beijing: China University of Geosciences).

Geng, Y. Y. (2010). SHRIMP zircon U-Pb dating and geochemical characteristics of granites in the northern margin of the Yangtze block. master dissertation. Beijing: China University of Geosciences.

Guo, Z. W., Deng, K. L., and Han, Y. H. (1996). *Formation and evolution of Sichuan Basin*. Beijing: Geological Press, 120–138.

He, D. F., Li, Y. Q., Huang, H. Y., Zhang, J., Lu, R. Q., and Li, D. (2020). *Formation, evolution and hydrocarbon accumulation of multi-cycle superimposed basins in sichuan*. Science Press, 49–83.

Hu, J. M., Cui, J. T., Meng, Q. R., and Zhao, C. Y. (2004). Zircon U-Pb age of the Zhashui pluton in Qinling Mountains and its geological significance. *Geol. Rev.* 50 (3), 323–329.

Li, H. K., Lu, S. N., Chen, Z. H., Xiang, Z. Q., Zhou, H. Y., and Hong, G. J. (2003). Zircon U-Pb geochronology of rift-type volcanic rocks of the yaolinghe group in the South qinling orogen. *Geol. Bull. China* 22 (10), 775–781.

Li, J. H., Zhang, Y. Q., Xu, X. B., Dong, S. W., and Li, T. D. (2012). Zircon U-Pb LA-ICP-MS dating of fenghuangshan pluton in northern dabashan mountains and its implications to tectonic settings. *Geol. Rev.* 58 (2), 581–593.

Li, R. B., Pei, X. Z., Liu, Z. Q., Li, Z. C., Ding, S. Q., Liu, Z. G., et al. (2010). Basin-mountain coupling relationship of foreland Basins between dabashan and northeastern sichuan-the evidence from LA-ICP-MS U-Pb dating of the detrital zircons. *Acta Geol. Sin.* 84 (8), 1118–1134.

Li, S. J., Sun, D. S., Cai, L. G., Gao, P., and Li, T. Y. (2018). Detrital zircon U-Pb geochronology of Micangshan Mountain piedmont zone, northern sichuan Basin and its significance to basin-mountain evolution. *Geotect. Metallogenia* 42 (6), 1087–1107.

Ling, W. L., Gao, S., Oyang, J. P., Zhang, B. R., and Li, H. M. (2002). Age and tectonic setting of the Xixiang group: constraints on isotopic chronology and geochemistry. *Sci. China (Series D)* 32 (2), 101–112.

Liu, S. G., Luo, Z. L., and Zhao, X. K. (2003). Coupling relationships of sedimentary basinbasin-orogenic belt systems and their dynamic models in west China-A case study of the longmenshan orogenic belt- west sichuan foreland basin system. *Acta Geol. Sin.* 77 (2), 177–186.

Liu, Y., Gao, S., Hu, Z., Gao, C., Zong, K., and Wang, D. (2010a). Continental and oceanic crust recycling-induced melt-peridotite interactions in the trans-north China orogen: U-Pb dating, Hf isotopes and trace elements in zircons from mantle xenoliths. *J. Petrology* 51 (1), 537–571. doi:10.1093/petrology/egp082

Liu, Y., Hu, Z., Zong, K., Gao, C., Gao, S., Xu, J., et al. (2010b). Reappraisement and refinement of zircon U-Pb isotope and trace element analyses by LA-ICP-MS. *Chin. Sci. Bull.* 55 (15), 1535–1546. doi:10.1007/s11434-010-3052-4

Liu, Y. S., Hu, Z. C., Gao, S., Günther, D., Xu, J., Gao, C. G., et al. (2008). *In situ* analysis of major and trace elements of anhydrous minerals by LA-ICP-MS without applying an internal standard. *Chem. Geol.* 257 (1–2), 34–43. doi:10.1016/j.chemgeo.2008.08.004

Ludwig, K. R. (2003). *Isoplot 3.00: A geochronological toolkit for microsoft excel*. Berkeley, California: Berkeley Geochronology Center.

Qian, T. (2015). Stratigraphic framework of the northern Yangtze foreland basin in the early-middle jurassic: A record of continent-continent collision. PhD dissertation. Beijing: China University of Geosciences.

Qu, H. J., Dong, Y. P., Ma, Q., Zha, X. F., and Xu, Z. Y. (2009). Reversion of paleocurrent directions and its tectonic significance in the late triassic and jurassic period in yunyang chongqing. *J. Northwest Univ. Nat. Sci. Ed.* 39 (3), 528–532.

Shen, Z. Y., Xiao, A. C., Wang, L., Guo, J., Wei, G. Q., and Zhang, L. (2010). Unconformity in the lower triassic of micangshan area, northern sichuan Province: its discovery and significance. *Acta Petrol. Sin.* 26 (4), 1313–1321.

Shi, Y., Yu, J. H., and Santosh, M. (2013). Tectonic evolution of the qinling orogenic belt, Central China: new evidence from geochemical, zircon U-Pb geochronology and Hf isotopes. *Precambrian Res.* 231 (1), 19–60. doi:10.1016/j.precamres.2013.03.001

Sun, D. (2014). The structural character and meso-cenozoic evolution of Micangshan Mountain structural zone, northern Sichuan Basin. PhD dissertation. China: Chengdu University of Technology.

Sun, W. D., Li, S. G., Chen, Y. D., and Li, Y. J. (2000). Zircon U-Pb dating of granitoids from South Qinling, Central China and their geological significance. *Geochimica* 29 (3), 209–216.

Wang, R., Hu, Z., Long, S., Liu, G., Zhao, J., Dong, L., et al. (2019). Differential characteristics of the upper ordovician-lower silurian wufeng-longmaxi shale reservoir and its implications for exploration and development of shale gas in/around the Sichuan Basin. *Acta Geol. Sin. Engl. Ed.* 93 (3), 520–535. doi:10.1111/1755-6724.13875

Xie, J. Q. (2014). Formation age and composite evolution of nappe structure in North Dabashan Mountain. PhD dissertation. Evanston, Illinois: Northwestern University.

Yang, Y. M., Wang, X. J., and Chen, S. L. (2022). Sedimentary system evolution and sandbody development characteristics of Jurassic Shaximiao Formation in the central Sichuan Basin. *Nat. Gas. Ind.* 42 (1), 12–24.

Zhai, M. G., and Bian, A. G. (2000). Late neoarchean supercontinent assembly and late paleoproterozoic-mesoproterozoic breakup in the North China craton. *Sci. China (Series D)* 30, 129–137.

Zhang, G. W., Yu, Z. P., Dong, Y. P., and Yao, A. P. (2000). On precambrian framework and evolution of the qinling. *Acta Petrol. Sin.* 16 (1), 11–21.

Zhang, G. W., Zhang, B. R., Yuan, X. C., and Xiao, Q. H. (2001). *Qinling orogenic belt and continental dynamics*. Beijing: Science Press, 1–855.

Zhang, S. G., Zhang, Z. Q., Song, B., Tang, S. H., Zhao, Z. R., and Wang, J. H. (2005). On the existence of neoarchean materials in the douling Complex,Eastern qinling-evidence from U-Pb SHRIMP and Sm-Nd geochronology. *Acta Geol. Sin.* 78 (6), 800–806.

Zhang, X., Xu, X. Y., Song, G. S., Wang, H. L., Chen, J. L., and Li, T. (2010). Integrative genome-wide approaches in embryonic stem cell research. *Geol. Bull. China* 29 (4), 510–516. doi:10.1039/c0ib00068j

Zhang, Z. Q., Zhang, G. W., Tang, S. H., Zhang, Q. D., and Wang, J. H. (2000). The age of the Hannan intrusive complex and its cause of rapid condensation. *Chin. Sci. Bull.* 45 (23), 2567–2571.

Zhao, F. Q., Zhao, W. P., Zuo, Y. C., Li, Z. H., and Xue, K. Q. (2006). U-Pb geochronology of neoproterozoic magematic rocks in hanzhong, southern shaanxi, China. *Geol. Bull. China* 25 (3), 383–388.

Zhao, J. H., Zhou, M. F., Yan, D. P., Yang, Y. H., and Sun, M. (2008). Zircon Lu-Hf isotopic constraints on Neoproterozoic subduction-related crustal growth along the western margin of the Yangtze Block, South China. *Precambrian Res.* 163 (3–4), 189–209. doi:10.1016/j.precamres.2007.11.003

Frontiers in Earth Science

Investigates the processes operating within the major spheres of our planet

Advances our understanding across the earth sciences, providing a theoretical background for better use of our planet's resources and equipping us to face major environmental challenges.

Discover the latest Research Topics

See more →

Frontiers

Avenue du Tribunal-Fédéral 34
1005 Lausanne, Switzerland
frontiersin.org

Contact us

+41 (0)21 510 17 00
frontiersin.org/about/contact